Differential interferometry of the Broad Line Region of quasars : innermost structure of quasars using optical interferometry and reverberation mapping

Suvendu Rakshit

UNIVERSITE NICE SOPHIA ANTIPOLIS

European Community Erasmus Mundus Joint Doctorate
International Relativistic Astrophysics Ph.D. Program

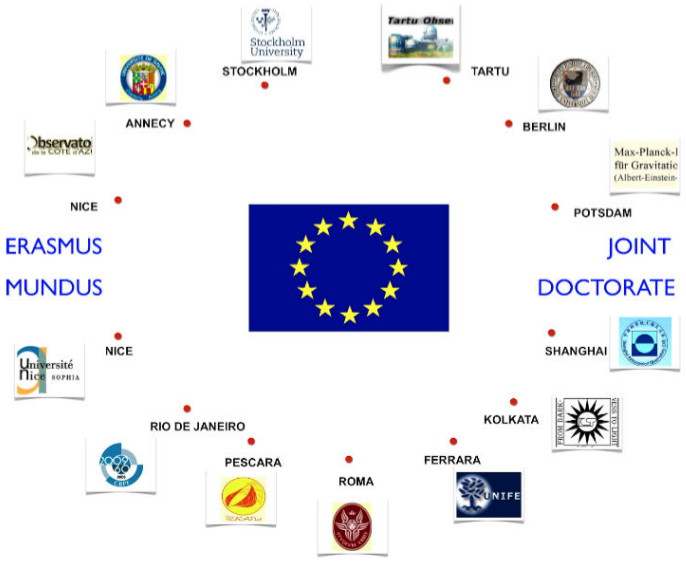

Differential interferometry of the Broad Line Region of Quasars

Innermost structure of quasars using optical interferometry and reverberation mapping

Presented and defended by

Suvendu RAKSHIT

Erasmus Mundus Fellow

Defended on
the 17th of July 2015

Jury:

Walter Jaffe	Professor, U. Leiden, Leiden	Reviewer
Gerd Weigelt	Professor, MPIFR, Bonn	Reviewer
Fabien Malbet	Director of Research, IPAG, Grenoble	Examiner
Patrick Petitjean	Astronomer, IAP, Paris	Examiner
Eric Slezak	Astronomer, Lagrange, OCA	Examiner
Romain Petrov	Director of Research, Lagrange, OCA	Supervisor

UNIVERSITÉ NICE SOPHIA ANTIPOLIS
ECOLE DOCTORALE INTERNATIONALE
D'ASTROPHYSIQUE RELATIVISTE

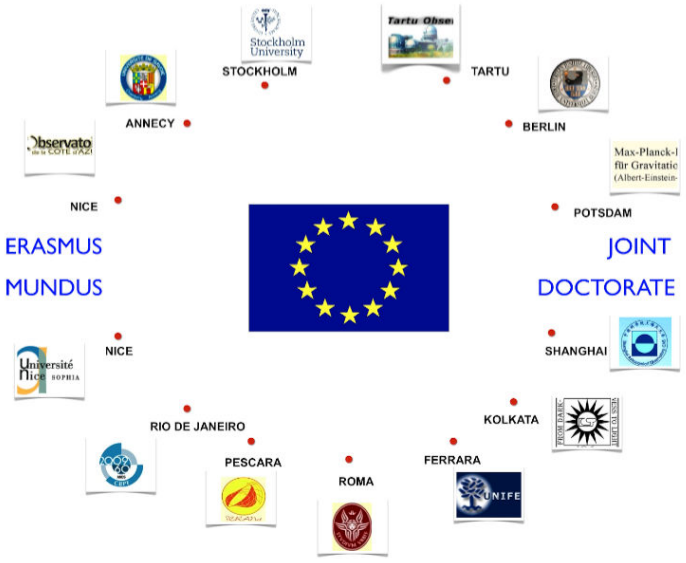

Interférométrie Différentielle des régions à raies larges (BLR) des quasars

Règion centrale des quasars en combinant interferomètrie optique et cartographie des èchos lumineux.

Suvendu RAKSHIT

Boursier Erasmus Mundus

Soutenue le
the 17th of Juillet 2015

Jury:

Walter Jaffe	Professeur, U. Leiden, Leiden	Rapporteur
Gerd Weigelt	Professeur, MPIFR, Bonn	Rapporteur
Fabien Malbet	Directeur de Recherche, IPAG, Grenoble	Examinateur
Patrick Petitjean	Astronome HDR, IAP, Paris	Examinateur
Eric Slezak	Astronome HDR, Lagrange, OCA	Examinateur
Romain Petrov	Directeur de Recherche, Lagrange, OCA	Directeur de thèse

Abstract

Active Galactic Nuclei (AGNs) and the subclass quasars are powered by the accretion of matter onto a super massive black hole (SMBH) surrounded by an accretion disk, which is surrounded by the broad line region (BLR) where clouds are orbiting around the SMBH with high velocity. The study of the BLR is crucial to understand geometry and kinematics of the central engine, accretion mechanism, SMBH mass estimate and distance measurement across cosmic time. Reverberation mapping (RM) estimates BH masses using virial relation, which relies on a poorly known scale factor that depends on geometry and kinematic of the BLR. Optical interferometry (OI) with its high angular resolution can constrain the geometry, estimate scale factor, and calibrate the BH mass-luminosity relation obtained by RM.

Using "blind mode observation" at AMBER/VLTI, for the first time it has been possible to resolve the BLR of the quasar 3C273 in Paα. The first result shows a drop in differential visibility indicating an extended BLR much larger than RM prediction. I developed a three-dimensional geometrical and kinematical model that simultaneously predicts all RM and OI signals, showing that differential measures can provide strong constraints on the BLR. A Bayesian model fit of the simulated OI data sets show BH mass can be constrained with an uncertainty less than 0.15 dex, which can further be reduced by combining OI data with RM data. A global fit to the 3C273 data shows that the Paα BLR is extended beyond the dust inner rim, inclined close to face-on and has a spherical structure, where Keplerian rotation and macroturbulent velocities have similar contribution. The mass of the SMBH in 3C273 is found to be about $5 \times 10^8\, M_\odot$. Comparing to the RM virial mass, this provides the value of scale factor to be about 3.

To use BLRs as standard candles, I investigated the BLR parallax method from simulated RM and OI data finding an accuracy better than 20% on the distance estimation. I performed an evaluation of the potential of second-generation VLTI instruments such as GRAVITY, MATISSE, and possible instruments dedicated to BLR work (OASIS, OASIS+ and OASIS+fringe tracker). This suggests VLTI at its full potential with a next generation fringe tracker could allow us to observe 60 targets on a large range of

luminosity, sufficient to attempt a big unification from the study of BLR model parameters as a function of luminosity. The combination of RM, OI and spectro-astrometry could transform quasars in a decisive cosmological tool.

Résumé

Les noyaux actifs de galaxies (AGN), dont les quasars sont une sous classe, sont animées par l'accrétion de matiére autour d'un trou noir super massif (SMBH). Le disque d'accrétion est entouré par des nuages de gaz qui se déplacent à grande vitesse et produisent des raies d'émission trés larges et constituent la Broad Line Region ou BLR. L'étude des BLRs est cruciale pour comprendre la géométrie et la cinématique du moteur central des AGNs, contraindre le mécanisme d'accrétion et mesurer la masse du trou noir. Elle peut être utilisée pour mesurer la distance des quasars à des échelles cosmologiques. La technique de cartographie des échos lumineux, ou Reverberation Mapping (RM) permet d'estimer la masse du SMBH à partir d'une relation virielle qui est affectée d'un facteur de projection mal connu et trés dépendant de la géométrie de la BLR. L'interférométrie optique (IO) peut contraindre cette géométrie et donc ce facteur d'échelle et permet donc de calibrer la relation masse-luminosité des quasars fournie par RM.

Une nouvelle technique d'observation en aveugle avec l'instrument AMBER du VLTI a permis de résoudre pour la premiére fois la BLR du quasar 3C273 dans la raie. Les premiers résultats ont été une chute de la visibilité différentielle dans la raie d'émission ce qui indique une BLR trés étendue, bien plus grande que la prédiction du RM pour cette source. Une analyse soignée de nos données interférométriques et des données de RM a permis de confirmer ce résultat. Nous avons mis au point un modéle tridimensionnel de la géométrie et de la cinématique des BLRs qui permet d'estimer simultanément les mesures de RM et d'IO. Il nous a permis de montrer que l'IO contraignait fortement des BLRs malgré la résolution insuffisante du VLTI. Un ajustement de modéle Bayésien de données simulées montre que l'IO seule permet des mesures de masse avec une précision de 0.15 dex, qui peut être améliorée en combinant IO et RM. Ce modéle a été utilisé pour interpréter les observations de 3C273 et nous obtenons une BLR presque deux fois plus étendue que le bord interne du tore de poussiére, observé pratiquement de face et avec une structure sphérique avec une des vitesses de macroturbulence et de rotation globale à peu prés équivalentes. La masse du SMBH est de , ce qui correspond à un facteur de projection.

Nous avons évalué une méthode de mesure des distances, appelée BLR parallax à partir de la combinaison des mesures linéaires du RM et angulaire de l'IO. Nous montrons des précisions de distance typique de 20 % à 500 Mpc et nous donnons des pistes pour améliorer ce potentiel. Nous avons analysé le potentiel du VLTI avec ses instruments de seconde génération GRAVITY et MATISSE ainsi qu'avec des instruments optimisés pour

l'observation á moyenne résolution de BLR, comme OASIS et OASIS+, éventuellement combinés à un suiveur de frange de nouvelle génération. Nous montrons que le VLTI pleinement exploité permettrai de résoudre plus de 60 BLR avec une large gamme de luminosités, suffisante pour tenter une grande unification des modéles de BLR fondées sur l'étude de leurs paramétres en fonction de la luminosité et de leur spectre d'émission. La combinaison de l'IO et du RM, puis de la spectro-astrométrie transformerait alors les quasars en sondes cosmologiques majeures.

Acknowledgments

In 2012, when I arrived in Nice, I was very much excited about the new place, about the work and about the life here. First month in Nice was a bit difficult for me mainly because of the language, a different way of life and food, but things become perfect after some time. The first person I met in Nice was my supervisor Romain Petrov. My sincere and deepest gratitude to him for his kind and friendly behavior that made me very comfortable to discuss any kind of topic. He was always supportive and showed me the right direction to complete my work. He is the person who introduced optical interferometry to me and guided me to complete my PhD thesis work. I thank Stephane Lagarde for his initial help in modeling interferometric data and more useful discussions. I am very grateful to Anthony Meilland for his help to develop me code and discussions in many science topic. His friendly behaviors made me comfortable to discuss any kind of problems. I express my heartiest gratitude to Florentin Millour for teaching me AMBER+ data reduction and Martin Vennier for his help in data reduction. My deepest gratitude goes to Eric Fossat for sharing his ideas about time series analysis. I will always be grateful to Sebastian Hoenig for his advice and help during the last year of my PhD. I am thankful to many others like Hum Chand, Bruno Lopez, Farrokh Vakili for many useful discussions during these years.

Three years is a long time and would not have completed happily without the help of many people. It was possible due to the constant support and love of some persons who will be always in my heart. During that time, my parents Jaba Rakshit and Sunil Rakshit were always supporting me from India, encouraging me for my work and teaching me how to cook Indian food in which I had zero experience. Neha's supports and encouragements were with me since I started my thesis. She helped me to tackle all the problems that I faced during my PhD. She made my life easier by notifying me many small mistakes errors in my papers and manuscripts. I will be always grateful to my Didi Lipika, Jijaji Chandi and little Chandrima for their support during these years. I want to thank them all for being with me all the time.

We often say “Har ek friend jaruri hota hai” (every friend is mandatory). In last years, I got many friends with whom I shared my problems about work and life, and spent time happily. Specially I will never forget the supports and the encouragements that I have received from Mamadou, who is not only a friend but also a brother of mine. I will be always thankful to Narges, Zeinab, Samir, Husne, Arwa, Onelda, Sibila, Alvaro, Alkis, Srivatsan, Gaetan, Judit and many other friends for their support and the wonderful times that we spent together. I also thank Abhishek, Archana, Piyush and Subhajeet for their support from India. I express my gratitude to Parikshit, Veenth and Disha for their help. I am grateful to many other friends who will be always in my heart.

It would have difficult to complete all the administrative work without the help of Pascal Chardonnet, Pina Barbaro, Emmanuel Losero, Cathy Blanc and Delphine Saissi. I appreciate the help of Daniel Kamm, Arielle Willm and others to solve many technical problems. I am grateful to all of them. I am thankful to Khaled, Karima and Nathalie for cooking so good food everyday.

My deepest gratitude to all the jury members for spending their valuable time to review my thesis and for coming to attend my thesis defense. Their comments and suggestions helped me to improve this thesis.

Finally, I must acknowledge the “power” which kept me strong enough to overcome all the difficulties that I faced during these years.

Thanks to all for helping me to make my dream successful.

"So many things on the night sky
very different from each other
there must be reasons
finding them must be fascinating"

–suvendu

Dedicated to
Ma, Baba and Didi

Contents

Thesis summary in French

Note du traducteur

Cette thése "Erasmus Mundus" a été prépareée à l'Observatoire de la Côte d'Azur, dans le cadre de l'Ecole Doctorale Internationale d'Astrophysique Relativiste (IRAP) par une étudiant indien qui n'écrit pas le français. La Présidente de l'Université Nice Sophia Antipolis, qui est le noeud central du réseau IRAP et le lieu naturel de soutenance de cette thése niçoise, a autorisé un mémoire et une soutenance en anglais, à condition que:

- La page de couverture soit en français
- Le résumé, l'introduction et la conclusion soient traduits en français
- Le corps de la thése soit preésenté en français dans un résumé substantiel "d'au moins 4 pages".

Quand c'est le directeur de thése qui se charge de ce travail de traduction, celui-ci peut être tenté de combiner traduction et réécriture à son goût. J'espére avoir résisté à cette tentation pour traduire au plus près du texte anglais de l'auteur, en évitant les barbarismes de la traduction littérale mais en affectant aussi peu que possible le contenu scientifique et la structure de l'original.

Romain Petrov

1.1 INTRODUCTION A CETTE THESE

1.1.1 Objectifs de cette thèse

Les noyaux actifs de galaxies (AGN pour Active galactique Nuclei) sont des sources très brillantes, qui émettent ensemble 1/5 du flux électromagnétique total dans l'univers. Leur source d'énergie est l'accrétion de matière autour d'un trou noir super massif (SMBH pour Super Massive Black Hole). Le disque d'accrétion est entouré de nuages de gaz qui se déplacent à des vitesses de plusieurs milliers de km/s et émettent des raies très élargies, d'ou le nom de Broad Line Region (BLR) attribué à cette structure qui s'étend de quelques jours lumière à quelques centaines de jours lumière.

Les AGNs sont classés en toutes sortes de catégories en fonction des propriétés de leur émission, mais d'après le « modèle unifié » des AGNs toutes ces catégories aurait la même structure, et les différences seraient dues à l'angle entre l'axe de l'AGN et la direction de visée. Une sous classe d'AGN très brillantes ont été considérées comme des sources ponctuelles (des étoiles) d'où le nom d'objets quasi stellaires (QSO ou quasars). Ils présentent des raies d'émission très larges à de très hauts décalages vers le rouge. L'étude des QSO peut expliquer l'évolution des AGNs et la coévolution du trou noir central et de la galaxie hôte à des échelles cosmologiques. De plus, l'observation d'AGNs à très fort décalage vers le rouge peut contraindre l'évolution des trous noirs et la distribution des masses dans l'univers. L'étude des BLRs à une importance toute particulière dans ce contexte car elle permet de mesurer la masse du SMBH et de contraindre le mécanisme d'accrétion. Elles peuvent aussi être utilisées comme des chandelles standard pour l'estimation des distances. Toutefois, ces mesures demandent une bien meilleure connaissance de la géométrie et de la cinématique (i.e. du champ de vitesse) de la BLR, car les mesures de masse qui sont fournies par la technique d'échographie lumineuse (Reverberation Mapping ou RM) des BLRs sont très dépendantes de cette structure interne mal connue.

L'objectif principal de cette thèse est donc d'utiliser l'interférométrie optique (IO) à très haute résolution angulaire pour contraindre la géométrie et la cinématique des BLRs, bien que celles ci soient en deçà de la limite classique de résolution des interféromètres actuels. Nous allons étudier la combinaison d'observations par interférométrie optique (IO) et par échographie lumineuse (RM) pour étudier la morphologie des BLRs. Nous avons développé un modèle tridimensionnel de BLR to prédire simultanément les mesures d'IO et de RM. Nous examinerons les effets des différents paramètres de ce modèle sur ces mesures. Nous présentons aussi les premières observations interférométriques du quasar 3C273 et un ajustement global de ces résultats avec notre modèle. Une analyse de rapport signal à bruit (RSB) permettra d'évaluer le potentiel des instruments interférométriques existants comme de ceux qui sont sur le point d'être livrés ou proposés dans les prochaines années. Des quasars ont été observés jusqu'à un décalage vers le rouge de 7. Ils peuvent donc être utilisés pour étudier l'univers jeune, si on peut mettre au point une méthode de mesure directe de leur distance. Ils pourraient alors être utilisés pour mesurer le taux d'expansion de l'univers à différentes époques et tester la présence de matière ou d'énergie noire. Nous allons donc décrire une méthode géométrique de mesure de distance appelée « parallaxes des BLRs », qui pourrait contribuer à faire des QSO des « chandelles étalon » cosmologiques.

1.1.2 Structure de cette thèse

La section 1.2 contient une introduction générale aux AGNs, avec les composants essentiels de leur modèle unifié et une discussion de leur importance cosmologique. Le chapitre 2 décrit la technique de Reverberation Mapping, ses principaux résultats et ses limitations, que cette thèse essaye précisément de dépasser. Le chapitre 3 est consacré aux bases de l'interférométrie optique, à une présentation du VLTI et de l'instrument AMBER et à la technique d'observation et de traitement des données qui a permis d'atteindre des sources aussi faibles que les QSOs. Notre modèle géométrique et cinématique est présenté en détail dans le chapitre 4, qui décrit aussi la façon dont les mesures de RM et d'IO sont estimées puis utilisées dans un ajustement de modèle Bayésien. Les premières observations de 3C273 avec AMBER sur le VLTI sont décrites dans le chapitre 5, qui discute de la procédure de traitement et de calibration des données comme des paramètres issus d'un ajustement de notre modèle sur ces mesures interférométriques. Le chapitre 6 étudie le potentiel ultime du VLTI pour les observations de BLR par une analyse du rapport signal à bruit entre le signal estimé par notre modèle et le bruit attendu de différents instruments de seconde génération du VLTI. Le chapitre 7 présente une première analyse de la faisabilité des mesures directes de distance par la méthode des « parallaxes des BLRs », avec une estimation de la précision des mesures de distance à partir de données simulées d'IO et de

RM. Enfin, le chapitre 8 donne la conclusion de cette thèse et les perspectives de développement de notre travail.

8.1 CONCLUSION

Nous avons étudié l'application de l'interférométrie optique aux BLRs de noyaux actifs de galaxies pour évaluer la contribution de cette technique aux problèmes suivants :

- Contraindre la morphologie du « moteur » central à partir de contraintes sur la géométrie et la cinématique des BLRs.
- Améliorer les mesures de masse du trou noir super massif
- Etudier la possibilité de transformer les QSOs en chandelles cosmologiques standards

Nous avons développé un modèle de BLR pour estimer simultanément les mesures en IO et en RM. Nous avons montrés que les signaux interférométriques et notamment la visibilité et la phase différentielle augmentaient fortement les contraintes sur la masse du trou noir, la taille angulaire de la BLR, la distribution radiale de matière dans la BLR, son champ de vitesse, l'anisotropie de la réponse des nuages liées à leur épaisseur optique, l'épaisseur de la BLR, et l'inclinaison de l'axe de l'AGN. Nous avons créés des jeux de données simulés, affectés de bruits instrumentaux réalistes, pour des grilles de modèle sur des paramètres clefs comme la masse du trou noir, l'inclinaison et l'épaisseur de la BLR pour évaluer la précision d'estimation des paramètres et tout particulièrement de la masse, à partir d'un outil Bayésien d'ajustement de modèle de type Chaine de Markov dans une approche Monte-Carlo. Nous avons utilisé des valeurs typiques pour les quasars à l'exception de leur dimension angulaire qui a été basée sur nos mesures sur 3C273.

Les données d'IO seule permettront des mesures de masse avec une dispersion de l'ordre de 0.15 dex, ce qui est a comparé aux 0.30 à 0.45 dex des statistiques globales obtenues par RM. Nous confirmons que la dispersion des mesures de RM est due au facteur de projection f très sensible à la géométrie de la BLR, qui intervient dans l'estimateur viriel de masse. L'IO optique réduira très fortement cette dispersion en contraignant ce facteur de projection. Il est à noter que les meilleurs ajustements par RM

donnent des précisions de l'ordre de 0.15 dex sur des objets particulièrement bien étudiés et bénéficiant d'une analyse très fine des variations spectro-interférométriques. Même dans ce cas, l'IO contribue à une meilleure séparation des paramètres et la combinaison finale de l'IO et du RM devrait permettre d'améliorer globalement la précision. Nous avons estimé qualitativement ce gain mais une analyse complète des précisions attendues de la combinaison RM+IO reste à finaliser.

Une première application de l'IO aux BLR nous a permis de résoudre la BLR de 3C273 dans la raie Pa_α, avec l'instrument AMBER du VLTI. Nous avons constaté une chute de la visibilité différentielle dans la raie qui croit avec la base de l'interféromètre. Cela montre que la BLR est nettement plus étendue que le bord interne du tore de poussière qui domine l'émission continue en bande K. La phase différentielle mesurée est nulle à mieux qu'un degré près. Compte tenu de la grande taille de la BLR, une phase aussi petite est incompatible avec une géométrie de disque mince, que le champ de vitesse global dans ce disque soit dominé par une rotation képlérienne ou par un flux radial entrant ou sortant. Nous avons donc une géométrie très ouverte, loin d'un disque plat.

Nous avons analysé deux façons d'expliquer la très grande différence entre nos mesures angulaires en Pa_α (plus de 1500 jours lumière) et les mesures de RM dans les raies de Balmer (moins de 500 jours lumière).

1. Nous avons montré que le RM avec la fenêtre d'observation de 3C273 de sept ans était de toutes façon incapable de mesurer des tailles supérieures à 700 jours-lumière. Au delà de 800 jours-lumière de taille réelle, les résultats de RM donnent systématiquement un résultat compris entre 200 et 400 jl.
2. Une taille angulaire correspondant à 2142 jl en Pa_α peut être compatible avec une taille linéaire de 500 jl en H_α, puisqu'il peut y avoir jusqu'à un facteur 2 d'écart entre les courbes de niveau de photo-ionisations entre ces deux raies (même s'il est plus probable que l'écart soit de moins de 30%) et que, par ailleurs, les diamètres équivalents pour l'interférométrie optique et le Reverberation Mapping peuvent différer de plus d'un facteur 2, car la pondération des différentes parties de la BLR n'est pas la même dans les deux types de mesures, ainsi que le montre le chapitre 7.

En appliquant notre modèle et notre méthode d'ajustement à 3C273 nous trouvons une BLR peu inclinée (i~10°) et quasi sphérique. La macro turbulence et une rotation képlérienne ont des contributions à peu près équivalentes au champ de vitesse. Nous estimons la messe du trou noir central à $(5 \pm 1)10^8 M_\odot$, ce qui est comparable à l'estimation de Kaspi et al. (2000), malgré une géométrie et une taille différente. Nos mesures correspondent à un facteur de projection f~3 proche de la valeur obtenue par Grier et al. (2013) et assez loin des 5.5 de Kaspi et al. (2000). Notre objectif ultime est d'observer suffisamment de sources pour calibrer f en fonction de la luminosité et d'autres paramètres comme la largeur de raie.

En nous basant sur la précision obtenue sur 3C273, nous avons estimé le nombre de QSOs que le VLTI pourrait résoudre avec AMBER+, avec les instruments de seconde génération GRAVITY et MATISSE et avec les instruments possibles que sont OASIS, OASIS+ et OASIS+ couplé à un suiveur de franges de nouvelle génération. Pour cela nous avons extrapolé la précision des mesures différentielles de AMBER à ces nouveaux instruments. Nous montrons que GRAVITY permettra des mesures de grande qualité sur une douzaine d'objets, qui pourront et devront aussi être observés avec MATISSE (utilisant GRAVITY comme suiveur de franges). Avec OASIS et surtout OASIS+, le nombre d'objet monte à environ 40. Un suiveur de franges de nouvelle génération permettrait d'atteindre 30 à 60 objets avec GRAVITY et OASIS+ respectivement tout en étendant le nombre de sources observables avec MATISSE, qui pourra observer quelques raies d'émission en bande L, mais surtout fournir de fortes contraintes sur la géométrie du tore de poussière, qui interagit avec la BLR et est également sensible à la distribution de luminosité de la source centrale. Dans le visible, les UTs avec une optique adaptative atteignant un rapport de Strehl de 0.1 permettrait d'observer jusqu'à 130 sources jusqu'à V=15, alors que les ATs avec un Strehl de 0.5 permettrait d'atteindre V=14. Dans le visible les signaux seraient fortement renforcés par la possibilité d'observer dans les raies de Balmer. Le VLTI exploiter à son plein potentiel devrait permettre de calibrer les relation taille et masse luminosité, ainsi que peut être une relation entre l'épaisseur de la BLR (l'angle d'ouverture ω) et la luminosité.

Elvis et Karovska (2002) ont proposé une méthode de « parallaxe des quasars » pour mesurer leur distance à partir des mesures linéaires du RM et angulaires de l'IO, avec un facteur de correction qui dépend de la géométrie de l'objet. Plus récemment, Hönig et al. (2014) ont appliqué une méthode du même type au tore de poussière de NGC4151 et obtenue une mesure de distance à 13% près. Dans leur cas, la géométrie du tore telle qu'elle est vue en bande K est très simple puisqu'il s'agit d'un anneau. Dans ce cas les différents paramètres de modélisation affectent de la même façon les rayons vus par RM et IO et affectent peu la mesure de distance. Nous avons fait une première estimation de l'application de cette méthode aux BLR et à partir de données simulées nous obtenons une précision

de 16% à 500 Mpc. Nous pensons que cette précision peut être améliorée avec des données RM de meilleures qualité comme celle de la récente campagne LAMP (Bentz et al, 2010b, Pancoast et al. 2014b). Toutefois, il nous reste à évaluer cette méthode pour l'ensemble des sources accessibles. Nous n'avons pas pu estimer une distance pour 3C273 à cause de nos doutes sur les mesures de RM pour cet objet et de la nécessité de calculer les facteurs d'échelle entre les raies de Paschen et les raies de Balmer. Un des développements de ce travail est une modélisation de ce type avec le code de transfert de rayonnement CLOUDY, dont l'utilisation devrait être grandement facilitée par le fait que nous avons de fortes contraintes sur la géométrie de la distribution de nuages dans la BLR. L'application de cette méthode à toutes les cibles du VLTI est potentiellement très riche puisqu'elle donnent des mesures d'intérêt cosmologique jusqu'à z=0.8 environ.

8.2 TRAVAUX A FINALISER

8.2.1 Calibration et interprétation des données sur 3C273

8.2.2 Article sur les parallaxes de BLRs

8.2.3 Développement du modèle

8.3 PERSPECTIVES FUTURES

8.3.1 Utilisation des instruments de 2nde génération du VLTI

8.3.2 Reverberation Mapping photométrique

8.3.3 Reverberation Mapping dans les raies d'émission

8.3.4 Observations avec GAIA

8.3.5 Spectro-astrométrie

9 ANNEXE A : PUBLICATIONS

9.1 ARTICLE « DIFFERENTIAL INTERFEROMETRY OF QSO BLRS – I. IMPROVING THE REVERBERATION MAPPING MODEL FIT AND BLACK HOLE MASS ESTIMATES »

Rakshit, S, Petrov, R, Meilland, A and Hönig, A, MNRAS 447, 2420-2436 (2015)

9.2 COMMUNICATION « VLTI/AMBER DIFFERENTIAL INTERFEROMETRY OF THE BROAD-LINE REGION OF 3C273 »

Petrov, R G, Millour, F, Lagarde, S, Vannier, M, Rakshit, S, Marconi, A, Weigelt, G, SPIE 8445 (2012)

9.3 COMMUNICATION « AGN BLR STRUCTURE, LUMINOSITY AND MASS FROM COMBINED REVERBERATION MAPPING AND OPTICAL INTERFEROMETRY OBSERVATIONS »

Rakshit, S and Petrov, R G, SPIE 9146 (2014)

10 BIBLIOGRAPHY

150 references

List of Figures

List of Tables

Abbreviations

AGN	**A**ctive **G**lactic **N**ucleus
BH	**B**lack **H**ole
BLR	**B**road **L**ine **R**egion
DI	**D**ifferential **I**nterferometry
HR	**H**igh **R**esolution
MCMC	**M**arkov **c**hain **M**onte **C**arlo
MR	**M**edium **R**esolution
OI	**O**ptical **I**nterferometry
QSO	**Q**uasi **S**tellar **O**bject
RM	**R**everberation **M**apping
SMBH	**S**uper **M**assive **B**lack **H**ole
SNR	**S**ignal to **N**oise **R**atio
VLTI	**V**ery **L**arge **T**elescope **I**nterferometer
2DFT	**2D F**ourier **T**ransform

Physical Constants

Speed of Light	c	=	3×10^8 ms^{-1}
Gravitational constant	G	=	6.67×10^{-11} m^{3}kg^{-1}s^{-2}
Solar mass	$M_\odot$	=	1.989×10^{30} kg
Solar luminosity	$L_\odot$	=	3.8×10^{26} w

Chapter 1

Introduction

Contents

1.1 This thesis

1.1.1 Goal of this thesis

Active Galactic Nuclei (AGNs) are extremely powerful objects in the night sky emitting 1/5 of the total power in the universe. They are powered by the accretion of matter onto a central super massive black hole (SMBH) surrounded by an accretion disk. The clouds in the broad line region (BLR), situated at a distance of a few light days to a few hundred light days away from the center, orbiting around the SMBH with velocity of a few thousands km/s, emit broad emission lines.

Depending on the emission properties, AGNs are classified into different categories, but according to the "unified model" they have same internal structure. The reason of these differences are due to the different viewing angles. The bright members of an AGN subclass look star-like due to their large distances. These objects are called quasars, which show very broad emission lines at large redshift.

Study of these objects can explain the evolution of AGNs, and the co-evolution of BHs and their hosts at cosmological distances. Moreover, formation and evolution of BHs and distribution of mass in the universe can be explained by observing high-redshift AGNs. In this context, the BLR has particular importance as it provides mass estimates of the SMBH and accretion mechanism, and can be used as standard candle. However, this needs better understanding of geometry and kinematics of the BLR. Reverberation mapping (RM) provides BH mass estimates but is affected by unknown geometry and kinematics.

Thus, the main goal of this thesis is to take advantage of high angular resolution near-infrared interferometry to show how OI can contribute to the understanding of BLR geometry and kinematics, in spite of the fact that all BLRs are expected to be unresolved or only partially resolved. I will combine optical interferometric (OI) observations with RM to constrain the BLR morphology. I will describe a three-dimensional BLR model to predict simultaneously both the OI and RM measurements. I will explain effects of different model parameters on both OI and RM data. I will present and discuss the first OI observation of 3C273 and a global model fit of the data. SNR analysis will be performed to evaluate the full potential of the current and upcoming interferometric instruments to see the feasibility of BLR observation within next few years. Since quasars can be found at redshift up to 7, they can be used to study the early universe. Thus, a method to measure directly the distance of high-redshift quasars is needed to constrain the expansion rate of the universe and prove dark matter. Hence, I will estimate angular distance to quasars using a geometrical method, "BLR parallax", to use them as standard cosmological candle.

1.1.2 Structure of this thesis

This thesis is structured in the following way. A general introduction of AGNs, its key components, unification model and its role in cosmology are described in section 1.2. Since roughly half of this thesis work is related to reverberation mapping, its basic concepts are summarized in chapter 2 with its key results and main limitations, which are important for this thesis. In chapter 3, I discussed the basic concept of optical interferometry including an overview of VLTI and AMBER instrument and data reduction process that I used to reduce raw data obtained from faint sources like quasars. A detailed description of a geometrical and kinematical model of BLR is presented in chapter 4, which also explains different observables of both RM and OI techniques including a direct model fitting approach using Bayesian framework. First interferometric observation of the BLR of 3C273 using AMBER at VLTI is presented in chapter 5 with a detailed description of the observation and data reduction process including the result of the Bayesian model fitting to the data. To see the full potential of the VLTI in observing the BLR of quasars, the result of a feasibility study of different second-generation instruments of VLTI is presented in chapter 6. Feasibility of quasar parallax method to estimate angular distance using BLR is presented in chapter 7 including the result of the simulation estimating distance accuracy from the mock interferometric and reverberation mapping data. Finally, the conclusion of this thesis and my future perspectives are written down in chapter 8.

Note that in the following chapters "we" represents all the collaborators associated with me in these projects. However, this does not mean that the statements have been endorsed by all of them.

1.2 Introduction to Active galactic nuclei

1.2.1 A brief history

In 1908, Edward A.Fath observed the nucleus of NGC 1068, the brightest AGN (Fath, 1908). He obtained six emission lines along with Hβ, which were re-observed by V.M. Slipher in 1917. In 1926, emission line spectra of three more objects were observed by Edwin Hubble, and two decades later, Carl K. Seyfert published the historical paper in which he stated that the nuclei of a small fraction of galaxies show high-ionization emission lines, which are broader than the absorption lines in normal galaxies (Seyfert, 1943). He, furthermore, noted that these lines were originating from a compact bright nucleus with a range of ionization parameter (see section 1.2.4.3). Then this new class of objects were named Seyfert galaxies. They are defined by a spiral structure with bright nucleus and emission lines. They represent about 3-5% of all galaxies.

After the advances of radio astronomy, many bright radio sources were detected and thought to be star-like objects in the optical (Hazard et al., 1963). Some of them are brighter than Seyfert galaxies by factor of 100 or more, and show strong broad emission lines at unexpected wavelength. These are known as quasi-stellar radio sources or quasars, which are the most distant and bright objects in the sky. In the 1960's, Maarten Schmidt discovered the first quasar 3C273 and measured its redshift from its optical spectrum (Schmidt, 1963). The large redshift of the objects implied an extremely high luminosity($\simeq 10^{12} - 10^{14} L_{\odot}$). After this first success, many such objects were detected in night sky. Later, it was found that many of those do not emit radio waves and termed as quasi-stellar objects or QSOs. Even if only about 1% of QSO-like objects in the optical domain have detectable radio emission, the radio-quiet objects (most of the QSOs) are nowadays also termed quasars since the underlying physics is the same for both. The 2dF* QSO redshift survey produced a sample of over 40,000 QSOs (Boyle et al., 2000), whereas the Sloan Digital Sky Survey data release 10† (SDSS DR 10) produced a catalog consisting 166,583 quasars. Note that Seyfert galaxies and quasars are the two largest subclasses of "active galactic nucleus", or AGN, the most luminous sources in the universe with a very compact nucleus, and much brighter than normal galaxy.

*http://www.2dfquasar.org/
†http://www.sdss.org/

TABLE 1.1: Different types of AGN and their observed emission

AGN Types	Narrow lines	Broad lines	X-rays	UV excess	far-IR excess	Radio loud	variable
Seyfert 1	yes	yes	yes	some	yes	no	some
Seyfert 2	no	yes	no	no	yes	no	no
Quasar	yes	yes	yes	yes	yes	some	yes
Blazar	some	no	yes	some	no	some	strong
BL LAC	no	some	yes	yes	no	yes	strong
OVV	some	some	yes	yes	no	yes	strong

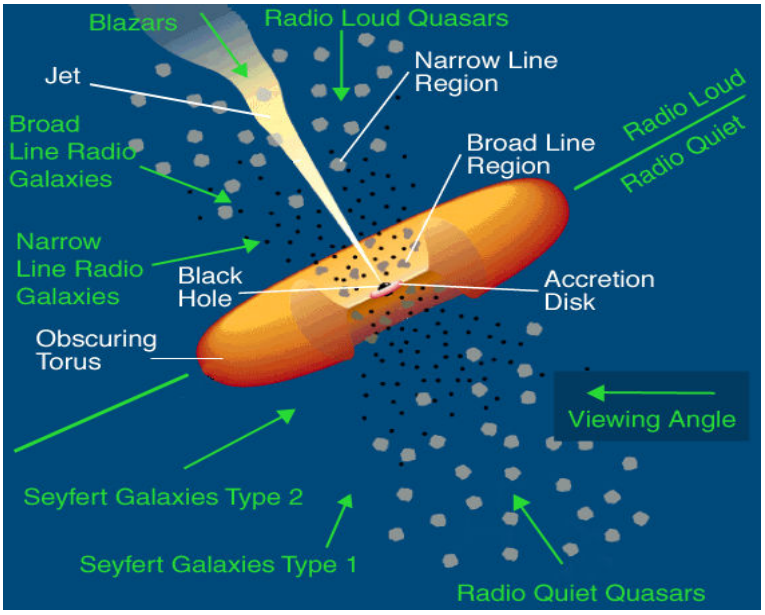

FIGURE 1.1: A Cartoon to explain different components of AGN based on Urry and Padovani (1995). Central black hole, broad line region, dusty torus and narrow line region are shown in white labels. Different types of AGN are shown in green labels explaining the unified model of AGNs. It says the differences are due to the observer viewing angle (green arrows). Credit: Pierre Auger Observatory.

1.2.2 AGN types

AGNs are divided in many categories depending on luminosity, presence of broad and narrow lines, variability etc. However, the major division comes from the presence of strong radio emission, which divided AGNs into two main classes: "radio loud" and "radio quiet" (if the ratio between radio flux in 5 GHz to optical flux in B band is greater than 10 then the object is radio loud otherwise it is called radio quiet). Radio loud objects exhibit strong radio emission, which originates from the jet, but radio quiet objects show weak radio contribution, but their emissions dominate in other wavelength. These objects are further classified into many different categories depending on observed emission profile such as the presence of narrow and broad lines, X-ray, UV and far IR excess, and variabilities. Table 1.1 summarizes different categories and the reason of this classification.

Antonucci (1993) in his unification model stated that all AGNs have similar structure, and the differences in their emission profile are due to observer line of sight

to the object (figure 1.1). Thus depending on the orientation of object relative to the observer line of sight, different classes of AGN are formed: optically violent variable (OVV; jet points directly), Blazar (jet points towards), Seyfert 1 or Quasar (jet points away but central structure still visible) and Seyfert 2 (edge-on view and central structure is blocked by obscuring dust torus).

1.2.3 Unified models of AGN

The aim of the unified models is to find simple explanation for all the apparent properties of different classes of AGNs as noted before. The first simple unification idea was proposed by Antonucci and Miller (1985), who found that the spectrum of Seyfert 2 galaxy NGC 1068 in polarized light shows signature of Seyfert 1 galaxy due to scattering of light from the BLR clouds, thus confirming the presence of the BLR, obscured by the dusty torus and not directly viewed due to its inclination with respect to the observer. This suggests that the inclination plays a crucial role to determine the observed properties. Thus galaxies, which show broad emission lines, are defined as type 1 and those with obscured broad emission lines are type 2.

It is also interesting to note that, many but not all Seyfert 2 show hidden BLRs in the polarized light. The absence of BLR signature in some Seyfert 2 observations in polarized light could be due to weak BLR emission compared to the underlying continuum, as well as, absence of strong emission from the central engine to illuminate the BLR. However, adding luminosity as a parameter could explain some of these properties. As a result, unification models now concentrate on unifying AGNs within the same class adding different parameters such as mass, Eddington ratio, luminosity with inclination. Unification of different classes of radio-loud AGN has been explain by Urry and Padovani (1995).

The unification model indeed provides very simple explanation of the observed differences in AGN including Seyfert galaxy. Our long term goal is to obtain a broad unification based on the relation between BH mass and other properties of AGNs such as luminosity, inclination, vertical height of the BLR and dust torus.

1.2.4 Components of AGN

The main components of AGN are as follows:

- A **super massive black hole** with $10^6 M_\odot < M < 10^{10} M_\odot$. Size of the event horizon $\sim 0.01 - 10$ AU.
- An **accretion disk**, major power house, surrounding the SMBH of size $<$ 1000AU. Matter attracted by the gravity of black hole spirals in and forms a disk. The disk is made of hot ($10^4 - 10^6$ K) and optically thick plasma.
- A **broad line region (BLR)** of size $0.01 - 1$ pc, made of gas clouds orbiting arround the SMBH with velocities of a few thousand km/s. The gas is ionized by the continuum radiation and emits lines which are very broad because of high Doppler shifts. BLR will be discussed in more detail later.

- A **dusty torus** of size $1 - 10$ pc. The torus is "optically thick". Inner rim of the torus which is at temperature ~ 1500 K dominates the K band emission.
- At large distance ($\sim 10 - 1000$ pc), there is another region where low density clouds are moving less rapidly ($\sim$ few 100 km/s). This is the **narrow line region (NLR)**, which emits permitted and forbidden narrow emission line.
- About 10% of AGNs have **jets**, perpendicular to the accretion disk, which extend from $0.01 - 10^6$ pc. Material inside the jets moves at relativistic velocity.

1.2.4.1 The Black Hole

In 1963, Hoyle and Fowler pointed out that the energy source of AGNs and Quasars could arise from the gravitational collapse of massive object. The existence of such a massive object, which is named as super massive black hole (SMBH), at the center of an AGN is very common (Lynden-Bell, 1969). Some of theses source are accreting matter at a very high rate (see later). Black holes (BH) with mass of $\sim 10^{10} M_{\odot}$ were detected at $z > 6$ (Wu et al., 2015) suggesting that the evolution of BHs have been linked with their parent galaxies since at the early universe. It was also suggested that SMBH grew faster than their host galaxy in the early universe (Wang et al., 2010). Interestingly, a tight correlation can be found between SMBH growth and the evolution of the host galaxy. Both quiescent and active galaxies show similar correlation between SMBH and the bulge of the host galaxy, such as the relation between BH mass and the bulge velocity dispersion ($M_{\rm BH} - \sigma_*$), and BH mass with bulge luminosity ($M_{\rm BH} - L_{\rm bulge}$) (Ferrarese and Merritt, 2000; Gebhardt et al., 2000a; Bentz et al., 2009a). In order to study growth of SMBH and evolution of galaxy, we need to have a better relation between BH mass and luminosity of AGN.

Reverberation mapping is a powerful tool to successfully provide such a relation (Blandford and McKee, 1982). However, the RM virial masses have large scatter due to the unknown geometry and kinematics (see chapter 2). Calibration of such relation is one of the goals of this thesis.

1.2.4.2 Accretion disk

Accretion of matter onto a SMBH is the major power source of AGN. Surrounding the central black hole, a structure of diffused material called accretion disk is present. As far away material with subsonic velocity is attracted by the central object and becomes supersonic as its Mach number increases toward the center. Because of friction in the accretion disk, material is heated up producing enormous amount of radiation across the electro magnetic spectrum. Matter spirals inward and loses angular momentum, which has to be balanced by the angular momentum gain of matter far away from the central source. Depending on the accretion rate, in-falling matter forms radiatively efficient thin accretion disk (Shakura and Sunyaev, 1973) or radiatively inefficient thick disk, which cooled by advection (ADAF; Narayan and Yi, 1994). Luminosity of the object depends on the accretion rate, $L_{\rm acc} = \epsilon \dot{M} c^2$, where ϵ is the radiative efficiency, $\dot{M}$ is the accretion rate and c is

the speed of light. Considering spherical symmetry, a theoretical limit for luminosity was defined, called the Eddington luminosity L_E, which is the maximum luminosity of the object with a balance between radiation force acting outward and gravitational force of the black hole acting inward:

$$L_{\rm acc} \leq L_E = 3.2 \times 10^4 \frac{M_{\rm bh}}{M_\odot} L_\odot \tag{1.1}$$

For very luminous accretion disks, whose luminosity exceeds the Eddington luminosity, a slim-disk model has been proposed by Abramowicz et al. (1988), a disk with low viscosity, optically thick, radiatively very inefficient and cooled by advection. In the context, SS 434 is a well-known galactic object with a super-Eddington accretion disk (Okuda et al., 2009).

1.2.4.3 Broad line region

The broad line region (BLR), a region of gas clouds surrounding the accretion disk orbiting with velocity up to 20000 km/s and emitting broad emission lines in the observed spectrum. The study of BLR is particularly important since it can provide details about the central black hole because of the virial relation, its growth history at a cosmic time scale. However, the apparent size is so small that even in the nearest AGNs resolving BLR clouds is a challenge for astronomers.

Since this thesis is based on the study of the broad line region (BLR), a detailed discussion about some of the important properties of the BLR is presented in this chapter, and in chapter 2.

Cloud properties: The assumption that clouds are the basic line emitting entity in the BLR of AGN, comes from the observational evidence of condensation in galactic HII regions and the interstellar medium. Moreover, clouds are needed for line intensity consideration, mainly the typical observed line width, which is very similar between low- and high-ionization lines, roughly within a factor 2. An ensemble of small thick clouds, where each of them produces many emission lines with a large range of ionization, can explain the observed line profile, and is consistent with the stratification and virial prediction (a detailed discussion can be found in Netzer, 2013). As an alternative, it was considered that broad emission is coming from extended envelope of the stars, and thus BLR is associated with stars, but in that case the mass of the stars in the BLR becomes too large, which is problematic since the total of the line emitting clouds is about $10^3 - 10^4\, M_\odot$ (Baldwin et al., 2003). How many clouds are in the BLR? The number of clouds can be estimated from the line profile shape. The number of estimated clouds required to produce smooth high resolution emission line profile for given gas velocity is very large $\sim 10^{6-8}$, considering individual clouds have typical line width ~ 10 km/s (Arav et al., 1997, 1998).

Clouds could survive over many dynamical times[‡] due to either confinement, magnetic or relativistic High Intercloud Medium (HIM), or because they are the part

[‡]Dynamical time scale of the BLR can be defined by the time that a line emitting cloud would take to cross the BLR, $\tau_{\rm dyn} \simeq R/\Delta V_{\rm FWHM}$, where R is the size of the region and $\Delta V_{\rm FWHM}$ is the typical velocity width. For a Seyfert galaxy, this corresponds to 3-5 years.

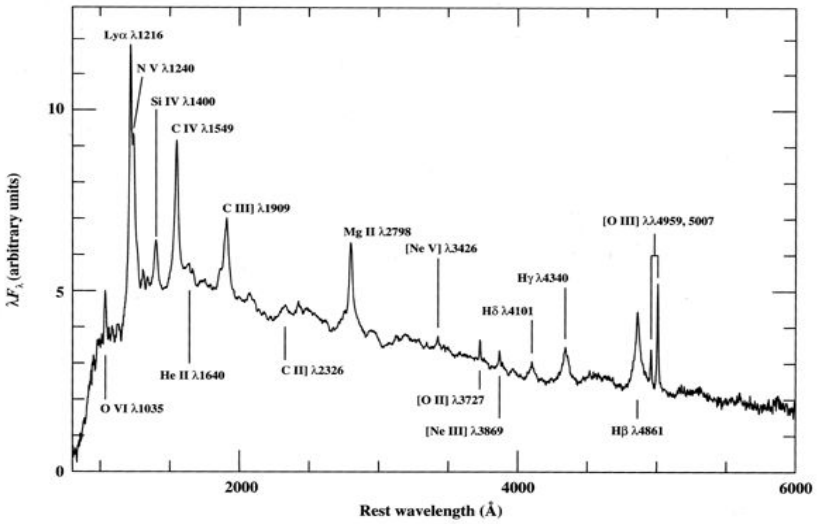

FIGURE 1.2: A mean QSO spectrum formed by averaging spectra of over 700 QSOs from the Large Bright Quasar Survey (Francis et al. 1991). Prominent emission lines are indicated. Taken from Peterson (1997).

of self gravitating bodies like stars. The required magnetic field for magnetic confinement is small ($\sim$ 1 G). Confinement due to HIM is problematic as it would smear the central source variation and the wings of the broad emission lines.

Broad line spectrum: AGN spectra show a wide variety of line strengths and profiles (see Table 1.1 in Peterson, 1997). The width of the emission lines range from 500 km/s to more than 10^4 km/s, which is the result of Doppler broadening. They also show a large variety in shape, from a "logarithmic", i.e the flux at radial velocity ΔV from the line center $F_\lambda(\Delta V) \propto -\ln\Delta V$, to a more complicated profile which is variable in time. Different lines in the same spectrum can have very different morphologies. AGN spectra often show several strong broad emission lines such Lyα (λ1216)+ Nv (λ1240), CIV (λ1549), Mg II (λ2798), Hβ (λ4861) as well as many other emission lines including Paschen series lines in IR. Due to large Doppler broadening spectral lines are often blended such as CIV doublets and helium line. Figure. 1.2 shows a mean spectrum of 700 QSOs with several prominent emission lines.

Some of the quantities that are often used to describe the BLR physical condition are summarized below.

Covering factor: Covering factor is defined as the fraction of sky covered by the BLR clouds as seen from the center. It is estimated from the fraction of ionized continuum photons absorbed by the BLR clouds and reprocessed emission lines. It is estimated to be of the order of 10 % from the equivalent width of the emission line, such as Ly α (Baldwin and Netzer, 1978).

Column density: The neutral hydrogen column density along any line-of-sight is defined as $\eta_{\rm H} = \int N_{\rm H}(l)dl$, where $N_{\rm H}$ is the number of neutral hydrogen atoms per cm^3. The estimated number, for which the emitted spectra in not sensitive to the column density, is between $10^{22} - 10^{24}$ cm^{-2}, where the lower limit is set by

the appearance of low excitation lines of Mg II and Fe II in AGN spectra, and the upper limit is set by observation of Ca II in some AGN spectra.

Filling factor: This indicates how much of the emitting volume actually contain line-emitting material, where rest of the volume can be assumed to be vacuum. Filling factor in quasar BLR is very low about 10^{-4} calculated from the observed intensity of emission lines.

Photoionization of the BLR: The emission line flux varies with time and follow the variation of the continuum flux. This correlated variation suggests that the BLR is photo-ionized by the radiation from the central continuum source. Photoionization models have been extensively used in the past to understand the emission from gaseous nebulae and many of the emission lines usually found in gaseous nebula are seen in AGN spectra as noted by Seyfert (1943). Our knowledge about the BLR physical condition and hence photoionization modeling have been improved due to the observational evidences such as higher spectral resolution and increased sensitivity in AGN spectra have revealed more complex BLR dynamics than previously thought. The ionization parameter is defined by the ratio of photon number density to particle density at the ionized face of the cloud

$$U = \frac{Q(\mathrm{H})}{4\pi r^2 n_{\mathrm{H}} c} = \frac{\Phi(\mathrm{H})}{n_{\mathrm{H}} c}, \tag{1.2}$$

where $Q(\mathrm{H}) = \int \frac{L_\nu}{h\nu} d\nu$, the number of hydrogen ionizing photons per second, depends on the specific luminosity (L_ν) of the central source, $\Phi(\mathrm{H})\,[\mathrm{cm}^{-2}\mathrm{s}^{-1}]$ is the surface flux of the ionizing photon, r is the distance of the cloud from the central source, n_{H} is the hydrogen number density and c is the velocity of light.

The photoionization models thus depend on the shape of the ionizing continuum SED, the element abundances (usually solar or cosmic), particle density, column density and the ionization parameter or the ionizing photon flux. Incident continuum strikes the front face of the clouds, producing high-ionized zone and emitting strongly in the high ionization lines like Lyα and CIV. However, the back side of the cloud, which is partially ionized due to heating from penetrating x-rays, strongly emits in the low ionization line such as Mg II and Fe II. Typical values of ionizing parameter and density are $\log_{10}U \simeq -1.5$ and $n_{\mathrm{H}} \sim 4 \times 10^9 \mathrm{cm}^{-3}$ for the BLR. The limit on the gas density comes from the width and the presence or absence of forbidden and/or semiforbidden lines. The small value of covering factor ($\sim 10\%$) and a very small filling factor (10^{-4}) as well smooth emission line profile indicates that the BLR consists of a large number of line emitting clouds, which occupy small parts of the total volume and intercept small fraction of the total ionizing continuum.

The success of early reverberation mapping observations improved our understanding about BLR, however, these findings initially imposed a number of problems. The estimated time lag through photo-ionized modeling is an order of magnitude larger than measured from the RM observations. This suggests that the line emission originates closer to the central source and gas density is denser than previously believed. Models with standard BLR parameters produce large intensity ratios between different Balmer lines (Lyα/H$\beta \sim 50$, Hα/H$\beta \sim 10$) but the observed values are far lower (Lyα/H$\beta \sim 3$, Hα/H$\beta \sim 4$). Moreover, different

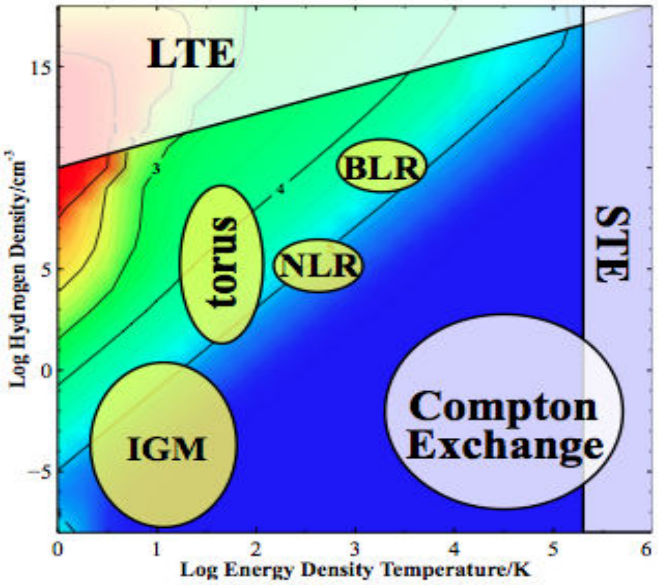

FIGURE 1.3: Physical and thermodynamical limits (in white) and different regions in AGNs (in yellow) are shown in annotated version for illustration. A wide range of densities, and various energy-density temperatures of the 10^6 K blackbody, are shown. Taken from Ferland et al. (2013).

emission lines exhibit very different lag times. For instance CIV has lower lag than Hβ suggesting that the BLR is stratified. Clouds with various density are distributed around the central source, and the emission comes from the clouds only when the optimal conditions (density and photon flux) are satisfied for that line Baldwin et al. (1995). This is further explained by figure 1.3, which shows that the NLR, molecular torus, and BLR are just due to the different atomic and molecular physics, spanning several orders of magnitude in $n_{\rm H}$ and radiation field intensity (see Ferland et al., 2013).

Correlation between line and continuum emission: AGN emission lines are strongly correlated with the continuum properties. Radiation from the central source hits the gas clouds photoionizing them (see chapter 2). Line intensity is directly proportional to the continuum intensity but depends on shape of the incident continuum, exact label of ionization, gas kinematics etc. This correlation allows us to understand the physics of accretion mechanism and the BLR, and this is the basis of reverberation mapping technique, which will be discussed in detail in chapter 2. There are some other observationally well established correlations, such as Hβ line width, X-ray continuum slope, and Eddington ratio ($\lambda_E = L/L_E$). A relationship known as "Baldwin effect", between the equivalent width (EW) of CIV λ1549 and the continuum luminosity measured near the line wavelength, was discovered by Baldwin (1977), and later found to be followed by several other lines. But, some lines like Hα and Hβ show very weak correlation with continuum luminosity. There is strong evidence showing better correlation with λ_E than continuum luminosity, indicating the possibility that line EW is related to the accretion rate. The correlation between EW and $M_{\rm BH}$ was also found weaker than $M_{\rm BH}$ and L.

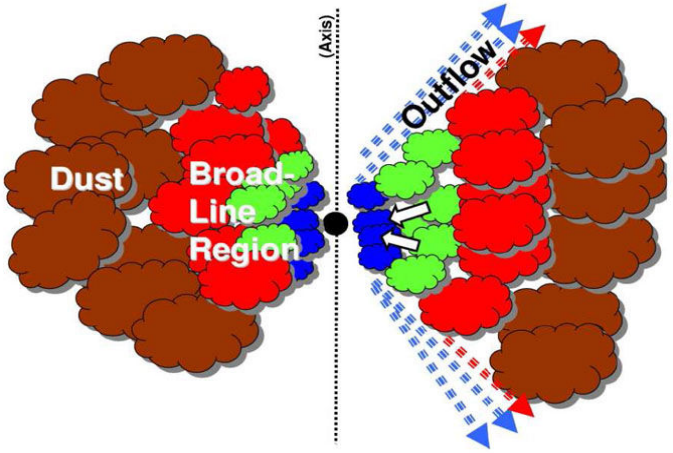

FIGURE 1.4: Figure 6: A schematic view of the BLR and torus of an AGN in a plane through the axis. The figure is approximately to scale (except that the black hole is shown too large.) Figure from Gaskell (2009).

A schematics diagram of AGN central engine is presented in figure 1.4 showing that BLR clouds are surrounding the central objects. They absorb the continuum photons and re-emit them as emission line photons allowing us to study the geometry and kinematics of the central engine, the accretion mechanism, and the central black hole growth history.

1.2.4.4 Dusty torus

A dusty region surrounding the central part of AGNs, located at a distance of few parsec, made of molecular gas as well as warm dust at $T \sim 1500$ K are emitting at near-IR, and cooler dust $T \sim 300$ K emitting at mid-IR. This was thought to be the outer boundary of the BLR. A combination of silicate and graphite grains of few nm to μm size is the key ingredient of this dust. The silicate absorption feature indicate AGN dust is very different than normal interstellar dust. Torus in AGN is important since it alters the spectral energy distribution (SED). Spectropolarimetric observations of Seyfert 2 galaxies by Antonucci and Miller (1985) show strong signature of the broad lines in the polarized light but invisible in total light. This suggests a dust obscuration effect where broad line emission is overwhelmed by the unpolarized continuum. If the object is viewed face on, central engine is visible and unobscured by torus, whereas its emission is blocked for edge-on view due to dust obscuration. The overall picture, a "bird nest" structure, of the BLR and dust torus is shown in figure 1.4 as suggested by Gaskell (2009).

The resolution needed to resolve the torus is beyond the capability of a single-dish telescope and hence no direct evidence was available, until Jaffe et al. (2004) resolved NGC 1068 with Very large telescope interferometer (VLTI). Since then, many AGNs have been successfully observed in the N and K bands. This allowed to constrain the size of the innermost dust torus structure and revealed its complexity. Burtscher et al. (2013) rejects the existence of a simple size-luminosity relation in AGNs, because the $L^{0.5}$ scaling of bright sources fails to represent properly fainter sources, and there are clearly several components, with at least

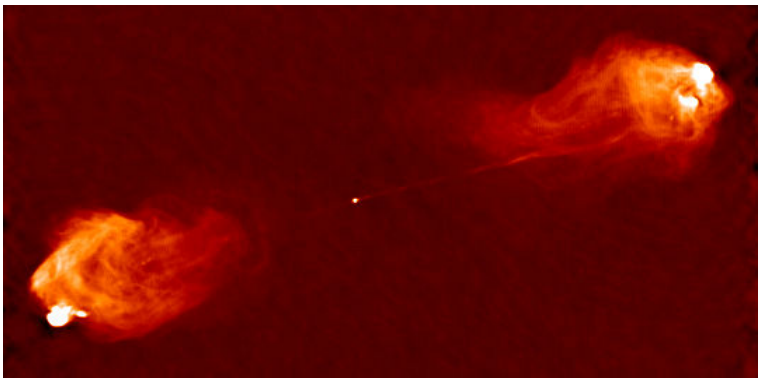

FIGURE 1.5: VLA image of Cygnus A showing a 50 kpc jet extended out from the bight core located at the center. Image courtesy of NRAO/AUI

a cooler more equatorial structure and a hotter more polar one. Both the Keck interferometer (KI) and the VLTI measurements, summarized in Kishimoto et al. (2012), show that in the K-band, the dust torus inner rim size is fairly close to a $R_{\rm rim} \propto L^{0.5}$ size as first indicated by the infrared RM observations of Suganuma et al. (2006) and Koshida et al. (2014), with a size excess with regard to $\propto L^{0.5}$ that increases as L decreases but remains small in the K-band (more discussion can be found in section 2.4). Later, we will use this infrared RM dust size as a lower limit of the inner rim size to estimate the feasibility of interferometric observations of BLR.

1.2.4.5 Narrow line region

At a distance of the order of 100 pc, there is a photo-ionized region, called narrow line region (NLR), where the gas clouds have velocity less than 1000 km/s and produce "narrow" lines. As this region is far away from the central source, it is unaffected by the possible presence of absorbing material. The presence of forbidden lines in the NLR suggests a small density about $10^4\,{\rm cm}^{-3}$ and column density about $10^{20-21}{\rm cm}^{-2}$. NLR has a covering factor of the order of 0.01, which is obtained from the luminosity of entire NLR dividing the luminosity of the continuum. NLR can be resolved in many objects suggesting a double cone geometry, called the "ionization cone". Recent high-resolution maps of NLR from modern integral field unit (IFU) instruments reveal complex geometry with nonuniform gas distribution, which is attributed to anisotropic illumination of the gas due to central obscuring torus (Storchi Bergmann, 2015). Velocity field of this region is also complex indicating presence of outflow plus rotation components.

1.2.4.6 The Jet

Relativistic Jets are commonly seen in radio-loud AGNs. The jet originates at a location where optical-UV and X-ray continuum originates. The exact mechanism behind the production of jet is yet unknown. According to the present understanding, the magnetic field lines in the inner accretion disk warp around and get locked in double helix configuration, and, as a consequence the charged particles

accelerate at a highly relativistic speed. Radio image taken with very large array (VLA) from radio galaxy Cygnus A is shown in figure 1.5 showing 50 Kpc jet extended out of the central bright core (bright spot).

The jet emission is highly beamed and often appeared to be very bright. Very low luminosity AGNs (like M87) as well as the very high luminosity quasars (like 3C273) show highly coliminated radio and optical jets. A wide range of apparent velocities can be found in radio jets and usually a Lorentz factor $\Gamma = (1-\beta^2)^{(-1/2)}$ is used to quantify them (where $\beta = v/c$). Radio loud objects with jets often show broad, nonthermal continuum contribution due to synchrotron radiation from the charged particles in the jet.

In the context of this thesis, jet is relevant because of

- Its contribution in the near-IR SED,
- Its position angle can be used to constrain the orientation of the central structure since jet emits perpendicular to accretion disk. Jet position angles have been obtained for many AGNs from VLBA observation (Lister et al., 2009). Thus, we will use the position angle constraint derived from the observed radio-jet orientation. However, note that, interferometric observation could also constrain position angle, if observations are available at many different angles.
- observer viewing/inclination angle can also be constrained from apparent jet speed by following simple equation.

$$\beta_{obs} = \frac{\beta \sin\theta}{1 - \beta\cos\theta}, \tag{1.3}$$

which is maximum of $\Gamma\beta c$ when $\sin\theta = 1/\Gamma$. For example, inclination of 3C120 is $i < 20^\circ$ constrained by its superluminal jet (Marscher et al., 2002). Note observed emission line profile provides strong constraint on the inclination angle (see chapter 4).

1.2.5 Spectral energy distribution of AGN

AGN continuum is spread over the entire electromagnetic spectrum from radio to gamma ray. The spectrum is relatively flat and nonthermal as shown in figure 1.6. It consists of many complex structures: the broad and narrow emission lines, broad thermal excess components in IR and optical UV bands, and pseudocontinuum structure such as the small blue bump which is comprised of the line emission from iron and from the H-Balmer series (Elvis et al., 1994).

In the X-ray region, the continuum consists of several components, a power-law continuum, a "soft excess" with X-ray energy bellow 1 KeV (Arnaud et al., 1985), and a "reflection bump" in hard X-ray band with energy 10 to 30 KeV (George and Fabian, 1991). For many objects, the soft excess is due to emission that exceeds the extrapolation from the observed hard X-ray power-law continuum, however least understood in AGN continuum. This spectrum is non-thermal in

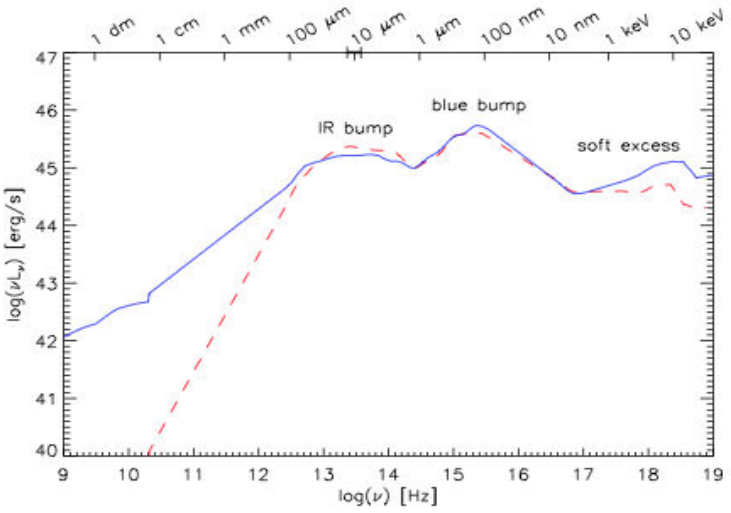

FIGURE 1.6: Mean quasar spectral energy distribution for radio-loud (blue line) and radio-quiet (red dashed line) quasars. The energy distribution was adapted from Elvis et al. (1994). In the spectral regions around the wavelengths of 1 mm and 10 nm, no data is available and the curve is interpolated. Figure from Tristram (2007).

nature and believed to be due to Compton scattering of optical/UV photons by hot or nonthermal electrons in the hot corona above the accretion disk (Liang, 1979). At 6.6 KeV, there is a Fe K-alpha broad emission line. Both Fe K-alpha and "reflection bump" is thought to be due to fluorescence and reflection from "cold" material, possibly from the accretion disk.

The Big Blue Bump (BBB) continuum component in AGNs ranges from 10 to 400 nm, and sometime down to soft X-ray side. This thermal radiation emits at temperature 10^4 to 10^5 K. Although the exact origin is unclear, it probably arises from the accretion disk due to black body radiation from optically thick gas or due to free-free emission from optically thin gas. This spectral window emits half of the bolometric luminosity for an unobscured AGN.

The broad infrared bump extends from $\sim$ 1 to $\sim$ 300 μm, separated from BBB by a deep minimum at 1 μm. This infrared bump is thought to be emitted from reprocessing of the BBB emission by the dust of dusty torus with temperature $\leq$ 1800 K and various distance from the central UV source (Barvainis, 1987). Infrared bump is due to thermal emission in the case of radio-quiet AGNs, while this bump in the case of radio-loud AGNs is due to both thermal and non-thermal components, though often only one component is dominant (Haas et al., 1998).

For this thesis, the SED features in the UV and near-IR are very important, since near-IR continuum originates from the inner rim of dust torus. We will use the SED shape to interpret K band interferometry measurements or the scaling of angular size of torus with temperature. Moreover, the emission line features in the K band can be constrained by our work. This will help to do modeling of the UV/optical variability of AGN to predict emission line light curve. The flux at different bands, such as V, K, L etc can also be obtained from the SED profile, which will be used in chapter 6.

1.3 AGN evolution and cosmology

AGNs have been observed over a distance range of few Mpc to redshift (z) beyond 7. More than 40 of those have been found with redshift larger than 6. The population of theses quasars peaks at redshift $1.5 < z < 2.0$ suggesting that at earlier times in the Universe there have been many more quasars per unit volume than today. The study of BH evolution suggests that the most massive BHs grew first while the less massive BH started their growth much later time and are still growing at a fast rate. On the other hand, the existence of BHs with mass about $10^{10} M_{\odot}$ at the early universe suggests that massive BH must have been common at the very early universe.

The reason"why BH mass measurement is important?" is that the formation and evolution of BH in the universe is unclear. A powerful tool to study AGN evolution with time is to study their redshift-dependent luminosity function (LF). Combination of such LF with BH masses, can provide mass function of BH, vital to study distribution of masses across the cosmic time. The relations between BH masses with luminosity and Eddington ratio of AGN have been found, but those masses are highly scattered, measured by RM virial relation that depends on the unknown f factor. Moreover, BH mass estimates provide constraints on the evolution of host galaxy. High accretion rate and fast growth of the BH is thought to be due to galaxy interactions and merging since cold gas away from the center of galaxy can not reach close to the BH due to high angular momentum, and gravitational interaction with a nearby galaxy can distort the morphology of the parent galaxy allowing the gas to reach the SMBH. To study the formation history of galaxy, it is thus necessary to have better relation connecting BH masses with host galaxy luminosity as well as velocity dispersion. The continuum variability which could be due to the instability in the accretion disk or variable accretion rate is also related to the BH masses (see chapter 2). Thus, having accurate BH mass measurements will allow us to improve our understanding of the accretion mechanism. Better constraints on the variability of AGN light curves will thus provide better distance measurements using parallax method which could constrain cosmological constant and prove dark energy and modified gravity theories (see chapter 7).

A tight correlation has been found between accreting SMBH mass and some properties of the host galaxy, such as stellar velocity dispersion, bulge luminosity, and the bulge mass (Ferrarese and Merritt, 2000; Gebhardt et al., 2000a; Bentz et al., 2009a). Considering only galaxy with secure BH detection, Marconi and Hunt (2003) showed that all the correlation have similar intrinsic dispersion of 0.3 in $\log(M_{\rm bh})$ at a given $L_{\rm bul}$, $M_{\rm bul}$ or σ^*. Moreover, applying the correlations between $M_{\rm bh}$ and host galaxy properties, it is possible to estimate black hole mass function or total mass density in the local universe (Salucci et al., 1999), and hence accretion efficiency, Eddington ratio (L/L_E) and the average lifetime of BHs (Marconi et al., 2004).

In general, the correlations indicate a bridge between galaxy formation and the evolution and growth of BH in the universe. Such correlations suggest that SMBHs are affected and influenced the evolution of their hosts. The ratio of BH to the

bulge mass is a powerful tool to understand this co-evolution of BH and their host. In the local universe, this ratio found to be dependent on the BH mass, but smaller dependency was found in the case of galaxy that host massive BH. However, this is not clear in high-redshift galaxy, where the estimation of BH mass comes from reverberation mapping virial relation but in that case the measurement of stellar mass is highly uncertain due to much fainter stellar light then high luminous non-stellar continuum. Some evidence suggest that the ratio of stellar mass to BH mass was larger in the past than today. The existence of quasar at high redshift provides insight on the early universe, throughout much of the subsequent cosmic evolution, and thus the formation of the discrete structure in the universe from the primordial gas can be studied.

Chapter 2

Reverberation mapping

Contents

Variability is one of the main characteristic of AGNs. A significant magnitude variation (≥ 0.1 mag) over a time scale as short as day can be found in their light curve. Such a rapid variability indicates a compact continuum emitting region, which must be of the order of a few light days from the source coherence argument. This variation can be found at all wavelengths in electromagnetic spectra. However, the physical origin of the variation is highly debated. Accretion disk instabilities such as magnetohydrodynamics instabilities, variable accretion rate and obscuration of the nuclear source, or micro-lensing due to star could be the possible origins of the variability. Similarly, broad emission lines often vary in flux and in profile shape with a time scale of months to years. The variability in longer time scale is dramatic but in shorter time scale the variation is more subtle (a detailed review in this topic can be found in Peterson, 2001).

Variability was thought to be a powerful tool to study the geometry and kinematics of AGNs since the early 1980s. Since then, many multi-years monitoring were conducted to obtain Ultraviolet (UV) or optical continuum and emission lines variations in Seyfert 1 galaxies. UV spectra obtained by IUE monitoring on NGC 4151 showed close coupling in UV and optical continuum variation (Ulrich et al., 1991). Interestingly, this revealed that emission line variations are correlated with continuum variations. However response of different emission lines are vary different, in amplitude as well as in time scale (Antonucci and Cohen, 1983; Bentz et al., 2010a). Spectroscopic monitoring of NGC 4151 led to remarkable findings,

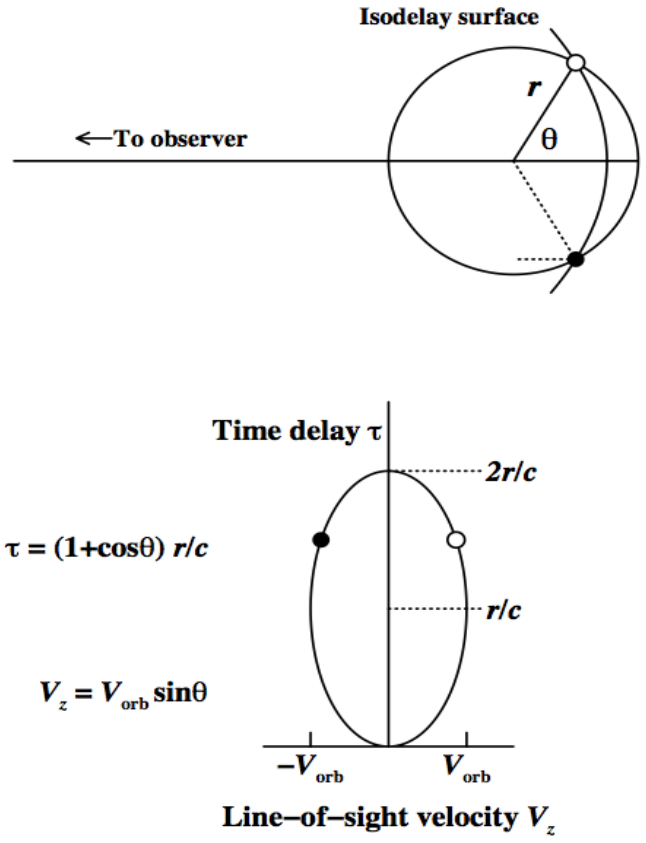

FIGURE 2.1: In the upper panel, clouds orbiting clockwise in a thin spherical shell is shown. The dotted line shows the extra path traveled by an ionizing photon to a BLR cloud plus the path of emission line photon until the path of the continuum pulse is the same as this line photon. All photons coming from the isodelay surface have the same delay. The lower panel shows a simple velocity-delay map that is the projected BLR orbit into velocity and time delay axis.

such as the response of the Balmer lines to the continuum variation on less than a month time scale, and the variation of higher order Balmer lines and HII λ4686 line with higher amplitude than Hβ and Hα (Antonucci and Cohen, 1983).

2.1 Reverberation mapping theory

2.1.1 Basic principle

Observing the response of the emission lines to the continuum variation, it is possible to estimate the geometry and kinematics of the BLR. Emission line responds to the continuum after a time delay, which is due to the light travel time within BLR, suggesting that emission line "reverberate" the changes in continuum. Hence, this technique of observing line and continuum variability to infer the BLR size is termed as "reverberation mapping" after Blandford and McKee (1982).

The idea is easy to understand if one thinks of the BLR as a collection of discrete clouds, each small with regard to the overall BLR, with a definite position and velocity. The variations of the continuum produced in the compact central accretion disk will be echoed in the emission line with a delay related to its position and a Doppler shift given by its radial velocity. For the purpose of illustration, the response of clouds orbiting in a clockwise thin spherical shell of radius R is shown in figure 2.1. The continuum pulse originating from the center propagate outward with the speed of light. It will then be absorbed and reprocessed by the BLR clouds located at a distance $r = c\tau$ producing the emission line photons. A distant observer will simultaneously record both continuum pulse and emission line response from the front side of the shell. However, the emission line response that is coming from another part of the shell will be delayed in time, which is due to the extra path traveled by the light from the continuum source to the BLR cloud and then to the observer. This delay can be written as

$$\tau = \frac{r}{c}(1 + \cos\theta) \tag{2.1}$$

where $0 \leq \theta \leq 2\pi$. After a given time delay τ, observer will see the emission line photons that lie along a surface of constant delay called "isodelay surface". The corresponding Doppler velocities of this clouds are $\pm v_{\rm orb}\sin\theta$. If we project the circular orbit along velocity and time delay axes, the projected map becomes an ellipse centered at $(0, r/c)$ with axes equal to $2v_{\rm orb}$ and $2r/c$ as shown in the lower panel of figure 2.1. The projected maps will change depending upon the inclination of the orbit or with other model parameters. Construction of response function of a BLR in the context of such a simple case is quite straight forward. The surface area of a thin spherical shell is $2\pi r^2 \sin\theta d\theta$, and if we consider a constant line response per unit area (η) of the BLR clouds, the emission line response of the ring can be written as

$$\Psi(\theta) = 2\pi\eta r^2 \sin\theta d\theta. \tag{2.2}$$

From Eq.2.1, a fixed infinitesimal unit of lag can be written as

$$\frac{d\tau}{d\theta} = -\frac{r}{c}\sin\theta. \tag{2.3}$$

The line response can be written in terms of time delay

$$\Psi(\tau)d\tau = \Psi(\theta)\left|\frac{d\theta}{d\tau}\right| d\tau \tag{2.4}$$

$$= 2\pi\eta r c d\tau, \tag{2.5}$$

where $\Psi(\tau)$ is called 1-D response function or transfer function. Eventually, the transfer function of a thin spherical shell is constant between $\tau = 0$ ($\theta = 2\pi$ for clouds lies along the observer line of sights) and $\tau = 2r/c$ ($\theta = 0$ for the clouds far side of the BLR). Such a transfer function is shown in figure 2.2, more model RM transfer functions are shown in the figure 2.2.

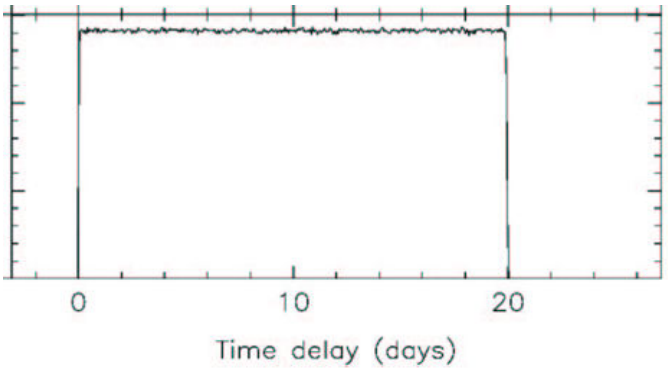

FIGURE 2.2: Response function of thin spherical shell. It is flat top profile extended from 0 to $2r/c$. Plot from Peterson (2001).

2.1.2 Method and observables

The main goal of reverberation mapping study is to recover the transfer function by studying the continuum and line flux variability. The main assumptions of reverberation mapping are: 1) The continuum emitting region is very small compared to the BLR and can be considered as point source, 2) Emission line clouds respond instantaneously to the changes in the continuum and the BLR is stationary during the reverberation monitoring campaign, and 3) The relationship between the observed line flux and continuum flux is simple, though not necessarily linear (see for a review Peterson, 2001).

The relationship between continuum and line emission can be written in terms of "transfer equation"

$$L(v,t) = \int_{-\infty}^{\infty} \Psi(v,\tau) C(t-\tau) d\tau \tag{2.6}$$

where $L(v,t)$ is the emission line flux at line of sight velocity v and time t, $C(t)$ is the continuum light curve, and $\Psi(v,\tau)$ is the RM "transfer function*" at v and time lag τ. The transfer function is basically the emission line response to a δ-function continuum pulse. The goal of the reverberation mapping is to recover the transfer function from the continuum and line light curve. However, due to noisy and sparse data, most reverberation mapping is focused on recovering velocity integrated 1-D response function $\Psi(\tau)$ from velocity integrated line light curve $L(t)$

$$L(t) = \int_{-\infty}^{\infty} \Psi(\tau) C(t-\tau) d\tau \tag{2.7}$$

and use in combination of line profile i.e. $\Psi(v) = \int \Psi(v,\tau) d\tau$.

Because of poor quality data, the most common technique to estimate the BLR size is to perform simple cross-correlation between line and continuum light curve

*This "transfer function" terminology is traditional in RM papers. It is different from the transfer function definition in standard signal processing as well as in optical interferometry.

to obtain the temporal shift that maximizes the correlation. The cross-correlation function is defined by

$$\mathrm{CCF}(\tau) = \int_{-\infty}^{\infty} L(t)C(t-\tau)dt. \tag{2.8}$$

After simple calculation one can find that the cross-correlation function is simply the convolution of transfer function with continuum auto-correlation function (see Peterson, 2001). The centroid of the CCF is defined by

$$\tau^*_{\mathrm{cent}} = \frac{\int \tau \mathrm{CCF}(\tau)d\tau}{\int \mathrm{CCF}(\tau)d\tau} \tag{2.9}$$

and is related to the mean response time or the centroid of the transfer function

$$\tau_{\mathrm{cent}} = \frac{\int \tau \Psi(\tau)d\tau}{\int \Psi(\tau)d\tau} \tag{2.10}$$

Note that these two quantities are same only if we have an infinite and well sampled time series. Thus, a key problem in RM is to find the true τ_{cent} in spite of time window and sampling problems. Thus, much work is going on for the best possible interpolation of the observed light curves (see Zu et al., 2011).

2.2 Model response function

In this section, I will provide some examples of transfer function considering different types of BLR geometry where the clouds are orbiting with Keplerian velocity: 1) face-on ring, 2) face-on extended thin disk, 3) inclined disk and 4) shell geometry.

The geometry of a **face-on ring** BLR is shown in of figure 2.3-1a. The clouds are orbiting with Keplerian velocity $V_r = \sqrt{GM_{\mathrm{bh}}/r}$. The line of sight velocity and time lag can be written as

$$V_z = \pm V(r)\sin\theta \sin i \tag{2.11}$$

and

$$\tau = \frac{r}{c}(1 + \cos\theta \sin i). \tag{2.12}$$

Since, the BLR is face-on ($i = 0$), the line of sight velocity component is zero. Time lag is also zero except at the location of the BLR cloud and subsequently shows a spike at time r_{blr}/c. As a result, in figure 2.3-1b, the 2D velocity-lag diagram a point appears at the location (0, r_{blr}/c). The sum of 2D velocity-lag diagram along velocity axis gives the 1D response function of BLR shown in figure 2.3-1c, and sum along time delay axis gives the line profile shown in figure 2.3-1d.

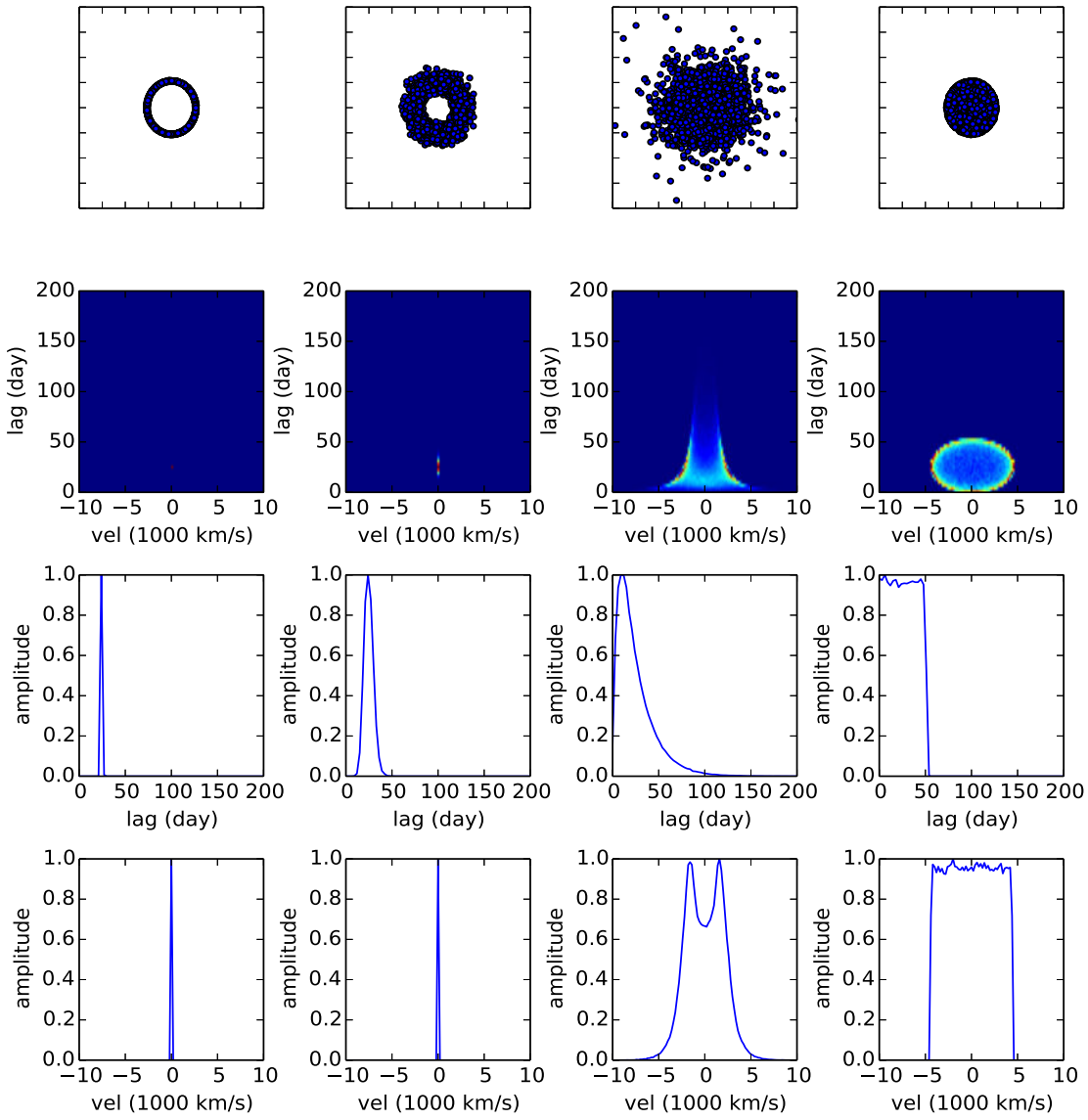

FIGURE 2.3: Response function for different types of BLR geometry. Left to right: 1) face-on ring, 2) face-on extended thin disk, 3) inclined disk and 4) spherical shell. Top to bottom: a) geometry of the BLR, b) 2D velocity-delay diagram or 2D response function, c) 1D response function and 4) line profile.

The 1D response function is a delta function at the location of BLR radius, while line profile shows a spike at zero velocity. Note that response functions and line profiles are normalized by their maximum intensity.

A **face-on extended** thin disk BLR geometry is shown in figure 2.3-2a. Since the clouds are spatially extended, the response comes from various radii of the BLR, and hence the response function is no longer flat but extended according to the distribution of the clouds as shown figure 2.3-2b, which is very similar to figure 2.3-1b, except the line response (figure 2.3-2c) extends up to $2r_{\rm blr}$. Line profile (figure 2.3-2d) shows a spike at zero, which is due to face-on view.

The response function of an **inclined disk** geometry can be calculated by summing the response over different circular orbits. Such an inclined disk with an extended BLR is shown in figure 2.3-3a. As the orbits are inclined, line of sight velocity is no-longer zero, changing the line profile from a delta function ($i = 0°$) to a double peaked profile (figure 2.3-3b). The 2nd response function clearly shows the total response from all different orbits of the disk, and due to large number of orbits, the 2D response function shows a smoothed profile. The extended clouds distribution results in a very extended response function (figure 2.3-3c), which is more than two times than before. The wings of the line profile (figure 2.3-3d) is extended from -$V_r(r_{\rm min})\,{\rm sin}i$ to +$V_r(r_{\rm min})\,{\rm sin}i$, where $r_{\rm min}$ is the inner radius.

A **shell** geometry, such as one shown in figure 2.3-4a, can be constructed from randomly oriented thin circular orbits with inclination ranging between 0 to 2π. As inclination decreases from $i = 90°$ to $0°$, the projected line of sight velocity decreases from $\pm V_r$ to 0. Similarly, the time lag decreases from $[0,\ 2r_{\rm blr}/c]$ to $[r_{\rm blr}(1 - {\rm sin}i)/c,\ r_{\rm blr}(1 - {\rm sin}i)/c]$. For $i = 0$, the geometry becomes a ring. Since the BLR orbits are randomly oriented, the projected velocity-time delay diagram appears to be filed up with the response from all the orbits whose size decreases down to zero with decreasing inclination (figure 2.3-4b). Note that, in this case, the 1D response function (figure 2.3-4c) and line profile (figure 2.3-4d) are rectangular functions due to the equal response from all the clouds. Response functions for more complex geometries, in the context of a geometrical and kinematical model, will be discussed in chapter 4.

2.3 Mean and rms spectrum

The BLR size derived from reverberation mapping can be used to determine virial mass of the central black hole knowing its velocity field. Information regarding the dynamics of BLR is encoded in the line profile, which is used to estimate two quantities; the Full Width at Half Maximum ($FWHM$) and velocity dispersion (σ_l). Combining width of the spectrum (ΔV) with BLR size, one could infer the virial mass using the following equation:

$$M = f\frac{r\Delta v^2}{G}, \tag{2.13}$$

where f is a scale factor that depends on the geometry and kinematics of the BLR.

One concern in the reverberation mapping BH mass estimation using Eq.2.13 is to determine which line-width estimator gives the best mass measurement. Since the ratio of these two measurements ($FWHM$ and σ_l) varies on object to object as well as on spectral properties. A general tendency is to take all spectra of an object, obtained during the whole monitoring campaign, and estimate their "mean" and "root-mean-square" spectrum (thereafter mean and rms spectrum[†]). An example of such mean and rms spectrum is shown in figure 2.4 from Peterson (2001). The top panel shows the mean spectrum of NGC 5548 computed from

[†]mean spectrum is the average spectrum of all the spectra obtained during the campaign, whereas rms spectrum is based on the variation around this mean.

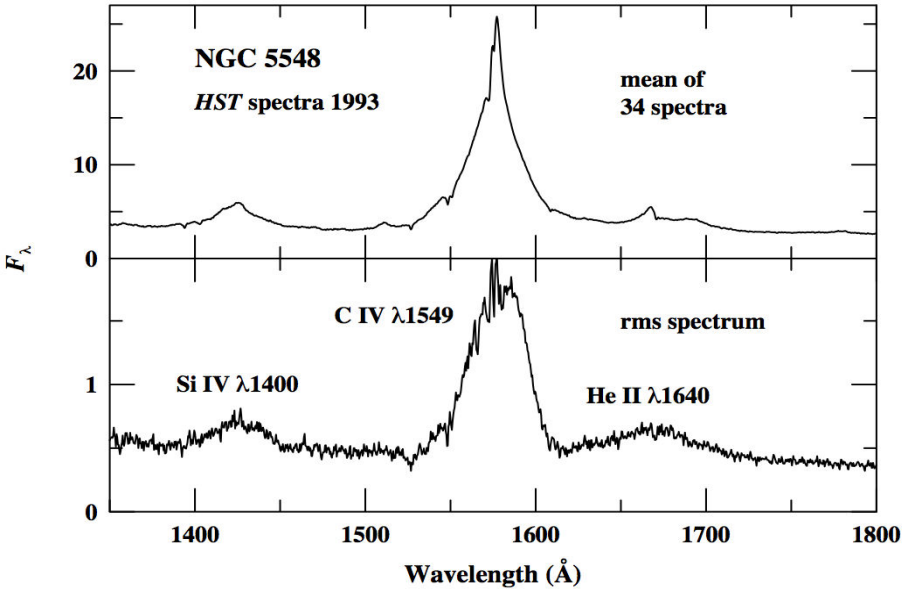

FIGURE 2.4: Upper panel shows the mean spectrum of NGC 5548 computed from 34 HST spectra and the lower panel shows the rms spectrum which is computed from the same data by computing rms flux at each wavelength. Constant features such as narrow line contribution and host galaxy contribution have been disappeared from the rms spectrum.

34 HST spectra whereas the lower panel shows the rms spectrum of the same data. The rms spectrum clearly isolates the constant features or slowly varying components, such as narrow emission line and the host galaxy contribution of the spectrum. However, the variability amplitude of the rms spectrum is low and often too noisy. Collin et al. (2006) showed that both $FWHM$ and σ_l measured from rms spectrum have higher uncertainty than the mean spectrum since the former tend to be more noisy. However, they found that for both line width estimators, the width of Hβ line in the mean and the rms spectrum are correlated, though mean spectrum is typically 20 % broader than rms spectrum. This suggest that if the narrow line contribution and other contamination features can be taken into account, the line width inferred from mean spectrum is consistence with rms spectrum. Thus care should be taken when dealing with single epoch spectra to estimate BH mass via virial relation since the variable part of the emission line can not be isolated.

Collin et al. (2006) suggested that σ_l (second order moment of the line profile is equal to the standard deviation for a Gaussian profile) is a less biased mass estimator, and virial mass calculated using σ_l is more consistent than $FWHM$, since virial mass calculated using σ_l is insensitive to the line profile, line ratios, inclination etc., but virial mass estimated using $FWHM$ is affected by the above factors. Hence the use of $FWHM$ and a constant scale factor in virial relation will underestimate or overestimate the masses of the central object. The reason why $FWHM$ is more sensitive to inclination than σ_l is that the former is sensitive to the line core that arises in a Keplerian disk component whereas the later is more sensitive to the line wings arising in Disk wind component.

2.4 Size-luminosity relation

Much efforts were made to estimate BLR size from the continuum and the line variability. Several highly sampled multi-wavelength reverberation mapping campaigns were undertaken that successfully recovered time lag of around 50 AGNs but mostly with Hβ line except for few AGNs where multiple emission lines lag were measured. After the success of first better sampled multi-wavelength reverberation mapping, International AGN watch program, during 1988-89 (Peterson et al., 1991), new campaigns were focused on better quality light curve. Kaspi et al. (2000) observed 17 PG quasars with a time span of 7 years for different Balmer lines providing a size-luminosity relationship. In this context, a homogeneous decent sampled data can be found in Peterson et al. (2004). Recent reverberation mapping campaigns such as Lick AGN Monitoring program (LAMP; see Bentz et al., 2009b) are focused on obtaining highly sampled light curve to constrain the BLR, and estimate better time lag and BH mass. Result of a similar recent high quality reverberation mapping program is presented in Bentz et al. (2006) and Grier et al. (2012). Direct model fitting of the LAMP data successfully estimated BLR size and BH mass without virial scale factor providing its detailed geometry and kinematics (Brewer et al., 2011; Pancoast et al., 2012, 2014a). However, this was done only for few very low luminous AGNs, and even with the better quality RM data, parameter degeneracy remains (see chapter 4 and 7). Few attempts were also made to find the size-luminosity relation for high redshift ($2.2 \leq z \leq 3.2$) and high luminous quasars using CIVλ1550 broad emission line (Kaspi et al., 2007). These observations suggest that

- Different emission lines come from different regions of BLR and arise only when the combination of emissivity and responsivity optimized for that emission line, suggesting ionization stratification of the BLR: higher-ionization lines have shorter time lag and originate closer to the Black Hole than the lower-ionization line.
- Studies of rms spectrum also suggest that BLR is virialized, which means the higher-ionization lines are broader than lower-ionization line ($\tau \propto \Delta V^{-2}$).
- BLR size is related to the AGN luminosity L via a simple relationship, which is approximately $R \propto L^{1/2}$.

Prior to the advance in reverberation mapping, photo-ionization modeling predicted the existence of such size-luminosity relationship (Ferland and Mushotzky, 1982), which was searched even with the first undersampled reverberation mapping observation (Koratkar and Gaskell, 1991), but Kaspi et al. (2000) found a well defined version of this relation, which is $R \propto L^{0.7}$ by studying few PG quasars over a time span of 7 years. However, after several improvements such as better light curve sampling (Bentz et al., 2009b), improved light curve interpolation technique to remove the gaps between different epochs (Zu et al., 2011) and measuring AGN luminosity subtracting the host galaxy contribution (Bentz et al., 2009c), the final relationship looks like $R \propto L^{0.54}$, which is quite close to photo-ionization model prediction. This recent $R - L$ relation, which is obtained for Hβ broad emission line, is shown in figure 2.5. The intrinsic scatter of this relation is 0.13 dex. This

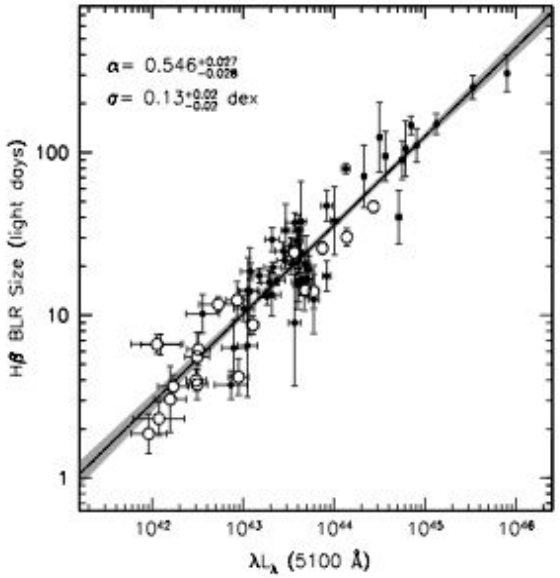

FIGURE 2.5: The Hβ BLR size vs. the 5100 $\AA$ AGN luminosity as shown in Bentz et al. (2013). Best fit is indicated by solid line and the uncertainty is shown by gray-scale region. The empty circle represents the result from new observations since Bentz et al. (2009c).

suggests, with an accurate host corrected AGN luminosity, $R - L$ relation in Hβ would allow to obtain BLR size as good as best individual reverberation mapping lag measurements (which is accurate to 0.09 dex). Although $R - L$ relation is well-calibrated only in Hβ, some observations indicate similar relation also holds for CIV and UV continuum, however, much efforts are needed to actually have a well-calibrated one (Kaspi et al., 2007).

Current reverberation mapping campaigns however focus on getting highly sampled light curves to estimate accurate time lag, but are mainly limited to the low to intermediate luminosity region and very low redshift $z < 0.2$ because the targets are selected for their apparent brightness, known variability or favorable position in the sky. Certainly, there is a need to expand the reverberation mapping population to calibrate $R - L$ relation for high redshift objects as well. The problem is that the BLR size increases with luminosity and also with redshift as $R \propto (1 + z)^{0.5}$, hence at large redshift, objects are having longer time lag, which means long duration reverberation mapping campaigns, and sufficient sampling is needed to estimate time lag with good accuracy (see Horne et al. (2004) and chapter 5). Another problem is that the line center shifted with redshift as $(1+z)$, and hence for high redshift objects one needs to observe high ionization lines that are coming closer to the central source and hence CIV line is potentially more important than Hβ.

Outer boundary of the BLR

The outer boundary of BLR is the most important parameter in the photoionization model since it determines the actual BLR size, gas velocities as well as line ratio of different lines. Recent reverberation mapping observations suggest that the dust sublimation radius is a factor of 4-5 larger than the mean Hβ BLR size

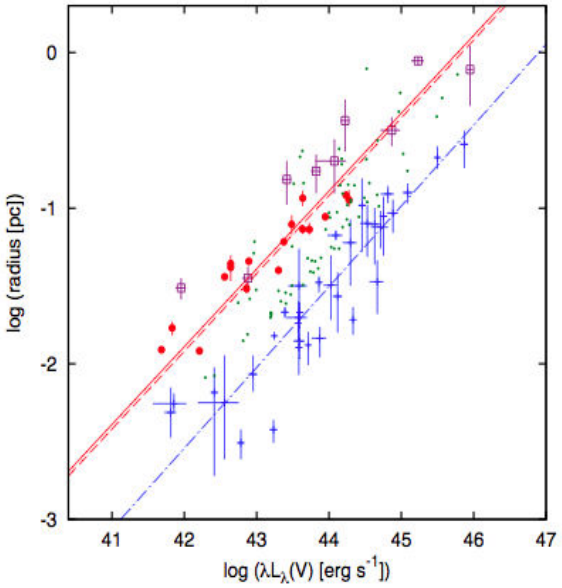

FIGURE 2.6: Size-luminosity relation of BLR and dust obtained from RM and OI observations. Radius of inner most dust torus from RM (red filled circle), K-band interferometric observation (purple open square), Hβ BLR radius from RM (blue cross) and location of the hot-dust clouds obtained from the spectral energy distribution (green dot) is plotted against V-band luminosity. The lines represent the best fits of the different data sets. This plot is taken from Koshida et al. (2014), a detailed description can be found there.

(Koshida et al., 2014). This suggests that the existence of dust grains beyond the sublimation radius may be a natural boundary of the dust-free BLR. Two independent techniques support this hypothesis.

Monitoring of several AGNs in dust reverberation mapping campaign clearly shows time lag between K-band, which is interpreted as the emission from the innermost dust torus, and V-band, which is due to the central source (Suganuma et al., 2006; Koshida et al., 2014). In the case of dust reverberation mapping, the V-band continuum is absorbed by the innermost dust and re-emitted in K-band and hence dust time lag provides size of dust sublimation radius. On the other hand, optical interferometry in near-IR K-band successfully resolved the emission from inner rim of dust torus at different temperatures for a handful number of AGNs (Kishimoto et al., 2009a, 2011a,b). These interferometric observations also provided an independent size-luminosity relation of dust in K-band. However, the dust reverberation radius is smaller by a factor of two compared to the interferometric radius of the innermost dust torus. This apparent difference between interferometric and reverberation mapping radius observed in the same band could be due to the fact that the former is a flux weighted radius and the latter is response-weighted (Kishimoto et al., 2011b). Since dust temperature decreases with radius, the flux-weighted radius would be larger at large distance than inner boundary of dust, due to flux contribution from lower temperature dust at larger radii. On the other hand, reverberation mapping radius is weighted on a larger amplitude of flux variation and thus coming from a compact emitting region or at smaller radii in the dust torus. The radius of the innermost dust torus as obtained from dust reverberation mapping (red filled circle) and K-band interferometric observation

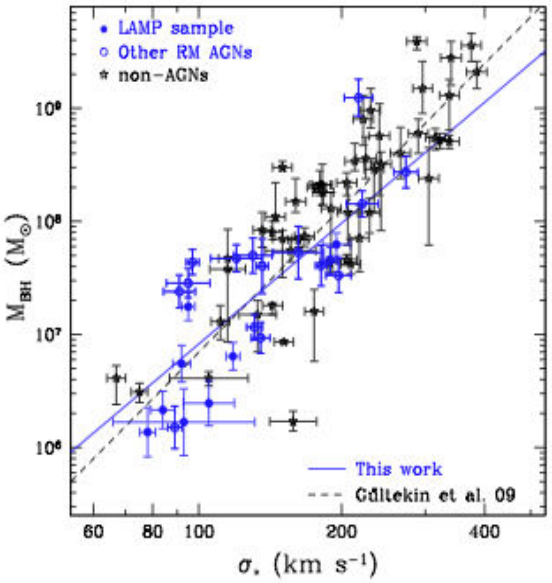

FIGURE 2.7: The $M_{\rm bh} - \sigma_*$ relationship of quiescent galaxy (black) and AGNs (blue) as shown in Woo et al. (2010).

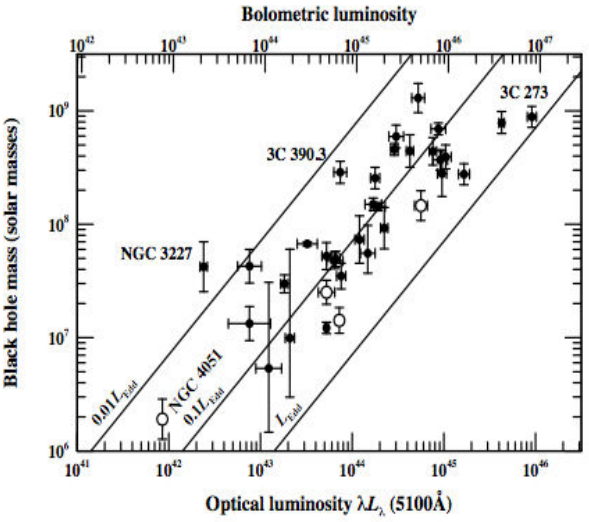

FIGURE 2.8: BH mass - luminosity relation for a sample of 35 reverberation mapping AGNs. The open circles represent NLS1s. From Peterson et al. (2004).

(purple open square), and the Hβ BLR radius (blue cross) as well as the locations of the hot dust clouds (green dot) from spectral energy distribution (SED) fitting of type-1 AGNs are plotted against optical V-band luminosity in figure 2.6, including the best-fit lines for dust and BLR reverberation mapping, showing clear differences in radii of different regions (for a detailed discussion see Koshida et al., 2014).

2.5 Mass-luminosity relation

As noted earlier, study of multiple emission lines suggests that the lines with shorter lag tend to be broader than those with longer lag, and consistent with "virial relation" (Peterson et al., 2004; Peterson and Wandel, 1999). SMBH masses estimated using Eq.2.13 depends on f, which is determined by measuring BH mass with other technique.

Since there is no other direct technique to estimate BH mass, a common practice is to use the relationship between BH mass and host-galaxy bulge velocity dispersion, $M_{\rm bh} - \sigma_*$. It has been seen that the $M_{\rm bh} - \sigma_*$ relation for quiescent galaxies (Ferrarese and Merritt, 2000) is consistence with the AGNs (Gebhardt et al., 2000b; Onken et al., 2004), although host-galaxy bulge velocity dispersion in AGN is difficult to measure due to its bright nucleus and distant position. However, the assumption allowed to compute a statistical average value of the scale factor, which is $< f > \sim 5.5$ (Onken et al., 2004). The $M_{\rm bh} - \sigma_*$ relations for quiescent galaxy (black) and AGNs (blue) are shown in figure 2.7 from Woo et al. (2010) with an average scale factor $< f >= 5.25$. The scatter in scale factor is 0.4 dex, which is the main source of uncertainty in the BH mass measurement. The BH mass and luminosity relation is shown in figure 2.8, which shows a scatter around 30 % (Peterson et al., 2004).

To reduce the uncertainty in BH mass estimate, a compulsory step is to reduce the scatter in scale factor, and thus it is necessary to constrain the BLR geometry and kinematics. Although reverberation mapping is a direct mass estimator where spatial resolution is replaced by time resolution, the dependence on another method, $M_{\rm bh} - \sigma_*$ relation, makes it a secondary mass estimation method. Very recently few attempts have been made to directly model high quality reverberation mapping data keeping BH mass along with other BLR geometry and kinematics parameters as free (Pancoast et al., 2014a). This study shows very different scale factor for individual objects ranging from 0.7 (0.2) for NGC 6814 to 42.6 (6.1) for Mrk 1310 measured using rms (mean) profile. This suggests that f depends strongly on geometry and kinematics of the individual object. An alternative technique is needed to estimate the black hole mass independent from the virial scale factor constraining the geometry and kinematics of the BLR, and hence calibrating mass-luminosity relation. Such a technique is optical interferometry, which has the potential to spatially resolve the BLR clouds. In the following chapters, I will discuss how optical interferometry can directly estimate BH mass and constrain the BLR geometry and kinematics.

2.6 Summary

Reverberation mapping is a powerful tool, which uses variability to study the BLR of quasar and successfully provided a size-luminosity and mass-luminosity relation. The size-luminosity relation, if properly calibrated, can be used for cosmological distance estimation. The main uncertainty in size-luminosity relation is due to inaccurate time lag estimation, which is due to poor light curve sampling, and

inaccurate luminosity measurement. Recently, many steps have been taken to obtain better quality light curve and host galaxy corrected luminosity measurements. However more efforts are needed to reduce the scatter. The main limitation is that all reverberation mapping targets are highly selective and limited to low redshift. Thus, it is necessary to expand the target list to higher redshift and luminosity as well as for different emission lines, to use the size-luminosity relation as standard candles. The mass-luminosity relation, on the other hand, suffers from the unknown scale factor problem. However, other technique such as interferometry, could solve this scale factor problem by constraining BLR geometry and kinematics, and estimating BH masses directly. This could also allow to estimate distances using "quasar parallax" method combining reverberation mapping data (Elvis and Karovska, 2002).

Chapter 3

Optical interferometry

Contents

3.1 Observing at High resolution

From the time of William Herschel, it was clear that the sharpness of an image is limited by atmosphere rather than the optics of the telescope. Reaching the diffraction limit of a single-dish was a big challenge in the past. A remarkable technique was proposed by Fizeau to overcome the diffraction limit of a single telescope by observing through a pair of holes. Following this, various methods have been proposed to overcome the diffraction limit of a telescope such as Speckle interferometry by Labeyrie (1970), Adaptive optics (Babcock, 1953; Beckers, 1993) and Aperture masking (Baldwin et al., 1986). Although, with the help of all the above techniques, it was not possible to resolve the central structure of AGNs.

Multi-telescopes optical interferometry (OI) is intended to provide very high angular resolution information, and ideally images, with resolution λ/B where λ is the observation wavelength and B is the interferometer baseline, i.e. the maximum distance between two apertures. After a long period of pioneering instrumental

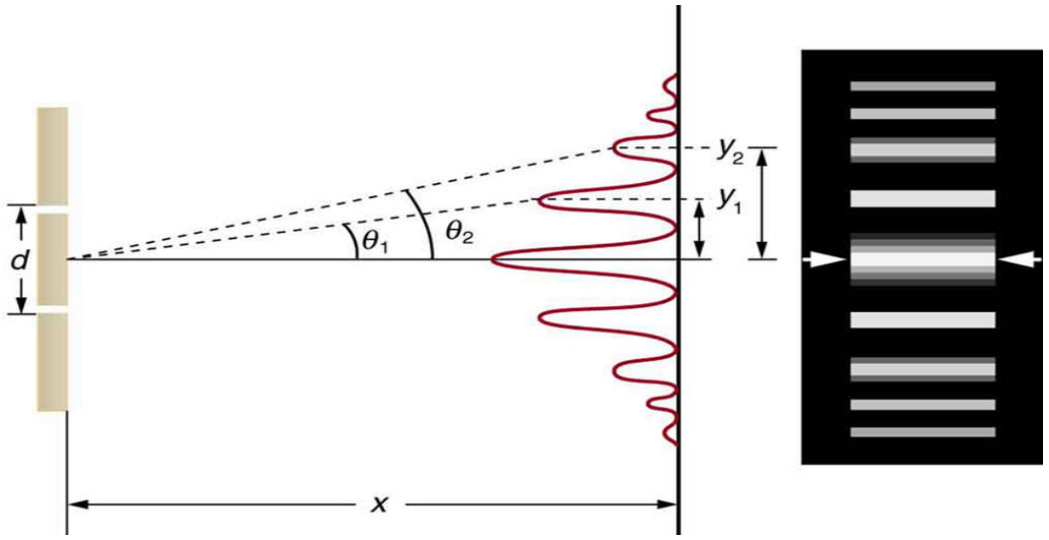

FIGURE 3.1: Young double slit experiment setup with a front screen with two holes and and a back screen to see the interference pattern. The intensity of the fringes decreases as angle increases from the center, and bright and dark fringes appear at the screen at different distances. Credit:voer.edu.vn

results, the 2000 decade has seen an explosion of the number of science papers produced by optical interferometry, mainly triggered by the the interferometric mode of the VLT, called the VLTI (Glindemann et al., 2000), and its AMBER and MIDI instruments, followed in number of papers by the US interferometers CHARA, PTI, IOATA, NPOI and KI. A recent review of OI science results can be found in Jankov (2011). The major OI instruments in operation are spectro-interferometers, which means that the interferometric measures are obtained in several spectral channels simultaneously with resolutions ranging from 30-40 (LR for low resolution) to 300-1500, often called medium resolution or MR, and 12000-30000, which is the high resolution (HR) domain. The cross analysis of interferogram, simultaneously obtained in different spectral channels, allows high accuracy differential interferometric observations, which give access to high dynamical features or to very unresolved objects with small signature ("differential interferometry" Petrov, 1989). The different spectro-interferometric measurements and their uses are presented later in this chapter in the context of the VLTI near infrared spectro-interferometric instrument AMBER (Petrov et al., 2007).

3.2 Basics of interferometry

Present OI is somehow a modification of the famous Young's double slit experiment, which was done in nineteenth century by Thomas Young, who used a screen with two holes and another screen as a detector for interferometric pattern as shown in figure 3.1. The former is now replaced by two individual telescopes separated by a distance that is usually referred as the baseline of the interferometer, whereas an interferometric beam combiner is used in place of the second screen. The light beams from two telescopes are then carefully combined and fringe pattern is produced due to interference of the light beams and provide information

about the source with a resolution $\theta \propto \lambda/B$, where λ is the observing wavelength. The observed intensity at the image plane is simply the modulus squared of the summation of the electric field arriving from two slits. If, we consider them as E_1 and E_2 respectively, then the observed intensity

$$I =< (E_1 + E_2) \times (E_1 + E_2) > \tag{3.1}$$
$$=< |E_1|^2 > + < |E_2|^2 > +2 < |E_1||E_2|\cos(\phi) >, \tag{3.2}$$

where ϕ is the phase difference between two electric fields, and the first two terms define the mean intensity of the fringes, while the third term refers to the visibility function.

We are mainly interested in measuring two quantities of the fringes, its amplitude and its phase. Fringe amplitude or contrast is the measure of the "Michelson visibility", which is related to the maximum and minimum intensities of the fringe pattern by

$$V_{\rm M} = \frac{I_{\rm max} - I_{\rm min}}{I_{\rm max} + I_{\rm min}}. \tag{3.3}$$

On the other hand, fringe phase gives the position of the fringe center with respect to the zero optical-path-difference (OPD) position (for a review, see Haniff, 2007).

An interferometer with baseline B yields the complex visibility of the source, i.e. the normalized Fourier Transform $\tilde{O}(\mathbf{u}, \lambda)$ of the source brightness distribution $O(\mathbf{r}, \lambda)$ at the spatial frequency $\mathbf{u} = \mathbf{B}/\lambda$. According to the van Cittert Zernike theorem

$$\tilde{O}(\mathbf{u}, \lambda) = \frac{\int\int O(\mathbf{r}, \lambda) \mathrm{e}^{-2\pi \mathrm{i} \mathbf{u}.\mathbf{r}} \, \mathrm{d}^2\mathbf{r}}{\int\int O(\mathbf{r}, \lambda) \, \mathrm{d}^2\mathbf{r}} = V_*(\lambda) \mathrm{e}^{\mathrm{i}\phi_*(\lambda)}. \tag{3.4}$$

The modulus $V_*(\lambda)$ of $\tilde{O}(\mathbf{u}, \lambda)$ is given by the contrast of the fringes and called the source absolute visibility. The relative position of the fringes yields the phase $\phi_*(\lambda)$ of the source complex visibility.

A schematic diagram of a two telescopes interferometer is shown in figure 3.2, which mainly consists of five different sections, each of which plays crucial role such as:

- Two collectors collecting the photons from the source we are looking at.
- A beam transport system to carry the signal from the telescope to the central laboratory where the beams can be combined. The distances between collector and beam combiner are d_1 and d_2 for two different telescopes.
- A delay line system to adjust the additional path travel by one beam compared to the other before combination.
- A beam combiner.
- A detector to store the signals obtained from beam combination.

Since the atmosphere constantly changes, the refractive index $n(\lambda)$ and hence the OPD also change. To overcome this, it is either necessary to make short exposures and extract the piston (OPD difference) from monochromatic delay before

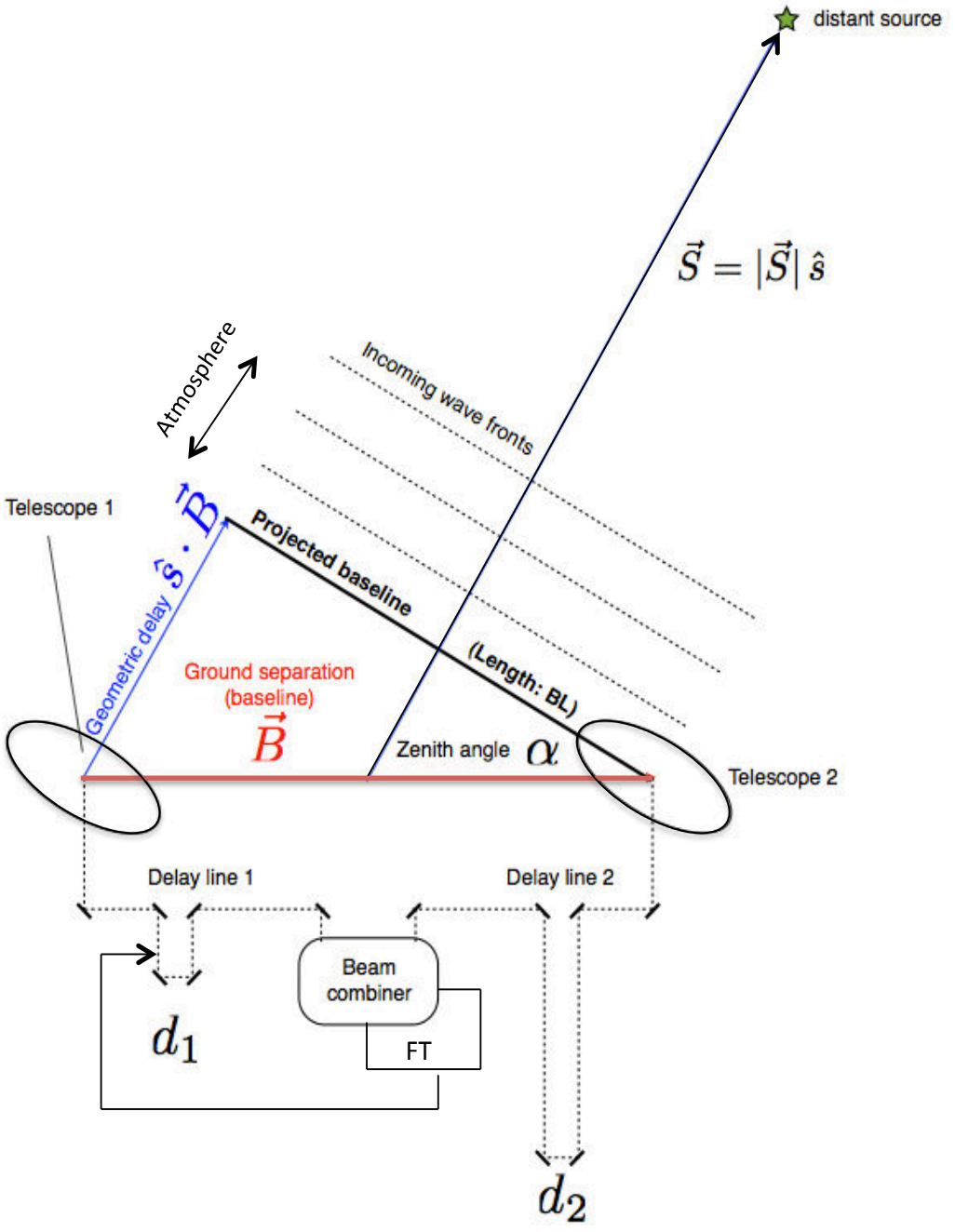

FIGURE 3.2: A simple cartoon to illustrate a two telescopes interferometer. Different parts play different role explained in the main text.

computing the differential phase (see later), or to use an adaptive system called a fringe tracker that freezes the OPD (with λ/u) and allows to use less exposures. The variation of OPD during the frame is a major reason for instrumental contrast change, and hence loss of visibility accuracy. Thus a fringe tracker increases substantially the measurement accuracy. Fringe tracker can be the instrument itself, or a specialized device operating at a different wavelength or different beam combination architecture (see Petrov et al., 2014).

The monochromatic electric field, at the beam combiner, for two different apertures, can be defined as a function time t by

$$\Psi_1 = A_1 \exp\left(\mathrm{i}k\left[\hat{s}\cdot\mathbf{B} + d_1\right]\right)\exp(\mathrm{i}\omega t) \tag{3.5}$$
$$\Psi_2 = A_2 \exp\left(\mathrm{i}k d_2\right)\exp(\mathrm{i}\omega t), \tag{3.6}$$

where, A_1 and A_2 are proportional to the collecting area of the telescope. If they are equally sensitive then $A_1 = A_2 = A$. The resulting intensity after the combination, can be written as

$$I = <|\Psi_1 + \Psi_2|^2> \tag{3.7}$$
$$\propto 2 + 2\cos\left(\mathrm{i}k\left[\hat{s}\cdot\mathbf{B} + d1 - d2\right]\right) \propto 2 + 2\cos(\mathrm{kD}), \tag{3.8}$$

where the quantity $D = [\hat{s}\cdot\mathbf{B} + d1 - d2]$ is often called the delay or the optical path difference (OPD) between two beams and $k = 2\pi/\lambda$. In reality D includes an atmospheric delay term that makes difficult to obtain the phase information in a two telescopes interferometer.

The projected baseline $\mathbf{B}$, i.e. the separation between two telescopes as seen from the source, can be defined as $\mathbf{B} = B_X\hat{i} + B_Y\hat{j} = \lambda(u\hat{i} + v\hat{j})$, where B_X and B_Y are the baseline components along x and y axis respectively. The spatial frequencies u and v are defined as

$$u = B_X \cos h - B_Y \sin\phi \sin h \tag{3.9}$$
$$v = B_X \sin\delta \sin h + B_Y\left(\sin\phi\sin\delta + \cos\phi\cos\delta\right), \tag{3.10}$$

where h is the hour angle, δ is the declination and ϕ is the latitude of the interferometer.

Since, at any given wavelength (λ_0), the detector has a finite bandpass ($\Delta\lambda$), the above monochromatic treatment is not applicable, and hence we need to consider the polychromatic case by integrating Eq.3.8 for uniform bandpass:

$$I \propto \int_{\lambda_0-\Delta\lambda/2}^{\lambda_0+\Delta\lambda/2} 2[1+\cos(2\pi D/\lambda)]\mathrm{d}\lambda \tag{3.11}$$
$$\propto \Delta\lambda\left[1 + \frac{\sin(\pi D\Delta\lambda/\lambda_0^2)}{(\pi D\Delta\lambda/\lambda_0^2)}\cos(k_0 D)\right] \tag{3.12}$$
$$\propto \Delta\lambda\left[1 + \frac{\sin(\pi D/\Lambda_{\mathrm{coh}})}{(\pi D/\Lambda_{\mathrm{coh}})}\cos(k_0 D)\right], \tag{3.13}$$

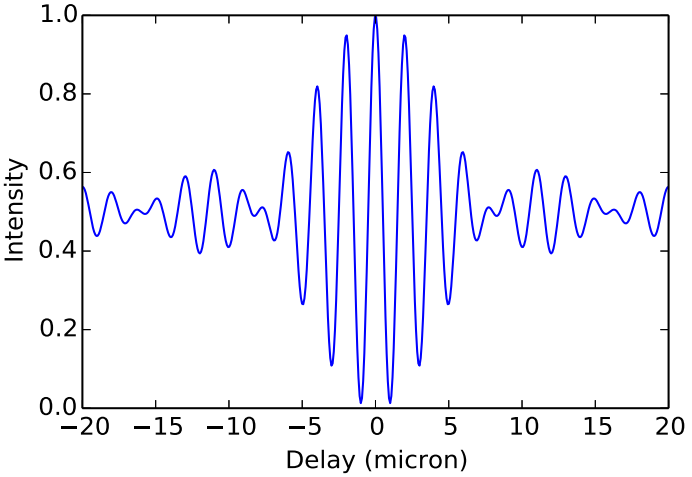

FIGURE 3.3: The resulting fringe pattern for a polychromatic source for a two-elements interferometer with spectral bandpass of 0.5 μm centered at 2 μm together with visibility amplitude 1. This corresponds to a coherence length of 8 μm, which can be identified by the first null of the sinc function.

where the quantity $\Lambda_{\rm coh} = \lambda_0^2/\Delta\lambda$ is called the coherence length and $k_0 = 2\pi/\lambda_0$. Thus, the response of polychromatic detector is a modulation of the fringes by a sinc function, which is so-called "coherence envelope".

The resulting fringe pattern for a two telescopes interferometer as a function of optical path difference (OPD) is shown in figure 3.3. Fringe contrast is modulated by coherence envelope. Thus, delay lines are needed to match the optical path better than $\Lambda_{\rm coh}$, otherwise the measured fringe visibility will not be the source coherence function. As the fringe contrast is reduced by the coherence envelop, the OPD should be $<< \Lambda_{\rm coh}$.

3.3 Spectro-interferometric measurements

A spectro-interferometric instrument such as AMBER (Petrov et al., 2007) provides several observables, in each spectral channel, absolute visibility, differential visibility, differential phase and closure phase (a detail discussion about these can be found in Petrov et al., 2007; Petrov, 2012). In this section, first, I will give equations related to spectro-interferometric measurements and then briefly discuss them.

Although the basic equation of optical interferometry is given by Eq.3.4, in reality what we measure is the Fourier interferogram $\tilde{I}(\mathbf{u}, \lambda)$ from the Fourier Transform (FT) of the fringe intensity distribution $I(\mathbf{u}, \lambda)$. In multi-axial instruments with n_T telescopes, like AMBER ($n_T = 3$), we have a single interferogram where the

three baselines are separated in frequency space.

$$\tilde{I}(\mathbf{u},\lambda) = \tilde{F}(\mathbf{u},\lambda)\sum_{i=1}^{i=n_T} p_{*i}(\lambda) + \sum_{i,j>i}^{i=j=n_T} \tilde{F}(\mathbf{u}-\mathbf{u_{ij}},\lambda)\sqrt{p_{*i}(\lambda)p_{*j}(\lambda)} \times V_{*ij}(\lambda)V_{Iij}(\lambda)\mathrm{e}^{i[\phi_{*ij}(\lambda)+\phi_{Iij}(\lambda)]}, \quad (3.14)$$

where $p_{*i}(\lambda)$ is the contribution of telescope i to the source flux collected in the interferometric channel; $\tilde{F}(\mathbf{u},\lambda)$ is a fixed instrumental function (product of the individual aperture transfer function by an instrument window transfer function); $V_{*ij}(\lambda)$ and $\phi_{*ij}(\lambda)$ are the source visibility and phase at the spatial frequency $u_{ij} = B_{ij}/\lambda$ where B_{ij} is the baseline length between apertures i and j; $V_{Iij}(\lambda)$ and $\phi_{Iij}(\lambda)$ are the instrumental visibility and phase terms respectively. After the correction of photometry and coherent flux (see chapter 5), the (average) Fourier interferogram at the spatial frequency u_{ij} yields an estimate of the complex visibility

$$C_{Mij}(\lambda) = V_{*ij}(\lambda)V_{Iij}(\lambda)\mathrm{e}^{i[\phi_{*ij}(\lambda)+\phi_{Iij}(\lambda)]}. \quad (3.15)$$

We have to calibrate $V_{Iij}(\lambda)$ and $\phi_{Iij}(\lambda)$ to obtain the source information $V_{*ij}(\lambda)$ and $\phi_{*ij}(\lambda)$. The instrumental contrast $V_{Iij}(\lambda)$ is calibrated by the observation of a reference source with known $V_{*ij}(\lambda)$ (ideally $V_{*ij}(\lambda) = 1$ for a fully unresolved source). The calibration procedure assumes that $V_{Iij}(\lambda)$ is constant in time, which is seldom the case. In practice the changes in instrumental contrast limit the accuracy on the absolute visibility $V_{*ij}(\lambda)$ to 0.05, or 0.03 in the best case (Petrov et al., 2007; Petrov, 2012).

However, the wavelength dependent $V_{Iij}(\lambda)$ is often very stable, particularly for MR observation where we look at a small wavelength range. This explains the interest to use the differential visibility

$$V_{d*ij}(\lambda) = \frac{|C_{Mij}(\lambda)|}{C_{Mij}(\lambda_{\mathrm{ref}})} = \frac{V_{*ij}(\lambda)}{V_{*ij}(\lambda_{\mathrm{ref}})}. \quad (3.16)$$

For simplicity, we assumed that the instrument differential visibility $\frac{V_{Iij}(\lambda)}{V_{Iij}(\lambda_{\mathrm{ref}})} = 1$.

The measured phase $\phi_{*ij}(\lambda)$ is affected by the instrumental achromatic differential piston δ_{ij} and instantaneous atmospheric piston. The phase introduced by the achromatic piston is $\phi_{ij}(\lambda) = 2\pi\delta^{ij}(\sigma)$, where $\sigma = 1/\lambda$. There are two ways to obtain phase information from the source complex visibility. The first one is the closure phase between triplets of baseline, for instruments with at least 3 telescopes:

$$\Psi_{ijk}(\lambda) = \arg[C_{Mij}(\lambda)C_{Mjk}(\lambda)C^*_{Mij}(\lambda)] = \phi_{*ij}(\lambda) + \phi_{*jk}(\lambda) - \phi_{*ik}(\lambda) = \Psi_{*ijk}(\lambda), \quad (3.17)$$

because the instrumental closure phase $\Psi_{Iijk}(\lambda) = \phi_{Iij}(\lambda) + \phi_{Ijk}(\lambda) - \phi_{Iik}(\lambda) = 0$ as discovered by radio astronomers more than 50 years ago. The second one is to use the differential phase. The phase of the reference channel can be well known in MR, continuum channel, where the source phase is supposed to be constant. Thus, we first fit the measured phase with a linear function of σ allowing us to

correct the residual piston

$$\phi_{d*ij}(\lambda) = \arg[C_{Mij}(\lambda)C_{Mij}(\lambda_{\rm ref})] = \phi_{*ij}(\lambda) - \phi_{*ij}(\lambda_{\rm ref}). \quad (3.18)$$

Note that reference channel can be defined in many ways and must be accounted in model fitting process.

Thus, spectro-interferometric measurements can be summarized as follows:

- **Spectrum:** Spectrum of the emission line is an important observable that contains informations on the physical conditions, chemistry and kinematics of the object. Each individual beam from each telescope provides one spectrum in the observing spectral window. It is necessary to calibrate the spectrum in the amplitude and wavelength, and averaging them in one spectrum. Thus a calibrator with known continuum and spectral features, and magnitude and position close to the science target has to be used. The spectrum is used to constrain kinematics of many objects (see for example Meilland et al., 2007).
- **Absolute visibility:** Absolute visibility is obtained from the fringe contrast, and it is the modulus of the source complex visibility (Eq.3.4). It gives information on the size of the source in the direction of observed baseline (if the source is centro-symmetric then absolute visibility should be same in all directions). However, note that, absolute visibility, obtained from any interferometer, depends on the instrument and atmospheric parameters, hence it has to be calibrated prior to use to constrain source morphology. Usually, a source with known visibility, known as "calibrator", is used to correct the "instrumental visibility" considering that both the calibrator and science target are observed in the same condition, which makes the calibration process difficult.
- **Differential visibility:** An accurate measurement of the visibility can be obtained from the Differential visibility, by self calibrating the absolute visibility with respect to the visibility of the reference channel or the broad band visibility defined in Eq.3.16. Our recent AMBER observation of 3C273 shows that the accuracy on the differential visibility can be as good as 1%, though the accuracy on absolute visibility is of the order of 5% (Petrov et al., 2012). The reason is that the differential visibility is free from the systemic effects that are present in absolute visibility, and also insensitive to the variation of the "piston", which is the average of the wavefront OPD, over a limited wavelength range. Moreover, differential visibility does not require a calibrator star to eliminate the instrument effects.
- **Differential phase:** Source absolute phase refers to the phase of the complex visibility (Eq.3.4). However, measuring absolute phase is not possible, since OPD changes with atmosphere. Because of this, an off-axis reference source is needed, which is however often not available. Moreover, a complicated system is needed to get rid of instrument and atmospheric effects. One way is to measure the differential phase as written in Eq.3.18. In order to calculate the differential phase we subtract first average slope and then average phase.

- **Closure phase:** The closure phase, which is a combination of phases measured on three baselines, as defined by Eq.3.17, is free from optical path affecting individual beams. Closure phase combined with accurate visibility can be used to reconstruct image of the astronomical source and to obtain detailed information about it (Lawson et al., 2006). However, note that, closure phase is difficult to measure and often difficult to interpret.

3.3.1 Differential interferometry of non-resolved sources

A non-resolved source has a global angular size Λ smaller than the interferometer resolution limit λ/B. In Eq.3.4, this implies that $o(\mathbf{r}, \lambda)$ is different from 0 only for values of $r < \lambda/B = 1/u$, i.e. the integral in Eq.3.4 can be limited to values $ur < 1$. Since Petrov (1989), we know that the interferometric phase for such a source is given by

$$\phi_{*ij}(\lambda) = 2\pi \mathbf{u}_{ij} \cdot \boldsymbol{\epsilon_{ij}}(\lambda), \tag{3.19}$$

where,

$$\boldsymbol{\epsilon_{ij}}(\lambda) = \frac{\int\int \mathbf{r} o(\mathbf{r}, \lambda) d^2\mathbf{r}}{\int\int o(\mathbf{r}, \lambda) d^2\mathbf{r}} \tag{3.20}$$

is the photocenter of the source. This result has been obtained from a first order limited development of the complex visibility $\tilde{O}(\mathbf{u}, \lambda)$. Extending this development to higher terms (Rakshit and Petrov, 2014) shows that the source visibility $V_{*\mathrm{ij}}$ is given by

$$V_{*\mathrm{ij}} = 1 - \alpha_{\mathrm{ij}}^2 \quad \text{where } \alpha = \frac{\pi\Lambda}{\sqrt{2}\left(\frac{\lambda}{B}\right)}, \tag{3.21}$$

and the closure phase decreases as α^3. However, photocenter decreases only like $\frac{RB}{\lambda}$ between the source size, $R \propto \epsilon(\lambda)$, and the interferometric resolution (λ/B), while 1-$V(\lambda)$ decreases like $(\frac{RB}{\lambda})^2$. Hence photocenter displacement can easily be measured for unresolved sources. Its application to unresolved sources had been proposed first for differential speckle interferometry by Beckers (1982) and extended to the long baseline interferometry by Petrov (1989).

3.4 Modeling visibility

As already mentioned in the previous section, modeling interferometric measurements provide the source brightness distribution though Eq.3.4, and hence in this section I will discuss some simple models and show how their visibility functions look like. This will help to understand how visibility changes with baseline length for different simple geometries. Various complex models that can be fitted to the observed data to better constrain the geometry and dynamics, will be discussed in the following chapters in the context of model fitting.

Intensity distribution and the corresponding visibility function is plotted in figure 3.4 for different simple geometries; point source, binary source, Gaussian and uniform disk.

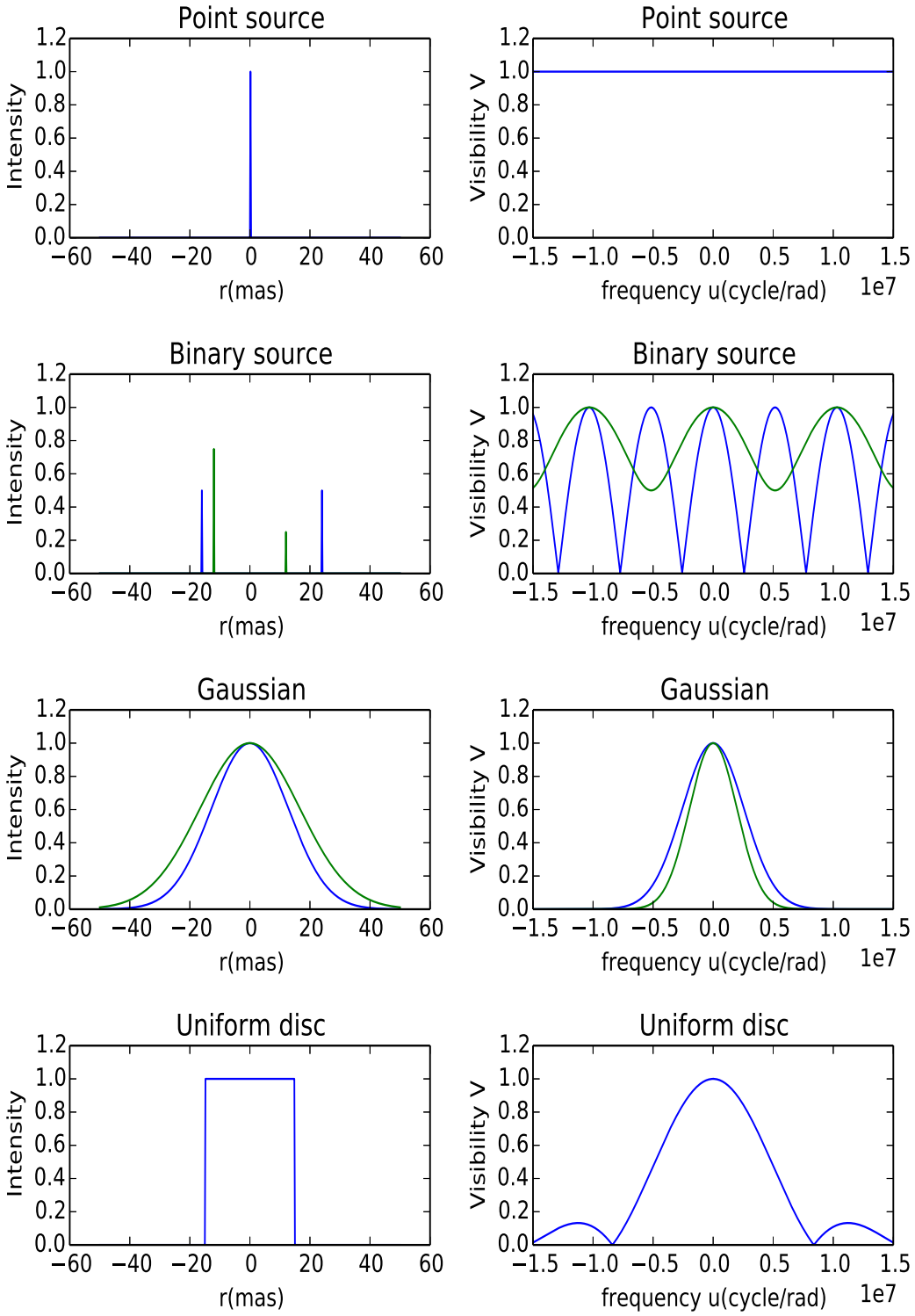

FIGURE 3.4: Examples of the visibility functions for various simple source surface brightness distributions are plotted. From top to bottom the models are point source, binary source, Gaussian and uniform disk. The surface brightness is plotted on the left while on the right corresponding visibility functions are plotted. Colors on the left panels corresponds to the right panels.

Point source:

Intensity distribution of a point source can be written in terms of a Dirac δ-function as shown in upper-left panel of figure 3.4:

$$I(r) = I_0\delta(r - r_0), \tag{3.22}$$

where, $r = \sqrt{(x^2 + y^2)}$ is the radial coordinate and r_0 is the position of the source. The Fourier transform of a point source gives a complex visibility whose amplitude is 1. Thus, the absolute visibility is always constant and is equal to 1 as shown in upper-right panel figure 3.4:

$$V(u) = 1, \tag{3.23}$$

where $u = B/\lambda$ is the spatial frequency as noted earlier. This shows that visibility of a point source is independent of spatial frequency or the length of baseline and always remain unresolved. If we have source phase information, which in this case is $\mathrm{e}^{-2\pi u\cdot r_0}$, we will have the information about its position, since source phase varies linearly with spatial frequency (u) with a slope of r_0.

Binary:

A binary system consists of two point sources or two Dirac-δ functions separated by distance d. The intensity distribution can be written is terms of radial coordinate as

$$I(r) = I_1\delta(r - \frac{d}{2}) + I_2\delta(r + \frac{d}{2}). \tag{3.24}$$

The fluxes of two sources are represented by I_1 and I_2 ($I_1 + I_2 = 1$) respectively. Note that visibility of a binary strongly depends on the projected baseline, and if the baseline is perpendicular to the binary, visibility function will be constant, $V(u) = 1$, as interferometer will see only one point source. The visibility function for a binary can be written as

$$V(u) = \sqrt{\frac{1 + f^2 + 2f\cos(2\pi ud)^2}{1 + f}}, \tag{3.25}$$

where $f = I_1/I_2$ is the intensity ratio of two point sources. The intensity distribution and corresponding visibility for two different binaries with different flux ratios are plotted in 2nd row of figure 3.4. Thus, flux ratio has a strong effect on visibility signature.

Gaussian:

Gaussian function often used to model source brightness distribution since a complex source at low resolution can be represented by a simple Gaussian, which can be defined with zero mean and standard deviation σ as

$$I(r) = \mathrm{e}^{-\frac{r^2}{2\sigma^2}}. \tag{3.26}$$

Its visibility function

$$V(u) = \mathrm{e}^{-2(\pi\sigma u)^2}, \tag{3.27}$$

FIGURE 3.5: VLTI during sunset with four 8-m unit telescope with few ATs. Credit:ESO/B. Tafresh

is also a Gaussian function as shown in 3rd row of figure 3.4. Note that, in Fourier space, source size is inversely proportional to the source size of real space i.e., an extended source in real space (for example green Gaussian) appears compact in the Fourier space.

Uniform disk:

Stellar surfaces are often described by a uniform disk. Its intensity distribution can simply be written as

$$I(r) = I_0 \quad \text{for } |d| \leq d/2 \tag{3.28}$$
$$= 0 \quad \text{else.} \tag{3.29}$$

Its absolute visibility is given by

$$V(u) = \left| 2\frac{J_1(\pi u d)}{\pi u d} \right|, \tag{3.30}$$

where J_1 is the Bessel function of the first kind of the order 1. Intensity distribution and corresponding visibility for a uniform disk are shown in lower panel of figure 3.4.

3.5 The VLTI

To observe faint targets such as AGN, it is necessary to use interferometers with large apertures (8-10 m) to collect a large number of photons. Thus, only two interferometers: Very Large Telescope Interferometer (VLTI) and Keck Interferometer (KI), have the capability to observe AGNs (Glindemann et al., 2000). Unfortunately, KI is no longer in operation. Other interferometers such CHARA, NPOI etc. have longer baselines, but consist of smaller telescopes and hence are mainly focused to study stars. As a consequence, present optical interferometric observation of AGNs only depends on VLTI. It offers several beam combiners such as MIDI working on mid-IR and AMBER working on near-IR. Mid-IR emission originates from warm dust ($T \sim 300$ K), and hence it was extensively used to study the dust structure, while AMBER works in near-IR K-band, where emission originates from hot dust and gas ($T \sim 1500$K), and hence is used to study inner structure of the dust torus and the BLR emission line in MR.

The VLTI is located at 24°40′S, 70°25′W at the top of Cerro Paranal in the Atacama desert at altitude of 2635 m. The unique location in the driest desert provides a great observation conditions; many clear nights with good stable seeing. Its remote location ensures minimum light pollution by human. These conditions allow infrared wave band to be transparent and thus a great advantage for high spatial resolution observation all over the year.

VLTI consists of four 8.0 m unit telescopes (UTs) located at fixed position and four movable 1.8 m auxiliary telescopes (ATs) as shown in figure 3.5. The maximum ground separation or baseline length of the UTs is 130 m, which is the distance between UT1-UT4, providing mili-arcsecond spatial resolution. We can combine three telescopes using AMBER (Petrov et al., 2007) offering simultaneous observation using three telescopes ($N_b = \frac{N_{\rm tel}(N_{\rm tel}-1)}{2}$) in near-IR and four telescopes using PIONIER (see section 3.5.2).

3.5.1 Light transportation and delay line

The most complicated system in VLTI is hidden underneath the UT platform and used to transport and combine the light beams, which is first received by individual telescope and then transfered via Nasmyth focus to the Coude room located underneath the platform. The wavefronts are then corrected from the atmospheric distortion by the adaptive optics (AO) system Multi-Application Curvature Adaptive Optics (MACAO; Arsenault et al., 2003). In near-IR or shorter wavelength, MACAO is very useful to correct wavefronts of the individual telescopes. In addition, another fringe tracking instrument, FINITO (Fringe-tracking Instrument of NIce and TOrino), a three-beams fringe tracker that operates in the H band, is used at VLTI to measure the relative phase difference between the light beams.

After the AO correction the light is transported to the delay lines, which consists of retro-reflector carriages on a movable rail as shown in figure 3.6. The complicated delay line system is thus used to adjust the optical path between the light beams, which was discussed before. Several variable curvature mirrors (VCMs) maintain the VLTI pupil fixed in the focal lab while the delay line moves by adjusting their curvature. An Infrared Image Sensor (IRIS) is used here to correct the additional delay introduced by the air in the VLTI delay line tunnel and is not corrected by the MACAO or FINITO. After optical delay adjustment, light is guided to the interferometric laboratory to combine different light beams. Beam compressors are also used to compress the light beam to obtain equal diameter beams before sending them to the beam-combiners.

VLTI provides unique opportunity to connect many UTs or ATs in near and mid-IR in interferometric mode. However, its complicated light transportation system, i.e., light has to go through several reflections, limits the sensitivity of the interferometer. Only about 15% of light received by the telescopes can thus reach the interferometric beam-combiners (Puech et al., 2006), and the global VLTI plus instrument plus detector efficiency is of the order of 10%.

FIGURE 3.6: VLTI delay line. Credit: ESO

3.5.2 VLTI instruments

Several instruments are dedicated to the interferometric observations at VLTI.

- MIDI: A two beams combiner works at the mid-IR wavelength ($8 - 13\mu$m, Leinert et al., 2003). It has two spectral resolution mode 230 and 30. It was used extensively in the case of AGN to study mid-IR emission from the dust torus. MIDI has recently been decommissioned.
- AMBER: A three beams combiner working on near-IR ($1 - 2.5$ μm) in J, H and K bands (Petrov et al., 2007). It has 3 spectral resolution mode; 12000, 1500, 30. This is the only instrument allowing to study BLR of AGN with resolution 1500 in K band and hence will be discussed later in detail.
- PIONIER: A four beams combiner in H band (Le Bouquin et al., 2011). It allows mainly imaging at low spectral resolution and not useful in studying AGNs so far (very faint in H band).

VLTI future instruments or the next generation instruments are

- MATISSE: A four beams combiner in L, M and N bands (Lopez et al., 2006). This will be very useful to study AGN dust torus geometry.
- GRAVITY: Four beams combiner in K band, with spectroscopic, fringe tracking and astrometric capabilities (Eisenhauer et al., 2008). Gravity would allow to observe BLR of AGNs. These applications will be discussed in chapter 6.

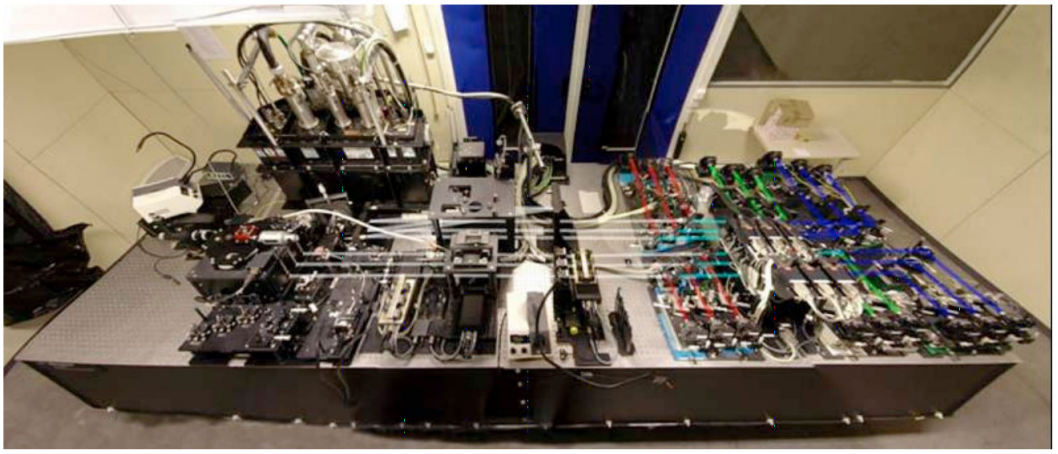

FIGURE 3.7: Composite photograph of the AMBER instrument in the integration room in 2003. Image from Petrov et al. (2007).

3.5.3 The AMBER instrument

Astronomical Multi-BEam combinerR (AMBER) is the first-generation general-user near-infrared (J, H, and K bands) interferometric beam combiner of the VLTI (A general description about AMBER can be found in Petrov et al. (2007), and its data reduction process has been explained in Tatulli et al. (2007)). Figure 3.7 shows a photograph of AMBER instrument with its different components. It combines light beams coming from three different telescopes. It is in operation at VLTI since 2004. AMBER fringes are spectrally dispersed and it provides interferometric observation at three different spectral resolutions: R $\sim$ 30 i.e. low, R $\sim$ 1500 i.e. medium, and, R $\sim$ 12000 i.e. high resolution. It was designed to obtain milli-arcsecond resolution to study the astrophysical objects like young and evolved stars as well as AGNs, and to possibly detect exoplanet signal. AMBER uses optical fibers and a dispersed fringe combiner using spatial coding.

Initially, AMBER and FINITO were expected to reach $K > 10$ and hence to study some AGNs. Mainly because of VLTI problems, the limiting magnitude of both systems was limited to about $8 - 9$ (AMBER in LR in K band) and FINITO limited to $8 - 8.5$ for MR observations. This is because both need an SNR > 1 for each short exposure and channel. In 2011, we implemented AMBER+, that can work in "blind mode" and for SNR $<< 1$ per frame and spectral channel (see section 3.6.1). This allowed LR as well as MR observations in $K = 10 - 11$ range. With some recent VLTI improvements this limit might be up to $K > 11$. This will be discussed in more detail in chapters 5 and 6.

The basic concept of AMBER design is shown in figure 3.8. It works in three steps. First, a single mode fiber (at the left) is used to filter beams coming from three telescopes to convert the phase fluctuation of the corrugated wavefront to intensity fluctuation. The amount of light entering the filter depends on the Strehl ratio*. The beams are then compressed into one dimensional elongated beams by a pair of conjugated cylindrical mirrors and guided to the entrance slit of the spectrograph. One part of the light is then separated from each beam using beam-splitters and

*It is the ratio of peak diffraction intensities of an aberrated vs. perfect wavefront.

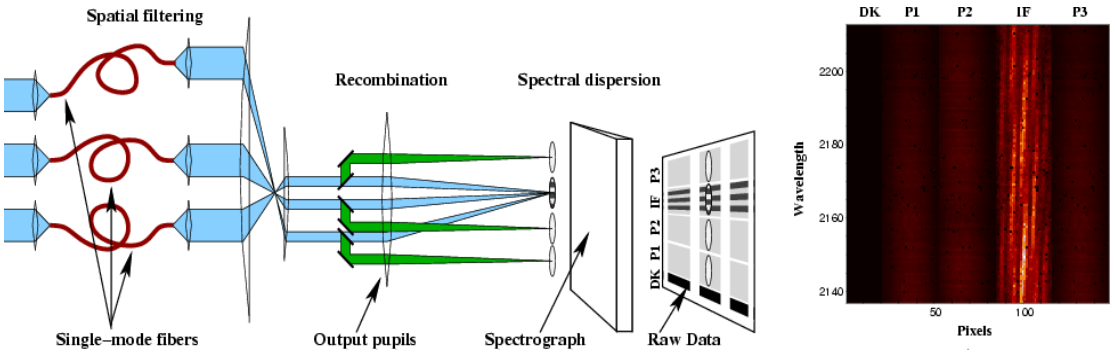

FIGURE 3.8: Basic layout of AMBER. The beams, from three telescopes, enter to the spatial filter (left) and then passing through complicated setup reach to the detector (right) where photometric and one interferometric data are recorded. See the text for detail. Right panel shows an example of AMBER reconstituted image from the raw data of HD135382 obtain in medium resolution. Each column in detector shows dark region (DK), three photometric regions (P1, P2 and P3), and one interferogram (IF). Image from Tatulli et al. (2007)

different tilt is applied to each beam to put them in different location on the detector, and as a result we obtain three photometric channels corresponding to each incoming beam. While the other part of light of the three beams are allowed to superimpose on the detector image plane obtaining interference fringes. A spectral dispersing element (prism or gratings) is used to disperse the beams in the pupil plane and hence all three photometric regions and one interferogram are spectrally dispersed allowing to record all observables on the detector.

AMBER has Rockwell/HAWAII detector with readout noise $11e^-$, cooled by liquid nitrogen at a temperature of 78 K, covering a spectral window of $0.8 - 2.5\mu$m (see Petrov et al., 2007; Tatulli et al., 2007). It consists of 512 $\times$ 512 pixel array in which first 20 pixels are masked and used to estimate read-out noise and bias during an exposure. These pixels are noted as "DK" in the figure 3.8, while the photometric outputs, noted as "P1", "P2" and "P3", are 32 pixels wide. The interferometric output, which stores interference fringes, is using $N_{\rm pix} = 32$ pixels.

Additionally, a calibration and alignment unit (CAU) is used to provide well defined artificial fringes for the interferometric calibration process, and a polarization corrector is used to eliminate one of the polarization of the incoming beams but losing 50% of the incoming photons. This polarization correction is necessary since single-mode fibers, which are used in AMBER, introduces a variable OPD between two polarizations and can destroy the instrumental contrast.

In an interferometer with multi-axial recombination mode, such as AMBER, there is a linear relationship between pixels of the interferogram and the instantaneous complex visibilities. This concept is known as Pixel to Visibility Matrix (thereafter P2VM; Tatulli et al., 2007; Chelli et al., 2009). In P2VM data processing (Tatulli et al., 2007), the shape of unresolved source fringe and calibrated giving a Visibility to Pixel Matrix (V2PM). Thus, we fit the best source complex visibilities on the 3 baselines that match the observed interferogram and photometric measurements. This is obtained through a geometrical inversion of V2PM that is the P2VM.

FIGURE 3.9: VLTI AMBER control room. Image taken in June 2013 before starting the observation.

This procedure works only if individual phase can be obtained in each frame, that assumes an SNR per frame is greater than 1.

3.6 Observing with AMBER

AGN observations with AMBER are preformed in "visitor mode" allowing the observer to be present at the VLTI operating room during observation along with ESO astronomer, unlike the "service mode" in which observations are performed only by ESO astronomers without the presence of observers. Observers can guide the astronomer on the strategies that need to be followed during the observation. This is particularly important as AGNs are observed in the non-standard AMBER+ "blind mode".

To ask for observing time, a proposal must be written and submitted to ESO[†]. Several cares should be taken to write the proposal such as information about source, its visibilities and suitable calibrators, selection of the baselines, list of backup targets in case of problem to observe desired target etc. Once the proposal is selected, observer in "visitor mode" is invited to go to the site. Prior to the observing night, different blocks of observations, depending on the strategies, are created using standard tool "Phase 2 Preparation Package" (P2PP[‡]), which are then used to perform observation through VLT control system. These blocks include information regarding templates, instrument setup, pointing interferometer

[†]http://www.eso.org/

[‡]A detail description can be found here:
http://www.eso.org/sci/observing/phase2/SMGuidelines/Documentation/P2PPTutorialAMBER.html

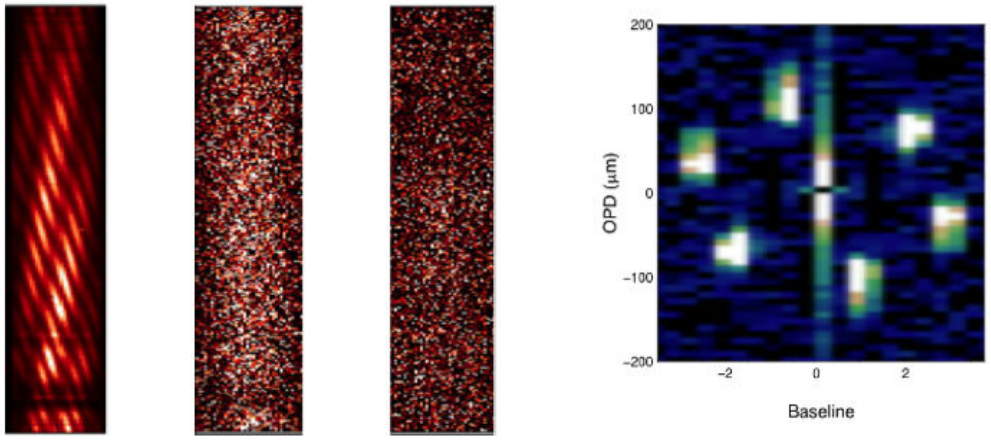

FIGURE 3.10: Fringe detection technique in blind mode observations. The three left figures are $x - \lambda$ interferograms with fringes dispersed in the vertical direction. The magnitudes are $K = 4$ (left), $K = 8.5$ (center) and $K = 9.7$ (right). The rightmost figure represents a $10^{'}$ average 2DFT of the interferograms for $K = 9.7$.

to the target, optimizing beam injection in AMBER, fringe search to obtain the exact zero OPD (ZOPD), and finally acquiring observation data. When fringes have been found and tracking of fringes is done, actual integration starts to record data (a photograph of VLTI/AMBER control room is shown in figure 3.9, which was taken before our observation).

Using P2PP, an observer can change some of the parameters such as wavelength range, spectral dispersion, or detector integration time (DIT). Night astronomer can use Breaker of Observing Blocks (BOB) to successfully execute the observation and can abort or redo some part if necessary.

3.6.1 Blind mode observation

A different approach was developed by our group to observe faint targets like QSOs with AMBER since to study the BLR emission line we need to resolve the emission line spectrally. Spectral resolution greater than 500 would give access more than 10 velocity bins allowing to constrain the global velocity field. A resolution around 200 would give access to the size and position of the BLR. However, to obtain such a resolution in near-IR, a traditional point of view is to have a fringe tracker to stabilize the fringes. It allows exposure times longer than the piston coherence time, and this is necessary to get out of the detector noise regime. Our first proposal for differential interferometric observation of BLR with AMBER/VLTI assumed fringe tracking, and an expected photocenter accuracy of 2μm for one hour of observation on a $K = 10$ magnitude object. This implied that two dozens of target could be observed using our observation technique (Marconi et al., 2003).

The limiting magnitude of the fringe tracker poses a problem for BLR observations. As per ESO call for proposal[§], medium resolution observation with AMBER/VLTI allows fringe tracking up to $K = 7.5$ with UTs, and at maximum $K = 8.5$ in very

[§]http://www.eso.org/sci/observing/phase1.html

good weather condition since the current fringe trackers need a sufficient SNR in extremely short exposures, to be able to freeze the piston at a fraction of wavelength. As a result, it is difficult to have fringe tracker to observe AGN in medium resolution. This makes observation of BLR very difficult.

Due to above problems, we have developed a new observing technique called "Blind mode observation" keeping in mind that it is not necessary to detect fringes in each individual frame. With the medium spectral resolution of AMBER, the coherence length in the K band is of about 3 mm. The atmospheric piston jitter has a RMS amplitude of typically a few tens of microns and the delay line model errors and drift are below 100 μm/mn. So, after centering the fringes on a bright calibrator, we have at least half an hour to observe a faint target with the guarantee that the fringes are present in the data, even if each individual frame looks just as detector noise. This is why it is called "blind mode" as no fringes can be seen on the detector nor by the Fourier transform. We still need to make exposures short enough to have a good fringe contrast. We must integrate values which are not sensitive to the piston value but still contain information about the source visibility, differential phase and closure phase.

The Blind mode technique can be summarized as:

- First, we find the fringes on a bright calibrator and we know that they will remain within the coherence length of MR observations (3 mm in K) for at least 10 minutes.
- Then, we observe the faint target, without detecting any fringes in individual frames (i.e. P2VM is useless) and we accumulate incoherently the 2-Dimensional Fourier Transform (2DFT) of the $x - \lambda$ interferograms similar to the REGAIN/GI2T and VEGA/CHARA data accumulation technique (Berio et al., 1999). The 2DFT data processing is discussed in the following section.
- Then data is processed (see section 3.6.2 and Petrov et al., 2012), and the fringe peaks appear in a few seconds in the average $|2\text{DFT}|^2$, showing the average piston. This average piston value is communicated to the operator, with typically half a minute delay, and allows him to correct for slow OPD drift. In MR observation, such corrections are useful typically in every 10 minutes, to keep the fringe peaks in a correct position (within 100 μm). A correct position is defined by fringe peaks well separated in the piston (i.e. λ direction). This is necessary because we cannot use the P2VM fit to separate the contribution of partially overlapping fringe peaks.
- The final data processing, described in Petrov et al. (2012), allows extracting unbiased visibility, differential visibility and differential phase from each 1 minute exposure of data.

This principle is further illustrated by figure 3.10, in which, on the left, three $x-\lambda$ interferograms have been shown with an image at the rightmost panel that shows $10^{'}$ average of 2D Fourier transform of the $x - \lambda$ interferogram. Among the three interferograms, the figure 3.10a (left) is for a bight star with $K = 4$ showing clearly

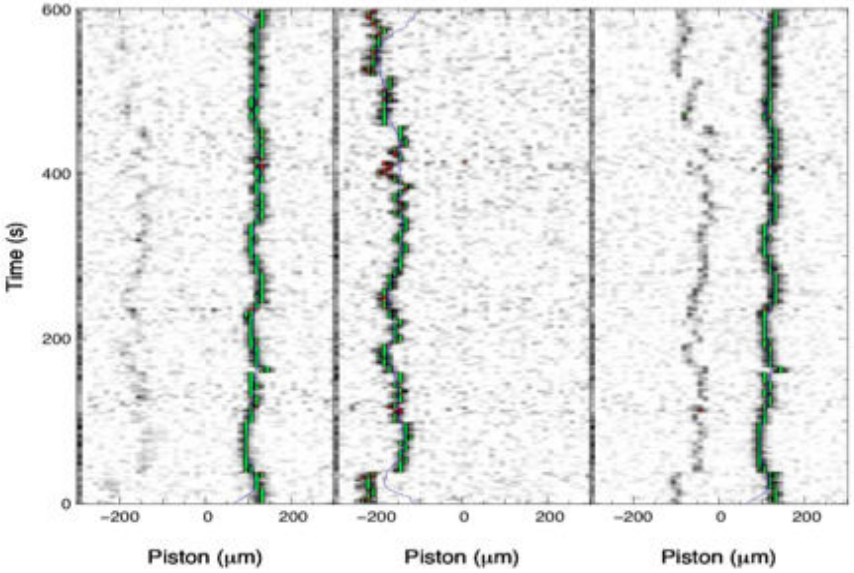

FIGURE 3.11: Measurement of piston (OPD) by 2DFT processing on 3C273. Each plot is a cut of the right image of figure 3.10 at the fringe peak frequency in the piston direction and repeated over time.

three well-separated fringes, while the figure 3.10b (middle) is for a faint source of $K = 8.5$. This is the limit of the P2VM operation, where fringes are quite hard to see, but frame-by-frame data processing detects fringes and measures a piston in at least in some frames. Figure 3.10c (right) shows interferogram with $K = 9.7$, in which fringes are invisible and any frame-by-frame processing fails. However, the 2D Fourier transform (2DFT) processing of this $x - \lambda$ interferogram of $K = 9.7$ yields the average power spectrum displayed in figure 3.10d with 3 clear fringe peaks. Piston offsets have been introduced to clearly separate the fringe peaks. The peak blurring corresponds to the piston drift in 10 minutes. We see here that it is smaller than 50 μm.

The position of the fringe peak in the 2DFT modulus can be used to evaluate and correct the piston value. Figure 3.11 displays the cuts of figure 3.10d in the piston direction at the frequency of each baseline, as they evolve in time. The position of the fringe peak yields the absolute piston (group delay) evolution with time.

In blind mode technique, we use a 2D Fourier transform of $x - \lambda$ interferograms, similar to the one used in REGAIN/GI2T and VEGA/CHARA (Berio et al., 1999). This particularly helps a straightforward and unambiguous detection of the average group delay after some integration time and as a result it is easy to use as a low frequency coherencing sensor correcting slow drifts of the OPD. Similar tools were used to analyze the dark current and sky images on detector (Li Causi et al., 2008).

Let us consider $i_m(x, \lambda)$ is the $x - \lambda$ interferogram of AMBER as shown in figure 3.10. First, we resample the data along λ direction to obtain equally spaced interfringe corresponding to the average wavelength ($\bar{\lambda} = 1/\bar{\sigma}$). Thus, in the new interferogram $i(x, \sigma)$, spectral channels are equally spaced in wavenumber $\sigma = 1/\lambda$, achieved by a bilinear interpolation to obtain an $x - \sigma$ image. If frames

are oversampled in both x and λ directions, then it is expected to have little impact on the quality of the data, and the information is present in the fringes as before. Then, we perform Fourier transform of the $i(x,\sigma)$ images in each spectral channels yielding 1D Fourier interferogram $I(u,\sigma)$, which is:

$$I(u,\sigma) = \mathcal{F}_x\left[i(x,\sigma)\right] = n(\sigma)F(u,\sigma)\sum_i n_i + \sum_{i,j>i}\sqrt{n_i n_j}\Omega(u,\sigma)\mathrm{e}^{2i\pi\sigma p_a^{ij}}, \quad (3.31)$$

where $n(\sigma)$ is the source spectrum as seen by the instrument, $F(u,\sigma)$ is the Fourier transform of the resampled window, n_i denotes the total contribution of telescope i to the photon in the interferogram, $\Omega(u,\sigma)$ is the Fourier transform of the source as seen by the instrument, and p_a^{ij} is the achromatic part of the piston difference in the baseline $i-j$. The quantity $\Omega(u,\sigma)$ can be written as:

$$\Omega(u,\sigma) = n(\sigma)V_I(u,\sigma)V_*(u,\sigma)\mathrm{e}^{\left[\phi_*(u,\sigma)+i\phi_I(u,\sigma)+2i\sigma p_c^{ij}(\sigma)\right]}F(u,\sigma), \quad (3.32)$$

where $V_I(u,\sigma)$ and $\phi_I(u,\sigma)$ represent the instrument visibility and phase respectively, while $V_*(u,\sigma)$ and $\phi_*(u,\sigma)$ are the source visibility and phase at the spatial frequency u and wavenumber σ. $p_c^{ij}(\sigma)$ is the chromatic part of the piston difference:

$$p^{ij}(\sigma) = p_i(\sigma) - p_j(\sigma) = p_a^{ij} + p_c^{ij}(\sigma), \quad (3.33)$$

where the achromatic OPD difference p_a^{ij} corresponds to OPD or "piston" difference between two beams, and $p_c^{ij}(\sigma)$ contains all the wavelength dependent terms in the OPD that are dominated by the dispersion in the VLTI tunnels. The former varies rapidly with time but the latter is dominated by the terms evolving more slowly as the source zenith distance changes. For simplicity, we will consider that the window function $f(x,\sigma)$ is flat and with constant size and hence $F(u,\sigma) = \delta(u)$.

A Fourier transform of the interferogram in Eq.3.6.1 in the wavenumber direction yields the 2D Fourier transform:

$$\hat{I}(u,\nu) = \mathcal{F}_\sigma\left[i(u,\sigma)\right] = \hat{n}(\sigma)\,\hat{F}(u,\nu)\sum_i n_i + \sum_{i,j>i}\sqrt{n_i n_j}\Omega(u,\nu)\,\delta(\nu - p_a^{ij}), \quad (3.34)$$

and the average power spectrum:

$$D(u,\nu) = <|\hat{I}(u,\nu)|^2> = |\hat{n}(\nu)\,\hat{F}(u,\nu)|^2\sum_i n_i + \sum_{i,j>i}\sqrt{n_i n_j}|\Omega(u,\nu)|^2 < \delta(\nu - p_a^{ij}) >, \quad (3.35)$$

$D(u,\nu)$ shows a low frequency peak and one fringe peak for each baseline at the position $u = B_{ij}\bar{\sigma}$ and $\nu = p_a^{ij}$ as illustrated in figure 3.10d. The typical size of the fringe peak is given by the spectral coverage of the initial interferogram. For AMBER, in medium resolution, this is between $\lambda_1 = 2\,\mu$m and $\lambda_2 = 2.3\,\mu$m yielding a fringe peak width of $\lambda_1\lambda_2/(\lambda_2 - \lambda_1) = \lambda^2/\Delta\lambda = 15\,\mu$m. Under standard conditions, it takes at least a few seconds for the piston to drift by that value, and this sets a limit of the blind-mode technique: we can observe sources producing a

fringe peak of sufficient SNR in a few seconds to allow a piston measurement and correction. If the classical limit of the instrument is set by the necessity to detect SNR = 3 fringes in say 100 ms and we consider that blind observation can manage the same SNR = 3 criteria over say 10 s, then we can afford a fringe peak SNR per frame of 0.3. In detector noise regime, this corresponds to a source 10 times fainter and hence a gain of 2.5 magnitudes. The gain is even more important with regard to a fringe tracker that must reach an SNR of the order of 3 in a much shorter frame time. The SNR gain of the AMBER+ mode is discussed in more detail in chapter 6.

3.6.2 2DFT data processing

During the blind mode observation, we introduce piston offsets, as shown in figure 3.10, so that fringe peaks are well separated in the piston direction and do not overlap allowing us to get rid of the cross-talk problem, which is very common to AMBER and other all-in-one multi-axial beam combiners. The separations of the piston as shown in figure 3.11 are about $100 - 200\mu$m, which are very small compare to the coherence length of 3 mm. As the fringe peaks are well separated, we can go ahead by processing them individually. This means solving only the part of Eq.3.6.1 and Eq.3.6.1 that is connected to the baselines. Thus the new interferogram associated to each baseline ij is

$$I^{ij}(\sigma) = \sqrt{n_i n_j}\Omega^{ij}\mathrm{e}^{2i\pi\sigma p_a^{ij}} \tag{3.36}$$

where

$$\Omega(\sigma) = \Omega(u = B_{ij}\hat{\sigma}, \sigma) = n(\sigma)V_I(\sigma)V_*(\sigma)\mathrm{e}^{\left[\phi_*(\sigma)+i\phi_I(\sigma)+2i\sigma p_c^{ij}(\sigma)\right]}. \tag{3.37}$$

We then compute differential cross spectra (DCS) $W^{ij}(\sigma)$ at each σ to calculate differential measurements at the frequency u_{ij}. DCS is computed between a 2D interferogram forcing all of its channels to be zero except the channel σ and a 2D interferogram in which only σ channel have been forced to zero[¶]:

$$W_\sigma^{ij}(\nu) = \mathcal{F}\left[I^{ij}(\sigma^{'}).\delta(\sigma^{'} - \sigma)\right] \times \mathcal{F}\left[I^{ij}(\sigma^{'}).\left(1 - \delta(\sigma^{'} - \sigma)\right)\right]^* \tag{3.38}$$

$$= n_i n_j \Omega^{ij}(\sigma)\left[\hat{\Omega}^{ij}(\nu - p_a^{ij}) - \Omega^{ij}(\sigma)\right]\mathrm{e}^{-2i\pi\sigma(\nu - p_a^{ij})}. \tag{3.39}$$

If we know the exact achromatic piston p_a^{ij} from the 2DFT power spectrum then the above equation could be simplified to

$$W_\sigma^{ij}(\nu = p_a^{ij}) = n_i n_j \Omega^{ij}(\sigma)\left[\hat{\Omega}^{ij}(0) - \Omega^{ij}(\sigma)\right] \tag{3.40}$$

$$= n_i n_j \Omega^{ij}(\sigma)\left[\int \Omega^{ij}(\sigma^{'}\, d\sigma^{'}) - \Omega^{ij}(\sigma)\right] \tag{3.41}$$

$$= n_i n_j \Omega^{ij}(\sigma) R(\sigma), \tag{3.42}$$

[¶]It makes sure that DCS has no power spectrum terms affected by a quadratic bias.

where the quantity $R(\sigma)$ is nearly constant. For simplicity, we will consider $R(\sigma) \simeq R$, even though we use the actual value of $R(\sigma)$ during practical data processing. If we further assume that individual telescope collect equal number of photons i.e. $n_i = n_j = n$ and $V_I^{ij}(\sigma) = V_I$, we have $|W_\sigma^{ij}(p_a^{ij})| \simeq n(\sigma)V_I^{ij}(\sigma)n^2V_I^2$, which means that the DCS is proportional to the square of the flux and the square of the visibility but its variations with σ are proportional to the source differential visibility.

If we do further calculation, we can find a calibrated measures $E^{ij}(\sigma)$ from the information of the spectrum $n(\sigma)$, the fluxes n_i and n_j and from the DCS on the science and the reference source:

$$E^{ij}(\sigma) = \frac{\frac{W_{\sigma*}^{ij}(p_{a*}^{ij})}{n_*(\sigma)n_{i*}n_{j*}}}{\frac{W_{\sigma cal}^{ij}(p_{acal}^{ij})}{n_{*cal}(\sigma)n_{ical}n_{jcal}}} = \frac{\Omega_*^{ij}(\sigma)R_*}{\Omega_{cal}^{ij}(\sigma)R_{cal}}, \tag{3.43}$$

where the subscript "*" refers to science target and "cal" refers to calibrator related to the science target. If we further assume that the instrumental visibility and phases are same for science and the calibrator, then we can simplify the above equation to:

$$E^{ij}(\sigma) = V_*^{ij}(\sigma) \exp\left(i\phi_*^{ij}(\sigma) + 2i\pi\sigma[p_{c*}^{ij}(\sigma) - p_{ccal}^{ij}(\sigma)]\right) \frac{R_*}{R_{cal}} \tag{3.44}$$

Finally, to get the differential visibility and phase, we divide $E^{ij}(\sigma)$ by its average over σ. This allows us to avoid errors in the calibration of the ratio R_*/R_{cal}, for example from the changes in the instrument visibility. Thus, the estimator of the differential visibility is

$$\phi_{d*}^{ij}(\sigma) = \arg\left(\frac{E^{ij}(\sigma)}{< E^{ij}(\sigma) >_\sigma}\right) = \phi_*^{ij}(\sigma) + 2\pi\sigma\Delta p_c(\sigma), \tag{3.45}$$

and the differential visibility is:

$$V_{d*}^{ij}(\sigma) = \frac{\mathcal{R}\left[E^{ij}(\sigma)\exp\left(-i\phi_{d*}^{ij}(\sigma)\right)\right]}{< \mathcal{R}\left[E^{ij}(\sigma)\exp\left(-i\phi_{d*}^{ij}(\sigma)\right)\right] >_\sigma} = \frac{V_*^{ij}(\sigma)}{< V_*^{ij}(\sigma) >_\sigma}. \tag{3.46}$$

The term $2\pi\sigma\Delta p_c(\sigma)$ is due to change in the chromatic dispersion between science and calibrator. This dispersion can be minimized by a correction of the computed chromatic OPD. One simple way is to fit the differential phase variation outside the line since differential phase is expected to have a sharp variation through line. We thus use a polynomial fit of the chromatic OPD and the phase offset for all the spectral channels outside the line. More about the data processing and calibration will be discussed in chapter.5.

Chapter 4

Geometrical and kinematical model of BLR

Contents

4.1 Introduction

Despite more than 40 years of intense study, the geometry and kinematics of the BLR are quite unknown. Intensive reverberation mapping spectrophotometric variability studies have been successfully provided some insights about the physics of BLR. The observational evidences indeed suggest that the BLR is photo-ionized,

since high ionized lines come closer to the central source than low ionized lines. However, it is not clear that the BLR has a thin geometry or a thick one, dominated by rotational motion or by random turbulence component. A summery of various simple but possible BLR models can be found in Collin et al. (2006).

There are strong evidences that suggest the existence of disk like geometry with radial velocity field in the BLR but mainly applicable in the case of radio-loud AGNs. A fraction of AGNs shows double peaks in their Balmer line profile that usually associated with the disk like structure. In the case of super-luminous object, Rokaki et al. (2003) found that equivalent width of Hα line is anti-correlated with various beaming indicators, which could be associated with a disc-like BLR co-rotating with the accretion disc. Moreover, a sample of 12 double peaked Hα line profiles by Eracleous and Halpern (1994) suggests the presence of disk like emitting region. These emission lines are well fitted with a simple relativistic disk model. On the other hand, radio-quiet objects show few evidence in favor of thin disk BLR geometry. For example, polarization across Hα, which can be seen in significant fraction of Type 1 AGNs, can be explained as a presence of thin line emitting region surrounding the accretion disk (Smith et al., 2005). Since the BLR clouds must absorb significant fraction of the continuum in order to produce its large equivalent width and hence it should have significant width or opening. Large quasar spectroscopic survey indicates that the C IV and Mg II lines have small dispersion in the distribution of line widths which implies that BLR can not be flat disk (Fine et al., 2008, 2010). Various authors proposed BLR models where line emitting gas spans from the outer accretion disk to the inner dust torus and the scale height increases with radial distance (Gaskell, 2009; Goad et al., 2012). The above evidences suggest that BLR structure is neither flat nor spherical and hence to understand the underlaying physics we need to constrain BLR geometry and kinematics by high quality datasets.

Recent high quality reverberation mapping data starts exploring the previously unknown BLR geometry and kinematics. For example, recent Lick observatory reverberation mapping data successfully provided velocity-delay map of few AGNs providing some signatures of Keplerian and inflow velocity profiles (Grier et al., 2013). On the other hand, dynamical modeling of reverberation mapping data using Bayesian approach started constraining the geometry and kinematics of the BLR (Pancoast et al., 2011, 2014b). Direct modeling of data allows to estimate BH mass which does not depend on the scale factor. Dynamical modeling of Lick reverberation mapping data of 5 Sy1 AGNs suggests that the BLR kinematics are consistence with inflow motion or elliptical orbit or the combination of both (Pancoast et al., 2014a). Even if advanced RM model fitting can constrain many parameters of a complex model, degeneracies between these parameters remain, as we will illustrate on simple cases in further chapters. We therefore need to complement RM with another technique.

In this chapter we describe a BLR model intended to constrain BLR geometry and kinematics. We are interested not only to fit reverberation mapping data but also to fit interferometric data. For this purpose we will first introduce a geometrical and kinematical model in section 4.2 to predict both the interferometric and reverberation mapping observables and then explain in section 4.3 how the key BLR model parameters can be constrained from differential interferometric and RM

signature. In section 4.4, we estimated expected uncertainty on key parameters from simulated OI data. Finally, this chapter is concluded in section 4.5.

4.2 BLR model

To make a geometrical and kinematical model of the BLR we first proceed to define its geometry i.e. the spatial distribution of clouds, and then added kinematics to it i.e. the velocity of clouds.

4.2.1 Geometrical model

Our geometrical model includes cloud spatial distribution function and an angular distribution. Cloud distribution is flexible enough to reproduce varieties of radial distribution. We than add an opening angle which allows us to go from a flat geometry to a spherical one. We also define an inclination angle to describe the disk orientation with respect to the observer. Furthermore, a position angle is introduced to take care the position of the observer in the azimuthal direction. Thus, using few model parameters we can create various BLR geometries.

4.2.1.1 Radial distribution of Clouds

The radial distribution of clouds is defined by a function $R_d(r)$ which is defined here as a list of points randomly distributed according to a normal distribution of standard deviation $\sigma_{\rm blr}$ limited by an inner radius $R_{\rm in}$ below which we exclude the presence of clouds. This is the inner limit to have atomic lines due to the radiation from the central source. As a first application of our model, we used a truncated Gaussian distribution whose probability distribution is defined by

$$P(l < r < l + dl) = \frac{1}{\sigma_{\rm blr}\sqrt{(2\pi)}} \exp\left(-\frac{l^2}{2\sigma_{\rm blr}^2}\right) \quad \text{for } r \geq R_{\rm in}. \tag{4.1}$$

Later, as in chapter 7, we will use other distributions.

4.2.1.2 Opening, inclination and position angles

Once we have radial distribution of the clouds, we distributed them in x-y plane by assigning random positions where the azimuthal angle (ϕ) is randomly taken between 0 to 2π. Then we apply a random rotation to the clouds by opening angle ω to pull up a 3D configuration in (x, y, z) from the 2D configuration. The opening angle allows to make a thick geometry out of a thin geometry. The zero opening corresponds to the flat geometry whereas 90° opening produces a spherical geometry. In doing so, we found the concentration of cloud near the +y and -y axis and it causes non-axisymmetric distribution. To restore the axisymmetry of the cloud distribution we applied a random rotation between 0 to 2π.

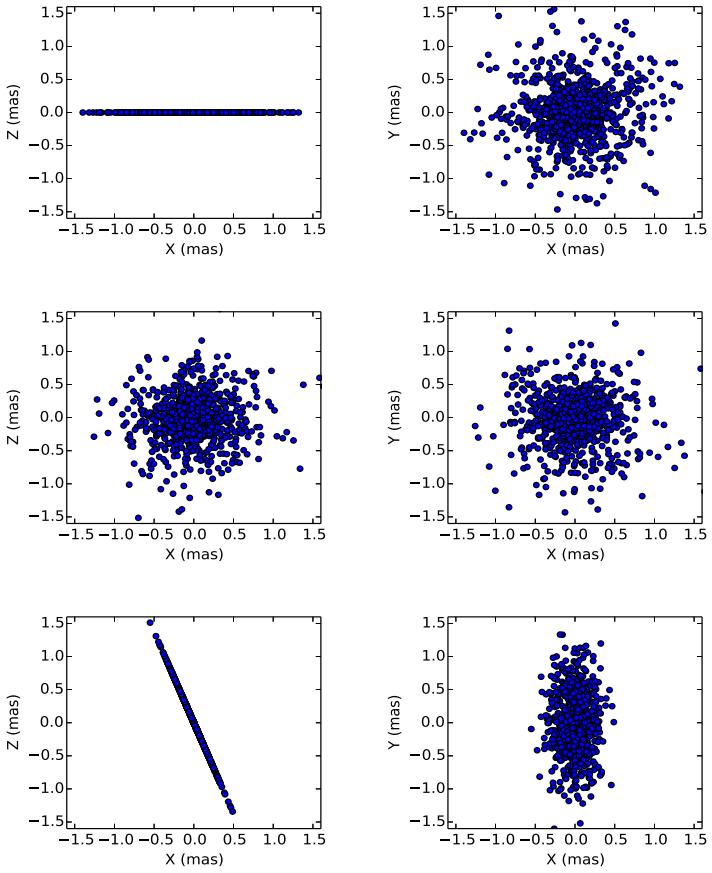

FIGURE 4.1: Effect of opening and inclination, for edge on view (left) and face-on view(right). Top to bottom: A. $\omega = 0°$ and $i = 0°$ B. $\omega = 90°$ and $i = 0°$, and C. $\omega = 0°$ and $i = 70°$.

After creating a 3D configuration, we applied a rotation about y-axis with angle i defined as inclination angle. i=0 refers to a "face on" (observer seeing along z axis) and $i = 90°$ is for "edge on" view. We further rotate the clouds with an angle Θ to take into account the position angle of the system, which is along North to East. Position angle $\Theta = 0°$ means the semi-major axis is along North. Note that position angle is important for interferometric observation, but it has no effect on the RM signal. Figure 4.1 shows different geometries, when observer is seeing edge-on (left panel, observer along y axis) and face-on (right panel, observer along z axis). In figure 4.1A, the BLR has a disk like geometry for $\omega = 0$, and as $i = 0$ for edge-on view the observer only sees the surface of a ring (left panel), while for a face-on view the geometry looks like a disk. However, for $\omega = 90°$, the geometry becomes spherical (see 4.1B), and both face-on and edge-on view look identical. For a thin inclined disk (4.1C), the geometry becomes ellipse in face-on view.

4.2.1.3 Anisotropy

The cloud's apparent brightness can be affected by a geometrical effect related to its optical thickness and to its position, named "anisotropy" (Goad et al., 2012;

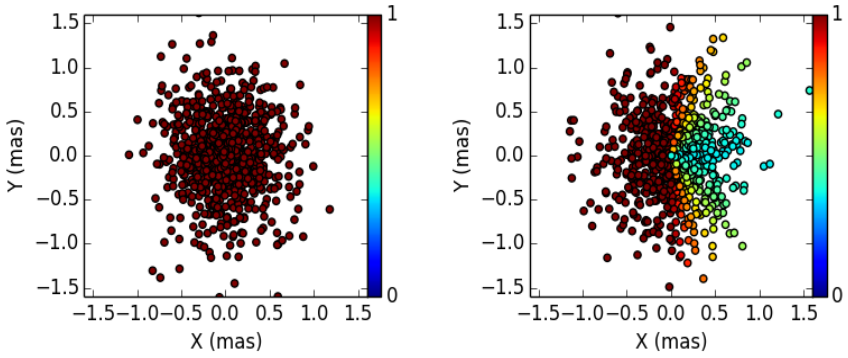

FIGURE 4.2: Effect of anisotropy parameter for a thin disk at $i = 40°$. Optically thin clouds ($F_{\rm anis} = 0$) contribute equally (left panel), while in the case of optically thick clouds ($F_{\rm anis} = 1$), contribution is more from the surface facing the observer (right panel).

O'Brien et al., 1994). If the cloud is optically thick, then the observer sees only the fraction of its surface that is facing towards him. If the cloud is optically thin, then all points of the cloud contribute to its intensity in all directions. This effect, similar to a "moon phase", is described as

$$I(\phi) = (1 - F_{\rm anis} \cos\phi \sin i), \tag{4.2}$$

where the anisotropy factor $F_{\rm anis}$ goes from 0 for optically thin clouds to 1 for optically thick clouds. The effect of anisotropy is shown in figure 4.2 for no anisotropy case ($F_{\rm anis} = 0$) on the left panel and full anisotropy case ($F_{\rm anis} = 1$) on the right panel. All clouds contribute equally in the former case, while in the latter case contribution is more from the clouds which is facing the observer.

4.2.2 Kinematical model

Each cloud is emitting a line with profile $L_{\rm XYZ}(\lambda)$ depending from the local physical conditions and hence from the cloud position. This profile is convolved by the instrument spectral PSF $P_I(\lambda)$. If we observe at relatively low spectral resolution, from 200 to 1500, we can consider that $P_I(\lambda)$ is much broader than $L_{\rm XYZ}(\lambda)$ and, as a first approximation, we can consider that the line shape details are lost in the convolution. Each cloud is emitting the same line profile $L(\lambda)$, but for its intensity, which can be included in the radial intensity distribution $R_d(r)$:

$$L_{\rm XYZ}(\lambda)\, P_I(\lambda) \simeq R_d(r)\, L(\lambda) \tag{4.3}$$

$$L(\lambda) = \mathcal{N}(\lambda - \lambda_0, \sigma_0), \tag{4.4}$$

as we choose to represent the local line profile by a Gaussian function centered at the emission line wavelength λ_0 and with standard deviation σ_0 that is a parameter of the model. When $\sigma_{\rm OS}$ is describing the source line width, it refers to the local contributions in the cloud (thermal broadening, micro turbulence etc). If $\sigma_{\rm OS}$ refers to the source and $\sigma_{\rm OI}$ to the instrument, and both profiles are Gaussian,

then

$$\sigma_0^2 = \sigma_{\rm OS}^2 + \sigma_{\rm OI}^2. \tag{4.5}$$

In practice, $\sigma_{\rm OS} \simeq 10$ km/s $<< \sigma_{\rm OI}$ and σ_0 (except if we use and enhance $\sigma_{\rm OS}$ to represent an enhanced local turbulent velocity field as in section 4.3.3.)

4.2.2.1 Tangential and radial velocity components

From the position of the cloud in this r, θ, ϕ spherical referential we can define its local velocity considering several possible components:

a) An orbital component, tangential to the circle:

$$V_{\rm orb} = V_a(\frac{R_{\rm in}}{r})^{\beta}, \tag{4.6}$$

The parameter β defines different orbital velocity laws (Stee, 1996). For Keplerian motion $\beta = 0.5$ and amplitude $V_a = \sqrt{\frac{GM_{\rm bh}}{R_{\rm in}}}$, where $M_{\rm bh}$ is the BH mass.

b) A radial component (inflow or outflow):

$$V_{\rm rad} = V_c(\frac{R_{\rm in}}{r})^{\gamma}, \tag{4.7}$$

where γ is the power law index of this radial velocity. Freefall corresponds to $\gamma = 0.5$ and $V_c = \sqrt{\frac{2GM_{\rm bh}}{R_{\rm in}}}$. $\gamma = -1$ is an outflow case with outflow velocity amplitude V_c set at the inner radius $R_{\rm in}$ of the BLR (Welsh and Horne, 1991).

In source $x - y$ coordinate, the components of velocity vector can be defined as:

$$V_x = V_{\rm orb} \sin\phi + V_{\rm rad} \cos\phi \tag{4.8}$$
$$V_y = -V_{\rm orb} \cos\phi + V_{\rm rad} \sin\phi, \tag{4.9}$$

where $0 < \phi < 2\pi$ is the azimuthal angle. Rotations are then applied with ω and i to obtain observer line of sight velocity components in 3D. The composition of these orbital and radial velocity laws constitute the global velocity field of the BLR.

4.2.2.2 Macroturbulent velocity

We have also considered a local macroturbulent velocity component of amplitude $V_{\rm turb}$. Note that the direction of macroturbulence velocity is random and thus it is independent of inclination angle. Several authors Collin et al. (2006); Goad et al. (2012) relate the amplitude $V_{\rm turb}$ to the thickness $H(r)$ of the BLR at the radius r

$$|V_{\rm turb}| = V_{\rm orb}\, P_{\rm turb}\, H(r). \tag{4.10}$$

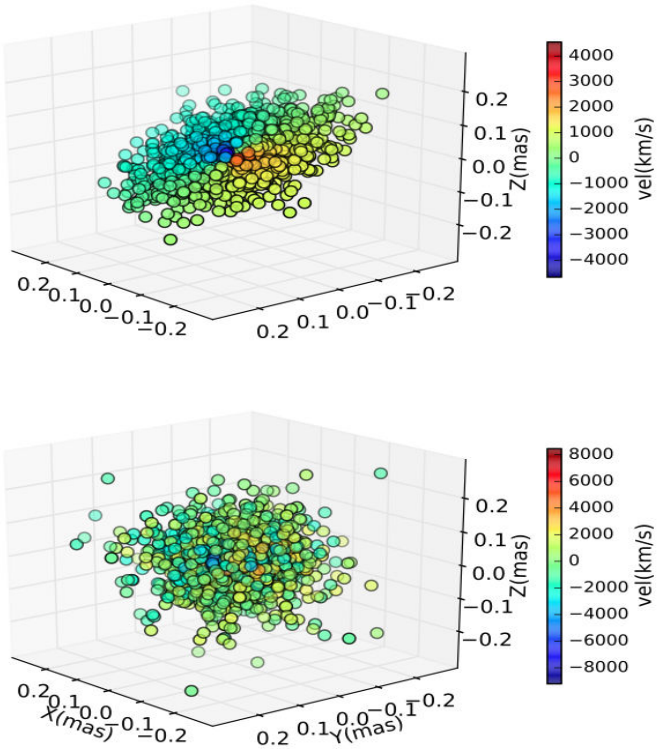

FIGURE 4.3: Cloud distribution with the velocity (km/s) in color code. $M_{\rm bh} = 1e8 M_\odot$, $i = 30°$, $R_{\rm in} = 1000 R_g$, $\sigma_{\rm blr} = 0.1$ mas with flat Keplerian disk geometry $\omega = 0°$ (upper plot) and spherical geometry $\omega = 90°$ (lower plot).

Since, in our model $r \sin\omega$ is typical thickness at radius r, hence we set $H(r) = r \sin\omega$. The multiplicative parameter $P_{\rm turb}$ tunes the amplitude of the turbulence velocity. Hence, in our model, the macroturbulence can be turned off both for a flat disk ($\omega = 0$) and for $P_{\rm turb} = 0$.

4.2.3 Intensity map

For each cloud, the line is Doppler shifted by the projected velocity component V_z and the contribution of each cloud to the BLR intensity is:

$$I_{\rm blr}(i,\lambda) = R_d(i)\,\mathcal{N}\left[\lambda - \lambda_0\left(1 + \frac{V_z(i)}{c}\right), \sigma_0\right], \tag{4.11}$$

where i refers to the contribution of i-th cloud. To get a BLR intensity map $I_{\rm blr}(X,Y,Z,\lambda)$ we add the contribution of all the clouds located in (X, X+dX, Y, Y+dY, Z, Z+dZ) box at each λ. From this 4D intensity map, we calculated 3D map, $I_{\rm blr}(X,Y,Z,\lambda)$, by summing along Z direction and then normalizing it to have the maximum intensity of 1.

In Figure 4.3, we show scatter plot of clouds. The upper panel shows a flat Keplerian disk ($\omega = 0$, $\beta = 0.5$, $V_{\rm rad} = 0$, $i = 30°$, $R_{\rm in} = 1000\,R_g$, where $R_g \equiv GM_{\rm bh}/c^2$). The lower panel shows a spherical distribution of Keplerian orbits ($\omega = 90°$). The colors represent the velocity in the direction of the observer. Note

TABLE 4.1: Model parameters and the observables.

Parameter	Symbol	Ref. value
BH mass	$M_{\rm bh}$	$1e8\,M_{\rm sun}$
BLR inner radius	$R_{\rm in}$	$200R_g$
BLR width	$\sigma_{\rm blr}$	0.4 mas
Inclination	i	30°
Opening angle	ω	0°
Rest line width	σ_0	85 km/s
Macroturbulence	$P_{\rm turb}$	0
Anisotropy	$F_{\rm anis}$	0
Continuum size	$R_{\rm rim}$	0.25 mas
Disk position angle	Θ	90°
Object Redshift	z	0.02
Measure	Symbol	Observing Technique
Absolute visibility	$V_{\rm abs}(\lambda)$	OI
Differential visibility	$V_{\rm diff}(\lambda)$	OI
Differential phase	$\phi_{\rm diff}(\lambda)$	OI
Spectrum	$s(\lambda)$	RM or OI
2D Response function	$\psi(v,\tau)$	RM
1D Response function	$\psi(\tau)$	RM

that the velocity range in the spherical case is twice as large for the same central mass and BLR size.

4.2.4 Continuum model

In the K-band, the continuum emission is strongly dominated by the hot dust near the sublimation radius $R_{\rm rim}$ (Kishimoto et al., 2007, 2009b). As this structure remains unresolved both for the VLTI and the KI, we have access only to its equivalent radius. We choose to represent it by a narrow ring whose radius ($R_{\rm rim}$) will give the right visibility observed in the continuum, when such a measurement is available, or proportional to $L^{0.5}$ with a proportionality constant deduced from Suganuma et al. (2006). For most of this thesis, we consider that the ring is uniform and we do not introduce any skewing related to the inclination, although such a function is easy to introduce in a parametric form. A skewing of the continuum image, with a "face on" side brighter than the "back on" side will introduce a measurable phase effect that is briefly discussed in section 6.4.1. The continuum brightness distribution $I_{\rm con}(X,Y)$ is normalized to have $\int\int I_{\rm con}(X,Y)\mathrm{d}X\mathrm{d}Y = 1$.

4.2.5 Model parameters and observables

The global intensity is obtained by adding the BLR and continuum intensities

$$I(X,Y,\lambda) = I_{\rm con}(X,Y) + F\,I_{\rm blr}(X,Y,\lambda), \tag{4.12}$$

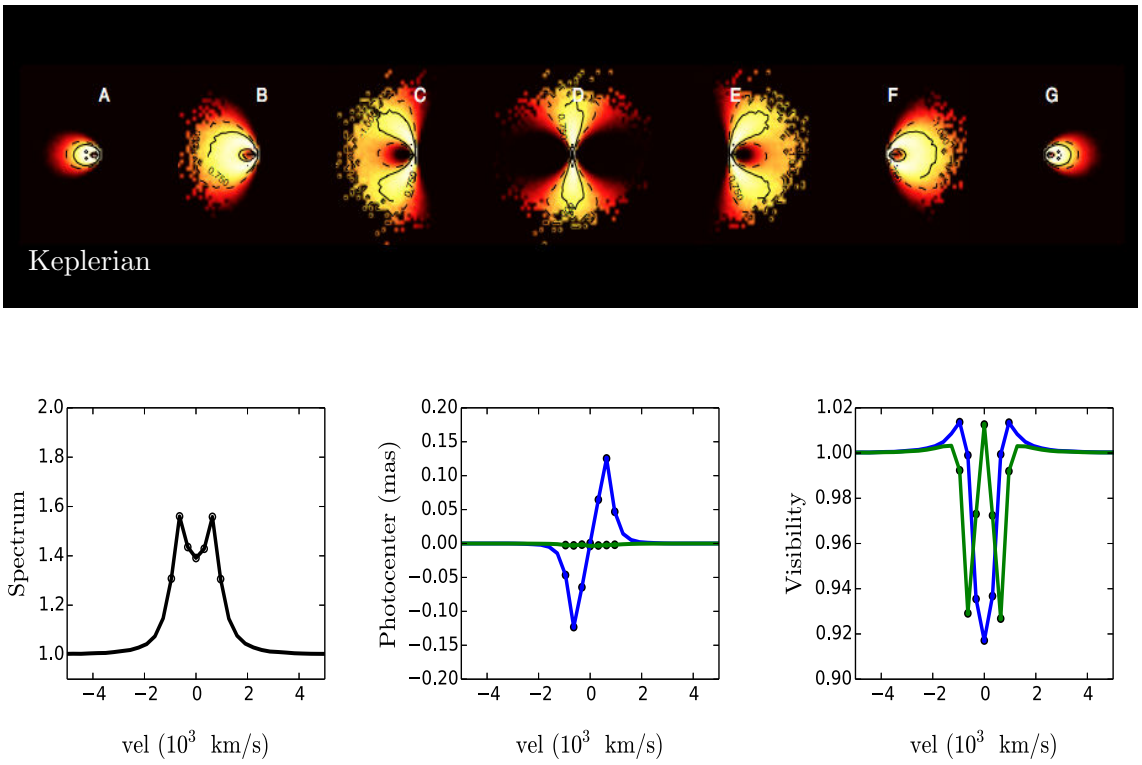

FIGURE 4.4: Line intensity map (upper panel) across the emission line for a flat Keplerian velocity field for seven different spectral channels (top panel). Emission line profile is shown in lower-left panel. Photocenter displacement (lower-middle) and visibility (lower-right) in parallel to the rotation axis (green) and perpendicular to the rotation axis (blue) with spectral resolution $R = 1500$. This model is computed considering a thin Keplerian disk $\sigma_{\rm blr} = 0.4$ and $i = 30°$.

where F is the maximum emission line flux, for a measured spectrum $S_M(\lambda_c)$=1 in the continuum. A Fourier transform of the intensity distribution $I(X, Y, \lambda)$ via Eq.3.4 yields the complex visibility and its modulus and phase, with the subsequent absolute and differential visibility and differential phase as mentioned in chapter 3.

4.2.5.1 Reverberation mapping response function

The time delay, between continuum and emission line echo, is a function of clouds position and defined by

$$\tau(r, Z) = \frac{r - Z}{c}. \tag{4.13}$$

A normalized histogram of the time delays τ and velocities in the observer direction V_z yields the 2D echo diagram $\Psi(v, \tau)$ and the subsequent 1D line profile $\Psi(v)$ whose FWHM gives the equivalent velocity range ΔV, and 1D response function $\Psi(\tau)$, whose centroid gives the equivalent time lag $\tau_{\rm cent}$. Table 1 summarizes the parameters used in our geometrical model as well as some typical values used in this chapter.

4.2.5.2 Spectro-interferometric observables

For a flat Keplerian disk model narrow-band line images (continuum is removed in plot) are plotted in the upper panel of figure 4.4 for different spectral channels. As we enter the line at maximum redshift, a line image appears in addition to the continuum. Emission line profile (lower-right panel) shows a double peaked profile. Line intensity shows maxima (B and F channels) related to the inclination and the equivalent outer edge of the BLR. The photocenter (lower-middle panel) shifting perpendicular to the rotation axis, goes through a extrema around channels B and C, then cancels in channel D in the center of line, where the image is symmetric. The blue wing images (E to G) mirror the red wing ones and the photocenter is shifted in the opposite direction. We see that the images in channels B and F show maximum intensity and extension in the direction $\perp$ to the axis and this corresponds to local minima in the visibility (lower-right) in $\perp$ baseline* (blue), while the maximum intensity and extension in the $\parallel$ direction is in channel D yielding the local visibility minima in $\parallel$ baseline (green). Different special cases with RM response function will be discussed in section 4.3.1, and different kinematic models will be discussed in section 4.3.4.

4.3 Observable signatures of the model parameters

In this section, we illustrate the effect of the main model parameters on the OI and RM observables. We have tried to analyze the parameters in an order that allows to partially separate their observable effect and makes it therefore easier to illustrate typical spectro-interferometric signatures. We will discuss first the measurement of the equivalent angular sizes of the BLR that depends mostly from the global amplitude of visibility measures. Then we will examine how differential visibility and phase can solve the major BLR model ambiguity that is the degeneracy between inclination (i), thickness (ω) and the balance between local and global velocity field (σ_0). Then, we will show how the components of the global velocity field can be separated by differential phase measurements and we will also examine the signatures of other physical phenomena such as the clouds optical thickness and the macroturbulent component of the local velocity field.

*$\perp$ baseline means perpendicular to the rotation axis and $\parallel$ baseline means parallel to the rotation axis.

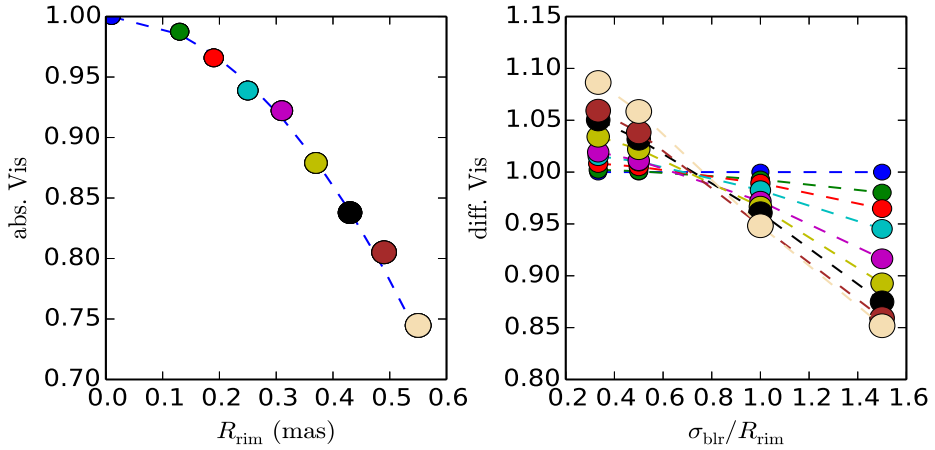

FIGURE 4.5: Average continuum absolute visibility amplitude as a function of $R_{\rm rim}$ (left panel) and differential visibility (visibility at the line center divided by average continuum visibility) in the line as a function of $\sigma_{\rm blr}/R_{\rm rim}$ (right panel) for 130 m baseline and parallel to the rotation axis. With a typical visibility accuracy of $\sigma_{\rm avis} \simeq 0.03$, $R_{\rm rim} < 0.15$ mas can not be estimated, and with differential visibility accuracy of $\sigma_{\rm dvis} \lesssim 0.001$, the relative size of $\sigma_{\rm blr}/R_{\rm rim}$ can not measured if $R_{\rm rim} \lesssim 0.1$ mas.

4.3.1 Interferometric BLR size

An estimation of the angular size of the BLR is critical to constrain the $r_{\rm blr}-L$ and the $M_{\rm bh}-L$ relations. Combined with the RM linear size measurement it can yield a direct distance (Elvis and Karovska, 2002). This angular size can be constrained by broad-band absolute visibility measured in the continuum combined with a relatively low spectral resolution differential visibility measurement with only one or a very few points in the emission line.

The left panel of figure 4.5 displays the average continuum absolute visibility amplitude as a function of $R_{\rm rim}$. With the typical visibility accuracy of current VLTI instruments, $\sigma_{\rm avis} \simeq 0.03$ (see chapter 6), we see that the smallest $R_{\rm rim}$ that can be estimated in the K-band with the VLTI baselines is $R_{\rm rim} \simeq 0.15$ mas. A fringe tracker, such as the one built-in in GRAVITY, should allow to reduce the absolute visibility error down to $\sigma_{\rm avis} \simeq 0.005$ and to access $R_{\rm rim} \lesssim 0.06$ mas. If the absolute visibility error can be reduced, the accuracy on the "dust parallax distance" can be improved as discussed in chapter 7.

The right panel in figure 4.5 displays the differential visibility (visibility divided by the average continuum absolute visibility) as a function of the ratio of $\sigma_{\rm blr}/R_{\rm rim}$. It has a very good accuracy, $\sigma_{\rm dvis} \lesssim 0.001$, limited only by fundamental noises, but it cannot yield the relative sizes $\sigma_{\rm blr}/R_{\rm rim}$ when $|V_{\rm diff}-1| < 0.001$, if $R_{\rm rim} \lesssim 0.1$ mas at the VLTI i.e. $(\lambda/B)/R_{\rm rim} \gtrsim 35$. That sets an upper limit for the super-resolution factor that can be expected from visibility measurements. The uncertainty on the angular size of the BLR will be dominated by the absolute visibility accuracy that is therefore a key specification for BLR size estimates.

Note that figure 4.5 confirms the prediction of Eq. 3.21 and sets the equivalence between the size parameters $R_{\rm rim}$ and $\sigma_{\rm blr}$: a flat Keplerian BLR model produces the same visibility than a thin ring when $\sigma_{\rm blr}/R_{\rm rim} \simeq 0.7$.

If we have differential visibilities for two different baselines (with $(\lambda/B)/R_{\rm rim} \gtrsim 35$ for the shortest baseline) we can obtain $\sigma_{\rm blr}$ and $R_{\rm rim}$ without absolute visibility measures, but the accuracy of this method has not been evaluated yet.

4.3.2 Interferometric and Reverberation Mapping BLR sizes

The different parts of the source contribute to the interferometric and RM sizes with different weights. To illustrate this we considered different flat geometries with different combinations of $R_{\rm in}$ and $\sigma_{\rm blr}$ that produce the same equivalent time lag $\tau_{\rm cent}$, from a hollow thin torus (large $R_{\rm in}$ and small $\sigma_{\rm blr}$, black line in figure 4.6) to an extended BLR with almost no central hole (small $R_{\rm in}$ and large $\sigma_{\rm blr}$, pink line in figure 4.6). Figure 4.6 shows that these combinations produce very different visibilities. The peak of $\Psi(\tau)$ grows with $R_{\rm in}$ but the centroid $\tau_{\rm cent}$ remains constant. The shape of the $V_{\rm diff}(\lambda)$ remains constant, a "v" and "w" for $\parallel$ and $\perp$ baselines respectively, but its amplitude is almost proportional to $\sigma_{\rm blr}$. Measuring QSO distances from a combination of OI with RM requires a calibration of this effect, that will also influence the size-luminosity relation. This will be discussed in chapter 7.

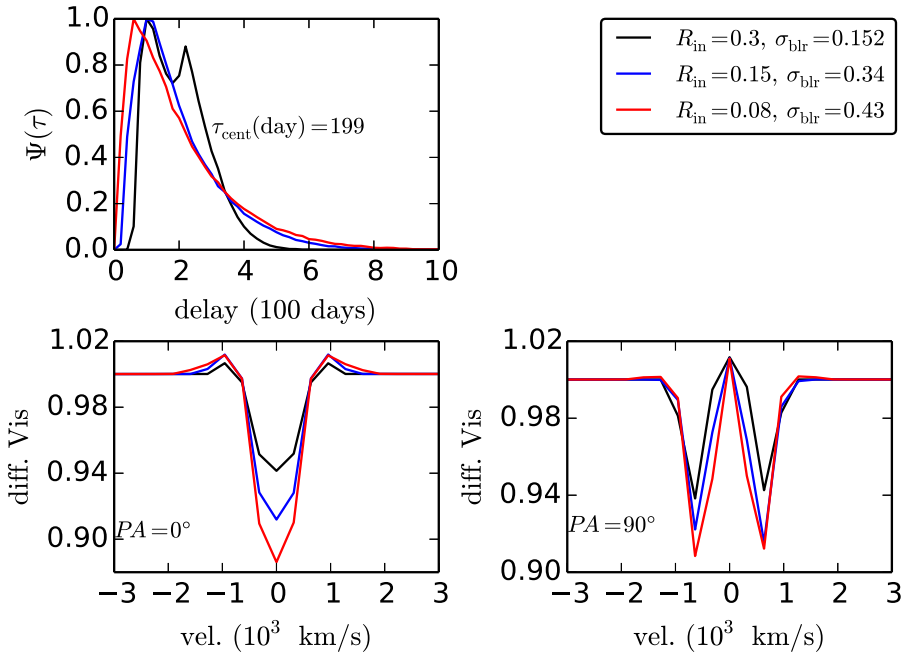

FIGURE 4.6: RM 1D Response function (upper panel) and visibility in two baselines $\parallel$ (lower-left panel) and $\perp$ (lower-right panel) for different BLR geometries that produce same $\tau_{\rm cent}$ but different visibilities.

4.3.3 Fundamental geometrical and kinematical parameters

After estimating the angular size of the BLR we will constrain three key parameters to understand the global BLR structure: i, ω and σ_0. Goad et al. (2012), Collin et al. (2006) and Fine et al. (2010) have shown that these parameters dominate

the RM scale factor f and hence the virial BH mass estimate. This is illustrated by figure 4.7 where the measured BH mass (left panel) and the scale factor f (right panel) are plotted as a function of i for various values of ω. These values result from the root mean square dispersion, σ_l of the variable line profile and the $\tau_{\rm cent}$ obtained from our model with a fixed input mass and each value of i and ω. f is the ratio of model input mass and the $M_{\rm out} = c\,\tau_{\rm cent}{\sigma_l}^2/G$. Figure 4.7 shows that changes in i and ω can introduce more than a factor 10 error on the mass estimate and shows how important it is to constrain these parameters.

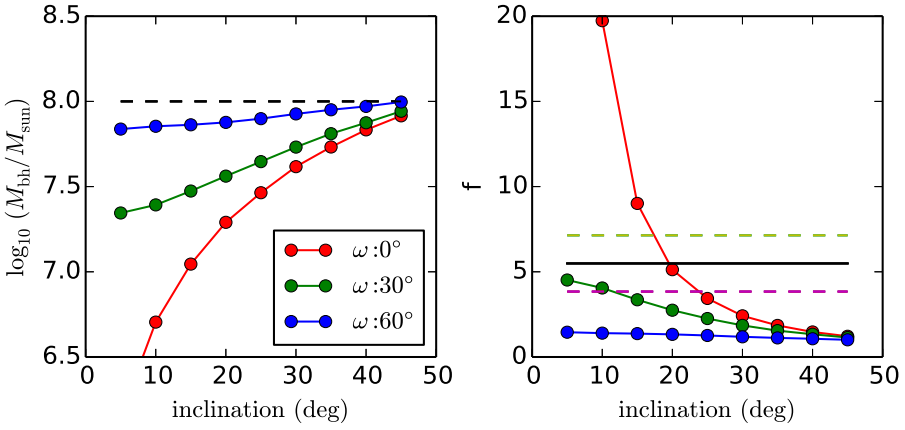

FIGURE 4.7: The simulated measured mass (left panel) and the scale factor (right panel) as a function of inclination for different opening angles $\omega = 0°$ (red), 30° (green) and 60° (blue). The input mass of this simulation is $10^8\,M_{\rm sum}$. We see that an error on i or ω can result in a very large mass error.

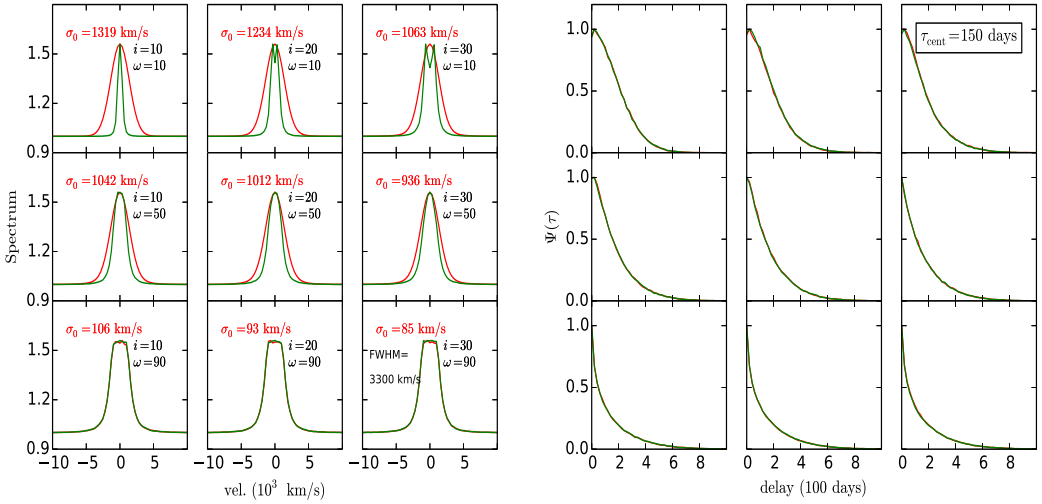

FIGURE 4.8: Spectrum (left panel) and 1D response function $\Psi(\tau)$ (right panel) for different inclination and opening angle. Green curves in each plot obtained with σ_0=85 km/s whereas the red curves are for different σ_0 as mentioned in the left panel.

Figure 4.8 shows the RM observables for a grid of $i-\omega$ with different line width σ_0 considering a fixed BLR size $\sigma_{\rm blr} = 0.4$ mas. Here σ_0 is used to represent various local turbulent velocity fields as discussed in section 4.2.2 (see also in section 4.3.5).

The spectra are in the left panel and the 1D response functions in the right panel. The green curves show the spectra obtained with a fixed $\sigma_0 = 85^{\dagger}$ km/s. The width of that spectrum is sensitive to inclination and opening angle. For small ω, an increasing i shows more and more clearly the typical double peaked line profile of a Keplerian thin disk. Increasing ω broadens the line profile and blurs the double peaks until a flat top line profile independent of i as we approach a spherical structure with large ω. The red curves represents line profiles broadened by a change in σ_0 in order to obtain an equivalent global line width $\Delta V = 3300$ km/s in all cases. The corresponding σ_0 is indicated in each picture. The σ_0 broadening blurs all line details, but for the largest opening angles. The 1D delay transfer function $\Psi(\tau)$ is independent of σ_0. Its exact shape very slightly changes with i, which shifts its maximum, and ω that makes the drop sharper for small delays, but the RM BLR size $c\tau_{\rm cent}$ is not constrained by these parameters. The overall conclusion of this figure is that RM alone cannot separate i, ω and σ_0 from ΔV and $\tau_{\rm cent}$ measures only. However, a detail line profile analysis could discriminate these parameters up to a certain accuracy.

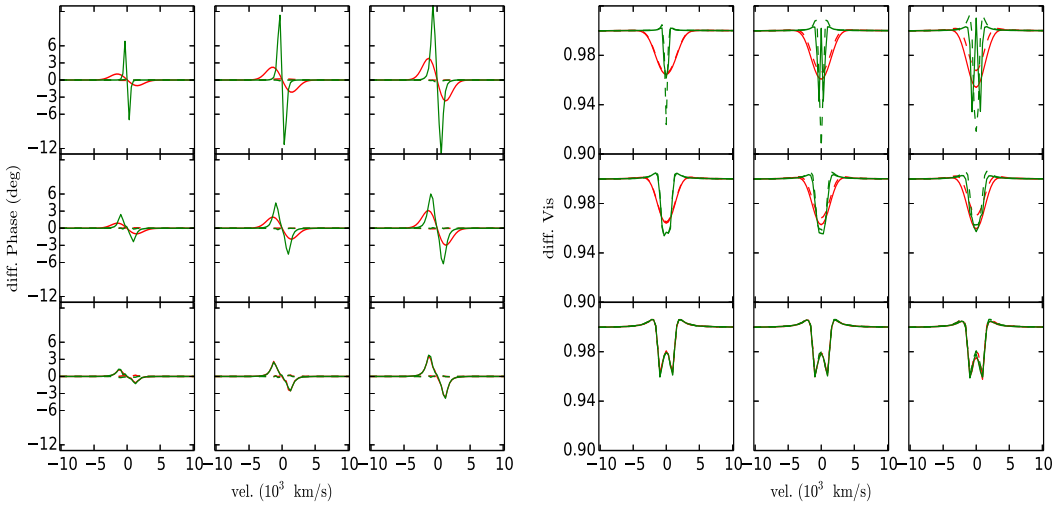

FIGURE 4.9: Differential phase in degree (left panel) and differential visibility (right panel) for the same grid as in figure 4.8 with $\parallel$ (dotted) and $\perp$ (solid) baselines.

To show the effect of i, ω and σ_0 on OI observables we plotted differential phase (left panel) and differential visibility (right panel) in figure 4.9 for $\parallel$ (dotted) and $\perp$ (solid) baselines. The photocenter shift between the line emitting region and the continuum source increases with i, which increase the line of sight velocities. It globally decreases with ω that makes the iso-radial velocity regions more and more symmetric. Differential phase for large opening angle shows sharp turns whereas the high local velocity case shape is much smoother and with reduced amplitude. An increase in σ_0, which blurs the iso-velocity zones, is another case for a decrease in the differential phase amplitude, but for an identical amplitude, the $\phi_{\rm diff}(\lambda)$ function shows much sharper angles for high ω than for high σ_0.

[†]This value of $\sigma_0 = 85$ km/s is used here considering AMBER MR ($R = 1500$) observation, which implies $\Delta V = 200$ km/s. The value of $\tau_{\rm cent} = 150$ days is a typical value as can be found in Kaspi et al. (2000). This values are used only for illustration.

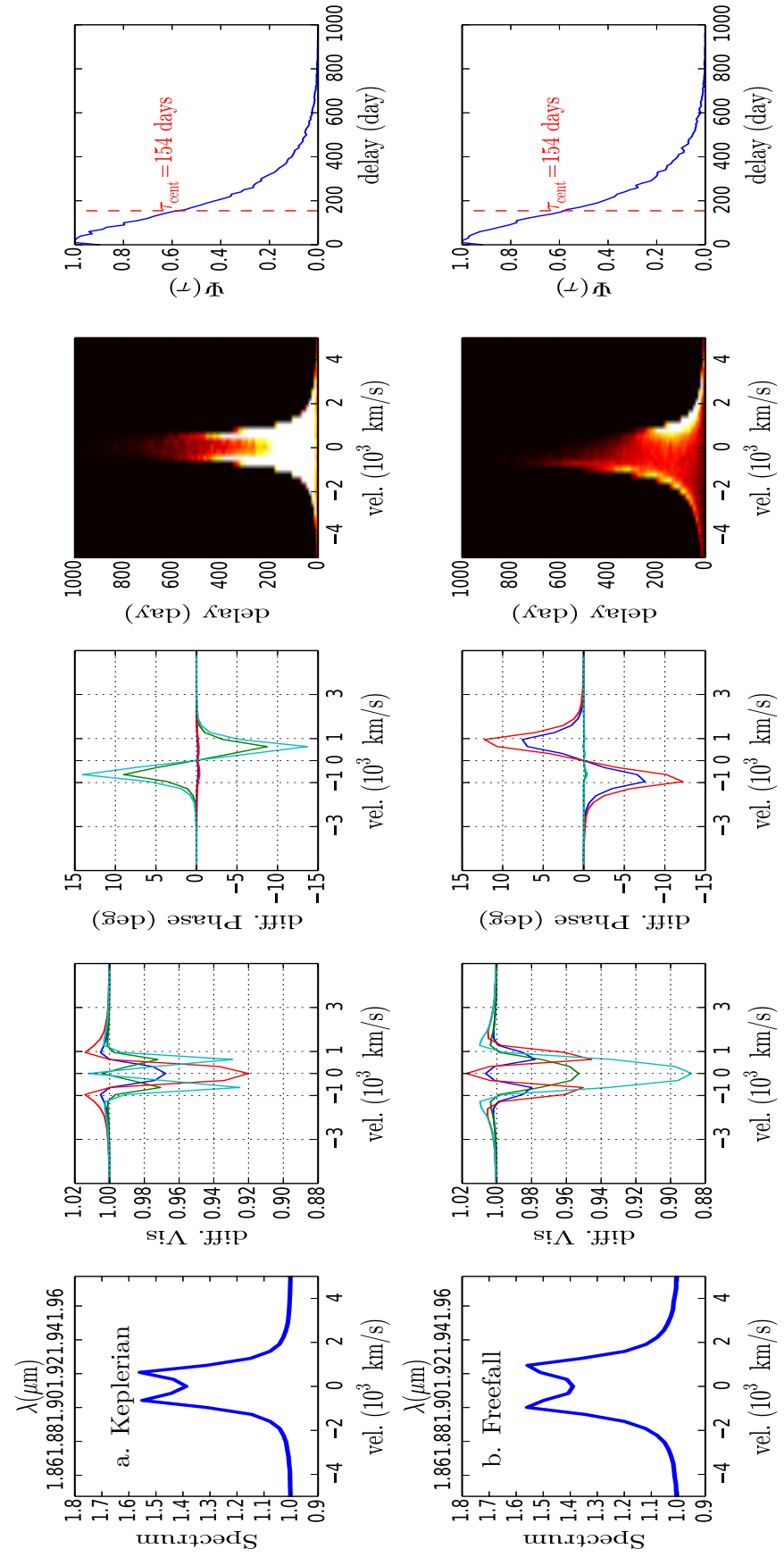

FIGURE 4.10: Spectrum (left), differential visibility (left-middle), differential phase (middle), 2D response function (middle-right), 1D response function (right) is plotted for different velocity profile for flat geometry case; Keplerian (upper row) and free fall inflow (lower row). OI observables are computed using baselines U1 (red), U2 (cyan), U3 (blue) and U4 (green).

Differential visibility is an even sharper marker of the different models, if we have a sufficient spectral resolution, i.e. sufficient SNR. In low spectral resolution, differential visibility is of little help. However, the fine shape of the differential visibility spectacularly differs in the different cases. Large opening angles yield a "w" shape that is independent from the direction of the baseline, while flat structures yield differential visibilities very sensitive to the baseline orientation, as it could be expected from figure 4.4, showing that the global size of the individual spectral bins is strongly different in the rotation axis and in the perpendicular direction. This baseline direction dependence is removed by a large local velocity field, but this changes the curve shape and width.

4.3.4 Kinematics of the global velocity field

Understanding the global kinematics of BLR has been a long standing problem as the sparsely sampled RM data was usually not enough to recover emission line as a function of velocity. However recently various authors have found signatures of rotation, inflow or outflow in the BLR, analyzing high quality RM data and recovering $\Psi(v, \tau)$ (Pancoast et al., 2012; Grier et al., 2013; Bentz et al., 2010b). On the other hand OI has been successful to provide signatures of rotation and expansion velocity in circum-stellar disks (Meilland et al., 2007; Stee, 1996; Meilland et al., 2012). To find the constrains that OI can provide on the kinematics of BLR we simulated OI as well as RM observables.

Figure 4.10, shows the spectrum, interferometric differential visibility and differential phase together with RM 2D and 1D response function for Keplerian rotation and free fall kinematics models in a thin disk (for detail about echo functions see Welsh and Horne, 1991). We considered VLTI baselines with different position angles: U1 ($B = 130\,\mathrm{m}$, $PA = 0°$), U2 ($B = 130\,\mathrm{m}$, $PA = 90°$), U3 ($B = 80\,\mathrm{m}$, $PA = 0°$) and U4 ($B = 80\,\mathrm{m}$, $PA = 90°$).

For a **Keplerian rotation law**, as strongly suggested by figure 4.4, we see that for a baseline perpendicular to the rotation axis (baseline with $PA = 90°$) the difference between the line and the continuum photocenter grow as we enter the line, cancels in the line center and reverses in the second half of the line. This gives a typical "S" shaped differential phase with an amplitude proportional to the resolution factor α defined by Eq. 3.21. In the direction of the rotation axis (baseline with $PA = 0°$), the photocenter displacement and the differential phase are 0. The differential visibility globally displays a "w" shape in $\perp$ direction and a "v" shape in $\parallel$ direction, with an amplitude depending from α and going from a peak over the continuum visibility (BLR smaller than the inner dust rim) to a visibility droop with a depth growing with α. For an **inflow**, the velocity amplitudes are larger for the same BH mass, as shown by the line profile and the 2D echo diagram, but this can be compensated by a mass change and hence introduces a mass uncertainty. The general shape of the curves are similar but $\parallel$ and $\perp$ directions are exchanged. The photocenter shift is now $\parallel$ to the rotation axis. The same exchange between $\parallel$ and $\perp$ direction can be observed on the differential visibility. The 2D echo diagram is different but this difference can be seen only on very high quality data.

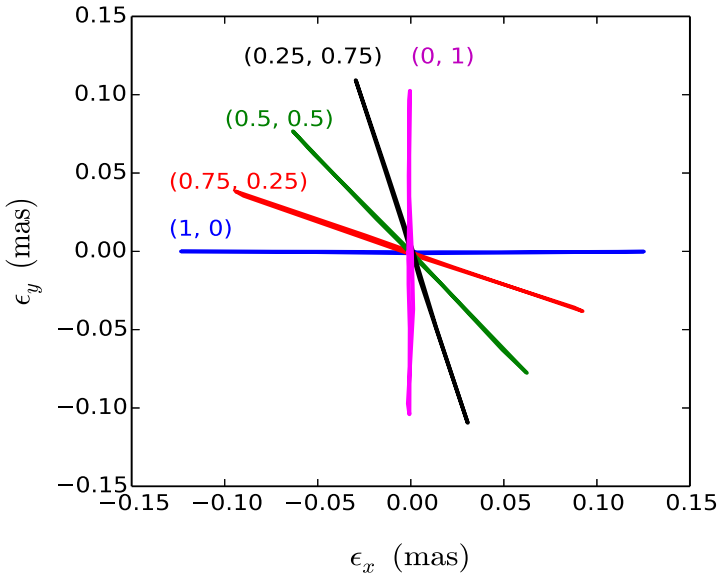

FIGURE 4.11: Photocenter displacement in the sky plane for different combination (V_k, V_f) of Keplerian ($V_k \times V_a$) and Freefall velocity ($V_f \times V_c$) amplitude. The photocenter for pure Keplerian case is represented in blue whereas pure Freefall is presented in magenta. In figure y is the projected direction of the symmetry axis i.e. position angle $\Theta = 90$.

The decisive capacity of differential measures from OI to discriminate between rotation and inflow/outflow is further illustrated by figure 4.11 that show the rotation of the global photocenter track with λ as the ratio between rotation and expansion changes, as first illustrated by Chalabaev (1992) for circumstellar disks. Here y direction is defined by the projected axis of symmetry i.e. position angle of the disk $\Theta = 90°$, which can be measured from the jet orientation or the OI broad-band observation. In this context, Stee (1996) has shown that the trajectory of the photocenter displacement vector $\vec{\epsilon}(\lambda)$ yields the strongest constraint on the velocity law index β and Meilland et al. (2007, 2012) showed that the equatorial disk of Be stars is strongly dominated by a Keplerian rotation ($\beta = 0.5$). The same approach can be applied to disk BLRs.

4.3.5 Macroturbulence

Several authors have suggested models where the cloud motions are dominated by random macroturbulence (Collin et al., 2006; Fine et al., 2008, 2010; Goad et al., 2012). Macroturbulence in the BLR can provide the internal pressure required to support the disk vertical extent (Shakura and Sunyaev, 1973). Collin et al. (2006) suggested various disk geometries and implemented turbulence velocity that depends on the scale height of disk. Goad et al. (2012) showed that for low inclination object macroturbulence dominates the Keplerian velocity and hence can produce significant broadening.

We used a similar approach, as defined in Eq. 4.10, to introduce a macroturbulent velocity component in our model. Figure 4.12 shows the effect of macroturbulence

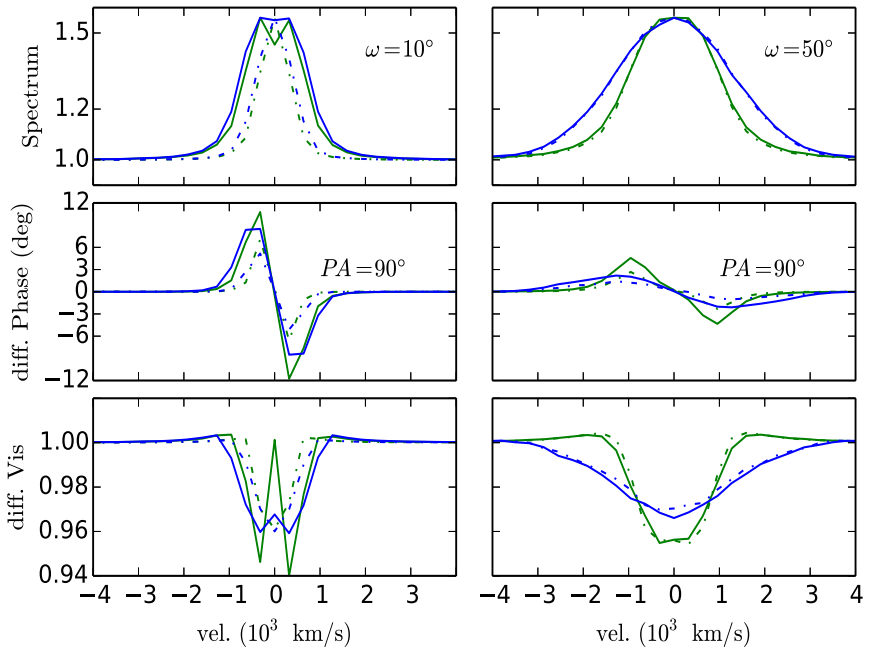

FIGURE 4.12: The effect of macroturbulence on different observables for different inclinations 10° (dash-dot line), 20° (solid line) for two different opening angles 10° (left column) and 50° (right column) for different macroturbulence parameters $P_{\rm turb} = 0$ (green) and 4 (blue).

on spectrum (upper), differential phase (middle) and differential visibility (lower) in the $\perp$ baseline, for different opening angle ω and turbulence parameter $P_{\rm turb}$. On the line profile, macroturbulence broadens the line and particularly enhances the response of the line wings (also discussed in 5.3). From the general shape of all other observables, it is impossible to discriminate between the effects of an increase of the local line width σ_0 and this of an increased macroturbulence. However, even if we cannot know if the local velocity field is dominated by σ_0 or by macroturbulence, we can separate it from the global velocity field and therefore obtain all the global geometric and kinematic parameters.

The main specific effect of the macroturbulence is to change the weight of the line wings. The ratio between the line FWHM and its standard dispersion σ_l increases when ω increases or i decreases (upper panel of figure 4.12). For known i and ω, this ratio FWHM/σ_l could be used to constrain the relative contributions to the local velocity field, but as this ratio can also be sensitive to geometrical parameters such as the radial distribution of clouds as well as to their exact spectral response[‡], a fine analysis needs a physical modeling of the cloud response that could be done in future.

[‡]at large radius the clouds have a stronger response with a Lorentzian line profile according to Goad et al. (2012)

4.3.6 Anisotropy

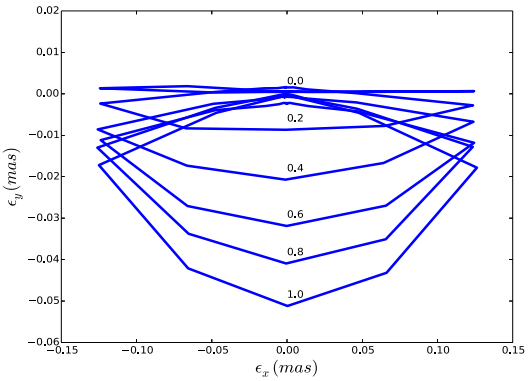

FIGURE 4.13: Shift of photocenter in the sky plane for different $F_{\rm anis}$ in the case flat Keplerian geometry.

The emission line optical depth of each cloud determines the anisotropy of the re-emitted light, from an isotropic emission for an optically thin cloud to a maximum anisotropy, with dark and bright sides, for a thick cloud. O'Brien et al. (1994) computed this for different strong emission lines and suggested that lines with large ionization parameter emitted anisotropically at some radii. Goad and Wanders (1996) and O'Brien et al. (1994) showed that anisotropy increase the time lag almost without changing the line profile, which can be a cause for mass estimate error.

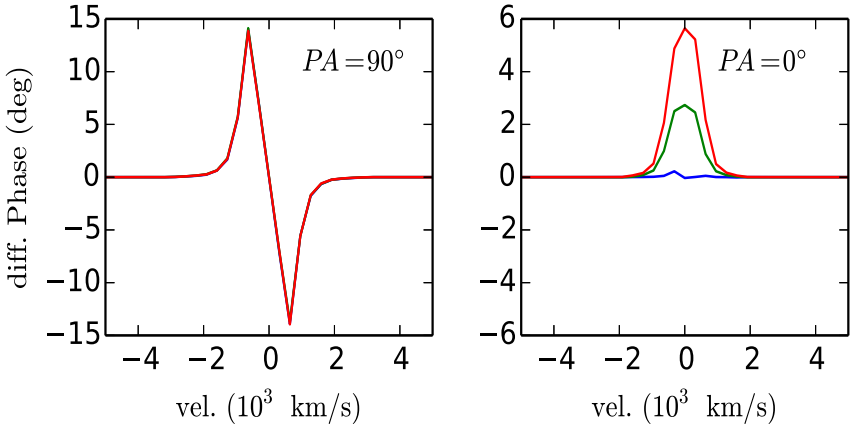

FIGURE 4.14: Differential phase for $\perp$ (left panel) and $\parallel$ (right panel) baselines is plotted for various anisotropic case: $F_{\rm anis}$=0 (blue), 0.5 (green) and 1.0 (red) for flat Keplerian disk with $i = 30°$.

To compute the effect on anisotropy we used Eq. 4.2 and its effect on the differential phase is shown in figure 4.14. We see a strong effect in the direction of the rotation axis and no effect in the $\perp$ direction. This is because the inclusion of anisotropy reduces the emission on the nearest side of the observer and increases to the furthest side, enhances its brightness and shifts the photocenter towards its direction. The photocenter along the $\parallel$ direction changes rapidly while the

photocenter in $\perp$ direction remain unchanged. Differential phase is therefore a good marker of anisotropy, particularly if we have a priori information on the axis position angle.

4.4 Parameter uncertainty from simulated optical interferometric data

In section 4.3 we described the observables signatures of the main BLR parameters. Eventually the BLR model parameters will be estimated from a global model fit of RM and OI observables. In this section we give a first estimate of the accuracy of some parameters after a global fit of OI observables with the SNR of a few typical observations. However, the main goal of this section is to illustrate a methodology. A detail analysis of the accuracy can be performed in the future.

4.4.1 Simulated datasets

To estimate uncertainty of the parameters from optical interferometry data, we created mock data sets using the values mentioned in Table 4.2a and Table 4.3a, considering Gaussian noise on all the spectro interferometric observables. We considered AMBER+ and GRAVITY with absolute visibility accuracy of 3% and 0.5% respectively. For AMBER+ we considered σ_{ϕ_D}=0.01 radian and $\sigma_{V_D} = \sqrt{2}\times \sigma_{\phi_D}$. For GRAVITY we took $\sigma_{\phi_D} \approx 0.002$ radian. We considered 0.2 % uncertainty on the line flux measurement. A justification of the typical values as well as a discussion of their sensitivity to observing conditions and source magnitude can be found in chapter 6.

TABLE 4.2: Simulated data with fixed $\sigma_0 = 85\,\mathrm{km/s}$

True parameters

Data sets	instrument	$\sigma_{\rm blr}$ (mas)	$\log(M_{\rm bh}/M_{\rm sun})$	$i(^\circ)$	$\omega(^\circ)$
A	AMBER+	0.4	8	30	40
B	GRAVITY	0.4	8	30	40
C	AMBER+	0.4	8	15	60

Recovered parameters

Data sets	$\sigma_{\rm blr}$ (mas)	$\log(M_{\rm bh}/M_{\rm sun})$	$i(^\circ)$	$\omega(^\circ)$
A	$0.378^{+0.015}_{-0.010}$	$8.059^{+0.126}_{-0.123}$	$24.8^{+5.4}_{-3.5}$	$39.2^{+9.0}_{-7.3}$
B	$0.379^{+0.017}_{-0.015}$	$8.020^{+0.085}_{-0.056}$	$28.5^{+2.0}_{-2.8}$	$37.2^{+4.7}_{-4.7}$
C	$0.386^{+0.026}_{-0.024}$	$7.997^{+0.106}_{-0.076}$	$15.7^{+4.4}_{-3.2}$	$58.7^{+6.9}_{-9.4}$

TABLE 4.3: Simulated data with fixed $\sigma_{\rm blr} = 0.4$ mas

True parameters

Data sets	instrument	$\log(M_{\rm bh}/M_{\rm sun})$	$i(^\circ)$	$\omega(^\circ)$	$\Delta v_0(2.35\,\sigma_0)$km/s
D	AMBER+	8	30	40	500
E	AMBER+	8	30	40	1500
F	AMBER+	8	10	60	1500

Recovered parameters

Data sets	$\log(M_{\rm bh}/M_{\rm sun})$	$i(^\circ)$	$\omega(^\circ)$	$\Delta v_0(2.35\,\sigma_0)$km/s
D	$8.008^{+0.088}_{-0.059}$	$28.3^{+3.0}_{-2.8}$	$36.6^{+4.9}_{-4.2}$	$684.8^{+86.8}_{-137.8}$
E	$8.138^{+0.060}_{-0.065}$	$20.8^{+5.4}_{-2.4}$	$40.9^{+3.3}_{-6.6}$	$1324.2^{+172.4}_{-169.7}$
F	$8.004^{+0.134}_{-0.085}$	$18.5^{+9.3}_{-5.5}$	$58.0^{+8.8}_{-18.4}$	$1481.2^{+81.4}_{-171.5}$

4.4.2 Recovering parameters from Simulated datasets

In order to recover the parameters of the data sets and their associated uncertainties, we optimized the likelihood function that we considered to be Gaussian assuming that the errors on the measurements are Gaussian[§], and defined by

$$p(\text{data}|\text{model}) = \prod_{i=1}^{N} \frac{1}{\sqrt{(2\pi\sigma_i^2)}} \exp\left[-\frac{(\text{data}_i - \text{model}_i)^2}{2\sigma_i^2}\right], \tag{4.14}$$

where σ_i is the uncertainty on data$_i$. Maximizing the likelihood is identical to minimizing the χ^2. We considered all OI observables i.e. spectrum, differential visibility, differential phase and absolute visibility are the part of our data sets and minimized the global χ^2. According to the Bayes' theorem, the posterior probability distribution $p(\text{model}|\text{data})$ is linked with the prior function $p(\text{model})$ which includes any previous knowledge about the parameters:

$$p(\text{model}|\text{data}) \propto p(\text{model}) \times p(\text{data}|\text{model}). \tag{4.15}$$

We assigned uniform prior to all the parameters except black hole mass for which we used log uniform prior. All the parameters are sampled from a large range: $\log_{10}(M_{\rm bh}/M_{\rm sun})$ ranges from 6.5 to 10, $\sigma_{\rm blr}$ ranges from 0.05 to 1.5, i and ω range from 0° to 90°.

To sample the parameters efficiently we used EMCEE package, developed by Foreman-Mackey et al. (2013), which is Python implementation of Affine Invariant Markov Chain Monte Carlo (MCMC) ensemble sampler by Goodman and Weare (2010). EMCEE explores the full posterior distribution using set of random points (thereafter "walkers") in each step. This means selecting randomly a set of values from the range of each parameter. The result of the walkers of the current step is used for the next step in order to optimize the maximum likelihood. The

[§]See http://ned.ipac.caltech.edu/level5/Stetson/Stetson3_2.html for a discussion about non-Gaussian error distribution.

walkers climb up towards the maximum likelihood in each steps. If the walkers are stucked in local minimum, then it would be necessary to use more walkers. To sample a highly multi-modal problem, one possibility is to run multiple MCMC simultaneously, which will be discussed in chapter 7.

In our simulations, we run EMCEE with 200 walkers and 200 steps. Thus we have 200 values on each parameters at each iteration, and this process is continued for 200 iterations. After few steps the parameters converge i.e. the width of the probability distribution of parameters stabilizes and does not change with further iterations. In figure 4.15, we plotted the mean and standard deviation of the probability distribution of all the parameters at each iteration for data set B showing that after few steps the mean and standard deviation do not change and remain almost constant. The steps before which it happens are called the "burn-in" steps. The probability distribution of the parameters is then calculated from the post burn-in samples. In all our data set, we consider 150 steps as "burn-in" phase since parameters remain stable after 100 iterations. Rest of the samples are considered as post burn-in phase and used to estimate the parameters and their uncertainties.

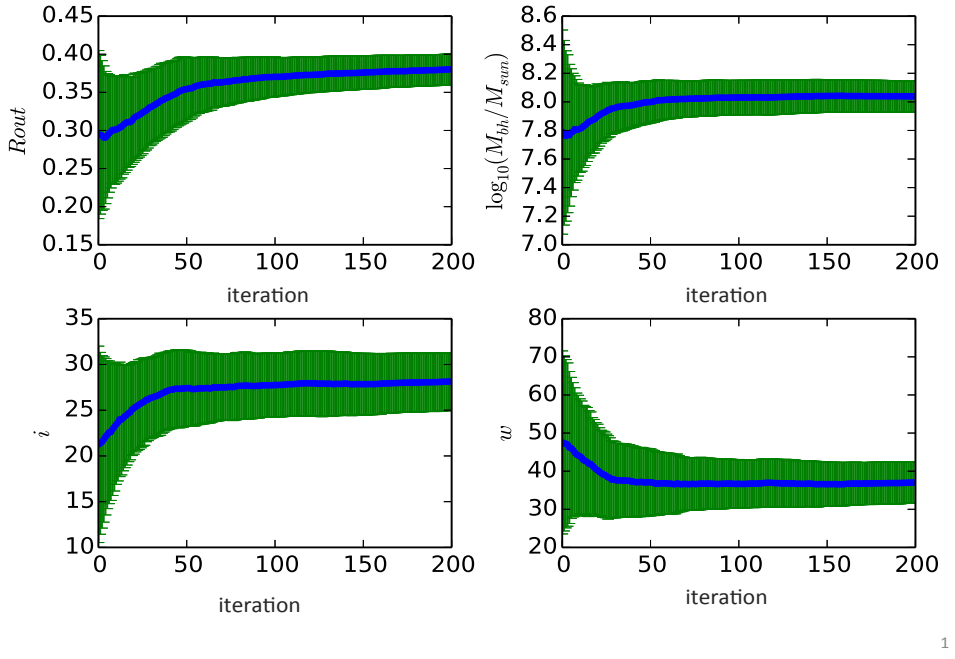

FIGURE 4.15: Mean (blue) and standard deviation (green) of the probability distribution of each parameters are plotted as a function of number of iteration during EMCEE run. After few iterations mean and standard deviation become fixed.

An example of the post burn distribution of samples is shown in figure 4.16, which is obtained for data set B. The scatter plots show the 2D distribution of samples with one σ ellipse representing the covariance matrix whereas the histograms show 1D cut of the samples. The direction of semi-major axis of the ellipse shows the correlation or anti-correlation between two parameters, while eccentricity of

the ellipse shows qualitative information on the dependency of two parameters (for example circle means the parameters are independent). In our plot ellipses indicate anti-correlation or degeneracy of the parameters $M_{\rm bh}$-i and $M_{\rm bh}$-ω, which globally underline the critical sensitivity to the inclination i. For all datasets, the recovered parameters and their one σ uncertainties are given in Table 4.2 and Table 4.3. Most of the parameters are recovered within one σ uncertainty. The maximum uncertainty in $\sigma_{\rm blr}$ is obtained in the case of dataset C, which is $0.386^{+0.026}_{-0.024}$ mas. Due to slight degeneracy between $\sigma_{\rm blr} - M_{\rm bh}$, $\sigma_{\rm blr}$ tends to be underestimated even if the result is within 1σ of the input value. This is important for distance measurement using "BLR parallax" as discussed in chapter 7. Inclination has maximum uncertainty in the case of dataset A, $i = 24.8^{+5.4}_{-3.5}$. Opening angle is constrained well in all data sets and one σ uncertainty is less than 10°. Although, $M_{\rm bh}$, i and ω are coupled in BLR differential measures, but the overall uncertainty remains quite good.

As discussed in section 4.3.1, OI can estimate the BLR size that can also be deduced from the RM typical time lag. Thus we can concentrate on the degeneracy between i, ω and σ_0 that impacts on the mass measurement. The results of a model fit with a fixed $\sigma_{\rm blr}$ are given in Table 4.3.

From a fit of the OI data only we obtain good constrains on all the parameters with AMBER+ quality level, with a mass accuracy of about $0.08 - 0.13$ dex. The largest uncertainty is obtained for a quite low 15° inclination. This uncertainty is quite similar to that achieved by Pancoast et al. (2011) with simulated RM data. However, when Pancoast et al. (2012) fit the real RM data of Mrk 50, they found a much larger uncertainty that they attribute to the modeling error. Remember that the statistical uncertainty of 0.15 dex obtained in traditional RM result (e.g., Bentz et al., 2009c; Denney et al., 2010) neglects the scatter of 0.44 dex in the RM scale factor f (Woo et al., 2010; Greene et al., 2010). In that context, our $0.08-0.13$ dex results dealing specifically with the major causes of f dispersion are very encouraging, even if it is a minimum value because this first global fit of OI data uses a very simplified model and a quite limited number of parameters. More accurate measurements of GRAVITY will bring very substantial improvement, as already indicated by data set B. A global fit of OI and RM data will further improve accuracy of the parameters.

4.5 Conclusion

We have developed a 3D BLR model to estimate both OI and RM observables. We have restricted ourselves to a limited set of parameters, as our first goal was to understand the typical OI signatures of the BLR features and to evaluate the potential of the QSO BLR observations with the VLTI. However, in future work our model can be very easily updated by changing the properties of the list of clouds making up the BLR, for example with a different radial distribution or by forcing the clouds to be located on a specific surface such as in bowl shaped BLR models.

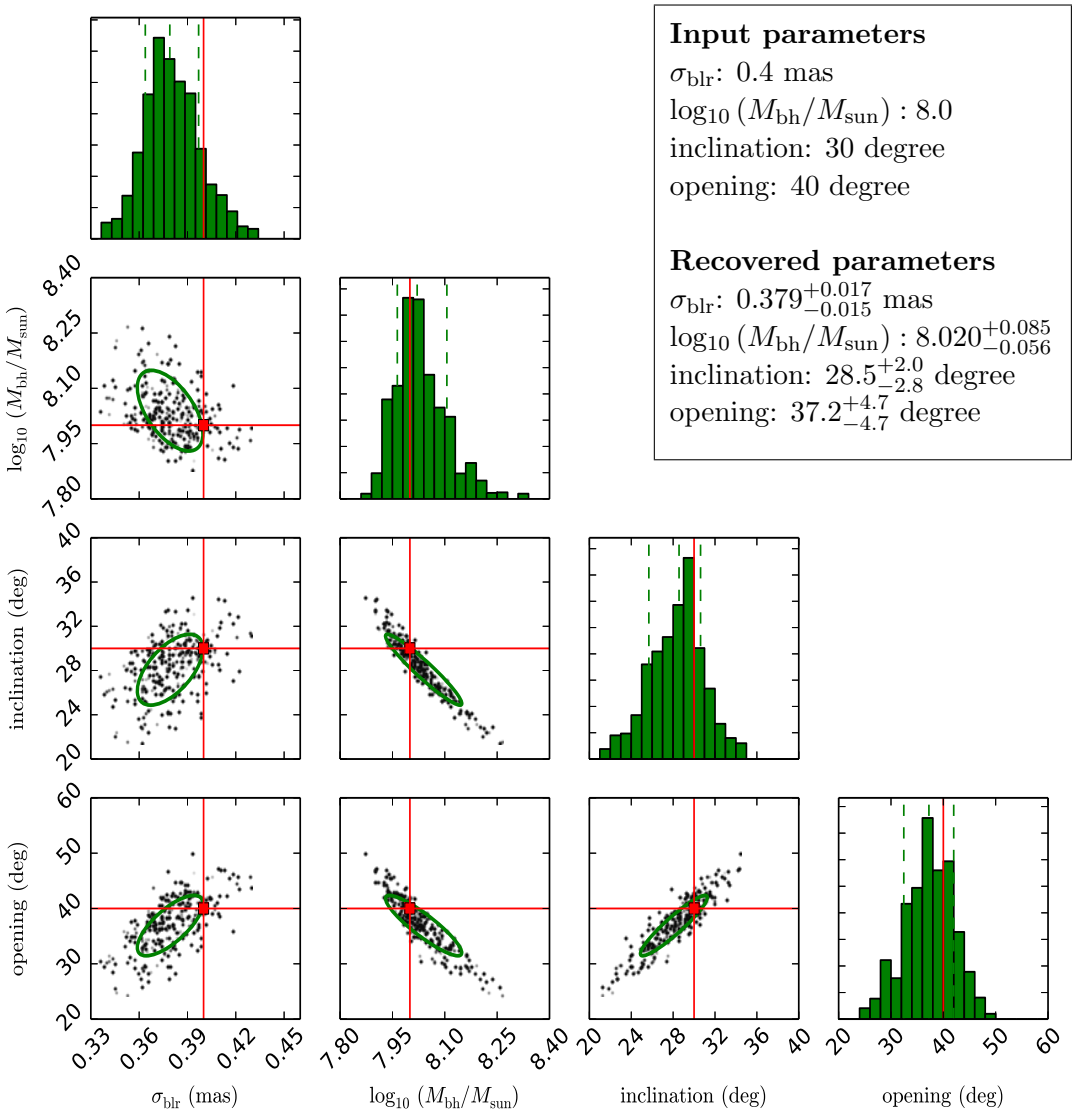

FIGURE 4.16: EMCMC post-burn distributions for dataset B. The red line shows actual input parameters of this data set. The scatter plots show the projected two-dimensional distributions and green ellipses represents the one σ regions of the projected covariance matrix. The histograms show the projected one-dimensional distributions with dotted green lines representing mean and the one σ uncertainties. From top-to-bottom and left-to-right, the panels show BLR width $\sigma_{\rm blr}$, $\log_{10}(M_{\rm bh}/M_{\rm sun})$, inclination i and opening angle ω.

We show that OI, with a spectral resolution of the order of 1000, will remove the degeneracies between the inclination i, the opening angle ω and the local velocity field contribution σ_0 that are the main cause for the dispersion of mass estimates from RM using only the equivalent time lag and width of the emission lines. Monte Carlo Markov Chain (MCMC) with the EMCEE package model fitting of differential visibility and phase confirmed that OI alone can measure the BH mass, i, ω and σ_0, if we have a good estimate of the BLR angular size. The resulting mass estimate accuracy will be of the order or better than 0.15 dex with AMBER+, (except at inclinations lower than 10°), and will be further improved with GRAVITY. This is much better than the standard mass dispersion of 0.30 to 0.44 dex that includes the effect of f dispersion (Bentz et al., 2009c; Woo et al., 2010). It is similar to the best advanced model fits of RM data by Pancoast et al. (2011, 2014b). Combining OI and RM will increase the number of usable equations and therefore the number of parameters that can be fitted and will decrease the number of a priori model assumptions.

We have underlined the importance of high accuracy absolute visibility measurements. A key condition is the possibility to use a fringe tracker (FT) that stabilizes the OI transfer function and reduces its calibration errors. However, there are many targets where absolute visibility measurements will not be accurate enough while we will still have accurate differential visibilities and phases. Then it will be necessary to obtain the size information from RM measurements, but this assumes that we can compute the scaling factor between OI and RM sizes discussed in paragraph 4.3.1 as well as the scaling factor between OI and RM observations made in different emission lines (see section 7.5 for a discussion).

When the global angular size of the BLR has been estimated, either from direct OI observables or from properly scaled RM observables, differential visibilities and phases, or even differential phases alone, are sufficient for accurate mass estimates, if the interferometric observations feature a sufficient SNR. In addition to i, ω and σ_0, these observables constrain the other BLR characteristics such as the nature of the global velocity field (rotation and inflow-outflow velocity laws) or the cloud optical thickness.

Chapter 5

Broad Line Region of 3C273

Contents

5.1 Introduction to 3C273

3C273 is the brightest quasar, located in the constellation Virgo, with $z = 0.158$ corresponds to angular size distance of about 540 Mpc* (at this distance 1 mas=2.617 pc), and K magnitude of 9.7 (figure 5.1). It is redshifted enough for the Paα line to be fall in the K band making it particularly suited for observing with AMBER because Paα is two times brighter than Brγ. Previously estimated width of the Paα emission line is about 3400 km/s, centered at 2.17 μm.

Kaspi et al. (2000) estimated time lag of 514^{+65}_{-64}, 382^{+117}_{-96} and 307^{+57}_{-86} light days (lds) between UV continuum (B band) to Hα, Hβ and Hγ emission lines, respectively, from the reverberation mapping (RM) variability study. This corresponds to a BLR size of 387^{+58}_{-50} lds.

On the other hand, the estimated absolute visibility of the inner rim dust torus in K band with KI is 0.979±0.017 corresponding to a size of 0.296±0.124 mas at the distance of 3C273, implying a torus inner rim radius of 0.81±0.34 pc (Kishimoto

*$H_0 = 73.0\,\mathrm{km\,s^{-1}Mpc^{-1}}$, $\Omega_\mathrm{m} = 0.3$ and $\Omega_\Lambda = 0.7$

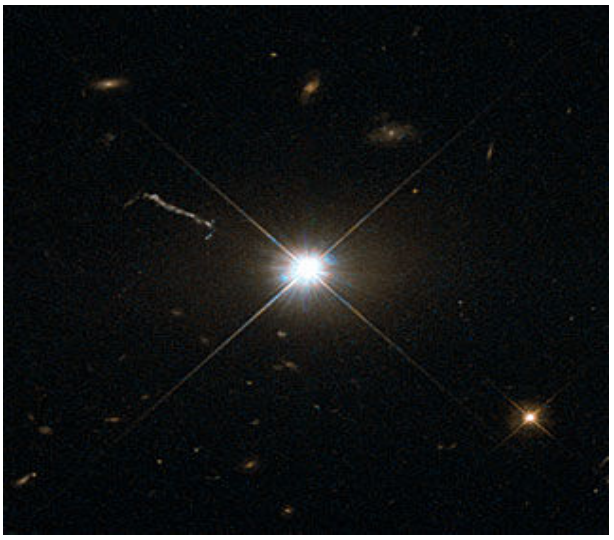

FIGURE 5.1: 3C273 image from Hubble's Wide Field and Planetary Camera 2 (WFPC2). Credit: ESA/Hubble & NASA

et al., 2011a). Thus, it is expected that Paα BLR size to be between Hα and inner rim size.

3C273 has a kilo-parsec jet, visible across the electromagnetic spectrum, shown in figure 5.2, having two distinct components: a small scale jet, which shows superluminal motion and observed with VLBI techniques, and a long jet visible at radio, optical and X-ray. Recent optical and radio data as well as polarization study suggest that the long jet has a position angle of 222.2° (Conway et al., 1993).

Several authors estimated inclination of 3C273, however, the results are very different in each case. Based on VLBI observation and jet beaming argument Unwin et al. (1985) estimated an inclination between 10° and 20° depending on its bulk Lorentz factor. However, Kundt and Gopal-Krishna (1986) estimated an inclination of $20° \pm 10°$ from the width of the lobes in the Jet. A limit on inclination $i = 8.5°$ was given by Lister et al. (2009) from the super-luminal motion of the inner jet. On the other hand, the orientation of the larger-scale jet in 3C273 differs from the orientation of inner small-scale jet by about 20°, for example Conway and Davis (1994) found an inclination between 30° to 35° and similarly Mikhailova et al. (2010) estimated inclination between 29° to 33°. However, this difference most probably due to apparent bend of the flow occurring between 8 and 20 mas from the core (see Conway and Davis, 1994; Stawarz, 2004).

Analyzing the variability of 3C273 in UV and optical light curve, Paltani et al. (1998) found two variable components that contributing to the blue-bump of 3C273, one of which shows short term variation associated to the geometrically thick accretion disk model, and another shows long term variation associated to the inner jet. In the infrared, a change in the variability by a factor of 2 has been detected on a timescale as short as one day in this object (Courvoisier et al., 1988), showing flux density has a power-law spectrum with spectral index 1.2 i.e. $f_\nu \sim \nu^{-1.2}$.

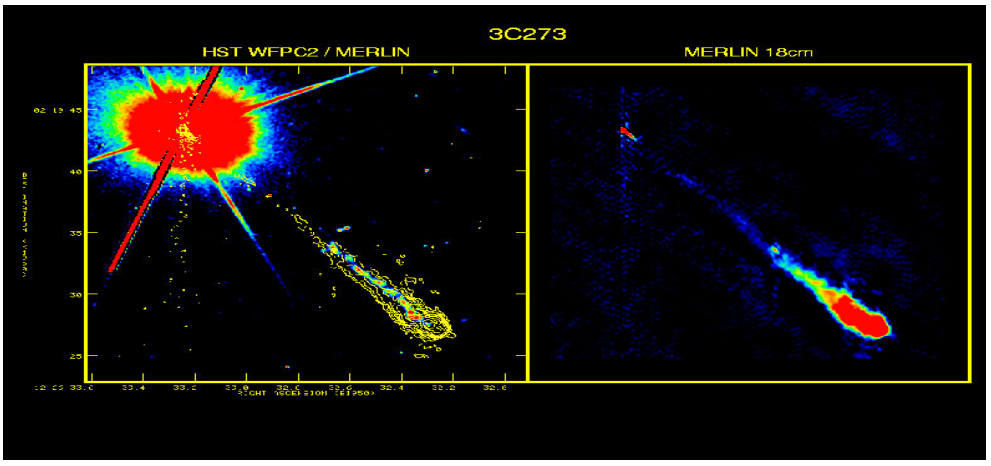

FIGURE 5.2: Jet of 3C273 visible across the electromagnetic spectrum is that in 3C273. Images obtained with HST (left) and MERLIN 18cm (right). Credit: Bahcall et al. (1995).

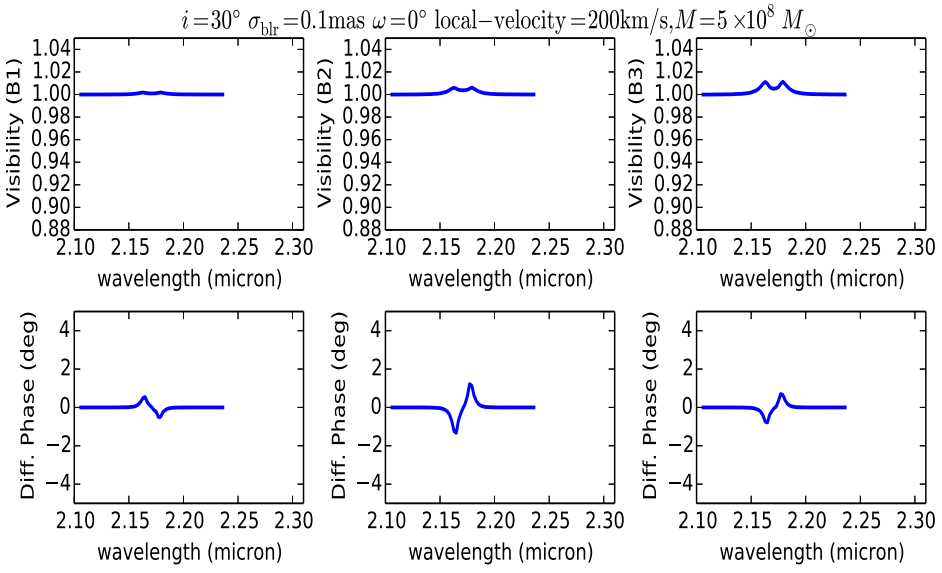

FIGURE 5.3: Differential visibility and phase is plotted for three different baselines of AMBER with a compact BLR of size $\sigma_{\rm blr} = 0.1$ mas, $i = 30°$, $\omega = 0°$ and a SMBH of mass $M_{\rm bh} = 5 \times 10^8 M_\odot$.

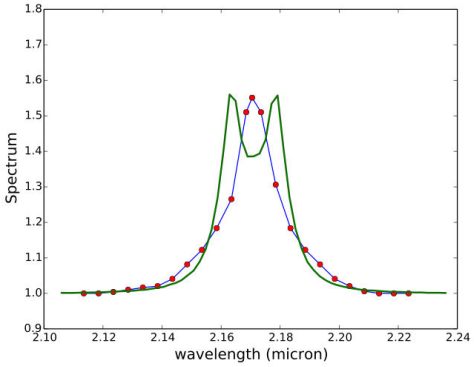

FIGURE 5.4: Model line profile of the same model as above.

Though, the above studies give very useful insight about 3C273 BLR, the geometry and kinematics of the central engine remain unknown, mainly due to the resolution needed to observe the BLR. We thus looked at the brightest QSO 3C273 with AMBER at VLTI. In this chapter, we will present the result of our first detection of a spectrally and spatially resolved emission line of 3C273. If we consider Paα BLR of 3C273 is very compact (similar to the RM BLR size), with a flat-thin disk geometry (zero opening) inclined at 30° having a central BH of mass $5 \times 10^8 M_\odot$, from figure 5.3 we find that differential visibility has a rise at the top of the continuum visibility of about 2%, and differential phase is up to 2°, if jet direction is along the rotation axis. Differential visibility appears to be double peaked while differential phase profile is "s" shaped. On the other hand, the Paα emission line profile (figure 5.4) appears to be double peaked in contrast to the observed line profile with SINFONI spectrograph (PI: A. Marconi).

This chapter is presented as follows. In section 5.2, we described our interferometric observation and data reduction process. In section 5.3, we presented Bayesian model fitting of 3C273 BLR. A detailed analysis of previous visible RM data is performed in section 5.4. Finally, we discussed our result in section 5.5.

5.2 Observation and Data reduction

5.2.1 Observation

We observed the quasar 3C273 in May 2011 with AMBER in medium resolution using the UTs 1,2 and 4. We used the "blind" mode observation technique as described in section 3.6 allowing us to increase the limiting magnitude of medium resolution (MR) observation. During observation, we first found the fringes on a bright calibrator and we knew that they will remain within the coherence length of MR observations (3 mm in K band) for several tens of minutes. Then, we observed the 3C273, without detecting any fringes in individual frame (i.e. P2VM is useless) and we accumulated incoherently the $|2\text{DFT}|^2$ of the $x - \lambda$ interferograms. The incoherent integration is done when the SNR is lower than 1 because

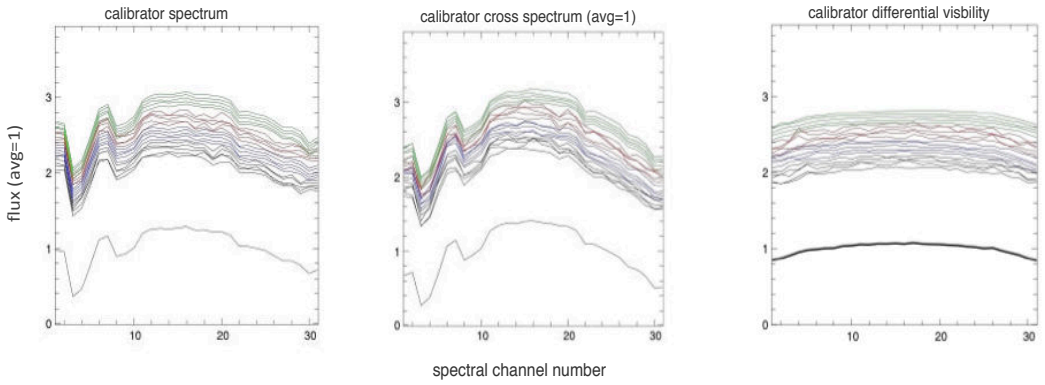

FIGURE 5.5: Differential visibility measured on a calibrator. Left (a): calibrator spectrum $n(\sigma)$. Center (b): calibrator DCS $|W^{ij}_{\sigma}(p^{ij}_a)| \simeq n(\sigma)V^{ij}_I(\sigma)n^2V^2_I$. Right (c): calibrator differential visibility $V^{ij}_{d*}(\sigma)$. All functions are divided by its average over σ. The curves are shifted for visualization. The wavelength range is from 1.99 μm to 2.33 μm. The black curves around 1 represent the time average while from top to bottom, the curves are obtained from four different calibrators of magnitude $K = 6.6$ (green), $K = 9$ (red), $K = 8.2$ (blue) and $K = 9$ in the longest baseline UT1-UT4=125 m.

in that case it is impossible to average the complex coherent flux (C) as the randomly variable phase will rapidly kill the amplitude of the average. Then, one incoherently integrates a phase independent quantity such as $|C|^2$.

The data was processed of the line in real time using AMBER+ advanced data reduction pipeline developed by F. Millour. The fringe peaks appear in a few seconds, showing the average piston that was then informed to the operator (an ESO astronomer who performs the observation), with typically half a minute delay, allowing him to correct for slow OPD drift. In MR observation, such corrections are useful typically after every 10 minutes, to keep the fringe peaks in correct position (within 100 μm), which is defined by the fringe peaks well separated in the piston direction (i.e. λ direction). This is necessary because we cannot use the P2VM fit to separate the contribution of partially overlapping fringe peaks.

We used frame times of 300 ms, and collected about 200 photons per channel and per frame. This represents about 3 photons per pixel and is well below the detector read out noise of $11e^{-1}$. The seeing conditions were very good, from 0.5 to 0.8 arcseconds, stable between 0.6 and 0.7 most of the time. During the half observing night presented here, we collected 47 exposures on 3C273, each with 200 frames of 300 ms, i.e. 1 hour and 20 minutes of open shutter time on 3C273 but only 47 minutes of actual integration. In addition, we recorded a collection of calibrators of different magnitudes. In spite of the fairly long DIT, the VLTI/AMBER visibility was between 0.2 and 0.4, depending on the baseline and the conditions.

5.2.2 Data reduction

We reduced the full data set using AMBER+, a FFT-based data reduction software for AMBER, developed by F. Millour, and modifying some of the functions (Petrov et al., 2012). The equations relevant to the data reduction has been written in

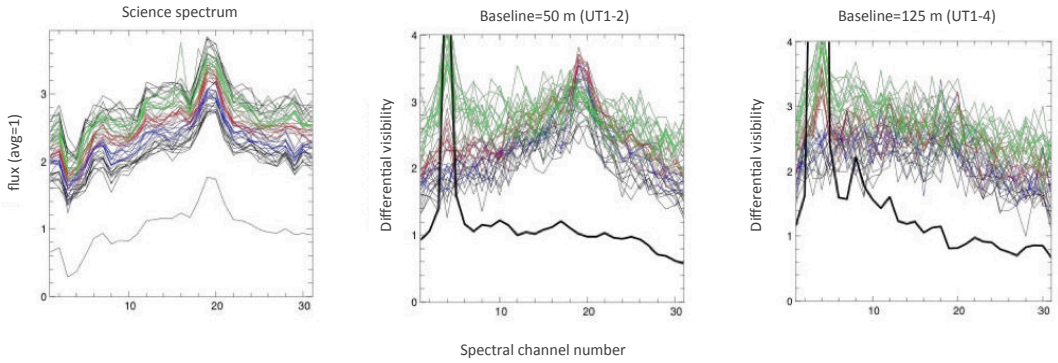

FIGURE 5.6: Differential cross spectrum and differential visibility on the 3C273. Left (a): 3C273 spectrum. Middle (b) and right (c): differential cross spectrum (thin color curves) and differential visibility (thick black) for 50m UT1-2 baseline (middle) and 125m UT1-4 baseline (right).

section 3.6. Figure 5.5 illustrates the data processing on a set of calibrators: figure 5.5a shows the measured spectrum $n(\sigma)$, figure 5.5b shows the measured cross spectrum $W_\sigma^{ij}(p_a^{ij})$ and figure 5.5c shows the calibrator differential visibility. We used 4 calibrators of magnitudes $K = 6.6$, $K = 9$, $K = 8.2$ and $K = 9$. The behavior of the differential visibility is very stable and can be calibrated with an accuracy better than 1% on the $K = 9$ target. We find differential visibility is bent, which mainly due to the effect of chromatic OPD that has not been corrected in this first data processing. The spectral 508 channels obtained in the AMBER medium resolution observations have been binned by groups of 16 for SNR reasons (on the science target), thus we now have 0.009 μm per channel, corresponding to a resolution $R = 240$.

The result obtained from 3C273 observations is shown in figure 5.6. Figure 5.6a shows the spectrum of 3C273. We note the same telluric and instrumental lines as for the calibrators, at 2.01 and 2.06 μm and the Paα emission line red-shifted at 2.17 μm. Figure 5.6b and 5.6c show the differential cross spectrum and the differential visibility for a 50 m (5.6b) and 125 m (5.6c) baselines. The emission line appears very clearly in the DCS in figure 5.6b while it is quite erased in the DCS in figure 5.6c. This indicates a differential visibility decrease in the line when the baseline increases, which can be seen in the differential visibility plots. However, figure 5.6 also shows a flux dependent bias of the DCS, which strongly affects the differential visibility in the telluric lines and casts suspicion on the variation in the emission line. In addition, the general shape of the differential visibility in the continuum is far from 1 and changes with the baseline. A bias analysis is needed before confirming the differential visibility measurement in the line.

Figure 5.7 shows the differential phases obtained on the calibrators and on the 3C273. On the calibrators, the differential phase displays the expected differential chromatic OPD. The 3C273 differential phases are always flat. The 3C273 observations were affected by the same chromatic OPDs, since 3C273 and all calibrators were less than 2° apart, and they were interlaced in time. This reveals a bias on the differential phase at the faintest magnitudes.

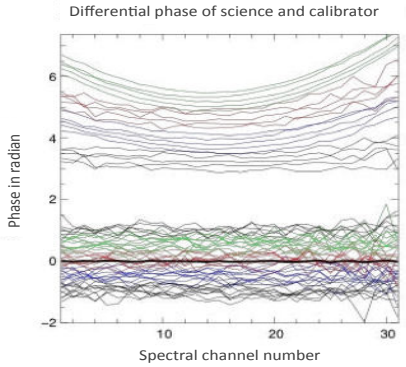

FIGURE 5.7: Differential phase of 3C273 (lower curves) as shown in Figure 5.6 and calibrator (upper curves) as shown in 5.5 in radian. All curves are at 0 average and shifted for visualization. The thick black line represents the average differential phase on 3C273. The color codes in 3C273 and in the calibrators are matched in time: we obtained first the black curves on 3C273, then the black curves on a calibrator, then the blue curves on the science followed by the blue curves on a calibrator and so on.

It is necessary to mention that there is a big time gap between the publication of preliminary result of this observation in Petrov et al. (2012) and current results. Thus, it will be better to summarize the history. The data was processed using an AMBER+ data reduction package mainly developed by Florentin Millour in 2011. It is an adaption of the GI2T 2DFT data processing to AMBER. The basic equations are given in chapter 3 and in Petrov et al. (2012). In a first step, AMBER+ computes the piston in each frame, from a block of frames temporally centered on it. In this block of frame, we compute the average $|2\text{DFT}|^2$ as explained in chapter 3, and use the fringe peak position to estimate the piston.

In a second step, we use this estimated piston to compute the differential visibility, coherent flux, and phase, in each frame and spectral channel. This assumes that for each frame, we compute n_λ 2DFT cross-spectra as explained by section 3.6.2. To have flexibility in the time averaging, F. Millour has chosen to manipulate a 4D data hypercube of size $n_x \times n_\lambda \times n_\lambda \times n_{\text{frame}}$, where n_x is the number of pixels in the interferogram, n_λ the number of spectral channels and n_{frame} is the number of frame in an exposure. This data cube is huge, more than 12 GB, at full resolution, which resulted in a software that is difficult to handle. In addition, AMBER+ is based on the "amdlib" standard AMBER software and uses the P2VM to estimate the photometric contribution of each beam and to find the fringe peak position.

In early 2012, we obtained the results presented in figure 5.6. It immediately appeared that the BLR seemed substantially more resolved than the inner dust rim that dominates the continuum interferomgram, which was in strong contradiction with RM expectations. But we also detected many problems that raised doubts about the validity of the results:

1. In the coherent flux, we see an obvious bias in the telluric lines at 2.01 and 2.06 μm, a strong drop in flux produces an apparent increase in coherent flux. Thus one could suspect that an increase in flux (like in the emission

lines), could result in an artificial decrease in the coherent flux and hence in the differential visibility.

2. The differential phase behavior on all calibrators is coherent with the expected chromatic dispersion in the air of the tunnels, while on 3C273 all phases appeared to be "flat", as shown in figure 5.7.

These two facts, and other minor problems, raised serious doubts on our surprising result.

In addition, as we were obliged to bin the spectral channels by group of 16 to get a decent SNR, our final resolution was poor (only R=240) and our visibility drop, even if confirmed, could be created by the contamination of the field by large scale structure, such as some NLR clouds. We therefore needed to

- make a very complete bias analysis, to confirm and if possible improve our visibility and phase measurements
- reduce the data again, with a smaller spectral bin, and therefore a higher spectral resolution, to eliminate possible NLR contaminations (that should be much less extended in velocity)
- if possible, check and improve the data reduction software

For a minimum second data reduction with a reduced spectral bin and a reduced spectral window, we had to wait up to 2014 i.e. three years after the first data reduction in 2012 due to the data reduction software problem, which was beyond the control of the author of this thesis. We had therefore to perform the bias analysis and the calibration using the data as it has been reduced.

5.2.3 Bias analysis

Both the differential visibility and phase show biases on the 3C273 that do not appear or appear only marginally on the faintest calibrators. The differential cross-spectral measurements are not affected by the "quadratic noise bias" that appears in the power spectra containing terms of square of zero mean noise.

On the 3C273, the DCS is overestimated in the lowest parts of the telluric lines. A careful look at the calibrator plots shows that some of the exposures on the faintest calibrators are slightly biased in the bottom of the line. The $K = 9$ calibrator is fainter in this line than 3C273 in the continuum around the emission line and in first approximation we should say that the 3C273 measurements are not biased around the emission line. We have used an estimate of this bias as a function of the correlated flux made in all available channels outside the emission line. It reduces, but does not cancel the bias in the telluric lines and does not change much the visibility variation in the emission line. This does not really correct the general shape of the differential visibility and differential phase of 3C273 in the continuum, which is mainly due to the "piston error" bias analyzed below.

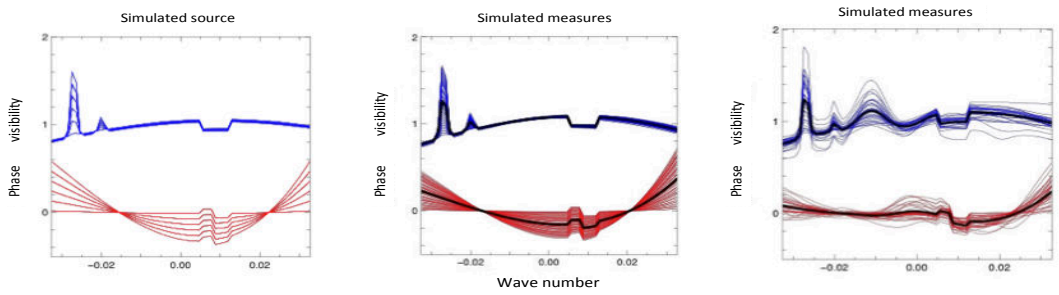

FIGURE 5.8: Simulation of the "piston error bias" effect on the differential visibility and phase. Left (a): simulated source. In blue (top) the source differential visibility. In red (bottom) the source differential phase in radians. The chromatic OPD and the telluric line bias evolve like in the observations. Center (b): simulated measurements with a piston rms=5 μm. The measurements are almost unaffected. Right (c): simulated measurements with a piston rms=50 μm. The measurements are severely affected but sharp differential variations survive.

5.2.3.1 Piston error bias

Differential phase estimated using Eq.3.40 assumes an accurate estimation of the achromatic piston p_a^{ij}. If we make an error of Δp on the estimation of the piston, the differential cross spectrum becomes

$$W_\sigma^{ij} = n_i n_j \Omega^{ij}(\sigma) < \left[\hat{\Omega}^{ij}(\Delta p) - \Omega^{ij}(\sigma)\right] e^{-2i\pi\sigma(\Delta p)} > \tag{5.1}$$

and our measurements are affected by a bias term

$$B(\sigma) =< \left[\hat{\Omega}^{ij}(\Delta p) - \Omega^{ij}(\sigma)\right] e^{-2i\pi\sigma(\Delta p)} > \tag{5.2}$$

This term cannot be corrected using calibrators, since the piston error depends on the source magnitude and on the observation conditions. $B(\sigma)$ depends on the source visibility, on the variations of instrument visibility with σ and on the chromatic OPD, since all these effects will change $\Omega(\Delta p)$. In particular, the biases on the DCS detected in the telluric lines will behave like strong and random variations of $V_I^{ij}(\sigma)$ and hence of $\hat{\Omega}^{ij}(\Delta p)$. Figure 5.8 displays a Monte Carlo simulation of the effect of $B(\sigma)$ on the differential visibility and phase. We have simulated a target with a flat visibility but a sharp local variation of 10% at the position of the emission line, and a zero differential phase but a sharp local variation of 0.05 radians. The object is affected by window and gain table correction errors, which bent the overall differential visibility, and by variable local biases that mimic the behavior of the DCS of the telluric lines. The differential phase is affected by a variation of the chromatic OPD similar to the one observed on the calibrators through the 3C273 observations.

Figure 5.8a displays the evolution of the real differential visibility and phase through the observations. To evaluate the bias term, we have generated one random piston error per frame, with a standard deviation of 5 μm in figure 5.8b (good calibrator case) and of 50 μm in figure 5.8c (worst 3C273 case). Each plot in figure

5.8b and 5.8c represents an exposure of 200 frames. We see that with a small piston error, the bias has almost no effect on the differential measures. This is coherent with the good measurements on the calibrators. With a strong piston error, both the differential visibility and phase are severely biased, and their error bars are increased. The average broadband visibility is substantially modified. However the sharp variations in the line are very well maintained for the differential visibility and somehow maintained for the differential phase. The global curvature of the differential phase is strongly affected, which looks similar to what we observe on the differential phase of 3C273. However, even when we simulate with exaggerated parameters, it seems that we are unable to kill a sharp differential phase feature of more than typically 3°. The simulation legitimates corrections of the smooth curvatures in the differential visibility and phase by a polynomial fit outside the emission line and outside the telluric lines. The simulation also shows that when the source is flat, i.e. when all chromatic OPD, window and detector biases are corrected from models in each frame before computing the 2DFTs, the tolerance to piston errors is much higher.

5.2.3.2 Photometric bias

To examine biases on photometry we plotted, in figure 5.9, the measured flux as function of an estimation of the true flux. The true flux was estimated by multiplying the average shape of the spectrum (avg=1 on spectral channels 14 to 28) computed on the 1/3 of the best exposures, with the average flux computed per exposure on spectral channels 14 to 28. A small bias is appeared in figure 5.9a at the bottom of the weakest atmospheric line. However, the bias disappears after eliminating the weakest channels (figure 5.9b), i.e. the first atmospheric bands at spectral bins 3 to 5. Thus we can ignore the bias on the photometry everywhere on 3C273, except in the deepest instrument-atmosphere absorption line.

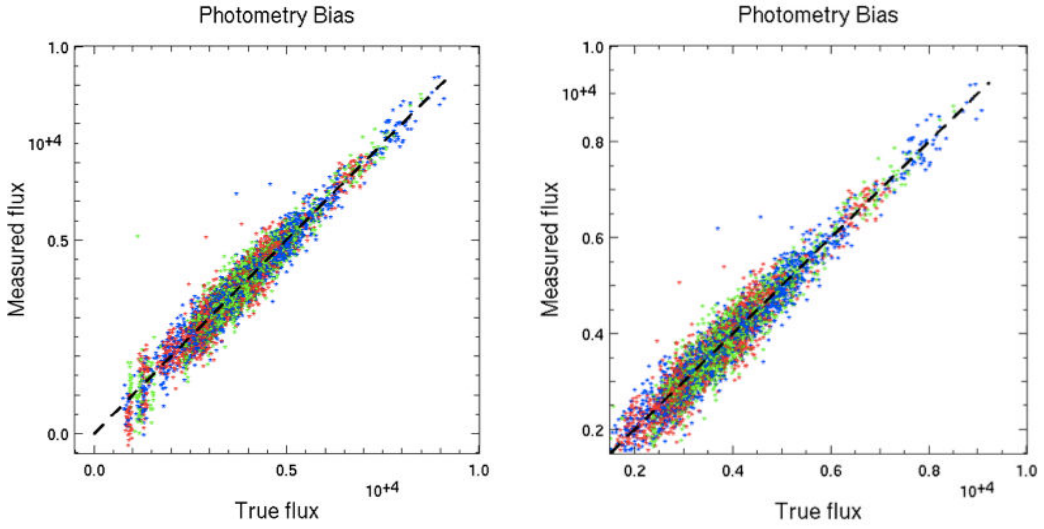

FIGURE 5.9: Bias on photometry. Left: Plots with all spectral channels. Right: Some channels are removed. See text for explanation.

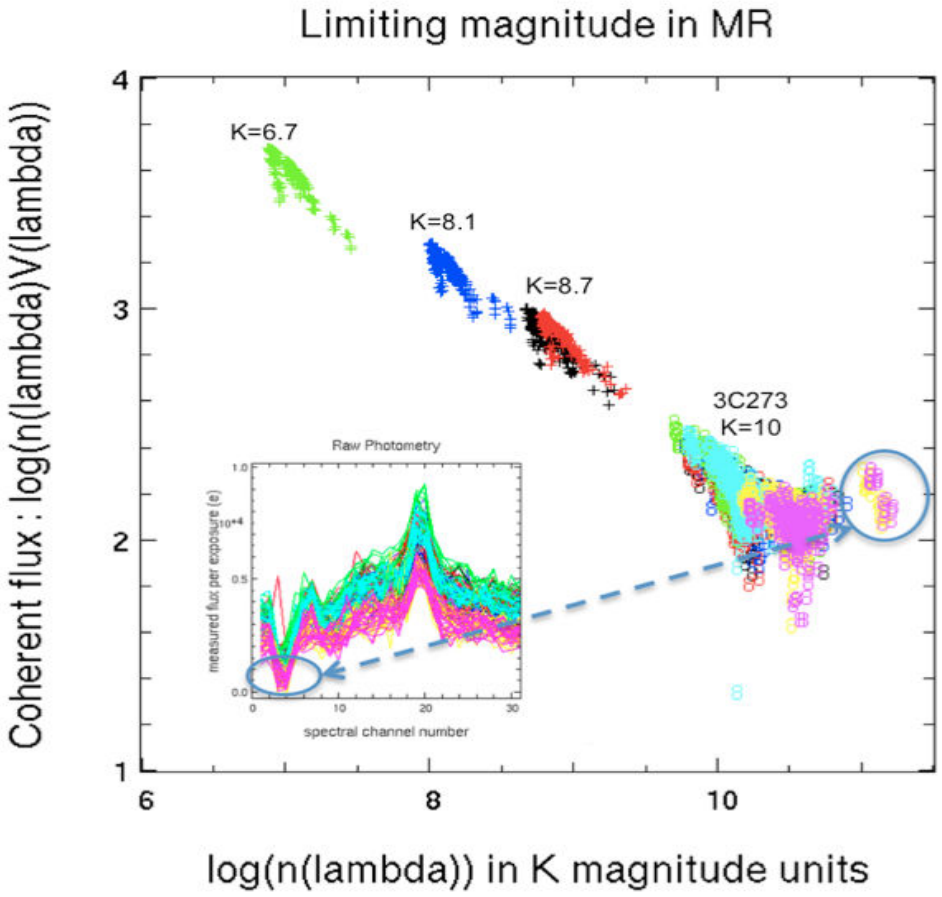

FIGURE 5.10: Coherent flux as a function of measured flux in a log-log scale. The flux scale has been converted in K magnitude. The global slope is an indication of the visibility and the ratio between coherent flux and measured flux. The points correspond to the different observations of 3C273 as well as 3 calibrators: BD+032657 ($K = 8.7$, observed twice), BD+022546 ($K = 8.1$) and TYC282-174-1 ($K = 6.7$).

5.2.3.3 Coherent flux bias

Figure 5.10 shows the bias in coherent flux (CF), $\sqrt{W^{ij}} \propto f(\lambda)V_I\sqrt{V_I^{ij}(\lambda)}$, as a function of measured flux (F) $f(\lambda) \propto \sqrt{n_{i*}n_{j*}n(\lambda)}$ on the ij baseline. If the differential visibility is constant (true for a calibrator after the correction of the chromatic OPD effects), the slope of the function yields the instrumental visibility. The ratio of CF and F gives the estimation of differential visibility and phase as discussed before. The measurement is therefore unbiased by flux fluctuations until CF remains proportional to F. In figure 5.10, these two quantities are plotted in log scales, which was matched with the source magnitude. The points correspond to three calibrators, BD+032657 ($K = 8.7$, observed twice), BD+022546 ($K = 8.1$) and TYC282-174-1 ($K = 6.7$), and the 3C273 ($K = 9.8$, observed 5 times). We see that the slope of CF/F is constant except for few aberrant points appeared at the lowest flux (inside the circle), in the bottom of the instrument plus atmosphere absorption line at 2.06 microns. This effect disappears after removing the spectral channels corresponding to the atmospheric lines. It can also be seen in figure 5.11,

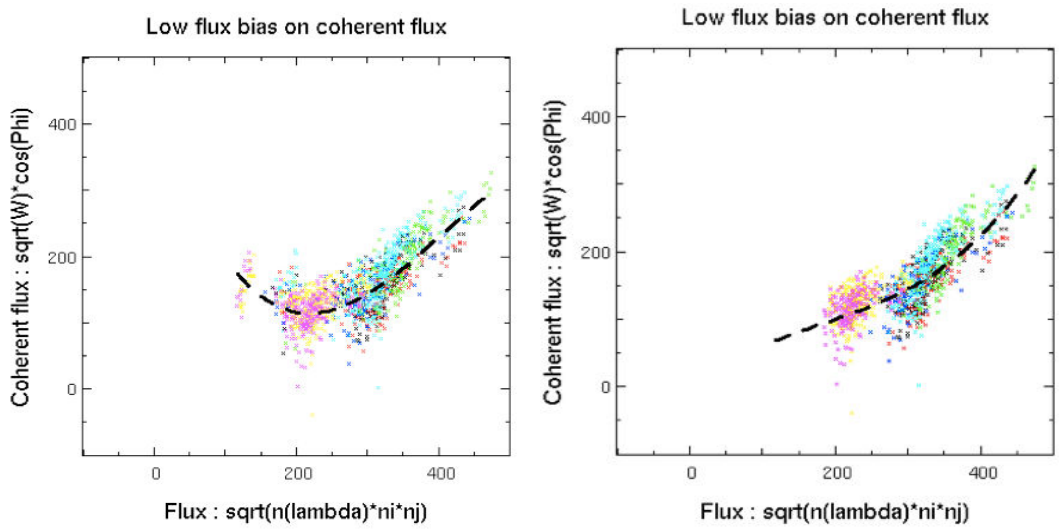

FIGURE 5.11: Bias on coherent flux in linear scale. Left panel: plot with all spectral channels. Right panel: After removing the atmospheric lines.

which is in linear scale. In the left panel, all spectral channels have been used. We see a clear bending of the CF as a function of the measured flux. This is illustrated by the dark points representing the average of the CF measured in a given bin of flux. We can use this curvature to correct our data. When we remove the points of the atmospheric lines from the plot (right panel), we see the function (CF/F) is straight (dark points) within the noise dispersion. Thus CF proportional to F is a correct approximation if the weakest channels are removed. This however sets the magnitude limit between $K = 10.5$ and $K = 11$ for practical data processing considering 2 hours of observations.

The conclusion of the bias analysis:

1. The photometric bias does not exist if we remove the telluric line channels in the faintest exposures of the 3C273 data
2. The piston error bias gives an explanation for the flatness of 3C273 differential phase in the 2012 processing
3. The piston error bias is strongly reduced if we eliminate the telluric line channels from the 2DFT analysis. The residual can be properly treated by a polynomial fit of the signal in the continuum outside the emission line.
4. After elimination of the telluric lines, the coherent flux become marginal and can be corrected by a simple fit, which also removes the bent of the continuum and the line.

Therefore, we re-reduced our 3C273 data after eliminating the telluric line. This time we binned the spectral channel by groups of 8 corresponding to a spectral resolution of R=480. After correcting from the coherent flux residual bias, we obtained differential visibility as shown in figure 5.12. We did a polynomial fitting to remove the chromatic OPD shown by blue-solid line. The raw-spectrum is also

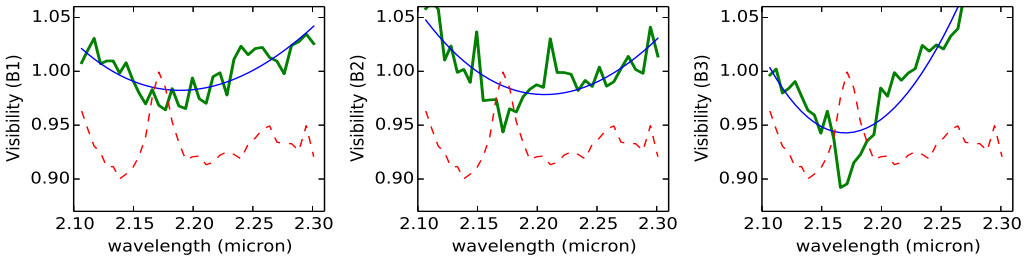

FIGURE 5.12: Visibility of 3C273 after correcting from the coherent flux residual bias. Continuum outside the emission line is fitted with a simple polynomial function (blue line). The emission line profile is over plotted to show its position in the spectral window (red-dashed line)

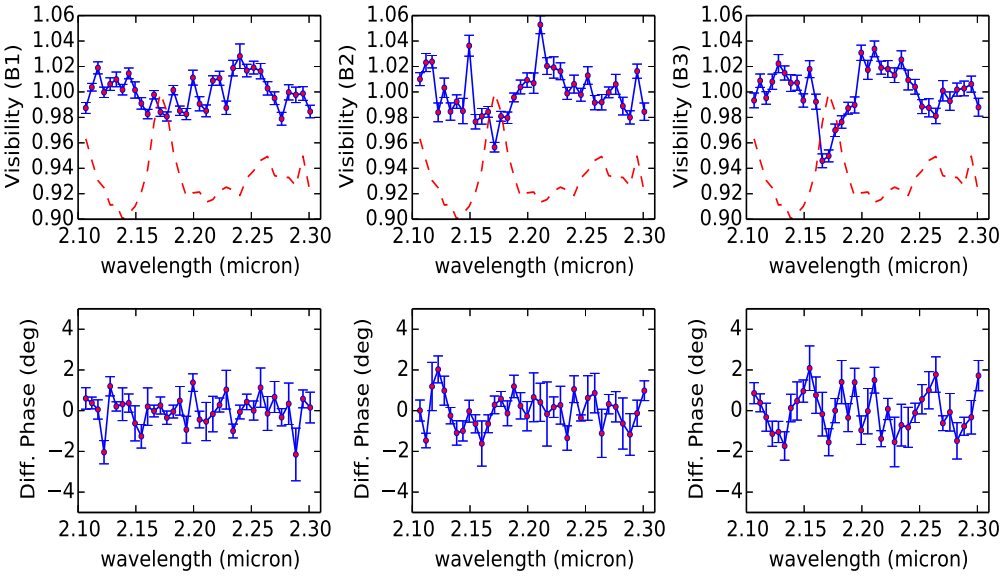

FIGURE 5.13: 3C273 result obtained after the final reduction and continuum subtraction. Plot shows differential visibility (upper panel) and phase (lower panel) for 50 m (left), 80 m (middle) and 125 m (right) baselines. The error bars in the plots are estimated from the temporal dispersion over the 47 exposures.

over plotted to show the position of the emission line. The selection of the window for the polynomial fit can slightly change the wings of the visibility profile in the line. The correction of the chromatic OPD is still in process at the moment of reduction of this thesis, but is expected to have only marginal change.

After removing the continuum slope, we get our final differential visibility and phase as shown in figure 5.13. This improves the accuracy on the differential visibility, which is ≤ 0.01 per channel. It drops on all baselines and drops increase with the baseline length. On the largest baseline (UT1-4), we achieved an SNR=10. Interestingly, differential visibility drop extends over the line. In the case of differential phase, no signature has been found larger than 1°.

5.3 Bayesian model fitting

5.3.1 Model of 3C273

To interpret our 3C273 interferometric observation, we used our geometrical and kinematical model as described in chapter 4 and also presented in Rakshit et al. (2015). The model parameters that we wanted to constrain are $\sigma_{\rm blr}$ that defines the width of the BLR, central BH mass $M_{\rm bh}$, inclination angle i, opening angle ω and macro-turbulence parameter $P_{\rm turb}$ since these are the main geometrical and kinematical parameters. Some of the parameters are kept fixed at the values obtained from literatures; $R_{\rm rim} = 0.25$ mas (Kishimoto et al., 2011a), $F = 0.58$ (from 3C273 spectra) and $\Theta = 222.2^{\circ}$ (from jet position angle).

5.3.2 Model fitting

As a first step, for visual inspection, we run two models with $i = 20^{\circ}$, $\sigma_{\rm blr} = 0.5$ mas, $w = 20^{\circ}$ and local velocity $\sigma_0 = 500$ km/s and with two different masses $M_{\rm bh} = 5 \times 10^8 M_{\odot}$ and $M_{\rm bh} = 50 \times 10^8 M_{\odot}$. The results are shown in figure 5.14. The corresponding fits of the spectrum is shown in figure 5.15. Both models provide a bad fit to the data. For model with low mass, figure 5.14, the line of sight velocity is very low making visibility signal very sharp although differential phase fits within error bar except the 80 m baseline (middle panel). The drop of the visibility although suggests an extended BLR. However, the line profile, shown in figure 5.15a, suggests that low inclination and low mass can not explain the result. If we increase mass then fits improve, shown in figure 5.14, however differential phase shows strong "S" shape signature. The line profile is broader than the observed one. This implies the BLR of 3C273 is not a flat disk, and central BH is not more massive than $M_{\rm bh} = 50 \times 10^8 M_{\odot}$. Also interesting to note that if the inclination is very small then we either need a very thick geometry close to spherical or a large contribution from micro- or macro-turbulence to explain the width of the emission line and the visibility curve.

In order to find a global solution, we need to explore the parameter space. Thus, we adapted Bayesian model fitting approach, described in section 4.4.2, and maximize the likelihood $p(\text{data}|\text{model})$, which is equivalent to minimizing the $\chi^2(\text{data}|\text{model})$. We used EMCEE package, developed by Foreman-Mackey et al. (2013), which is a Python implementation of Affine Invariant Markov Chain Monte Carlo (MCMC) ensemble sampler by Goodman and Weare (2010). We showed in section 4.4.2 that EMCEE is very efficient in sampling the parameter space and it can be run in parallel using many CPUs. Each MCMC simulations runs for 300 iterations and for 200 walkers. After few iterations, called "burn-in" iterations, we found that the width of the probability distribution of the samples become stable i.e., no variation of width of sample distribution ensuring the convergence of the model. We remove the burn-in iterations, and calculated best fit value and its 1 σ uncertainty of all free parameters from the rest of the samples.

We used four main key parameters $\sigma_{\rm blr}$, $M_{\rm bh}$, i and w as free parameters for global fitting keeping $P_{\rm turb}$ fixed. We also repeated MCMC fitting for different $P_{\rm turb}$ to

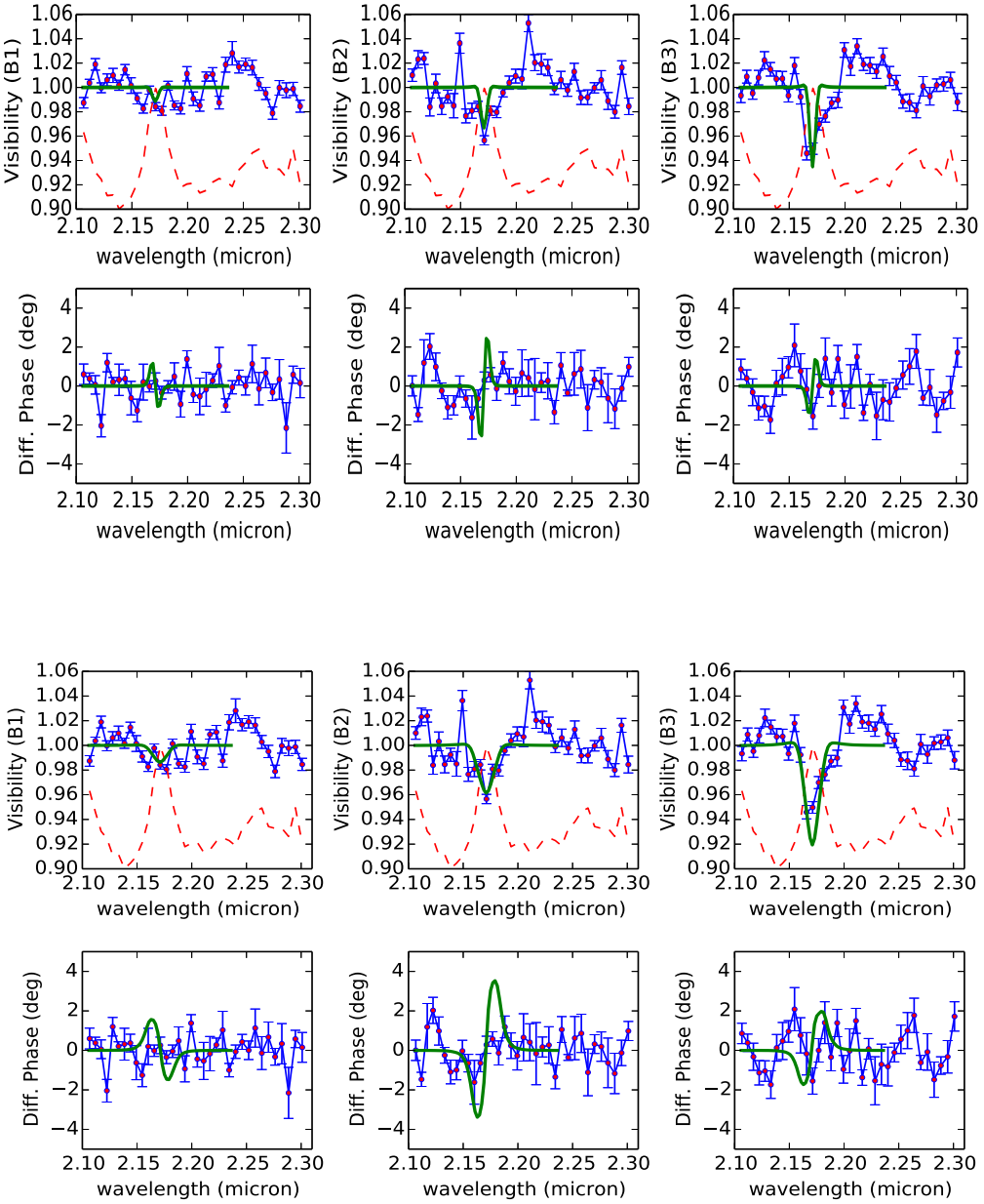

FIGURE 5.14: Comparison of the data (red points with blue error bars) and model (green line). Observed line profile is over plotted (solid-dashed line) showing the position of the line. The parameters of the model are same in both cases: $i = 20°$, $\sigma_{\rm blr} = 0.5$ mas, $\omega = 20°$, $dv = 500$km/s except the mass, which is $M_{\rm bh} = 5e^8 M_\odot$ for the first model as shown in upper panels (a) and $M_{\rm bh} = 50e^8 M_\odot$ for the second model as shown in lower panels (b).

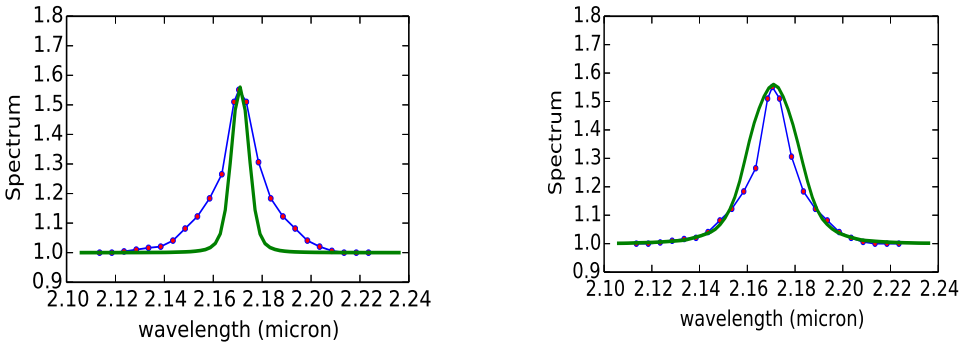

FIGURE 5.15: Emission line profiles corresponding to figure 5.14a and b.

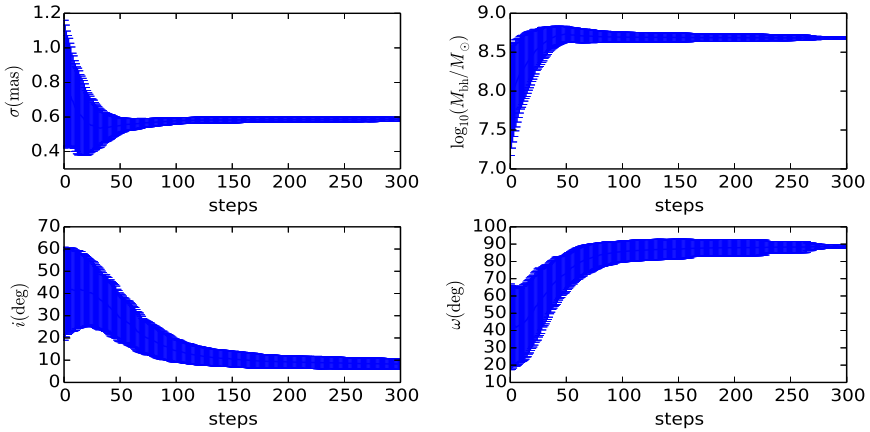

FIGURE 5.16: Mean and standard deviation of probability distribution of the parameters in each steps during MCMC fitting.

TABLE 5.1: 3C273 result

$\sigma_{\rm blr}$ (mas)	$\log_{10}(M_{\rm bh}/M_\odot)$	$i(^\circ)$	$\omega(^\circ)$	$P_{\rm turb}$ (fixed)
$0.585^{+0.011}_{-0.012}$	$8.682^{+0.017}_{-0.018}$	$8.4^{+3.7}_{-2.2}$	$88.6^{+1.0}_{-1.5}$	1

find its best value that fits the data. Once we have data and model, we just need prior on the parameters defining any previous knowledge about them. In our case, $M_{\rm bh}$ spans few order in magnitude thus, we used uniform prior in log on $M_{\rm bh}$ where $\log_{10}(M_{\rm bh}/M_\odot)$ ranges from 6.0 to 10.0. For all other parameters, we used uniform prior, where $\sigma_{\rm blr}$ varies between 0.05 to 1.5 mas, i between 5° to 90° (considering radio jet) and ω between 0° to 90°.

The mean and standard deviation of the sample distribution in each step during MCMC runs are plotted in figure 5.16. It shows that $\sigma_{\rm blr}$ and $M_{\rm bh}$ become stable after few iterations and have low standard deviation, except inclination and opening angle since these two parameters have opposite effects. Figure 5.17 shows the probability distribution of the parameters. The 2D scatter plot with

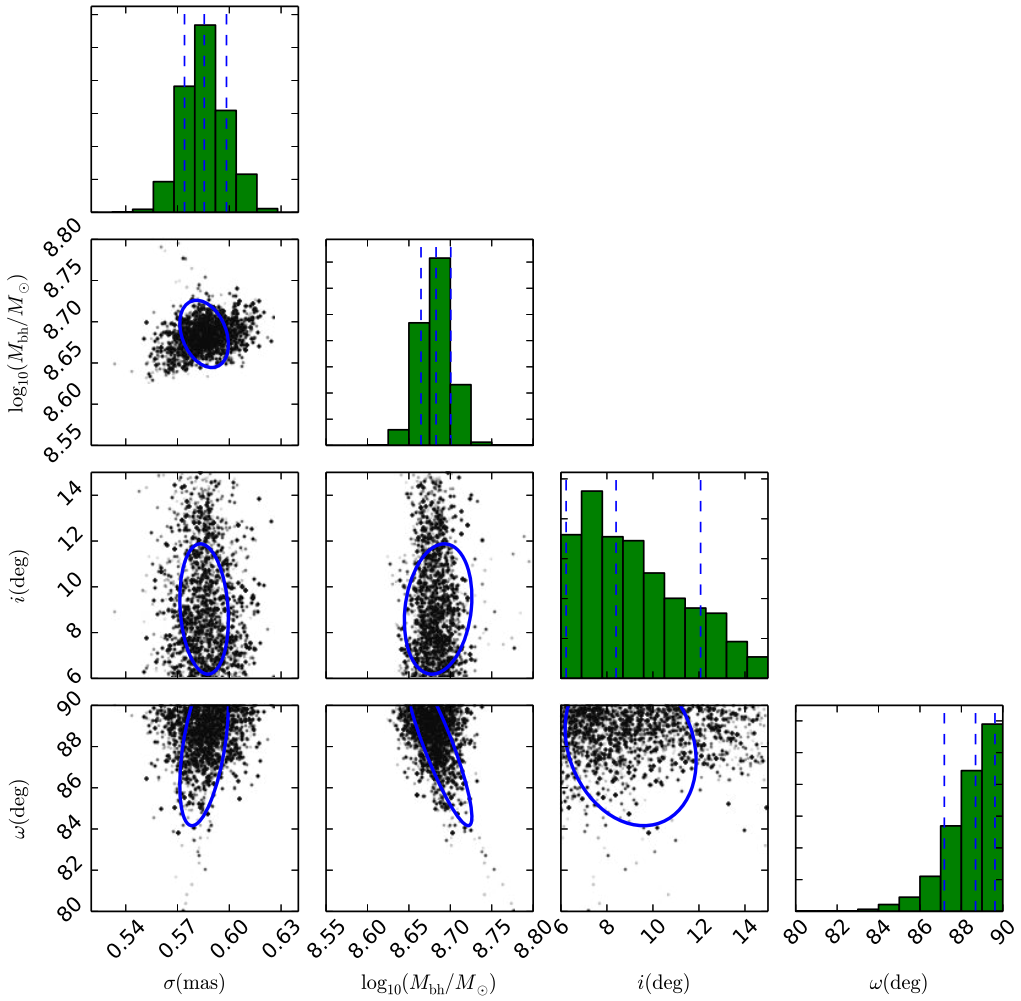

FIGURE 5.17: Parameters probability distribution obtained from MCMC fitting with $P_{\rm turb} = 1$. The scatter plots show the projected two-dimensional distributions and green ellipses represents the 1 σ regions of the projected covariance matrix. The histograms show the projected 1D distributions with dotted green lines representing mean and the 1 σ uncertainties. From top-to-bottom and left-to-right, the panels show BLR width $\sigma_{\rm blr}$, $\log_{10}(M_{\rm bh}/M_{\rm sun})$, inclination i and opening angle ω.

green ellipses of 1 σ regions of the projected covariance matrix is shown. The histograms represent 1D probability distribution of the samples with its mean and 1 σ uncertainties (green lines) for $\sigma_{\rm blr}$, $\log_{10}(M_{\rm bh}/M_\odot)$, inclination i and opening angle ω. The mean and 1 σ uncertainties of the parameters (see Table 5.1) are $\sigma_{\rm blr} = 0.585^{+0.011}_{-0.012}$ (mas), $\log_{10}(M_{\rm bh}/M_{\rm sun}) = 8.682^{+0.017}_{-0.018}$, $i = 8.4^{+3.7}_{-2.2}$ (deg) and $\omega = 88.6^{+1.0}_{-1.5}$ (deg). Note that we neglected error on $R_{\rm rim}$ measurement in the fitting process. This could increase the uncertainties on the parameters.

The fits of the differential phase and visibility (green line) using the mean value of the model parameters are shown in figure 5.18, and the corresponding fitted Paα emission line profile observed with SINFONI (blue) is shown in figure 5.19a. In all baselines, model fits all the spectro-interferometric measurements within the error

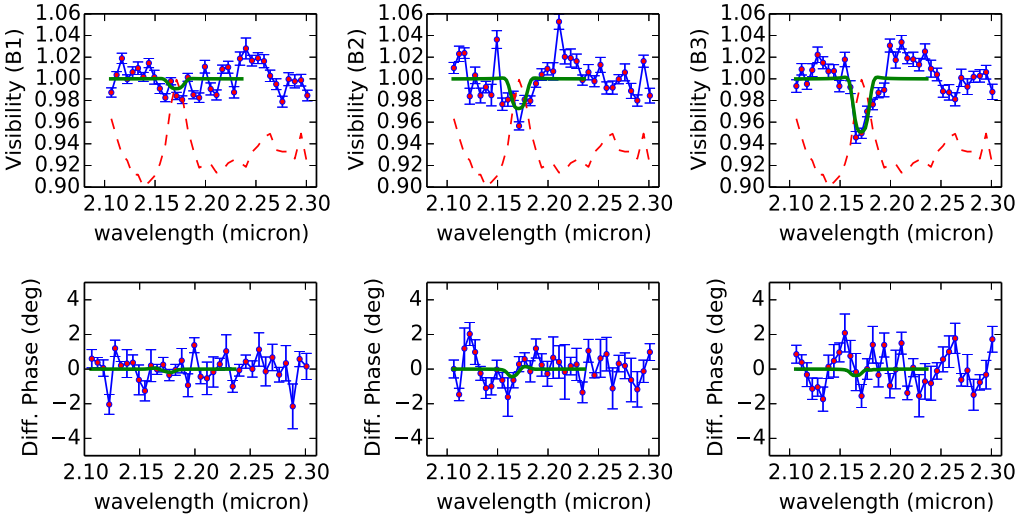

FIGURE 5.18: Global fit of the data from the best fit model obtained from MCMC fitting.

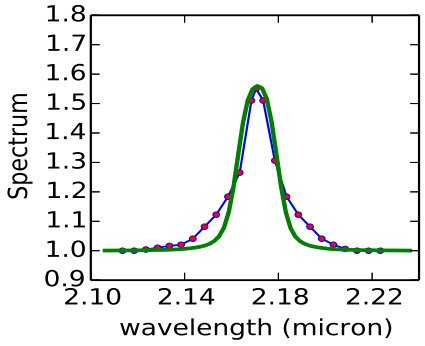

FIGURE 5.19: Global fit of the emission line profile.

bars. We see that both the model emission line and visibility profile are narrower in the wings. As discussed in chapter 4, this can be due to a high turbulence that enhance the line wings, or due to a different radial intensity profile (more curvy than a Gaussian) that could increase the line wings by adding more "fast" material near the center of the object. However, a spherical geometry with the presence of turbulence gives a better representation of the data. The best fit model is plotted in figure 5.20 for edge-on (left) and face-on (right) views. Note that in the plots, size of the clouds increases with the time lag. Both the images appear to be similar as the geometry of the BLR is close to spherical, and since the inclination is close to face-on plots appear to be circular.

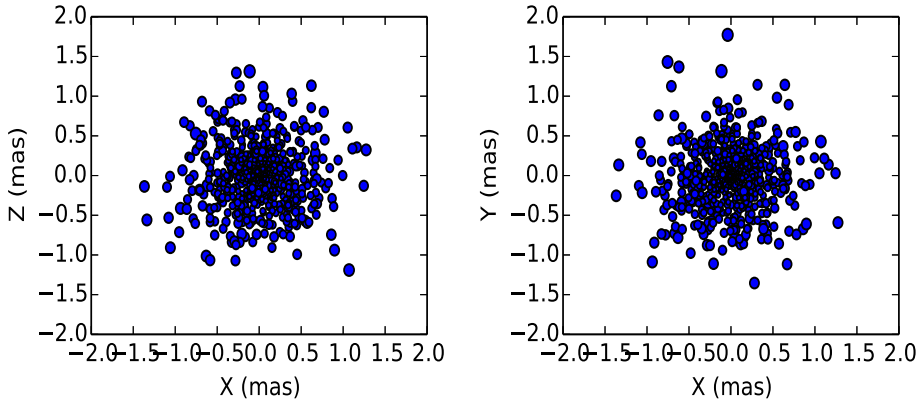

FIGURE 5.20: Geometry of the BLR of 3C273. Left: BLR observed edge-on i.e., along the y axis. Right: BLR observed face-on i.e. along the +z axis. In the plots, size of the clouds increases with the time-lag.

5.4 Reverberation mapping window problem

The result of our most clean 3C273 OI data result is that the angular size of the BLR is substantially larger than the inner dust rim, and much larger than visible RM estimates. Kaspi et al. (2000) have spectro-photometrically monitored 28 Palomar-Green quasars including QSO 3C273 to obtain relationships between BLR size and central BH mass with quasar luminosity. Spectrophotometric monitoring was performed for 7.5 years with 20-70 observing epochs per object. During the observation, both continuum and emission line flux variation was found.

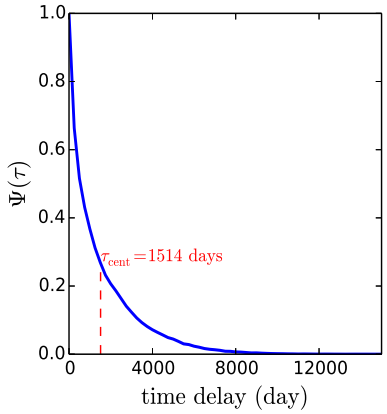

FIGURE 5.21: Model response function of the BLR. The red line shows the centroid of this response function, which is 1514 days.

We have collected the RM data of 3C273 from Kaspi et al. (2000). The light curves are very sparsely sampled, consists of 39 spectroscopic epochs in 7.5 years. With

simple cross-correlation analysis, the estimated mean BLR size of Hα and Hβ line emitting regions is 387^{+58}_{-50} lds. Our interferometric data suggests an extended BLR that has the centroid of the response function at $\tau_{\rm cent^*} = 1514$ days, as shown in figure 5.21. With a 7.5 years of observation, it is not possible to constrain such a large BLR size. Hence, we decided to analysis in depth the RM data. We first undertook analysis of the biases in RM data resulting from the time window and sampling problem, with E. Fossat who is an expert of similar problems in the analysis of the time series of spectra in astroseismology. After some interesting results, we decided to use the most recent RM methods to treat this problem and reanalyze the 3C273 RM data.

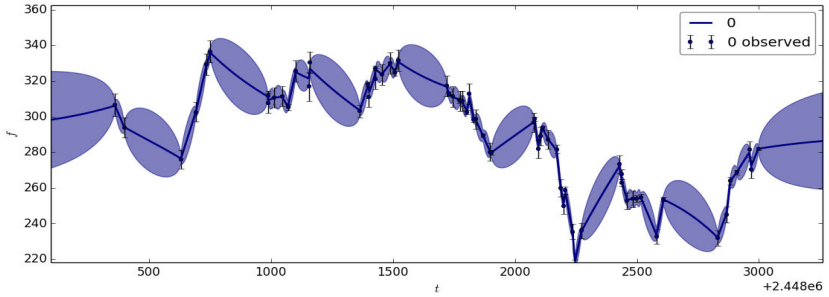

FIGURE 5.22: Interpolation of the 3C273 continuum light curve observed by Kaspi et al. (2000). The solid line is the best fit light curve and the filled region represents the 1 σ uncertainty region.

In RM, time window and sampling problems are treated by optimum interpolation procedure described in Zu et al. (2011). We thus make use of the software, which is Python code "Javelin" developed by Zu et al. (2011) for continuum light curve interpolation. Javelin allows simultaneous fitting of continuum and different emission lines light curves. It uses a damped random walk model, which is described in section 7.2. The fitted continuum light curve is shown in figure 5.22. Once we have a continuum light curve at all time, we can create an emission line light curve convolving a simple top-hat response function of centroid $\tau^*_{\rm cent}$. After cross-correlating the continuum and emission line light curves, we calculated the centroid ($\tau_{\rm cent}$) of the cross-correlation function (CCF). This step has been repeated for various $\tau^*_{\rm cent}$, allowing us to plot centroid of response vs centroid of CCF, as shown in figure 5.23.

As discussed in chapter 2, $\tau^*_{\rm cent}$ is equal to $\tau_{\rm cent}$ if light curves extend up to infinity. From figure 5.23, we see that the time-lags are unbiased until $\tau_{\rm cent} \simeq 600$ lds and then they remain bijectively related to the true input values up to $\tau_{\rm cent} \simeq 800$ lds, after which any input $\tau^*_{\rm cent}$ results in a measured $\tau_{\rm cent}$ randomly placed between 200 to 400 lds. This occurs mainly due to 7.5 years of time window. Hence, to detect a distinct peak in CCF for 3C273 Paα line, we need much longer duration monitoring campaign since our estimated Paα line emitting region is much larger than Hβ. According to the above simulation, the duration of the light curve or monitoring campaign should be more than 3 times of the maximum time lag ($2R_{\rm blr}/c$) to estimate accurately the mean response of the BLR. Similar suggestion

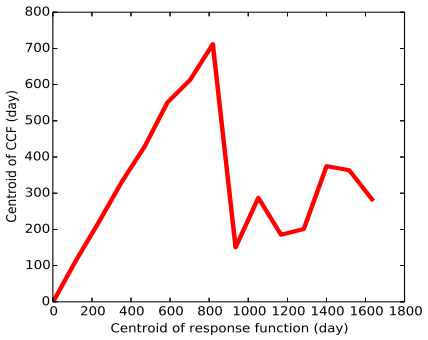

FIGURE 5.23: Centroid of the CCF is plotted against the centroid of response function. The time lag can not be measured if the centroid of CCF is greater than 800 days for a 7.5 years observing campaign.

was also given by Horne et al. (2004). Note that, to detect peak in CCF for high-ionization line like CIV, a shorter than 7.5 years monitoring should be sufficient, and thus for low-luminous objects much shorter campaign will be fine.

5.5 Discussion and conclusion

We successfully resolved the Paα emission line of the quasar 3C273 using a "Blind mode" observing technique with AMBER instrument at VLTI. An AMBER+ 2DFT data reduction algorithm was used to reduce the data as standard AMBER data reduction software can not be used at that faint magnitude. Emission line signature in few spectral channels has been detected. Differential visibility shows a drop that increases with baseline length showing a larger BLR than continuum dust sublimation radius. Moreover, we obtained differential phase of $0 \pm 1°$ in all baselines.

We used a geometrical and kinematical model to interpret our 3C273 observation, which is very flexible and can account various geometrical and kinematical models (see chapter 4). In order to sample the parameters space, we employed a MCMC simulation, and calculated probability distribution of each model free parameters. We found that 3C273 has a larger BLR, a Gaussian of standard deviation $\sigma_{\rm blr} = 0.585^{+0.012}_{-0.011}$ mas $= 1823^{+37}_{-34}$ lds or $\mathrm{HWHM_{blr}} = 2142^{+43}_{-39}$ lds, extended beyond the dust sublimation radius. Its response function has a centroid at about 1514 days (figure 5.21), which is about 4 times larger than Hβ emission line size obtained via cross-correlation by Kaspi et al. (2000).

This suggests that emission line gas clouds is extended beyond sublimation radius, and present in and above the inner rim dust torus. When the clouds are directly illuminated by the central source, they emit emission line photons. Heavily shielded clouds (dust) produce very weak lines, and contribute in the near-IR continuum. This result supports the recently proposed "Bowl shaped" BLR model by Goad et al. (2012), where the authors suggested that the clouds can be present on the surface of the dusty torus forming a "Bowl shaped" where height of the clouds

increases with its distance from the central source, and emits only when they are illuminated by the radiation of the central source. Note that the large BLR radius is also estimated recently by Landt et al. (2014) from recent near-IR spectroscopic study, suggesting that the BLR has an outer radius, and for 3C273 this is 15,551 light-days obtained from Paβ emission line spectroscopy.

One possible reason for this bigger BLR size measured by OI than RM is that the OI visibility depends on a flux weighted radius. Actually the impact of a given cloud on the visibility profile increases as the square of its angular radius (see chapter 4). Thus, it is weighted to the flux contribution from larger radius. On the other hand, the RM size is a response-weighted radius, weighted to the larger amplitude of flux variation, which comes from the compact emitting region or smaller radius. Kishimoto et al. (2011b) and Koshida et al. (2014) discussed the difference between RM and OI estimates in near-IR in the apparent size of the inner rim. OI estimated size of the inner rim is a factor of $1.5 - 2.5$ larger than RM (see figure 2.6). Since Paα is a lower ionization line than Hβ or Hα, the expected RM size of Paα emitting region could be 1.2 to 2 times larger than Hβ (Alessandro Marconi in private comunication, and also see Goad, 1995). Moreover, OI size could be two times larger than RM size. Thus, our estimated Paα size, about 4 times larger than RM Hβ size, is not in much contradiction with RM Hβ (or Hα) result. However, the BLR larger than dust inner-rim remains a surprise.

The differential phase estimates of $0 \pm 1^\circ$ suggest that the BLR of the 3C273 has a roughly spherical geometry, which is inclined at a very low inclination towards observer. High inclination and flat geometry will produce strong phase signature as shown in figure 5.14. Note that our estimated inclination is similar to the values obtained by Unwin et al. (1985) and Lister et al. (2009) from the observation of radio-jet. Due to the low inclination, a large opening of the BLR is needed to match the width of the emission line profile as well as the broadening of differential visibility shape. Our Paα emission line shows a Lorentzian profile, which is due to the emission from an extended region. It has been suggested that a Lorentzian profile could be due to the presence of turbulence (Goad et al., 2012). We also found the presence of macro-turbulence in 3C273 BLR broadening the emission lines and making it Lorentzian shape. Note that very large turbulence can also fit the line profile and differential phase without the need of a large opening angle, but then it would be difficult to explain the origin of such large turbulence velocity.

Our geometrical and kinematical model provides an estimate of the 3C273 BH mass $4.80^{+0.20}_{-0.17} \times 10^8 M_\odot$ (neglecting the error on $R_{\rm rim}$ measurement), which is similar to the mass obtained by RM mapping data by Kaspi et al. (2000), but an order of magnitude lower than Paltani and Türler (2005). The higher mass estimated by Paltani and Türler (2005) could be due to the problem of line width measurement. After a re-analysis of Kaspi et al. (2000) data, Peterson et al. (2004) found a virial product of $1.61 \pm 0.34 \times 10^8 M_\odot$. However, using a virial scale factor $f = 5.5$, they estimated a BH mass $8.86 \pm 1.87 \times 10^8 M_\odot$ of 3C273. Since, our measurement provides BH mass, which is independent of unknown virial factor (f), we estimate $f \simeq 3$ comparing with virial product of 3C273 estimated by Peterson et al. (2004). This f value is within the value of $f = 2.8$ obtained by Graham et al. (2011) from the scaling of $M_{\rm bh} - \sigma_*$ relation (see chapter 2) and $f = 4.3$ obtained by Grier et al. (2013) using high quality RM data to recover velocity-delay map. This value

is also close to the $< f >= 4.7$ obtained from recent dynamical model of RM high quality LAMP data by Pancoast et al. (2014a) although the dispersion around this mean is very larger of the order of 5, showing individual object have very different f. Our estimation of the virial factor suggests that BH masses estimated from RM data using $f = 5.5$ is overestimated by a factor of about 1.8. A handful number of objects can indeed allow to estimate a mean f value from interferometric data and calibrate the BH masses estimated using virial relation in RM technique.

Chapter 6

Feasibility of BLR observation

Contents

6.1 Introduction

Signal-to-noise ratio (often abbreviated as SNR or S/N) is defined as the ratio of signal amplitude to the noise RMS (root mean square), and it predicts the feasibility of an observation and allows to anticipate the accuracy on the recovered mode fitting parameters. To understand the feasibility of BLR observation with the IR instruments at VLTI, we did an SNR analysis. The aim is to estimate the number of objects that could be accessible with the current, upcoming and possible spectro-interferometric instruments in the near-infrared (near-IR) at VLTI to set the possibility of having a large unification scheme, which assumes that we can analyse enough sources to study correlations between the main morphological parameters and the luminosity for example.

Since the end of KI operation, the VLTI with Unit Telescopes (UTs) is the single interferometer with an IR SNR potentially sufficient for MR ($R = 500 - 1500$) observation in the K band. We have seen in chapter 4 that a spectral resolution of the order of $R = 1000$ is necessary to discriminate between some BLR models. Moreover, we believe that the 8 m UTs, due to their large collecting area, are

a key feature for an AGN program with such spectral resolution as other interferometric facilities, such as CHARA or NPOI, are equipped with substantially smaller telescopes and for the time being, these are far from the necessary limiting sensitivity.

In the case of each VLTI instrument we examine the possibility to observe a target, i.e. to detect and maintain the fringes on the target itself, and the accuracy of the absolute and differential visibility and phase that can be obtained on each target.

6.2 Current, incoming, and possible VLTI instruments

The VLTI is the interferometric mode of the very large telescope situated at Mount Paranal in Chile and installed by European Southern Observatory (ESO). It consists of four 8 m UTs and four 1.8 m auxiliary telescopes (ATs) offering high sensitive and high angular resolution observation. The UTs are fixed while ATs can be moved to 30 different locations, that would provide maximum baseline separation of 200 m, but currently offering a maximum baseline of 139 m between UT1 and UT4 (see figure 3.5).

AMBER+: AMBER is a first-generation near-IR spectro-interferometric VLTI instrument (Petrov et al., 2007). With its standard frame-by-frame processing, it cannot observe AGNs in medium resolution (MR) as the current VLTI fringe tracker (FT), used to stabilize fringes, is limited to about $K < 9$. However, AMBER can already operate in an alternative mode, called AMBER+ (Petrov et al., 2012), where the full dispersed fringe image is processed, in a way equivalent to a coherent integration of all spectral channels, whatever the SNR per channel is. It allowed observing successfully the quasar 3C273 in MR (R=1500). The fringes were detected with a SNR=3 in typically 1 s. To obtain differential visibility and phase with a sufficient accuracy (respectively 0.02 to 0.03 and 1° to 2°), it was necessary to bin the spectral channels down to a resolution 250. The results achieved with AMBER+ on 3C273 have been used to validate and calibrate our SNR computations.

OASIS: OASIS ("Optimizing AMBER for Spectro-Interferometry and Sensitivity"), minor AMBER modification proposed by Petrov et al. (2014), could be installed in a few months as soon as ESO accepts it to include in the VLTI planning. It uses spectral encoding to separate the fringe peaks, allowing to code the interferogram on 4 pixels instead of 32 pixels currently needed for AMBER. Moreover, the spatial filters with fibers would be bypassed by optimized optics which yields a gain in transmission of about 7 with regard to the current AMBER instrument. For MR differential observations, theses spatial filters are not necessary, as they basically improve the accuracy on the absolute visibility. However, as we have seen from chapter 4 that absolute visibility accuracy in the continuum is important, the idea is to combine OASIS MR observations with GRAVITY or PIONIER LR observation that will allow accurate absolute visibility than their spatial filtering and stability obtained with very compact integrated optics.

OASIS+: OASIS+ would be a major improvement of AMBER. It could be developed as a visitor instrument in the 1 M€ range. The current AMBER detector

would be replaced with a new SELEX detector and the spectrograph which is optimized for BLRs, with a fixed spectral resolution, i.e. $R \simeq 500$. We note that OASIS+, or any other successor of the 2nd generation VLTI instruments, is not in the current ESO plans, but it gives an idea of what could be ultimate VLTI performance for AGNs.

GRAVITY: GRAVITY is the 2nd generation 4 telescopes beam combiner VLTI near-IR spectro-interferometric instrument that will be commissioned in 2016 (Eisenhauer et al., 2008). It is expected to provide astrometry accuracy of 10 μas and phase-referenced imaging with 4 mas resolution. It will have three spectral resolution mode 30, 450 and 1500. Gravity will provide all the interferometric measurements that presently AMBER does, but with 6 baselines observation. Visibility phase between the reference star and science object in all spectral channels as well as differential phase between two objects can be obtained from GRAVITY observations. Using these information it will be possible to obtain images exploring the complex visibilities, and for astrometry using the differential phase and group delay. Its main characteristic of interest for a BLR program is that it has an internal FT that should allow cophased observations up to $K = 10.5$. This allows much longer individual frame times, a higher instrumental visibility and a more stable one. The current GRAVITY plans do no foresee using without its fringe tracker. The GRAVITY internal FT will boost the accuracy of all measures on source bright enough to allow using FT (or with a nearby reference source bright enough for off-axis FT). The GRAVITY FT will have two effects:

1. It will improve the fundamental SNR but allowing much longer frame times, and hence differential visibility and phase SNR will be improved.
2. It will stabilize the VLTI/GRAVITY instrumental contrast and therefore will allow more accurate absolute visibility measurements.

The main drawback of the current GRAVITY FT is that it is optimized for accuracy rather than for absolute sensitivity, and should therefore hardly allow observations fainter than $K \simeq 10.5$.

OASIS+FT: It refers to the use of OASIS+ with a second-generation FT, with a limiting sensitivity larger than $K = 10.5$. Such a FT would allow increasing the accuracy of the measurements just like the one in GRAVITY, and it would also extend the possibilities of GRAVITY. Currently proposed designs show that FT magnitudes higher than 13 in K-band should be achievable (Petrov et al., 2014; Meisner et al., 2012). I have participated to the study of a concept of "Hierarchical Fringe Tracking (HFT)", which is described in Petrov et al. (2014), where this kind of magnitude gain could be obtained:

1. Instead of dividing the flux of each telescope between the number of telescope pairs like the pairwise GRAVITY FT, all the flux of a telescope is used to cophased it with the one in the local pair. In the HFT, when two telescopes are cophased all the flux is transmitted as coming from a single telescope and use to cophase a pair of pairs.

2. In the central component of the HFT, which is a "Two telescopes Spatial Filter", the piston is measured using only 3 to 5 pixels that analyze the broad band signal in both polarizations, instead of using 4 pixels per spectral channel (5 in the GRAVITY FT) and polarization.

The estimated magnitude gain, with the same detector and control algorithms is between 2.5 to 3.5.

MATISSE: MATISSE is another 2nd generation 4 telescopes beam combiner VLTI instrument that will offer an extremely large spectral coverage, from 3 to 13 μm (covering 3 spectral bands L, M and N) with a spectral resolution ranging from 30 to 4500. MATISSE offers several possibilities to study AGNs:

1. It will give much better constraints on the dust torus morphology than MIDI or the K band instruments. This can allow more reliable absolute visibility estimate and thus better models of the torus than the ring model used in most of this thesis.
2. In MR in the L band, we will be able to observe BLR in Brγ emission line for low redshift targets.

6.3 Interferometric signal and noise

From a general formalism described in Petrov et al. (1986) and updated in Vannier et al. (2006), it is easy to show that the noise on the coherent flux computed from each interferogram is given by:

$$\sigma_c = \sqrt{n_T n_* t_{\rm DIT} + n_p \sigma^2_{\rm RON} + n_T n_{\rm th} t_{\rm DIT}}, \tag{6.1}$$

where n_* is the source flux per spectral channel, frame and second, n_T is the number of telescopes, $t_{\rm DIT}$ the frame exposure time, n_p is the number of pixels (for multi-axial instruments up to $n_T = 4$ we have $n_p = 4n_T(n_T - 1)/2$), $\sigma^2_{\rm RON}$ is the variance of the detector read-out noise and $n_{\rm th}$ is the background flux per spectral channel, frame and second. $t_{\rm DIT}$ must be short enough to freeze the turbulence. In good seeing conditions, it is possible to use $t_{\rm DIT} = 200$ ms. In K-band this value is much smaller than the detector noise and hence can be neglected for short exposures. However for long exposures such as in cophased mode $n_{\rm th}$ should be taken into account. In K-band, $n_{\rm th} = 1.07$ photons s^{-1}cm$^{-2}\mathring{A}^{-1}$ (In the λ^2 solid angle of a single mode spatial filter). For a pair-wise instrument like GRAVITY, the same formula applies with $n_p = 4$ and the flux of each telescope has to be divided by $(n_T - 1)$ that is the number of pairs each aperture is involved in.

The classical SNR on the coherent flux, per spectral channel and per frame (Vannier et al., 2006; Lagarde et al., 2012) is then given by:

$$\mathrm{SNR}_0 = \frac{C}{\sigma_c} \simeq \frac{n_* t_{\rm DIT} V_{\rm inst}}{\sigma_c}, \tag{6.2}$$

and

$$\sigma_\phi \simeq \frac{\sigma_c}{C\sqrt{2}}, \tag{6.3}$$

where $V_{\rm inst}$ is the instrument visibility.

The source flux per spectral channel per frame and per second is given by:

$$n_\star = n_0 AST\delta\lambda 10^{-0.4K_{\rm mag}}, \tag{6.4}$$

where n_0 is the number of photons $\rm s^{-1}cm^{-2}\mu m^{-1}$ from a star with $K_{\rm mag} = 0$, outside earth atmosphere, $n_0 = 45\times10^4$ photons $\rm s^{-1}cm^{-2}\mu m^{-1}$, A is the collecting area of telescope, S is the Strehl ratio with the VLTI adaptive optics system MACAO, T is the overall transmission of the atmosphere, the VLTI and the instrument, and $\delta\lambda$ is the spectral band-width equal to λ_0/R, where R is the resolution.

6.3.1 Standard processing

In the classical AMBER data processing (the P2VM approach described in Tatulli et al., 2007), the coherent fluxes measured in each frame are added coherently. This assumes that we have been able to measure the atmospheric piston in each frame with a sufficient accuracy of at least $\lambda/2\pi$. At best the piston is estimated from all the independent phase differences that can be extracted from the n_λ spectral channels.

$$p =< \frac{\Delta\phi}{2\pi}\frac{1}{\Delta\sigma} >_{n_\lambda/2} \tag{6.5}$$

$$=< \frac{\Delta\phi}{2\pi}\frac{2R\lambda}{n_\lambda} >_{n_\lambda/2} \tag{6.6}$$

and

$$\sigma_p \simeq \frac{\sigma_\phi\sqrt{2}}{2\pi}\frac{2R\lambda}{n_\lambda}\frac{1}{\sqrt{n_\lambda/2}} \tag{6.7}$$

and the condition $\sigma_p < \frac{\lambda}{2\pi}$ yields $\sigma_\phi < \frac{n_\lambda^{3/2}}{4R}$ at AMBER MR mode ($R = 1500$, $n_\lambda = 256$) this yields $\sigma_\phi < 0.7$ rad. The condition for coherent processing is that the $\rm SNR_0 = \frac{1}{\sigma_\phi\sqrt{2}} \simeq 1$. This limits the MR mode of AMBER without FT, i.e. with short exposure to $K \sim 8$.

An alternative is the so called incoherent addition, when we arrange the modulus of the coherent flux that is insensitive to phase errors. From Jaffe 2014 (private communication) we know that the $\rm SNR_Q$ on $|C|^2$ is

$$\rm SNR_Q = \frac{SNR_0^2}{\sqrt{1+2SNR_0^2}}\sqrt{N_{EXP}n_\lambda}, \tag{6.8}$$

where n_λ is the number of spectral channels and $N_{\rm EXP} = \frac{t_{\rm EXP}}{t_{\rm DIT}}$ is the total number of $t_{\rm DIT}$ frames processed in the $t_{\rm EXP}$ total time. If $\rm SNR_0 << 1$; $\rm SNR_Q \simeq SNR_0^2\sqrt{N_{EXP}n_\lambda}$ and this mode is a very poor way to increase the sensitivity.

6.3.2 AMBER+ processing

We have developed a new approach where the full-dispersed fringe image is processed, in a way equivalent to a coherent integration of all spectral channels, whatever the SNR_0 per channel is. This data processing is inspired by the GI2T and VEGA/CHARA (Berio et al., 1999), and explained in chapter 3 and 5. Then we still have to make a quadratic average on the frames and the SNR of this processing is given by

$$\mathrm{SNR}_+ = n_\lambda \frac{\mathrm{SNR}_0^2}{\sqrt{1 + 2 n_\lambda \mathrm{SNR}_0^2}} \sqrt{N_{\mathrm{EXP}}}. \tag{6.9}$$

In this case, SNR_+ is directly the fringe peak detection SNR, as shown in figure 3.10d. $\mathrm{SNR}_+ > 3$ yields $\mathrm{SNR}_0 \simeq 0.05$ for 20 s observations ($n_\lambda = 256$, $N_{\mathrm{EXP}} = 50$). The magnitude gain with regard to the standard mode is about 3, as we are in the detector noise regime with $\mathrm{SNR}_0 \propto n_*$.

The phase is estimated from the average coherent flux and its accuracy is given by

$$\sigma_\phi = \frac{< C >}{\sigma_c \sqrt{2\, n_b}} = \frac{1}{\mathrm{SNR}_0 \sqrt{2\, n_b} \sqrt{N_{\mathrm{EXP}}}} \tag{6.10}$$

with $N_{\mathrm{EXP}} = 36000$ for 2 hours of observations and n_b is the number of binning.

In AMBER+, a SNR analysis (Petrov et al., 2014) shows that

$$\sigma_{\phi+} = \sigma_\phi \sqrt{2 \frac{\sigma_\phi^2}{n_\lambda} + \frac{1 + n_\lambda}{n_\lambda}}. \tag{6.11}$$

6.4 Fringe detection limit

In figure 6.1 we plotted the fringe detection limit $\log_{10}(\mathrm{SNR})$ as a function of K_{mag} using Eq. 6.8 and Eq. 6.9 for different instruments like standard AMBER performance with 0.2 s per frame, AMBER+ performance with incoherent 2DFT processing (see chapter 3), OASIS module and OASIS+ module. The parameters used for the calculation are presented in Table 6.1. We found AMBER+ could reach up to $K_{\mathrm{mag}} \sim 10.5$ and the potential limit of the new OASIS and OASIS+ is greater than 13.

We note that fringe detection limit for GRAVITY is not included in this plot as GRAVITY will use an internal FT working up to K_{mag}=10.5. Nevertheless, it should be possible to use GRAVITY without the internal FT in a mode similar to AMBER+ mode, allowing to observe targets fainter than $K_{\mathrm{mag}} = 10.5$ with performances intermediate between AMBER+ and OASIS.

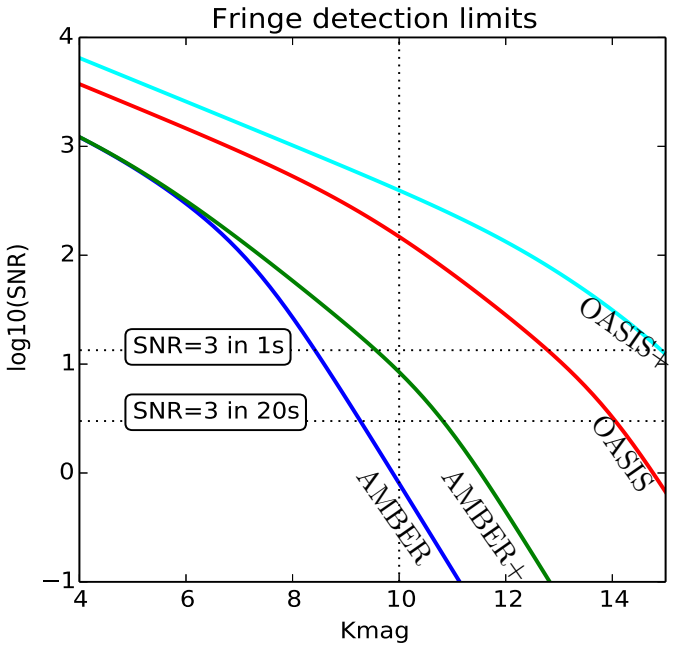

FIGURE 6.1: Fringe detection limits (log10(SNR)) for different VLTI instruments: from left to right: standard AMBER performance with 0.2 s frames (blue), current AMBER+ measured performance with incoherent 2DFT processing (green), OASIS module (red) and OASIS+ module (cyan). The AMBER+ curve (given here for a maximum of 20 s) is compatible with our experimental result of fringe detection with SNR=3 in 1 s. The horizontal dotted black line shows the threshold fringe detection limit of SNR=3 in 1 s and 20 s. The vertical dotted black line corresponds to $K_{\mathrm{mag}} = 10$.

TABLE 6.1: Parameters for fringe detection limit[a] and differential observation of BLR[b] plot.

Instrument	**Parameters**												
	n_T	$t_{\rm DIT}$ (sec)	n_p	$\sigma_{\rm RON}$	$n_{\rm th}$	$V_{\rm inst}$	n_λ	$N_{\rm EXP}$	n_0[c]	A (cm^2)	S	T	R [d]
AMBER	3	0.2	32	11	1.07	0.25	512	100[a], 36000[b]	45	497628	0.5	0.01	3000
AMBER+	3	0.2	32	11	1.07	0.25	512	100[a], 36000[b]	45	497628	0.5	0.01	3000
OASIS	3	0.2	4	11	1.07	0.25	512	100[a], 36000[b]	45	497628	0.5	0.01 $\times$ 7	3000
OASIS+	3	0.1	4	3	1.07	0.5	512	200[a], 72000[b]	45	497628	0.5	0.01 $\times$ 7	1000
GRAVITY	4	60	4 [e]	11	1.07	0.75	512	120[b]	45	497628	0.5	0.01	1000
OASIS+FT	3	60	4	3	1.07	0.75	512	120[b]	45	497628	0.5	0.01 $\times$ 7	1000
MATISSE	4	0.1[f]	72	15	1.67×10^3	0.5	512	36000[b]	45	497628	0.5	0.01	950
VISIBLE[g] with UTs	4	0.02	4	0	0	0.5	461[h]	50[a], 360000[b]	1000	497628	0.1	0.02	1500
VISIBLE with ATs	4	0.02	4	0	0	0.5	461	500[a], 360000[b]	1000	$\pi \times (180)^2$	0.5	0.02	1500

[c]unit is in photon s^{-1}cm^{-2}$\mathring{A}$

[d]Resolution per spectral pixel. The actual spectroscopic resolution is typically $R/2$.

[e]GRAVITY has a pair wise beam combiner and must be analyzed as a 2T interferometer, with 1/3 of the flux in each aperture.

[f]0.1s for MATISSE without FT and 10s with FT

[g]only photon noise

[h]Considering wavelength range of $5500 - 7500\mathring{A}$ and spectral resolution $R = 1500$.

6.4.1 Signal estimation

In the following, we estimate three interferometric quantities: the absolute visibility in the continuum (V_c), the amplitude of the differential visibility ($\Delta V_{\rm diff}$) and differential phase ($\Delta\phi_{\rm diff}$) variations in the line.

To estimate the absolute visibility signal we used the Eq. 3.21. The amplitude of the differential visibility variation in the line is given by:

$$\Delta V_{\rm diff} = 1 - V_*/V_c = \frac{1}{V_c}\frac{V_c F_c + V_l F_l}{F_c + F_l}, \tag{6.12}$$

where V_* is the source visibility, V_l the source visibility averaged over the line, V_c the visibility in the nearby continuum and F_l and F_c=1 are the line and continuum flux, respectively.

We consider two extreme cases for the differential visibility signal: $R_{\rm blr} << R_{\rm rim}$ and $R_{\rm blr}$=2$R_{\rm rim}$. In the first case, we assume that the BLR is fully unresolved by the interferometer, i.e., $V_{\rm blr}$=1. Thus, using Eq. 6.12 for the unresolved BLR (i.e. V_l=1) we obtain:

$$\Delta V_{\rm diff} = -\frac{F_l}{1+F_l}\frac{\alpha_c^2}{1-\alpha_c^2}, \tag{6.13}$$

where $\alpha_c = 2\frac{R_{\rm rim}}{\lambda/B}$.

For the large BLR case, the line visibility can be written as V_l = 1 - 2 $(2\alpha_c)^2$, consequently:

$$\Delta V_{\rm diff} = 3\frac{F_l}{1+F_l}\frac{\alpha_c^2}{1-\alpha_c^2}. \tag{6.14}$$

Finally, the typical differential phase amplitude for the BLR is given by

$$\Delta\phi_{\rm diff} = \pi\frac{F_l}{1+F_l}\alpha_l \cos\omega, \tag{6.15}$$

where $\alpha_l = \frac{2R_{\rm blr}}{\lambda/B}$. If the inner rim of the dust torus is inclined and skewed, differential interferometry will also be sensitive to the difference between the global line and the continuum apparent photocenter with maximum amplitude of

$$\Delta\phi_{\rm diff} \simeq \frac{\pi}{2}\frac{F_l}{1+F_l}\frac{\alpha_c}{\sqrt{2}}. \tag{6.16}$$

Thus, maximum photocenter of skewed rim depends on the flux ratio of line and continuum.

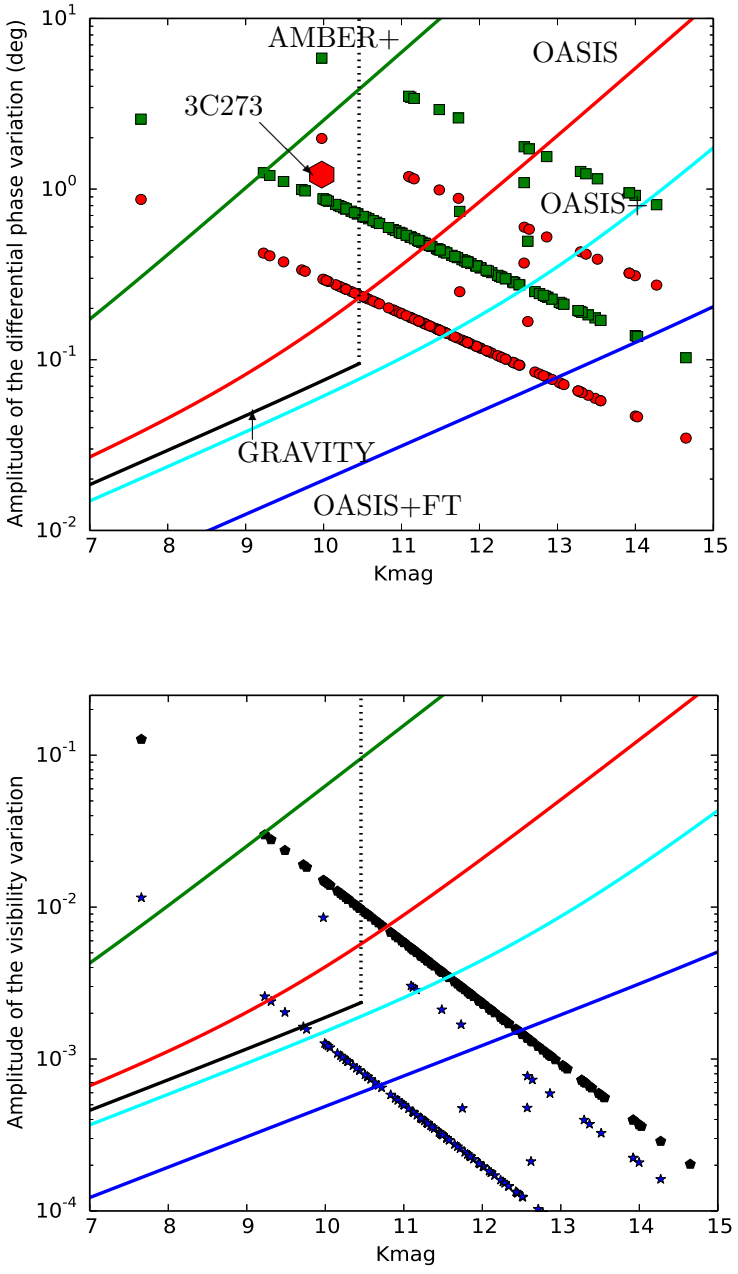

FIGURE 6.2: Feasibility of BLR observation with 135 m baseline using differential phase (upper panel) and absolute and differential visibility (lower panel) measurements. The solid lines represent the differential phase (up) and differential visibility (down) for AMBER+ (green), OASIS (red), OASIS+ (cyan) and GRAVITY (black) for $n_b = 2$. Note that the black dotted line represents the observing limit of GRAVITY internal fringe-tracker (i.e. K=10.5). Each symbol represents one Sy1 AGN observable at Paranal. On the upper panel, the amplitudes of the differential-phase variation are computed either using the $R_{\rm blr}$ estimated from visible RM (red circles) or assuming the skewness of the dust inner rim (green squares). The red polygon marked by 3C273 is obtained considering explicit 3C273 error, taking into account the binning of 16, while rest of the plot is made with $R = 1500$ and no binning. On the lower panel, the differential and absolute visibility for each object are plotted as blue stars and black polygons, respectively.

6.4.2 Selection of targets

We collected a list of all Sy1 and QSOs observable with the VLTI found in the SIMBAD catalog with search criteria $K_{\rm mag} < 13$, $V_{\rm mag} < 15$ and dec $< 15°$. For each source we estimate the inner rim radius from its magnitude thanks to an extrapolation of Suganuma et al. (2006) known measurements. From this rim radius we evaluate the possible values of the continuum visibility, differential visibility and phase. These values are compared to the SNR estimates deduced from the source estimated K magnitude. We use the CMB corrected redshift for each target from NED and K magnitude from 2MASS point source catalog. We collected the list of objects from Bentz et al. (2013) that have classical RM BLR size. Then we fitted the radius with their K magnitude and extrapolate for the objects that do not have the RM BLR size.

For each target, we use the strongest emission line in the K-band given the actual redshift of the target. To compute the interferometric observables we used the following values for the normalized line flux F_l.

- $F_l = 0.6$ when Paα is in the K-band ($0.08 \leq z < 0.25$)
- $F_l = 0.3$ when Paβ is in the K-band ($0.4 \leq z < 0.87$)
- $F_l = 0.06$ when Brγ is in the K-band ($z < 0.08$)
- $F_l = 0.12$ when Paγ is in the K-band ($z \geq 0.87$)

These mean values are deduced from the IR line intensity measurements in Landt et al. (2008). The dispersion of line strengths is very large. For example the Brγ line flux goes from 0.01 to 0.18 with a 0.07 mean. This limited dataset does not allow good statistics but we used it to estimate that about one third of the targets where Brγ must be used, will eventually be impossible to observe ($F_l < 0.02$) while our signal estimates are actually pessimistic for half of the targets where F_l is larger than the mean values used here.

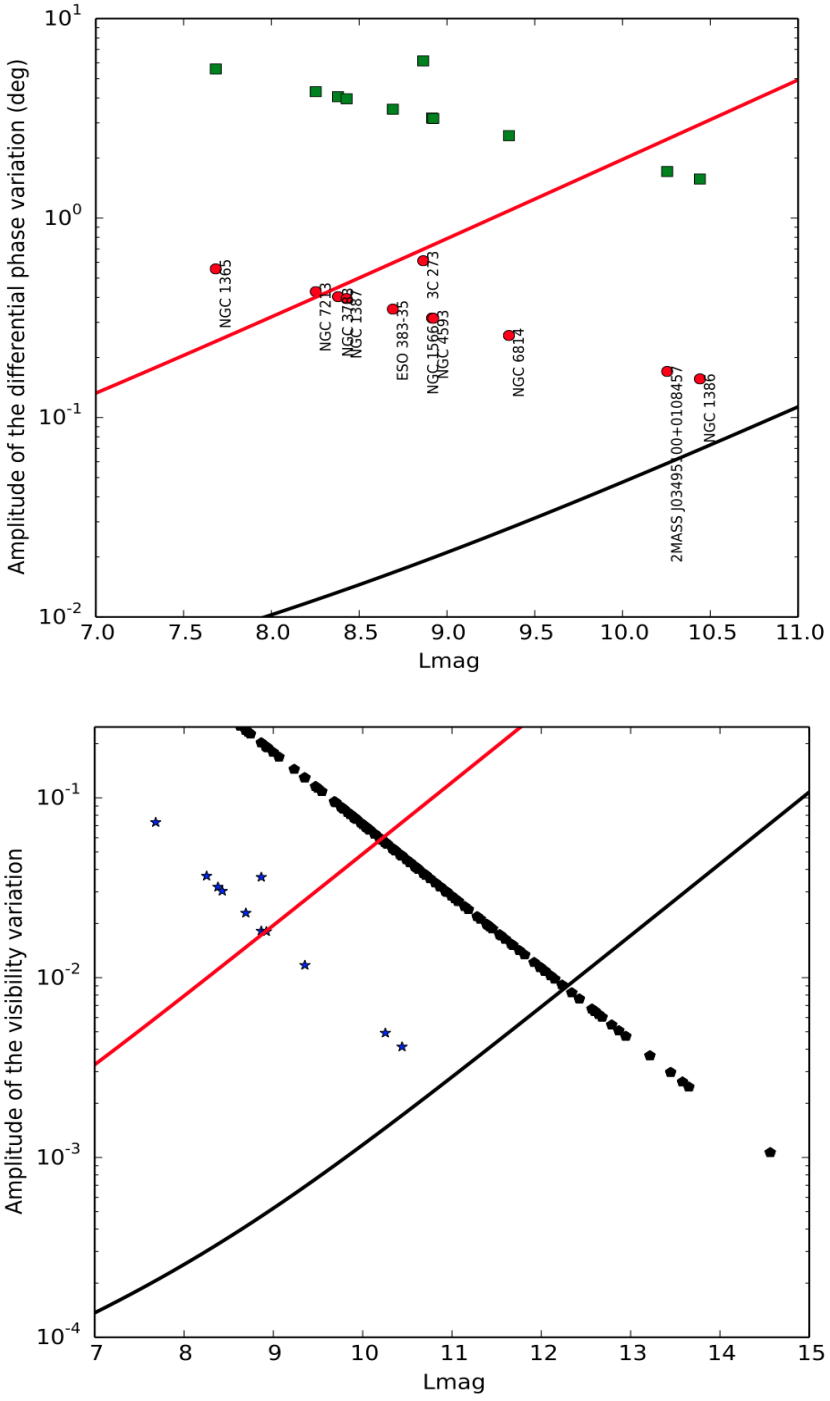

FIGURE 6.3: Feasibility of observation of BLR with MATISSE. The points represent the same things as in figure 6.2. The solid lines represent differential phase accuracy (upper panel) and differential visibility accuracy (lower panel) as a function of L magnitude for MATISSE without FT (red) and with FT (black).

6.4.3 Feasibility of observation

6.4.3.1 K band observation

Figure 6.2 summarizes the feasibility of observation of BLRs with current, upcoming, and possible VLTI instruments. We found that AMBER+ would observe at most a few sources whereas GRAVITY will provide high quality differential measurements on 10 to 15 sources for which it would also give decisive absolute visibility measurement. On the other hand, OASIS would at least double the number of differential phase measurement (with respect to GRAVITY). Moreover, OASIS+ would again double this accessible number of targets then the OASIS number. A next generation FT would boost the GRAVITY list of targets. The ultimate VLTI performance would be obtained with the new generation FT and OASIS+. Remember that an instrument accessing more targets also gives much better results on the brighter targets. OASIS+FT would allow to access targets with four decades of luminosity range, critical for an unification model based on key parameters with luminosity.

6.4.3.2 L band observation

In figure 6.3, we plotted differential phase (upper panel) and visibility variation (lower panel) as a function of L band magnitude for MATISSE without (red) or with (black) external FT. Each point represents one Sy1 AGN, labeled by name, which has an emission line in L band, and limited to the $K = 10.5$, so that they can also be observed using GRAVITY as FT. Although it will be possible to estimate differential visibility (blue star) only for few objects, absolute visibility can be estimated for many objects up to $L = 15$ using MATISSE. We see that for a few objects, which have redshift such that the best line is in the L band, MATISSE can observe emission lines. This will specially help to compare the emission line sizes at different wavelengths to constrain the geometry of the BLR and dust. Note that MATISSE is mandatory to constrain the equivalent dust torus sizes (i.e. the absolute visibilities in the continuum) necessary to properly calibrate the emission lines differential measures. Measuring L band interferometric size combined with L band reverberation mapping will allow to measure distances using "Dust parallax" (Hönig et al., 2014) as discussed in chapter 7.

6.4.3.3 Visible observation

The first goal of an OI operating in the visible would be to obtain BLR actual image thanks to the higher spatial resolution. However, even for the largest known BLR such an image requires a full resolution of at least 0.1 mas and this implies multi-kilometric baselines (1.5 km at 0.7 μm) that are not available at any current interferometer with large aperture. Thus, we should use the improved angular resolution and much stronger emission lines in the visible to perform the kind of differential observations discussed in this thesis, but possibly with much better accuracy.

Hence, we studied the feasibility of BLR observations in the visible mode at the VLTI. We considered both UTs and ATs. The parameters are listed in table 6.1. We calculated SNR with V magnitude for UTs and ATs as shown in figure 6.4. SNR obtained with UTs of Strehl ratio 0.1 and $N_{\rm EXP} = 50$ (1 sec observation) is shown by green line. This shows that with UTs we can reach up to $V = 15$ if we have adaptive optics (AO) providing a Strehl ratio of 0.1 in the visible which is challenging but feasible. The red curve represents the SNR obtained with ATs of Strehl ratio 0.5 with $N_{\rm EXP} = 3500$ (70 seconds observation), while the blue curve is obtained with $N_{\rm EXP} = 500$ (10 seconds observation). ATs with Strehl ratio 0.5 will be helpful but quite long exposures are needed to reach up to $V = 15$ with SNR > 3. Such Strehl ratio at 0.7 μm on a 1.8 m telescope is quiet feasible, but will be out of reach of the currently planned AO for the ATs.

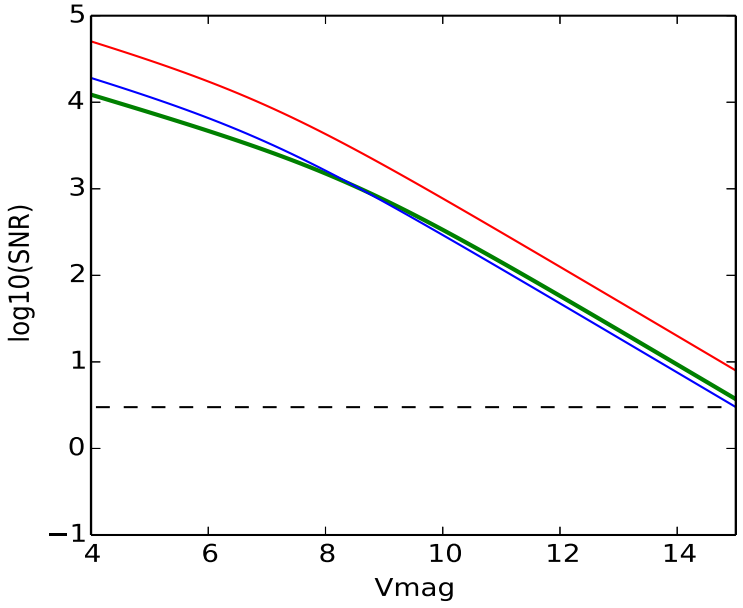

FIGURE 6.4: Plot of log10(SNR) as a function of V magnitude. SNR for UTs with Strehl ratio 0.1 with $N_{\rm EXP} = 50$ (1 second observation; green curve), and ATs with Strehl ratio 0.5 with $N_{\rm EXP} = 3500$ (70 seconds observation; red curve), and with $N_{\rm EXP} = 500$ (10 seconds observation; blue curve) for $t_{\rm DIT} = 0.02$ are shown. The dotted black line shows the fringe detection limit of SNR=3.

Differential phase (up) and visibility accuracy (down) are plotted as a function of V magnitude in figure 6.5. In this case, we considered 2 hours of observation i.e. 360000 exposures with UTs (green) and ATs (blue). Each individual source represents Sy1 target observable from Paranal as described in section 6.4.2 and used in section 6.4.3.1. However, in this case we considered that Hα lines can be detected for all the sources. Since Hα line is up to 10 times brighter than Paα (see Landt et al., 2008), we gain in flux, and as a result, we see that differential phase can be measured for all the 134 objects up to $V = 15$ with UTs in visible, while ATs can also provide access to objects up to $V = 14$. It could be possible to estimate differential visibility as well as absolute visibility for a few objects using UTs or ATs. Having both differential visibility and phase, it will be possible

to fully constrain BLR models. Differential phase alone will be also helpful to constrain the kinematics of the BLR and hence could be used to estimate angular diameter distance using parallax with a much better accuracy than in the K band as the gain in differential phase accuracy is of the order of 190 if $K = V$ and of the order of 60 if $K - V = 2.5$.

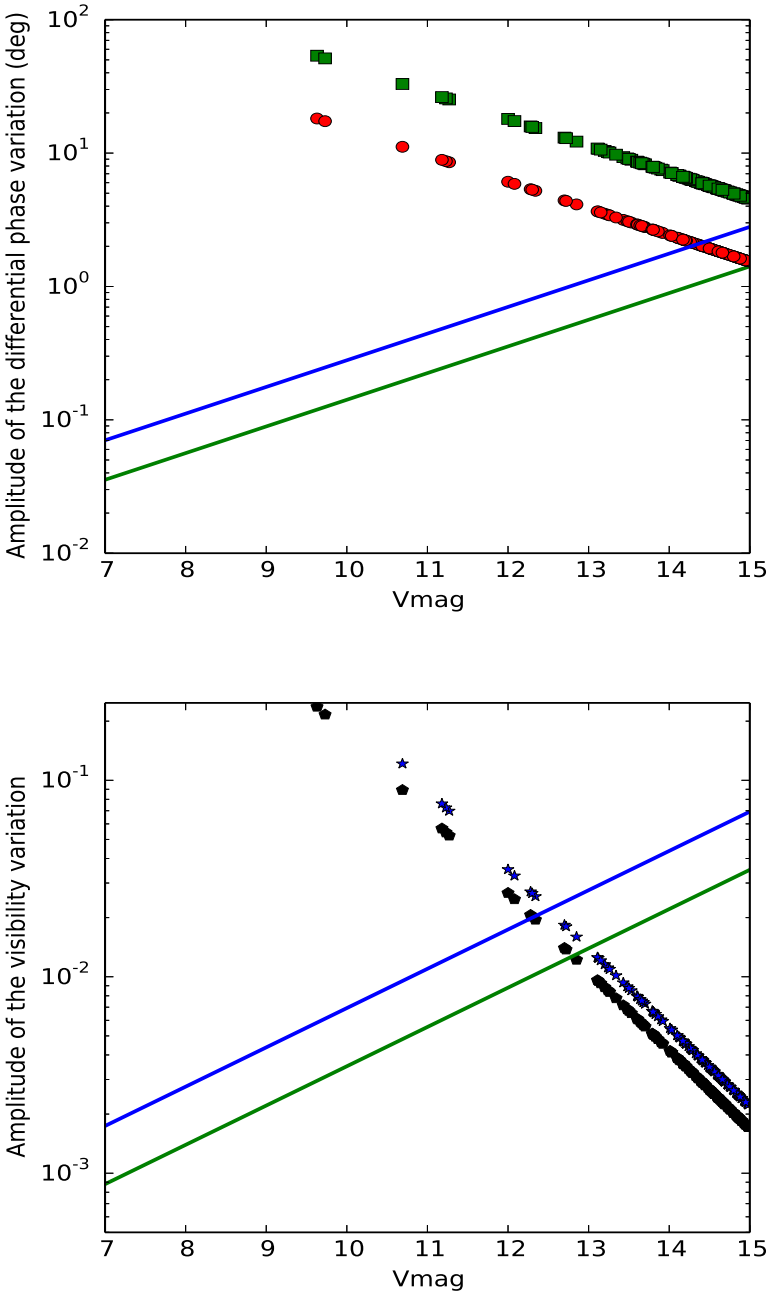

FIGURE 6.5: Feasibility of BLR observation with a visible mode of VLTI (considering Hα line). The solid curves represent differential phase (up) and differential visibility (down) for a visible mode with UTs (green) and ATs (blue) corresponding to figure 6.4. Rest of the symbols are as noted in figure 6.2.

6.5 conclusion

To evaluate the potential of OI to observe BLR of quasars with the current and near future VLTI instruments, we have computed the expected accuracy for absolute visibility, differential visibility and phase with current (AMBER+), near future (GRAVITY) and possible (OASIS, OASIS+ and OASIS+FT) VLTI instruments. This SNR analysis has been checked on our real 3C273 data from AMBER+ and the values for the other instruments are deduced from elementary cross-multiplications based on the known changes in detector noise, number of measures, transmission and exposure time of the new instruments. We have considered the possible SNR for all QSOs and Seyfert 1 observable at Paranal brighter than $K = 15$ that is the potential limit for VLTI observations with OASIS+.

Even if all these BLRs remain unresolved with the VLTI in the K-band, we see that measures are possible on many targets. GRAVITY, limited by its internal FT at $K = 10.5$, will give a full data set on half a dozen sources. For about fifteen sources it will have only absolute visibility and differential phase that still allows to fit all parameters. OASIS will allow a small increase in the number of targets while OASIS+ will reach more than 50 targets. A FT working fainter than $K = 10.5$ would allow a major breakthrough by extending the number of GRAVITY targets to about 30 and of OASIS+ targets to more than 50, if it can be operated up to $K = 13$, which seems well within the reach of the currently proposed designs (Petrov et al., 2014; Meisner et al., 2012). As the main contribution of OI will come from differential measures, study of the innermost part of the torus that can constrain the continuum measures in K-band, will be performed in L-band by the VLTI second generation instrument MATISSE (Lopez et al., 2012) that can also do some BLR observations in lines in the L-band.

A visible mode of VLTI can access more than 130 targets up to $V = 15$ providing differential phase signature, helpful to constrain BLR kinematics and to obtain more accurate BLR parallax measures. This could also provide differential visibility measurements for few targets, which is along with differential phase, could provide strong constrain on the BLR models. This indeed will help to calibrate the RM $R - L$ and $M - L$ relations obtained using Hβ lines. Combining RM data with interferometric measurements, parallax distances could be measured for many objects.

Such a large sample of targets would allow a general unification of BLR model by studying for example the key parameters such as the projection factor f, the BLR thickness ω, the local velocity field parameter σ_0 or the ratio of rotation and inflow as a function of the luminosity (see chapter 4). The VLTI, with its full potential, could allow exploring four to five decades of luminosity range. Full imaging of BLRs requires the improvement of the angular resolution by a factor of at least ten that requires a major breakthrough on sensitivity of OI in the visible, on CHARA for example, or the construction of a new interferometer with much larger baselines (such as recently proposed Planet Formation Imager in near/mid-IR, Monnier et al., 2014). These are long term goals, while differential interferometry of quasars with the VLTI has already started, will substantially expand very soon

with GRAVITY and can reach its full potential with a new generation FT and a specialized light instrument like OASIS+ in less than 5 years.

Chapter 7

Distance measurement using BLR parallax

Contents

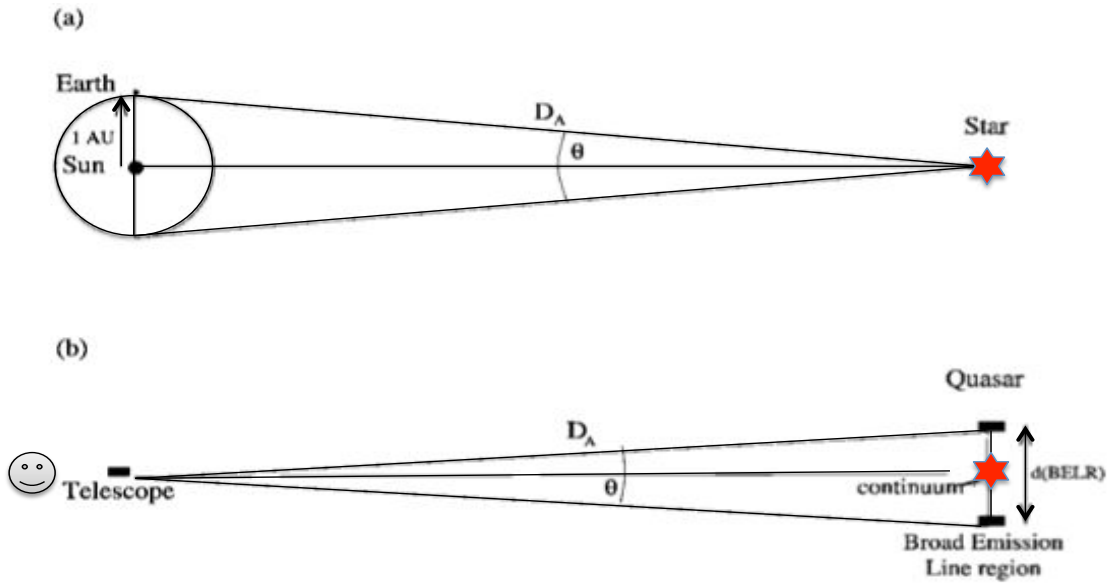

FIGURE 7.1: Measuring geometrical distance. a) Parallax distance to a star and b) Distance to a quasar using Broad line region. Image from Elvis and Karovska (2002).

7.1 Introduction

One of the fundamental challenges in modern astronomy remains the distance measurement of astronomical objects. It can constrain the time evolution of the cosmic scale factor that represents relative expansion of the universe. One hypothesis is that although the universe contains a significant amount of ordinary matter (Ω_m), which de-accelerates the universe, a significant amount of possible energy in the vacuum (Ω_Λ), known as Einstein "cosmological constant", would accelerate the universe putting a negative pressure (Carroll et al., 1992). Distance measurement using Type-I supernova led to the remarkable discovery of acceleration of the universe having a non-zero cosmological constant, and the dark energy (Riess et al., 1998; Perlmutter et al., 1999). Type-I supernovae are extensively used to estimate distances, however they are limited to $z \sim 1.7$ (Riess et al., 2001), beyond which an alternative technique is needed to estimate reliable distances. This is crucial in order to constrain cosmological model and the nature of dark energy.

Quasars, a high luminous class of AGNs, can be easily found up to $z \sim 7$, offer a possibility to use them as standard "candles". Several methods were proposed to estimate distances such as using quasars BLR (Haas et al., 2011; Watson et al., 2011; Czerny et al., 2013), using well-established R-L relationship (Kaspi et al., 2000; Bentz et al., 2013) as well as using hot dust emission (Kobayashi et al., 1998; Oknyanskij, 1999; Yoshii et al.; Hönig, 2014). A simple and model independent method using parallax was proposed for both the BLR (Elvis and Karovska, 2002) and the dust (Hönig et al., 2014). This method as proposed by Elvis and Karovska (2002) involves a combination of RM variability study of the BLR or of the dust to estimate a linear size, $\mu(\mathrm{ld}) = c\tau(\mathrm{days})$ with interferometric observation to measure equivalent angular size, $\rho(\mathrm{mas})$ (figure 7.1). The angular distance can be written as

$$D_A(\mathrm{Mpc}) = 0.173 \times \frac{\tau(\mathrm{days})}{\rho(\mathrm{mas})(1+z)} \tag{7.1}$$

where z is the redshift and the factor 0.173 is just a geometrical conversion factor. Note that Eq.7.1 assumes both ρ and μ refer to the same physical size, however both the sizes depend on geometry of the object and weighting on different measurements.

Recently Hönig et al. (2014) applied this method to the dust, thereafter, "dust parallax", in which they used dust photometric RM to measure linear size of the inner-rim dust torus, and interferometry to measure the equivalent angular size. Using dust parallax, they estimated angular distance to NGC 4151 with an accuracy of 13.5 % showing the capability of simple parallax method using AGNs to estimate distances. Hönig et al. (2014) also showed that the different parameters in the model multiply both RM size μ and OI size ρ by the same factor. Both RM and OI observation of inner dust were performed successfully for a handful number of objects (Koshida et al., 2014; Kishimoto et al., 2011a), hence this method is very feasible. However the dust reverberation observation needs longer monitoring and especially costly for high luminous objects since dust inner radius is scaled with $L^{0.5}$. On the other hand, observing BLR with OI has been started when Petrov et al. (2012) successfully resolved the emission line of bright quasar 3C273

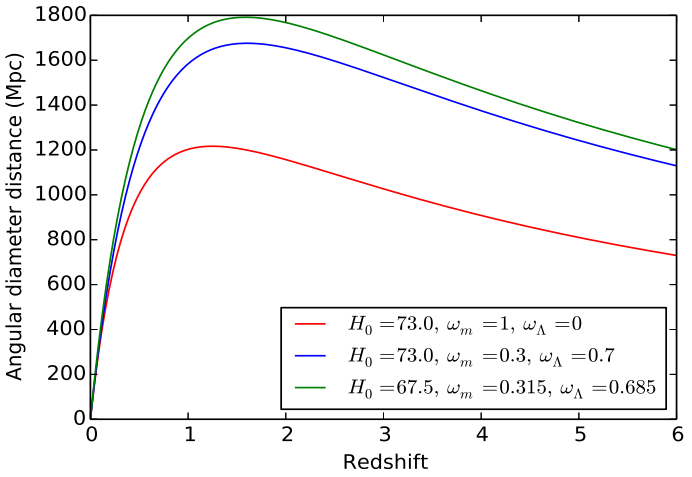

FIGURE 7.2: Angular distance vs redshift for various cosmologies: universe with no cosmology constant (red), with cosmological constant (blue), and with recent plank cosmology result (green). Here, Ω_m, Ω_Λ refer to matter and vacuum density respectively, and H_0 is the Hubble constant in the unit of km/s/Mpc.

for the first time, and as shown in chapter 6, OI could observe a large number of BLR with upcoming instruments. Thus, both the BLR and dust parallax seem to be a good distance measurement method. The variation of angular distance as a function of redshift is plotted in figure 7.2 for different cosmologies. Quasars could provide angular distances beyond redshift $z = 1.7$ allowing to constrain cosmological parameters and the distribution of dark energy.

Hence, in this chapter, we will use the quasar-parallax method on the BLR to estimate the accuracy on the angular distances using both simulated RM and OI data. We will present simulations showing the feasibility of this method. Structure of this chapter is as follows. We described continuum modeling approach in section 7.2. An improved BLR model is presented in section 7.3. Test to estimate distances using parallax method from simulated RM and OI data is presented in section 7.4. Result of the simulations is discussed in section 7.5 with a conclusion and future perspective in section 7.6.

7.2 Modeling continuum light curve

We adopt the approach of Kelly et al. (2009) to model the continuum light curve, which is a damped random walk model (Zu et al., 2011; Kelly et al., 2009; MacLeod et al., 2010). The model is a white noise process with two parameters; an amplitude of variability parameter (σ_d) and a variability time scale parameter (τ_d) that decreases exponentially. It was shown that the damped random walk (DRW) model can properly represent the variability of quasars continuum light curve. We generated the light curve from the following equations (for more detail, see Kelly et al., 2009)

$$x_i = \mathrm{A}x_{i-1} + \epsilon_i, \tag{7.2}$$

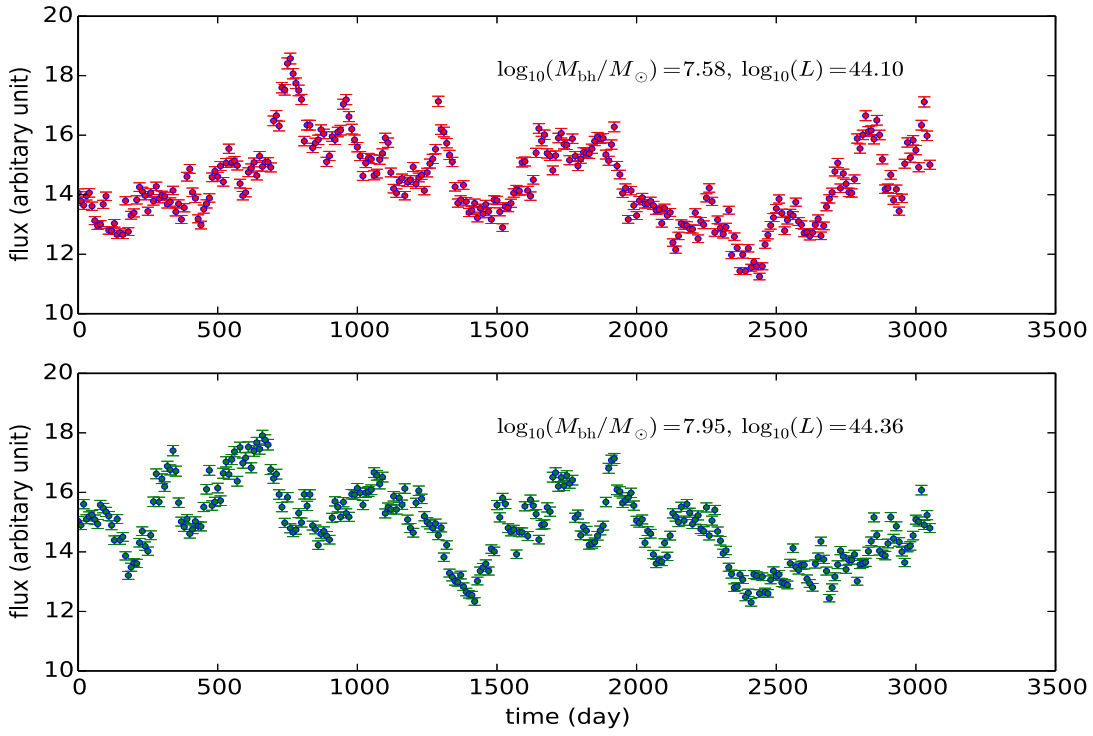

FIGURE 7.3: Continuum light curves for two different BH masses and luminosities.

where ϵ_i is a normally distributed random variable with zero mean and variance s^2, and the data x_i are observed at regular time interval. The variance can be written as

$$s^2 = \frac{\tau_d \sigma_d^2}{2}\left(1 - \mathrm{e}^{-\frac{2\Delta t}{\tau_d}}\right) \tag{7.3}$$

and $\mathrm{A} = \mathrm{e}^{-\Delta t/\tau_d}$, is usually constrained as $|\mathrm{A}| < 1$ in order to ensure stationarity; a time series is said to be stationary when its mean and covariance do not vary with time. The case $\mathrm{A} = 1$ corresponds to a random walk.

Thus, we have two parameters in this model, the relaxation time or damping time scale, τ_d, that can be interpreted as the time required for the time series to become roughly uncorrelated, and σ_d describing the variability of the time series on timescales short compared to τ_d. Kelly et al. (2009) suggested that τ_d can be associated to a characteristic timescale, such as the time required to smooth out local accretion rate perturbations. On the other hand, σ_d represents the variability resulting from local random deviations in the accretion disk structure, such as caused by turbulence and other random magneto-hydrodynamic effects. Interestingly, Kelly et al. (2009) and Li et al. (2013) found that σ_d and τ_d are related to some of the key parameters of the AGN, such as $M_{\rm bh}$, L, λ_e etc. According to Kelly et al. (2009)

$$\begin{aligned}\log \sigma_d^2 = (-3.83 \pm 0.17) - (0.09 \pm 0.19) \log \left(\frac{\lambda L_\lambda}{10^{45} \mathrm{ergs}^{-1}}\right) \\ - (-0.25 \pm 0.24) \log \left(\frac{M_{\rm bh}}{10^8 M_\odot}\right) [R\,\mathrm{mag}^2 \mathrm{day}^{-1}],\end{aligned} \tag{7.4}$$

and

$$\tau_d \quad = \quad (80.4^{+66.9}_{-35.8}) \left(\frac{\lambda L_\lambda}{10^{45} \mathrm{ergs}^{-1}} \right)^{-0.42 \pm 0.28} \quad \times \quad \left(\frac{M_{\mathrm{bh}}}{10^8 M_\odot} \right)^{1.03 \pm 0.38} \quad [\mathrm{days}]. \quad (7.5)$$

These relations indicate the importance of the accurate mass estimates discussed in chapter 4 and others. Figure 7.3 shows continuum light curve created with different central black hole masses and luminosities. It is assumed that light curves are observed once every 10 days over a duration of more than 8 years and have the uncertainty of 1% of the flux value. Note that, the variability is stochastic, it can not be repeated.

Once we have a continuum light curve, we just need to have a model response function of the BLR to obtain line light curve. The response function as well as all interferometric data can be simulated from a given geometrical and kinematical model.

7.3 Geometrical and kinematical model of BLR

In order to simulate both OI and RM data, we need to have a geometrical and kinematical model that self-consistently estimate all the observables. In chapter 4, we have described a 3D geometrical and kinematical model, which calculates all interferometric observables as well as reverberation mapping response function and line profile. Once we get emission line response function $\Psi(\tau)$ from our model (chapter 4), we can obtain emission line light curve by convolving a continuum light curve with it using Eq.2.7. Thus, we will have all the observables for a given model.

In this work, we have used the same model, described in chapter 4, except modifying the radial distribution of the clouds so that it can take any shape from very narrow Gaussian to a power law distribution, as used recently by Pancoast et al. (2014a,b) for modeling the RM data. The distribution is taken from a shifted gamma distribution whose probability density function is

$$P(x|\kappa, \theta) \sim x^{\kappa-1} \exp(-\frac{x}{\theta}), \quad (7.6)$$

where κ is the shape parameter and θ is the scale parameter of the distribution. After the change of variables, we represent the distribution considering three parameters; the mean radius μ (refers to linear size of the BLR), the shape parameter of the shifted gamma distribution β and a parameter F that is the fraction of μ at which gamma distribution starts. The radial position of cloud is now taken randomly from

$$r = R_s + \mu F + \mu \beta^2 (1 - F) \times \Gamma(\beta^{-2}, 1), \quad (7.7)$$

where $R_s = 2GM_{\mathrm{bh}}/c^2$ is the Schwarzschild radius of the central BH of mass M_{bh} providing the hard limit on the radius, and $\Gamma(\beta^{-2}, 1)$ is the gamma distribution with scale 1. The width of the BLR can be written as $\sigma_r = \mu\beta(1 - F)$. Radial distributions obtained from different set of parameters (μ, β, F) are shown in figure 7.4.

TABLE 7.1: Simulated data: Input parameters of the model

set	redshit	D_A	$L\,(\mathrm{ergs}^{-1})$	$\log_{10}(M_{\mathrm{bh}}/M_{\odot})$	μ (ld)	R_{rim} (mas)	$i(^{\circ})$	$\omega(^{\circ})$	noise and sampling
A	0.1324	467.0	45.05	8.45	244.5	0.28	39.3	22.2	1.0 %, 1.5%, 10 days[a]
B[b]	0.1324	467.0	45.05	8.45	244.5	0.28	39.3	22.2	0.5 %, 0.5%, 5 days
C	0.0887	328.5	44.38	8.28	98.5	0.18	30.7	20.9	0.5 %, 0.5%, 5 days

[a]The numbers represent flux uncertainty in continuum and emission line light curve, and observing night interval for reverberation mapping.
[b]Note that even with same continuum model parameters, continuum variability pattern is different than set A.

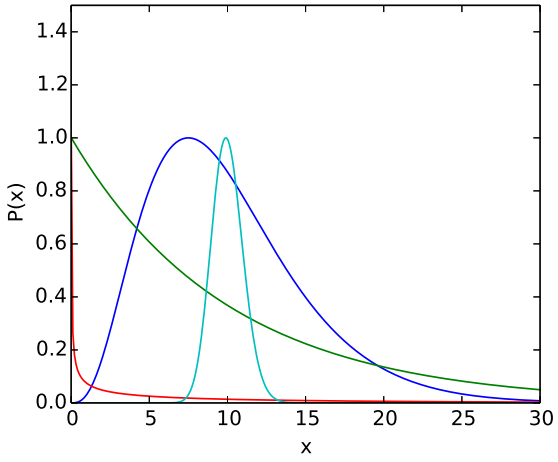

FIGURE 7.4: Probability distribution of shifted gamma function. Distributions are plotted for different values of shape parameter $\beta = 0.1$ (cyan), $\beta = 0.5$ (blue), $\beta = 1$ (green) and $\beta = 1.5$ (red) keeping $\mu = 10$ and $F = 0$ fixed.

After defining the radial distribution we built the rest of the model as already described in chapter 4, and we calculated all differential interferometric measures as well as RM measures for a given continuum light curve needed for angular distance measurement using Eq.7.1.

7.4 Simulation setup

In this chapter, our goal was to recover D_A and its uncertainty from simulated datasets. For this work, first mock RM (continuum and emission line light curves) and OI (spectrum, differential visibility and differential phase) datasets were created for few simulated objects, and then recovered those parameters by fitting the data sets.

7.4.1 Simulated datasets

We simulated data for objects, which were defined by their redshift (z), BH mass ($M_{\rm bh}$), luminosity (L), angular distance (D_A), BLR radial distribution parameters (μ, β and F), inner rim radius ($R_{\rm rim}$), inclination (i) and opening angle (ω). All the parameters were randomly picked up except β and F, which for simplicity were fixed at 0.5 and 0 respectively (represented by blue color in figure 7.4). We proceed as follows:

First, redshift of the object was picked up randomly from a $(1+z)^3$ distribution, where z lies between 0 to 0.2, considering local universe. BH mass was then taken randomly from $\log_{10}(M_{\rm bh}/M_\odot) = 6.5$ to 9.5, and an Eddington ratio was assigned, where $\log_{10}(\lambda_e)$ was taken from a Gaussian distribution of mean -1.5 and standard deviation 0.3. This allowed to calculate luminosity for a given mass and an Eddington ratio using $L(\text{ergs/s}) = M_{\rm bh}[M_\odot] \times 1.26 \times 10^{38} \times \lambda_e$ (Nobuta et al., 2012). Having luminosity and BH mass of the object, we created a continuum light curve as described in section 7.2.

To create mock RM emission light curves as well as interferometric data, mean radius of the BLR and the inner rim radius of torus were drawn from object luminosity following Bentz et al. (2013) and Kishimoto et al. (2011a,b) respectively. BLR radius was then scaled by a factor of 2 since near-IR emission line sizes at K-band could be larger than Hβ BLR size. Inclination (i) and opening angle (ω) were chosen randomly.

Since, our aim was to calculate the accuracy on the angular distance, we used an input angular distance D_A, calculated from redshift of the simulated object considering a standard cosmology with $H_0 = 73$ km/s/Mpc, $\Omega_m = 0.3$ and $\Omega_\Lambda = 0.7$. With this angular distance, we calculated angular size ($\rho \approx \mu/D_A$) of the BLR, using Eq.7.1 for the given linear size (μ), needed to create interferometric data. The main parameters that we used to simulate the data are shown in table 7.1. Here we are presenting only result of 3 simulations to see the feasibility of this method.

We created OI data for 4 baselines of length 80 m and 130 m with baseline orientation parallel and perpendicular to rotation axis. We added realistic noise in all datasets. We consider noise based on the upcoming interferometric instrument GRAVITY, i.e. uncertainty on differential phase $\sigma_{\phi_D} \simeq 0.002$ radian and differential visibility $\sigma_{V_D} = \sqrt{2} \times \sigma_{\phi_D}$ as discussed in chapter 4 as well as in Rakshit and Petrov (2014) and Rakshit et al. (2015). We considered a monitoring campaign of 8 years and line light curves starts 500 days after the first continuum monitoring. A long duration RM campaign was considered since our luminosity range is very wide, and size of the BLR scales as $L^{0.533}$. Hence to detect distinct peak in the cross-correlation function we need very long duration observation campaign, more than 3 times longer than the time-lag corresponding to the BLR size (see section 5.4).

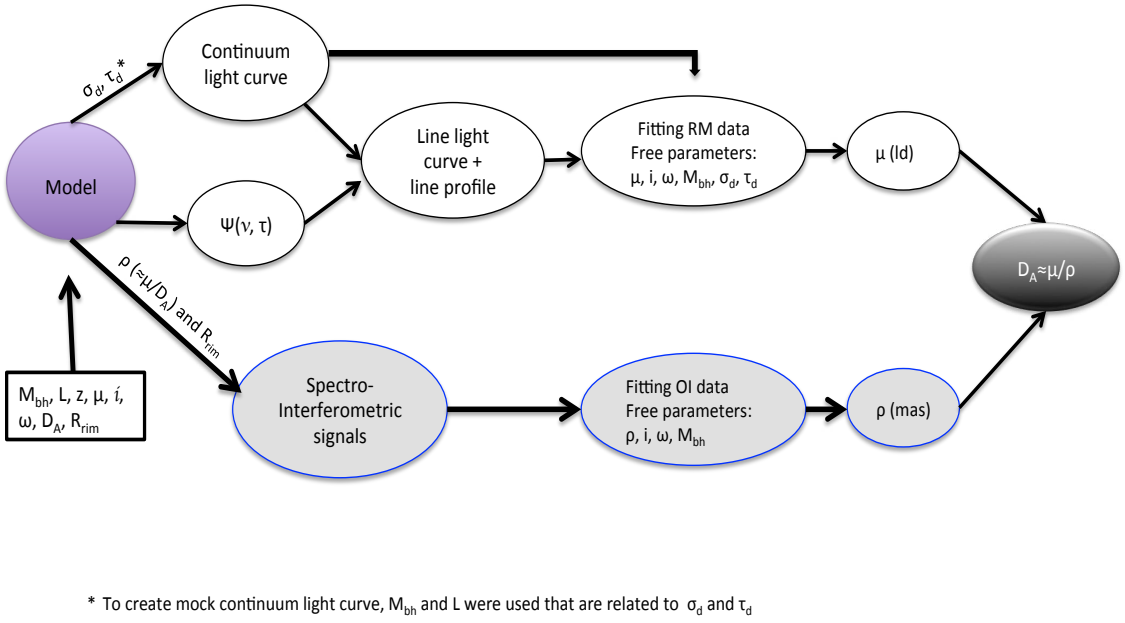

FIGURE 7.5: A graphical representation of the model to illustrate how the model process works. On one hand, it calculates first RM continuum light curve and BLR response function and then line light curve. Then we fit the model signals to the RM data and estimate parameters with its probability distribution. On the other hand, it calculates OI measurements and fits them to the OI data. During this fitting, we use the knowledge of the parameter-space from the probability distribution of the parameters estimated from RM data. Finally, using linear size calculated from RM fit, and angular size calculated from OI fit, distances are estimated.

7.4.2 Recovering model parameters

We used a Bayesian sampling algorithm and maximize the likelihood as described in chapter 4, where we wrote that the posterior probability distribution $p(\text{model}|\text{data})$ includes the prior function $p(\text{model})$ containing knowledge about the parameters:

$$p(\text{model}|\text{data}) \propto p(\text{model}) \times p(\text{data}|\text{model}). \tag{7.8}$$

For efficient sampling of the entire parameter space, we used EMCEE package, developed by Foreman-Mackey et al. (2013), which is a Python implementation of Affine Invariant Markov Chain Monte Carlo (MCMC) ensemble sampler by Goodman and Weare (2010) backed by Parallel Tempering (thereafter, PTMCMC), which allows to run N number of Markov chains at different temperatures (T) in parallel ensuring that Markov Chain is not being stuck in a local maximum and accelerate the process to converge to a globally optimized solution. Since, the parameter space is usually big and quite possible to have multiple modes, thus PTMCMC is a good option to find the global maximum. In PTMCMC, each parallel chain is sampled from a modified distribution $p(\text{model}|\text{data})^{\frac{1}{T}}$ depending on its temperature. For example, if N chains are used than n-th chain of temperature T_N is sampled from $p(\text{model}|\text{data})^{\frac{1}{T_n}}$. A sequence of temperatures, called the "temperature ladder", is formed with $T_1 < T_2 < ... < T_N$ corresponds to different

TABLE 7.2: Simulated data: Recovered parameters

set	μ (ld)	D_A (Mpc)	$\log_{10}(M_{\rm bh}/M_\odot)$	$i(^\circ)$	$\omega(^\circ)$
A	$212.5^{+40.0}_{-29.2}(244.5^a)$	$409.2^{+73.9}_{-65.3}(467.0)$	$8.29^{+0.25}_{-0.18}(8.45)$	$39.2^{+11.8}_{-10.8}(39.3)$	$24.9^{+10.8}_{-9.9}(22.2)$
B	$218.6^{+20.4}_{-18.8}(244.5)$	$416.0^{+62.8}_{-52.2}(467.0)$	$8.40^{+0.26}_{-0.27}(8.45)$	$41.2^{+10.7}_{-10.4}(39.3)$	$27.3^{+8.9}_{-10.4}(22.2)$
C	$87.7^{+12.1}_{-16.1}(98.5)$	$288.3^{+61.0}_{-58.8}(328.5)$	$8.31^{+0.38}_{-0.58}(8.28)$	$26.5^{+11.4}_{-9.12}(30.7)$	$25.0^{+12.8}_{-12.4}(20.9)$

[a]True input values are in the bracket.

chains $(1, 2...N)$. In PTMCMC, a parameter $\beta \equiv 1/T$ is used to set a temperature ladder (see Earl and Deem, 2005). Each chain exchange its result after some iterations and climb towards higher likelihood. For a chain at high temperature, known as "hot chain", the likelihood is flatter and broader, and more easily explore the parameter space, while a low temperature chain, known as "cold chain", which gives the optimized result, explores the peak of the likelihood by jumping between nodes found by the hotter chains. This process increases the convergence rate for multiple modes problem but computationally expensive since we need to run few MCMC chains in parallel.

We run the sampling for many iterations and look at the variation of width of the distribution as a function of iteration. We remove the "burn-in" steps, which are necessary to stabilize the parameters as already discussed in section 4.4.2, and took rest of the samples to calculate uncertainties on the fitted parameters.

The model fitting process is shown graphically in figure 7.5. It calculates OI and RM measurements and then used Bayesian model fitting approach to fit the data, and finally estimates the parameters and its uncertainties. The fitting is done in two steps:

A) We fit only RM data i.e. continuum and emission line light curves and emission line profile. In this case, we have a total of 6 free parameters, which include 4 BLR parameters i.e. μ, $M_{\rm bh}$, i and ω, and 2 continuum model parameters i.e. σ_d and τ_d. We assign uniform priors in log to μ and $M_{\rm bh}$ as they span few order in magnitude. Fitting of RM data allow us to recover linear size of the BLR with its uncertainty (in unit of light-days) along with rest of the parameters. Note that for continuum model we directly use σ_d and τ_d to fit instead of $M_{\rm bh}$ and L that were used only to create mock continuum data.

B) We fit OI data i.e. differential visibility and phase as well as emission line profile keeping four free parameters, ρ, $M_{\rm bh}$, i and ω. However, in this case, we assign priors on $M_{\rm bh}$, i and ω looking at the probability distribution of the parameters obtained from RM data fitting. We also assign uniform prior in log for angular size since it spans few order in magnitude. Fitting of OI data thus allows us to obtain angular size (in mas) as well as other parameters.

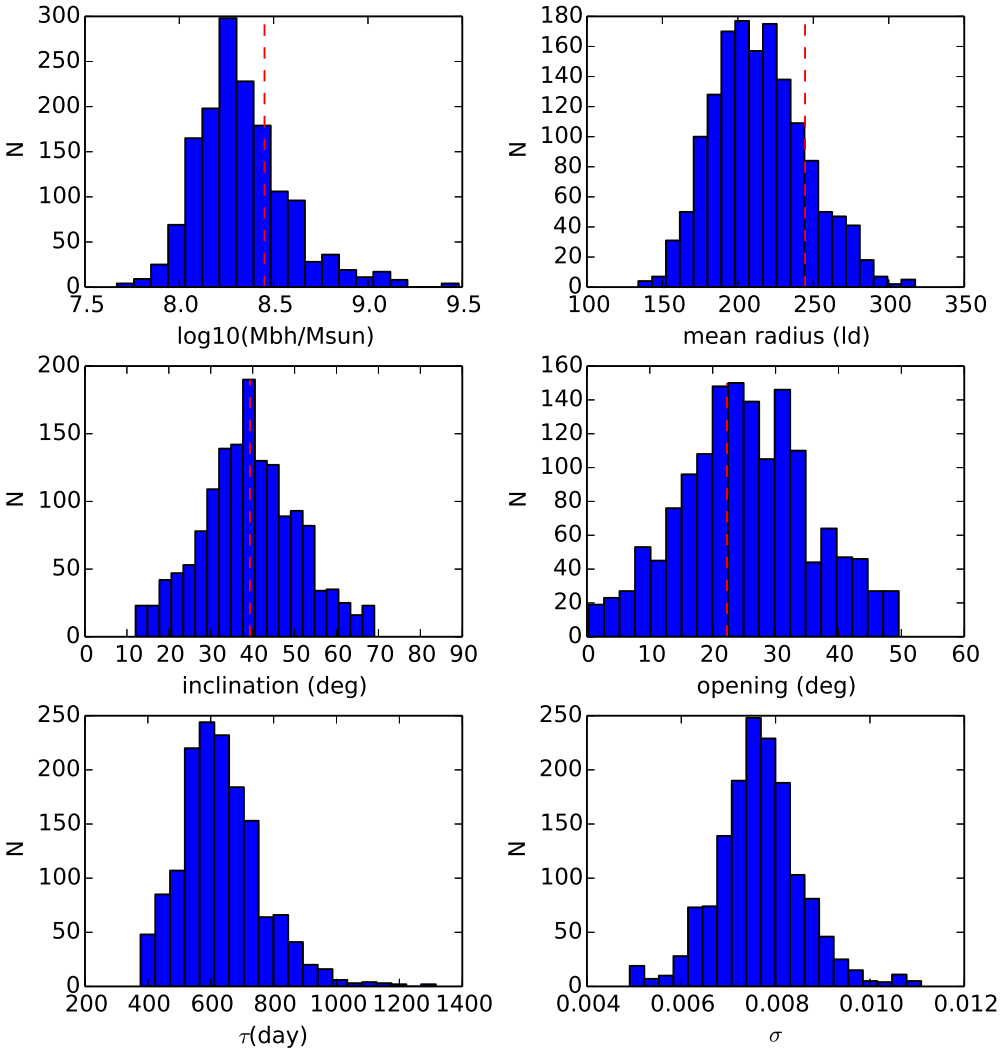

FIGURE 7.6: Probability distribution of model parameters obtained from fitting the RM data for data set A. The red dotted line shows the true input value used to create mock data.

7.5 Result and discussion

Figure 7.6 shows the probability distribution of different parameters with its mean value (red dotted line) recovered from dataset A. The recovered parameters and their 1 σ uncertainties are $\mu(\mathrm{ld}) = 212.5^{+40.0}_{-29.2}$, $\log_{10}(M_{\mathrm{bh}}/M_{\odot}) = 8.29^{+0.25}_{-0.18}$, $i = 39.2^{+11.8}_{-10.8}$ degree and $\omega = 24.9^{+10.8}_{-9.9}$ degree (see Table 7.2). For each dataset, the output parameters are recovered within 1 σ uncertainty. We see that with better sampling and lower noise in the light curves, μ is recovered with lower uncertainty compare to dataset A. Figure 7.7 shows the fit of the model to the RM continuum (top) and emission line (middle) light curves as well as emission line profile (bottom) using best fit model parameters for dataset A. The fits are indeed good.

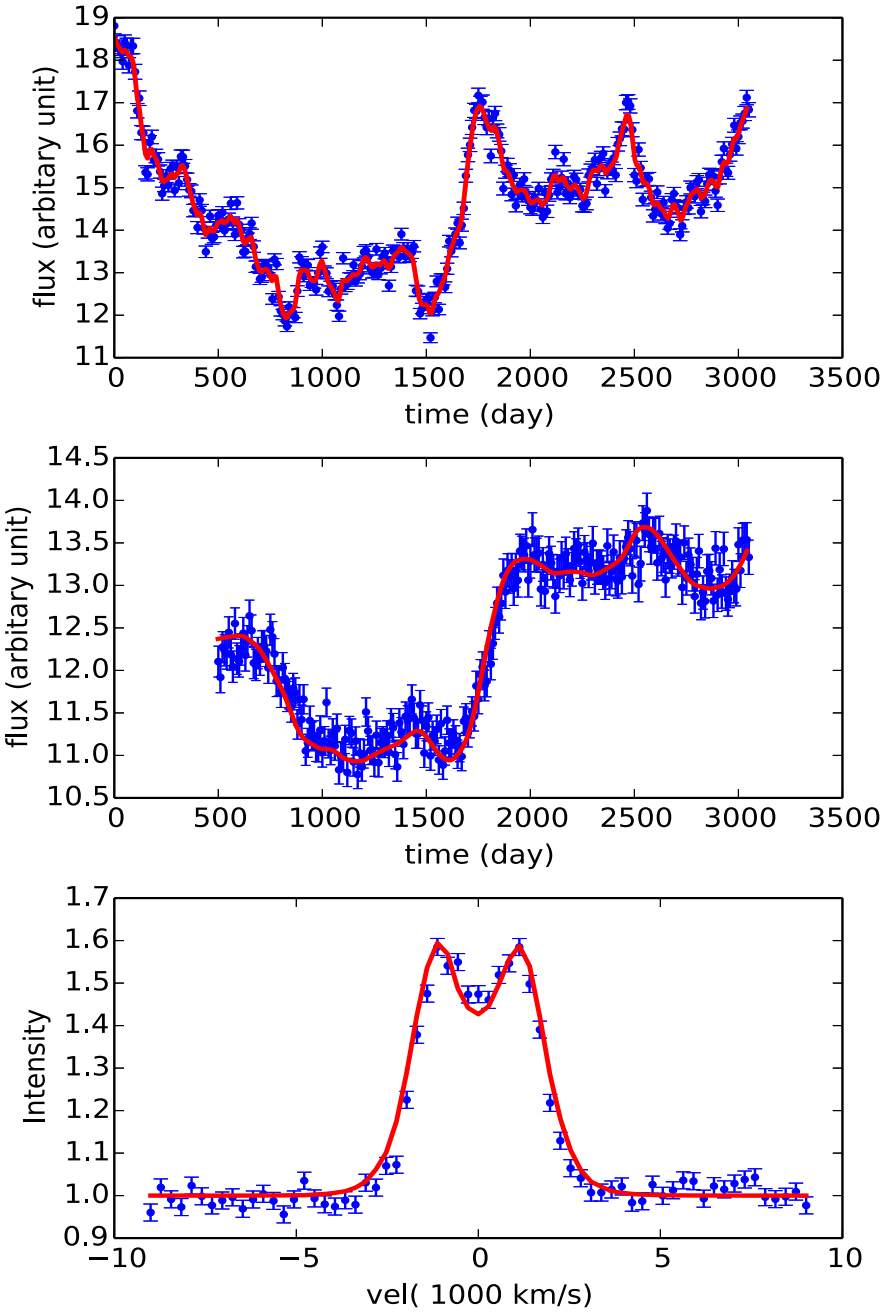

FIGURE 7.7: Fit of the RM data with the best fit parameters for dataset A. From top to bottom, the panels are continuum light curve, emission line light curve and spectrum. The blue points with errorbars are the data whereas the solid-red line represents the best fit model.

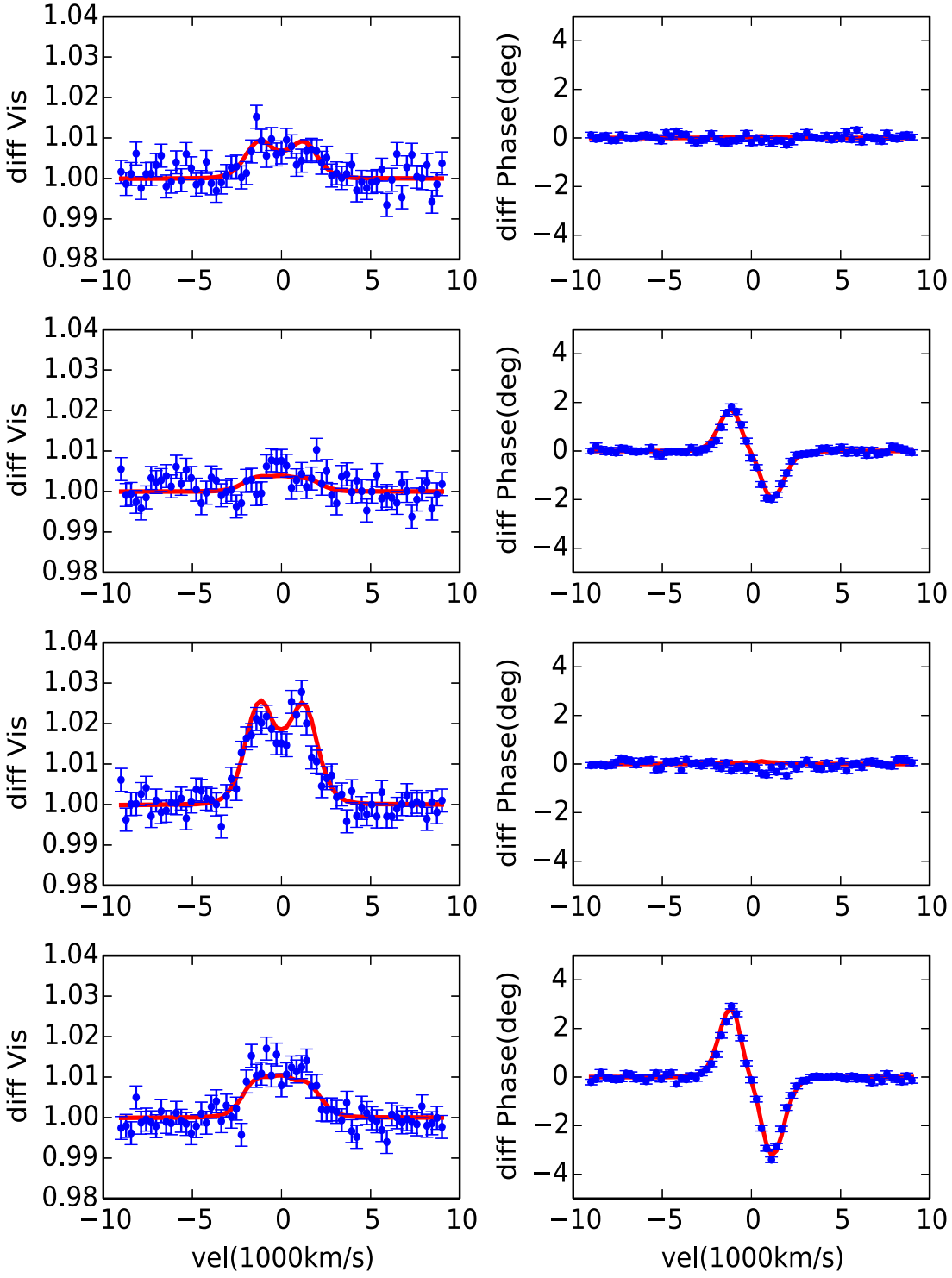

FIGURE 7.8: Fit of OI data with the best fit parameters for dataset A. Differential visibility (left) and differential phase (right) are plotted for four different baselines. From top to bottom: 80 m in parallel (first) and perpendicular (second) baselines, and 130 m in parallel (third) and perpendicular (fourth) baselines. The blue points with error bars are the data whereas the solid-red line represents the best fit model.

The accuracy on the parameters can further be improved with high quality data, which were obtained from recent high quality RM campaign aiming to constrain BLR geometry and kinematics (Bentz et al., 2010a; Barth et al., 2015). Some of these recent campaigns successfully provided 2D velocity-delay diagrams of few BLRs and thus enabled to constrain the BLR geometry and kinematics (e.g. Grier et al., 2013). Using direct model fitting approach to these highly sampled data, several authors have been successfully constrained many BLR model parameters with good accuracy (Brewer et al., 2011; Pancoast et al., 2012, 2014a). However, these campaigns are very selective to low-luminous object whose time delay is less than a month. Thus, with full spectral data, the parameters including the time delay, which is the most important for distance measurement, could be constrained with higher accuracy.

Model fitting of the OI data for dataset A is shown in figure 7.8 where we showed the fitting of differential visibility (left) and phase (right) with the best fit parameters for four different baselines: 80 m in parallel (first panel), and perpendicular (second panel), and 130 m in parallel (third panel) and perpendicular (fourth panel) baselines. The recovered angular size from the probability distribution of the samples is $\rho(\mathrm{mas}) = 0.090^{+0.007}_{-0.008}$. In all cases, the fitting is good. Note that when baselines are parallel to the rotation axis, we do not have any phase signature, however a strong "W" shaped visibility signature appeared at the top of the continuum (1st and 3rd panel) since the disk is relatively thin ($\omega = 22.2°$) and has relatively high inclination angle ($i = 39.3°$). This has already been discussed in chapter 4. The baselines perpendicular to the rotation axis (2nd and 4th panel) show "S" shaped differential phase profile as also shown in figure 4.9. This strong differential phase signature helped significantly to constrain the geometry as in all the baselines, expect the 3rd one, differential visibility has no strong signature to constrain the model parameters. Thus, differential phase or photocenter displacement is very much needed to constrain the BLR geometry and kinematics.

We showed a 2D scatter plot of linear size vs angular size in the upper-left panel of figure 7.9 with a cut of angular size in upper-right panel as obtained from the fits of OI data and a cut of linear size in lower-left panel as obtained from the fits of RM data. These histograms via Eq.7.1 give an angular distance measurement of $409.2^{+73.9}_{-65.3}$ Mpc with uncertainty about 16%. Although the mean of the histograms is far from the input value, it is within 1 σ uncertainty of the input D_A. This uncertainty is due to the week constraint on the μ from RM data. The parameters space with $M_{\rm bh}$, i, ω is highly degenerate. As can be seen in the left panel of figure 7.10, μ is constrained better with increased sampling rate and less noisy data. However, due to uncertainty on the OI data, we gain not much in distance accuracy (see Table 7.2). Note that since we fit a single-epoch spectrum instead of full spectral data, we are affected by the degeneracy of the parameters. However, this degeneracy could be removed up to some extent and the uncertainty on the recovered parameters from the RM data could be decreased by simultaneously fitting spectrum of each epoch observed during RM monitoring as shown in Pancoast et al. (2014a,b). This will provide better estimation of $M_{\rm bh}$, i, ω and hence better measurement of ρ from spectro-interferometric data. Thus, we could measure both the linear and angular sizes with less uncertainty. This will allow to gain the distance accuracy, which we would like to check in future.

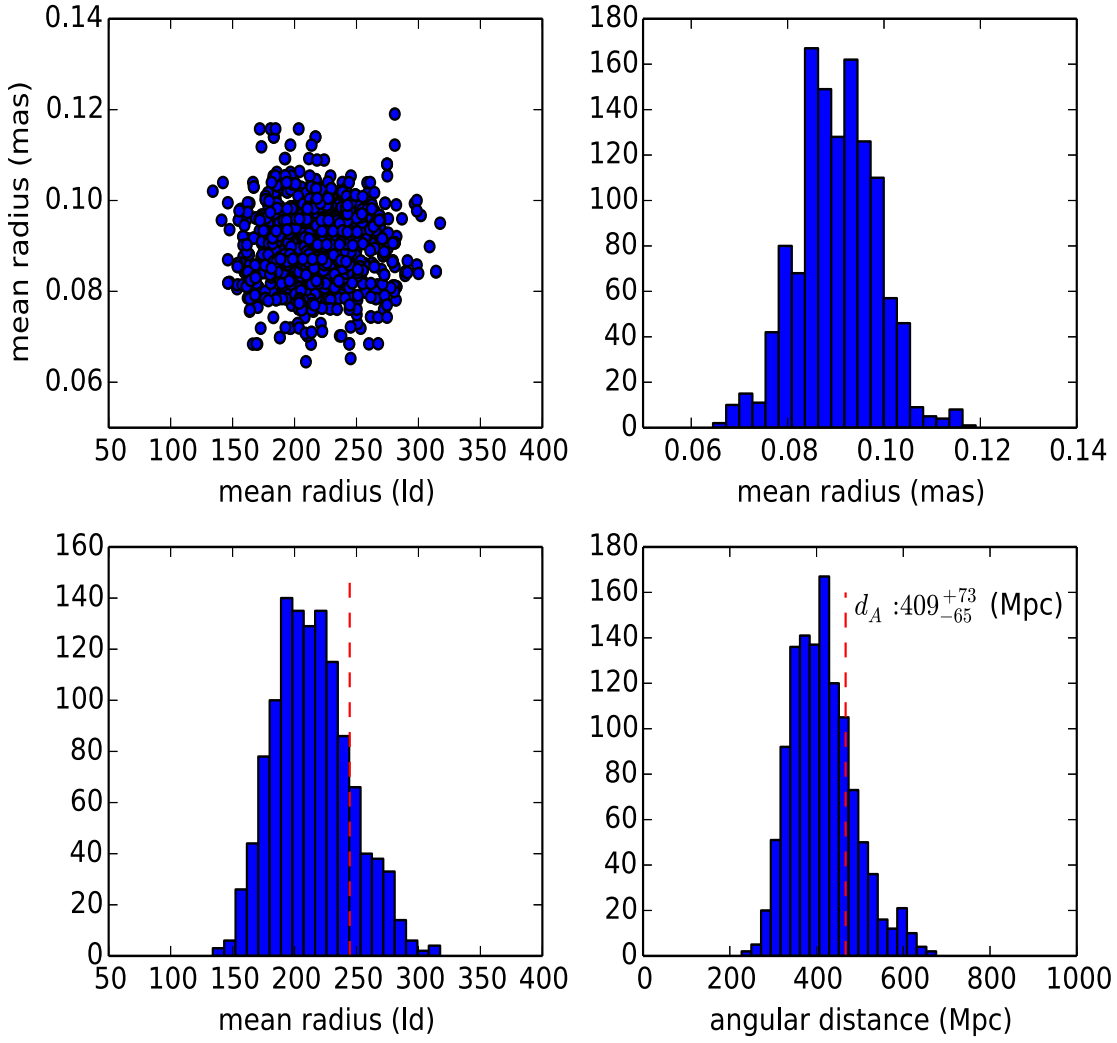

FIGURE 7.9: Angular distance from dataset A. Figure shows a scatter plot of linear size vs angular size of the BLR (upper-left), probability distribution of ρ (upper-right), μ (lower-left) and D_A (lower-right). The dotted red line in all the panels shows the true input parameter value.

Note that BLR parallax method will work only if we observe same emission line with RM and OI. Presently, there is no IR RM observation is available in the emission line, and interferometric observations are limited only to near- and mid-IR. Thus, it would be necessary to start near-IR RM campaign and for this, Paα and Paβ seem to be the best candidates as they are strong lines and unblended. Moreover, near-IR lines have some advantages compare to visible such as less dust extinction and weak host galaxy contamination (Landt et al., 2008, 2013). Hence, it would be desirable to observe at least few AGNs BLR in near-IR to find the time lag ratio between Paα and Paβ to Hβ. Photo-ionization calculations using "CLOUDY" code suggest that this lag ratio strongly depends on the geometry and can be larger than Hβ by a factor of 2 (see for example Goad, 1995). If VLTI observations with GRAVITY and MATISSE allow to constrain geometrical parameters as a function of luminosity, then CLOUDY could easily predict time lag ratios for different emission lines. Having that for few AGNs, we would use visible RM observation multiplying the lag ratio with near-IR interferometric observation.

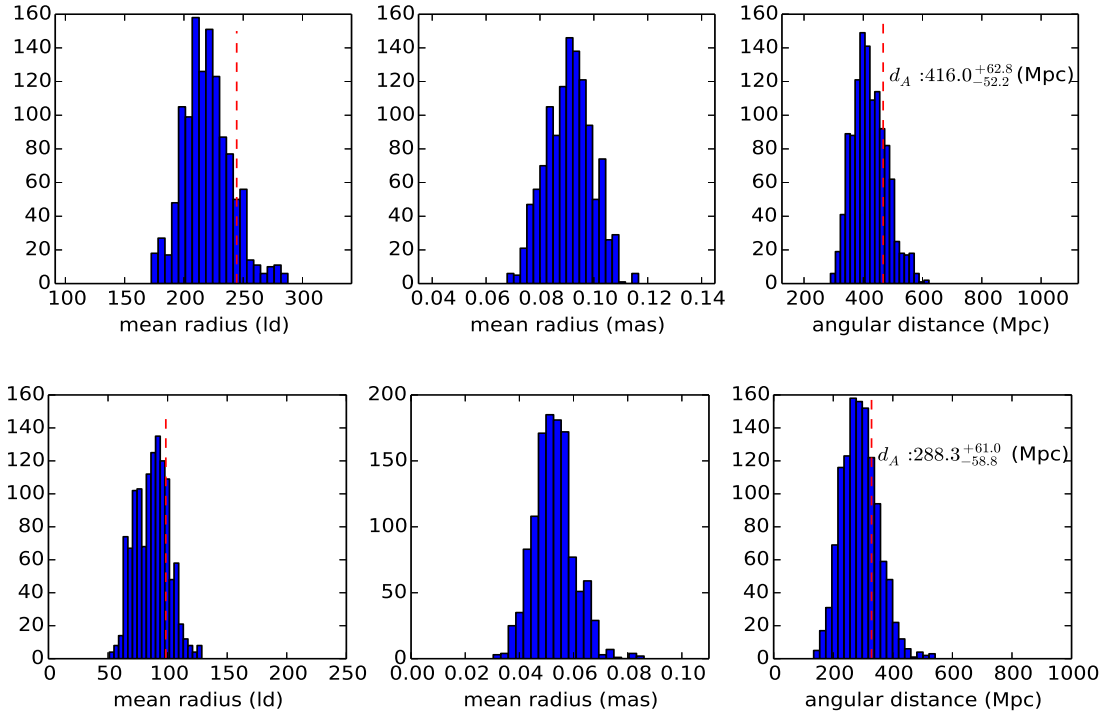

FIGURE 7.10: Probability distribution of μ (left), ρ (middle), and D_A (right) for datasets B (upper) and C (lower). The dotted red line in all the panels shows the true input parameter value.

On the other hand, since OI is limited to the near-IR, a visible/UV extension will allow to use this parallax method directly to use visible RM data (see discussion in chapter 6).

Another point is to determine which line is best for this technique to work on. A detailed discussion can be found in Elvis and Karovska (2002) about it. The size of the BLR increases with luminosity and it also increases with redshift. At a given redshift, high luminous objects are easier to resolve by OI and thus better target for interferometric observation, but problematic for RM observation as it needs long duration observation campaign. The line center also shifts with redshift as $(1+z)$, which means lines with shorter wavelength are better for RM. Few attempts have been made to find the BLR size of few high luminous and intermediate redshift ($z = 2.2 - 3.2$) objects observing CIV emission line variability in RM campaign (Kaspi et al., 2007; Trevese et al., 2014), which can be applied for many objects. Shorter wavelengths are better also for OI due to increase in the angular resolution (λ/B). OI in the visible is thus highly desirable. As shown in section 6.4.3.3, UTs (8.2 m telescopes) at VLTI with Strehl ratio of the order of 0.1 could allow to observe 130 targets in the visible reaching up to V band magnitude of 15. This could allow full modeling of the BLR and direct distance measurement using BLR parallax with RM data. The ATs (1.8 m telescopes) with Strehl ratio of the order of 0.5 could reach up to V magnitude 15, allowing to observe about few dozen targets with better SNR on differential visibility than the K band with UTs. This could allow much better constrains on geometrical parameters of BLR model.

On the other hand, instrument like upcoming E-ELT could provide angular size of many BLRs by measuring the photocenter displacement using spectro-astrometric technique with resolution 1500 as recently described by Stern et al. (2015). This can be obtained for several lines depending on redshift. Thus, photocenter displacement could be used to estimate angular size of the BLR and combining with RM data, it could allow to estimate distance measurement up to $z = 3$. However, as already discussed in chapter 4, photocenter displacement gives the differential phase signature for unresolved object and this is very useful to constrain the geometry, but would not be sufficient in some case, for example where the kinematics is dominated by turbulence, and geometry is spherical, or disk is close to face-on. Then, differential visibility signature would be necessary to estimate the angular size as already discussed in detail in chapter 4.

7.6 Conclusion and future perspective

We simulated RM and OI datasets to estimate the accuracy on the distance measurement using BLR parallax method. In the Bayesian framework, we fit the RM data, which allows us to calculate mean radius as well as other parameters like $M_{\rm bh}$, i, ω etc. Model fitting of OI data allows us to calculate angular size. Then using Eq.7.1, we recovered angular distance with uncertainty less than 20 %, which is slightly larger than the uncertainty estimated in dust parallax distance (13.5 %) by Hönig et al. (2014). The reason of this higher uncertainty is mainly due to the degeneracy of the parameter space and the quality of RM and OI data. Fitting individual emission line profile of different epochs obtained during RM monitoring could allow to reduce this uncertainty, which can be further reduced from better quality RM and OI data. Another improvement will be to fit first RM data and use the parameters probability distribution as prior for OI data fitting with only unknown parameter angular size. This will further reduce the uncertainty in angular size estimates.

BLR parallax method can be applied to the objects for which both OI and RM observations are possible in the same emission line. As shown in chapter 6, next generation GRAVITY instrument could allow to observe a dozen of object providing BLR angular size estimation including different model parameters. This will be a major step forward for distance measurement. Moreover, MATISSE instrument will allow to estimate rim size in L band and will be particularly useful for dust parallax. OASIS with next generation fringe tracker could allow to observe BLR of about 50 objects with redshift up to 1 and four decades in luminosity, and allow to measure distances using BLR parallax. To apply this method as a tool for cosmic distance indicator, a desirable step is to have VLTI working in the visible (Hönig et al., 2014; Elvis, 2014). Adaptive optics on UTs with Strehl ratio about 0.1 could allow to estimate distances of about 100 objects using BLR parallax in visible. Spectro-astrometry with E-ELT could allow to estimate angular size of the BLR up to $z = 3$. For this, RM from the space would be very useful, a first step of which has already started (De Rosa et al., 2015).

Chapter 8

Conclusion and future perspective

Contents

8.1 Conclusion

We have investigated the application of optical interferometry to the study of AGN BLRs in order to discuss

- geometry and kinematics of the central engine by constraining morphology of BLRs
- SMBH mass measurement in quasars
- the use of quasars as standard candles

We developed a geometrical and kinematical model of BLR of quasar to predict simultaneously RM and OI signals. We showed that OI signals, such as differential visibility and phase, can provide strong constrain on BH mass, BLR size, radial distribution of BLR, velocity field, anisotropy, inclination and thickness. We created mock OI datasets using few key model parameters such as BH mass, BLR

size, inclination and thickness of BLR. All parameters are typical for quasar (see Li et al., 2013) except the angular size was taken from Petrov et al. (2012). We added realistic noises to properly simulate OI data. The aim was to find accuracy of those parameters from OI data. We employed a MCMC model fitting algorithm, and using Bayesian statistics we sampled the parameter space.

We found that OI data alone can constrain BH mass with uncertainty less than 0.15 dex. Virial mass estimated by traditional cross-correlation analysis has uncertainty of 0.30 to 0.44, which includes the dispersion of unknown scale factor f (Woo et al., 2010). If f can be constrained then uncertainty on the BH mass estimation using virial relation can be reduced highly. Our model has confirmed that the geometry strongly constrain the effect of f factor, and OI measurements can constrain it since OI provides BH mass measurement independent of f. Direct model fitting of high quality RM data also provides constrain on the geometry and kinematics, and BH mass measurement with uncertainty comparable to our estimation, but parameters degeneracy remain. However, we have qualitatively illustrated the potential of the combination of RM and OI data that improve the overall constrain on the BLR geometry and kinematics and estimate BH masses with higher accuracy, but the full accuracy gain still have to be investigated.

As a first application of OI to BLR, we resolved Paα emission line region of a bright QSO 3C273. Its redshift of 0.158 and K band magnitude of 9.7 make it particularly suitable to observe with VLTI AMBER instrument. We detected a drop in the differential visibility in all baselines. This shows that the BLR is more extended than the inner rim of dust torus. However, differential phase has been found to be $0 \pm 1°$. Combined with this very large BLR size deduced from the visibility drop, the very small differential phase implies a geometry very far from a flat disk with global Keplerian or radial velocity field. We applied our 3D geometrical and kinematical model to interpret the data. In the framework of Bayesian statistics, using a MCMC algorithm, we sampled the parameter space to fit the model globally to the data. We found that 3C273 has an extended BLR, much larger than the RM Hβ emission line size.

We discussed two ways to explain the difference between our interferometric size in Paα and the RM size in Balmer lines.

1. The RM data can not measure properly size larger than about 700 ld, and after 800 ld systematically converges around a value between 200 and 400 ld.
2. The Paα size of 2142 ld could actually be compatible with the Hα size of about 500 ld, as there might be up to a factor 2 difference between Hα and Paα due to photoionization of BLR, and multiplied by a factor of about 2 between RM size and OI size that resulted from different weighting in RM and OI (see Koshida et al., 2014; Kishimoto et al., 2011b).

We found that the 3C273 has a roughly face-on ($i = 10°$) and spherical BLR. The clouds in the BLR are rotating in Keplerian orbit, but a significant contribution of turbulence velocity is present. Furthermore, we estimated a BH mass of 3C273 to be $5.30^{+0.24}_{-0.21} \times 10^8 M_\odot$, similar to the mass obtained by Kaspi et al. (2000). Comparing our directly estimated BH mass to the RM virial mass, we estimated

the RM scale factor to be $f \simeq 3$, which is close to the value obtained by Grier et al. (2013). Measurement of scale factor independently will help to calibrate BH masses that are estimated using virial relation. With more OI source resolved by OI and RM, we could calibrate f as a function of luminosity and probably with other parameters.

Motivated by our 3C273 result, we did a feasibility test to find the number of AGNs that can be observed with different instruments such as AMBER, GRAVITY, OASIS and OASIS+ (possible instruments) at VLTI with its full potential. We also obtain the accuracy on the absolute and different visibility and differential phase that can be obtained from different instruments. We found that next generation VLTI instrument GRAVITY could allow to observe a dozen of objects. For about 15 objects we will get absolute visibility and differential phase, still allowing us to constrain BLR geometry up to some extent. With OASIS and OASIS+, this target list could increase up to 40. Having an external FT, GRAVITY and OASIS+ number of targets could increase up to 30 and 50 respectively. Moreover, MATISSE in L band could observe emission lines of about 10 objects, and for many objects it will provide absolute visibility measurement, which is necessary to constrain dust torus geometry. VLTI in its visible mode with UTs of Strehl ratio 0.1 could provide differential visibility measurements of about 130 objects up to $V = 15$, for some of which we will have absolute visibility measurement. Differential phase with or without visibility measurement will be a key to estimate angular size for distance measurement using parallax. ATs with Strehl ratio 0.5 could also reach up to $V = 14$. In visible we will not only have the advantage of higher angular resolution but also will have the access to the bright Balmer lines. Thus, a visible mode at VLTI is highly desirable. VLTI with its full potential could allow to establish an independent $r_{\rm blr} - L$ and $M_{\rm bh} - L$ other than RM, and probably $i - L$ and $\omega - L$ relation.

A simply method, "Quasar parallax" was proposed by Elvis and Karovska (2002) to estimate distances using quasars based on the ratio of the linear size given by RM and the angular size given by OI, with a correction factor depending on the geometry of the source. Recently Hönig et al. (2014) applied this method to the dust torus of NGC 4151 estimating first direct distances using dust parallax with 13.5 % uncertainty. With a very simple "ring" like geometry of the inner rim of the dust, they showed that model parameter have very little influences on distance measurements since they have similar influence on both RM and OI measurements. After our first successful observation of the BLR of the 3C273, we made a preliminary investigation of the BLR parallax method. We created mock RM continuum and line light curves, and OI data adding realistic noises. Fitting the mock data, we found a potential accuracy on the angular distance better than 20 %. This uncertainty could be reduced with high quality RM data as model parameters can be better constrained in that case, which was shown recently by Pancoast et al. (2014a). The full dependence of BLR parallax method still needs to be estimated from a large sample of targets. On 3C273, our doubts about the actual RM size in Paα prevented so far an attempt to measure distance of 3C273 using this method. The full model including photo-ionization code CLOUDY could allow to estimate the lag ratio of Paα to Hα, which should be feasible as we have strong constrain on the BLR geometry. This could be applied to all the targets

that could be observed with VLTI to estimate angular diameter and its accuracy. The result will have remarkable significance as distance measurement with quasars at $z > 0.8$ would allow to constrain different cosmologies.

8.2 Ongoing work

8.2.1 3C273 data reduction and modeling

There are a few works that are ongoing about 3C273. Calibration of 3C273 data is not finished yet. This can be done very soon. In future we will also try to investigate the possibility to fit simultaneously visible RM data of (Kaspi et al., 2000) with our Paα emission line data, but this needs an estimation of lag-ratios between different line emitting regions. It can be calculated from our improved modeling after including photo-ionization physics.

8.2.2 Parallax distance

The work presented in chapter 7 is not finished yet. We really believe that the accuracy on linear size estimation can be improved by simultaneous fitting of multi-epoch spectra. It will also help to better constrain other BLR model parameters whose probability distribution can be supplemented to the OI data fitting and thus we can have better constrain on the angular size. This work is in process. We also want to test the feasibility of this method with spectro-astrometry of E-ELT. Recently Stern et al. (2015) proposed that E-ELT can spatially resolve 100μas BLRs, thus expected to provide constrain on the angular size of many objects with large redshift range. Thus, we will estimate the accuracy on the angular distance that can be obtain with spectro-astrometry of E-ELT and RM data.

8.2.3 Model development

We showed that our BLR model is capable to predict simultaneously OI and RM signals for various geometries and kinematics. Moreover, this can be easily improved considering elliptical orbits and non-linear response of BLR clouds on the incident continuum (Pancoast et al., 2014b; Li et al., 2013). This will be needed for fitting high quality RM data since current OI data is not accurate enough to fit many free parameters in model fitting. One important development is to include "photo-ionization" physics inside the model. With a precomputed grid of hydrogen density ($n_{\rm H}$) and photon flux ($\phi_{\rm H}$), we have computed radial emissivity of different emission lines. Having done that we could apply simultaneous model fitting of several emission lines data and constrain the photo-ionization model parameters. Again, this can be done with RM data since we have highly sampled light curves in several emission lines for many objects. For modeling OI data, we can use the precomputed radial emissivity in the model. Similarly anisotropy can also be computed from the same $n_{\rm H} - \phi_{\rm H}$ grid following Goad et al. (2012).

8.3 Future perspective

8.3.1 VLTI 2nd generation instruments

As discussed in chapter 6, VLTI next generation instruments like GRAVITY and MATISSE can combine all four unit-telescopes and provide simultaneously 6 baselines observation. They will also provide good quality data, and eventually will allow to constrain many more model parameters. GRAVITY is expected to start operation from 2017. This could provide very good differential phase measurement of a dozen of objects. Moreover, much better absolute visibility can be obtained from GRAVITY observations. This will be a major boost in MR observation of BLR. MATISSE on the other hand is expected to provide data from 2016. It could allow to provide images of the inner dust torus for a couple of objects. It will also provide dust size as a function of temperature by observing in L, M and N bands for all the GRAVITY objects. Thus, combining GRAVITY with MATISSE observations, we could develop a luminosity dependent model of BLR and dust (both depending from latitude distributions of luminosity).

8.3.2 Photometric reverberation mapping

Indeed emission line RM is the most powerful tool till now to estimate BH masses in AGN and to constrain the BLR geometry. However, due to sparsely sampled RM light curves, the scatter in these relations is still large. Moreover, emission line RM is observationally very expensive, since the reverberation spectra usually require observations with at least a 2 m-class telescope, need monitoring of objects from few months to several years to match distinct echo features, and are also prohibited at higher redshift.

As an alternative technique Haas et al. (2011) suggested photometric RM (PRM) in optical using a combination of narrow and broad band filters. In brief, the principle is that the narrow band filter plays crucial role to measure the flux of emission line, while broad band filter can be used to estimate the continuum. Narrow and broad band light curves can be used to get the time delay between continuum and emission line flux, leading to the BLR radius (Pozo Nuñez et al. (2012, 2014)). Since the photometric monitoring can be obtained more quickly than spectroscopic monitoring and that also using small telescope, so it opens a possibility of carrying out the RM study for larger sample of nearby AGNs, with reasonable telescope time. PRM will provide highly sampled light curves enabling us to constrain the geometry and kinematic of BLR as well to estimate accurate BLR size and BH mass, and hence improved $R - L$ and $M - L$ relations.

Thus, we are carrying out photometric reverberation mapping of 6 nearby AGNs, with V-band magnitude brighter than 15.0 using Aryabhatta research institute of observation sciences (ARIES) 1.3 m DFOT. This brightness criteria ensures that photometry can be carried out even on bright nights, with 1-2 m class telescope. The redshift range of members is chosen such that their H-β and H-α emission line respectively fall in the region of OIII and SII narrow band filter of ARIES 1.3 m DFOT. For continuum flux we wish to use the broad B and V-band observation.

The typical BLR size expected for our sample is at the most about 20 light days, which can be constrain very well by monitoring campaign of about 60-70 days. For three of our sources we are using OIII filter to cover H-β emission line, while for another three we are using SII filter to cover the H-α emission line.

8.3.3 Emission line reverberation mapping

Reverberation has been a powerful tool to estimate BH masses of AGNs. Recent high quality RM data enables to recover velocity-delay map providing kinematics signatures. Dynamical modeling of these data enables to constrain geometry and kinematics of the BLR and BH masses independent of virial factor. However, this has been done only for few objects. There is an immediate need to increase the sample size extending to high-luminosity and high redshift objects.

Therefore, with a group of ARIES, I am planning a 3 years RM campaign of a handful number of AGNs with recently installed 3.6 m Devasthal telescope. In early 2016 ADFOSC (ARIES Devasthal Faint object spectrograph) will be available for such spectroscopic RM observations. For some low luminous objects, we will do intensive variability monitoring to obtain highly sampled light curves not only to recover velocity-delay map by linear inversion with maximum entropy method but also to constrain their geometry and kinematics by direct modeling of BLR and Bayesian inversion technique. For few high luminous objects, we will monitor them once or twice per 2 weeks to estimate their BLR size via cross-correlation technique and Javeline fitting. This will allow to extend $R-L$ relation to the high luminosity region. Additionally, it would be interesting to measure emission line lag ratios for optical and near-IR lines, since no near-IR emission line RM data is available, and OI with AMBER or GRAVITY is limited to the near-IR. Thus, this will allow to estimate lag ratios between Hβ, Hα to Paβ and Paα. An extrapolation of these lag ratios could be used for high luminous object like 3C273 to find the difference between near-IR RM size vs OI size, and constrain the BLR and dust structure.

8.3.4 Observation with GAIA

GAIA will measure photometric and spectro-photometric variability of few hundred of thousand of QSOs but with a poor and irregular time sampling that depends on the source position (Proft and Wambsganss, 2015). It might be worth investigating if the time sampling of some of GAIA targets could be enough to constrain inner structure and physical process in BLR.

8.3.5 Spectro-astrometry

If we have a model (and the differential phase is not zero on other BLRs like in 3C273) spectro-astrometry with E-ELT could resolve the μas BLR providing its angular size measurement up to redshift more than 4 (Stern et al., 2015). This

measurements, accurate at the 1/1000 pixel level, would allow BLR parallax measurement up to redshift $z = 3$ for high-luminosity and $z = 2$ for low-luminosity objects, which is a preliminary result from Petrov et al. (2012) and will be investigated through our ongoing work on BLR parallax.

Appendix A

Publications

Some results of this thesis are published in scientific journals, which are attached in the following. The first paper (Rakshit et al., 2015) is described in detail in chapter 4 presenting a three-dimensional geometrical and kinematical model of BLR of quasar that can predict simultaneously all reverberation and optical interferometric signals. Model has several free parameters such as black hole (BH) mass, BLR size, inclination, opening angle, anisotropy, velocity field in terms of rotation, radial, macro- and micro-turbulence. We explain the effect of different parameters on the interferometric measurements. Moreover, we simulated mock interferometric data using some model parameters adding realistic noise. To explore the parameter space efficiently, we used Monte Carlo Markov Chain (MCMC), and fit the model to the simulated data in Bayesian framework. We recover all the parameters very efficiently within 1 σ uncertainty. Most interestingly, the uncertainty in BH mass is found to be within 0.15 dex comparable to the uncertainty in RM mass measurement.

In second paper (Petrov et al., 2012), a first result of our 3C273 observation using AMBER/VLTI after a preliminary data processing is presented. A new blind mode observation allowed us to detected Paα emission line. The first processing (after binning the spectral channel by 16) showed a drop in differential visibility that increases with baseline length, and differential phase is $0^\circ \pm 2^\circ$ in all baselines. Both differential visibility and phase shows bias on 3C273 that do not appear in the faintest calibrators. However, our bias analysis shows the differential signatures in the emission lines are real. Preliminary modeling suggest an extended BLR, which is larger than inner rim of dust torus, observed in the same band. Further data reduction, calibration and modeling of the data with a geometrical and kinematical model is presented in chapter 5.

In third paper (Rakshit and Petrov, 2014), which is based on the chapter 6, a feasibility study is presented to predict the number of targets and the expected signal that could be obtained with the different instruments of VLTI. We considered current AMBER+, upcoming GRAVITY, and possible up-gradation of AMBER (OASIS, OASIS+ and OASIS with an external Fringe Tracker). We found GRAVITY could allow to observe a dozen of AGNs, the number of which can be increased with OASIS. Thus, VLTI with its full potential could allow to

observe about 60 targets providing differential phase and absolute visibility sufficient to fit BLR model parameters, for some of the targets it would be possible to also have differential visibility measurement.

Monthly Notices
of the
ROYAL ASTRONOMICAL SOCIETY
MNRAS **447,** 2420–2436 (2015) doi:10.1093/mnras/stu2613

Differential interferometry of QSO broad-line regions – I. Improving the reverberation mapping model fits and black hole mass estimates

Suvendu Rakshit,[1⋆] Romain G. Petrov,[1] Anthony Meilland[1] and Sebastian F. Hönig[2]

[1] *Laboratoire Lagrange, UMR 7293, University of Nice Sophia-Antipolis, CNRS, Observatoire de la Cote D'Azur, BP 4229, F-06304 Nice Cedex 4, France*
[2] *Dark Cosmology Center, University of Copenhagen, Juliane Maries Vej 30, DK-2100 Copenhagen, Denmark*

Accepted 2014 December 5. Received 2014 November 13; in original form 2014 August 17

ABSTRACT

Reverberation mapping (RM) estimates the size and kinematics of broad-line regions (BLR) in quasars and type I AGNs. It yields size–luminosity relation to make QSOs standard cosmological candles, and mass–luminosity relation to study the evolution of black holes and galaxies. The accuracy of these relations is limited by the unknown geometry of the BLR clouds distribution and velocities. We analyse the independent BLR structure constraints given by super-resolving differential interferometry. We developed a three-dimensional BLR model to compute all differential interferometry and RM signals. We extrapolate realistic noises from our successful observations of the QSO 3C 273 with AMBER on the VLTI. These signals and noises quantify the differential interferometry capacity to discriminate and measure BLR parameters including angular size, thickness, spatial distribution of clouds, local-to-global and radial-to-rotation velocity ratios, and finally central black hole mass and BLR distance. A Markov Chain Monte Carlo model-fit, of data simulated for various VLTI instruments, gives mass accuracies between 0.06 and 0.13 dex, to be compared to 0.44 dex for RM mass–luminosity fits. We evaluate the number of QSOs accessible to observe with current (AMBER), upcoming (GRAVITY) and possible (OASIS with new generation fringe trackers) VLTI instruments. With available technology, the VLTI could resolve more than 60 BLRs, with a luminosity range larger than four decades, sufficient for a good calibration of RM mass–luminosity laws, from an analysis of the variation of BLR parameters with luminosity.

Key words: methods: statistical – techniques: interferometric – techniques: spectroscopic – galaxies: nuclei.

1 INTRODUCTION

Active galactic nuclei (AGNs) are powered by the accretion of matter on to a supermassive black hole (SMBH). The high-energy photons from the accretion disc illuminate gas clouds and dust clumps. According to the standard model of AGNs (Antonucci 1993; Urry & Padovani 1995), the broad emission lines are produced by an inner region of high-velocity gas clouds called the broad-line region (BLR). In Seyfert 2 AGNs, an edge-on clumpy dust torus shields the BLR. To understand QSOs we must characterize the geometrical and velocity distribution of the BLR clouds. This yields the mass and accretion rate of the central SMBH, and the mechanisms to transport material inwards to the accretion disc and outwards to the jet. It constrains the distribution of light emitted by the accretion disc, and hence constrains the accretion disc models.

So far, the only technique providing some direct constraints on the BLR geometry has been the so-called reverberation mapping (RM; Blandford & McKee 1982; Peterson 1993). Early RM observations have led us to estimate the BLR characteristic size, providing a size–luminosity relation, but have failed to directly constrain their actual geometry (Kaspi et al. 2000; Bentz et al. 2013). They have nevertheless provided mass estimation for the SMBH themselves used to establish an empirical mass–luminosity relation for SMBHs (Peterson et al. 2004; Vestergaard & Peterson 2006; Bentz et al. 2009b; Bennert et al. 2010). With improved precision, the size–luminosity relation would be a useful tool for cosmology, making QSOs usable as standard candles to independently estimate distances, and the mass–luminosity relation will constrain the global evolution of QSOs and host Galaxies (Watson et al. 2011; Bentz et al. 2013).

Spatially resolved observations of QSOs have been a major goal of optical and infrared long baseline interferometry (OI) since its origin. Interferometric observations of QSOs have however proven difficult in practice: their apparent magnitude makes them particularly hard to observe with interferometry. In addition, the BLR characteristic sizes deduced from RM observations suggest typical angular diameters smaller than 0.3 mas, i.e. about 10 times below the standard resolution limit of the largest infrared interferometers. Petrov et al. (2001) and Marconi, Maiolino & Petrov (2003)

⋆E-mail: suvenduat@gmail.com

have proposed to apply to BLRs the super-resolution capability of differential interferometry (Petrov 1989). This was one of the design specifications of the VLTI first generation instrument AMBER (Petrov et al. 2007). Because of the unexpectedly low performances of fringe stabilization at the VLTI, Petrov et al. (2012) introduced a new observation and data reduction technique that boosted the limiting magnitude of VLTI/AMBER in medium spectral resolution and allowed the first successful differential interferometry observation of the BLR of 3C 273. This success and the need to explain the data triggered the development of the geometric and kinematic model described in this paper. We use it to evaluate the contributions of spectro-interferometry with the VLTI, combined with RM, to discriminate between different BLR geometries, to constrain the key geometrical and kinematics parameters and finally to estimate the BH mass.

In Section 2, we overview the two BLR observing techniques reminding how their key observables are computed. In Section 3, we describe our BLR model and show how it allows estimating RM and OI observables. In Section 4, we display and discuss the RM and OI signatures of some key model characteristics. In Section 5, we compute the number of targets accessible to the VLTI with various existing, near future or possible instruments. We estimated the accuracy on the parameters that can be achieved with current OI in Section 6, and Section 7 gives a final synthetic discussion of the potential of OI with the VLTI to confront, check and extend the possibilities of RM, improve the mass–luminosity relation and the use of QSOs as standard mass tags.

2 OBSERVING TECHNIQUES

2.1 Reverberation mapping

Reverberation mapping (RM) is based on the spectro-photometric variability study of the continuum and line flux (Blandford & McKee 1982; Peterson 1993). A part of the continuum light emitted from the central compact source travels directly towards the observer. A fraction of this light is absorbed by the BLR clouds and emitted in a narrow spectral bin depending on the specific Doppler shift of each cloud. This echo of light is detected at a wavelength characterizing the radial velocity of the cloud with a time delay characterizing its distance to the central source as well as its relative distance to the observer. If $C(t)$ is the light curve of the continuum and $L(v, t)$ is the flux detected in the line at the radial velocity v and time t, we can write

$$L(v,t) = \int_{-\infty}^{\infty} \Psi(v,\tau) C(t-\tau)\,\mathrm{d}\tau, \tag{1}$$

where $\Psi(v, \tau)$ is the 2D probability density function of velocities and time lags for all BLR clouds. It is often called the RM echo function or the RM transfer function (Blandford & McKee 1982; Welsh & Horne 1991). A very accurate and well-sampled $\Psi(v, \tau)$, de-convolved from local line shapes and combined with physical constraints can in principle constrain almost uniquely the BLR geometry and velocity field.

However, because of sparse, undersampled and noisy data, most of early RM work has been based on the measurement of the typical time lag $\tau_{\rm cent}$ and dynamical line width ΔV. The time lag $\tau_{\rm cent}$ is the barycentre of the 1D transfer function $\Psi(\tau)$ resulting from the integration of $\Psi(v, \tau)$ over v. For infinite time series, $\tau_{\rm cent}$ is equal to the centroid of the cross-correlation CCF(τ) between $C(t)$ and $L(t)$, where $L(t)$ is the integration of $L(v, t)$ over v (Peterson 2001). The approximate width ΔV of the 1D dynamical line profile $\Psi(v)$ ($\Psi(v, \tau)$ integrated over t), is given by full width at half-maximum (FWHM) or the standard dispersion σ_l of the 'mean' or the 'rms' emission line profile (Collin et al. 2006).

A simple virial relation (Peterson et al. 2004) links the ΔV and $\tau_{\rm cent}$ to the mass of the central SMBH:

$$M_{\rm bh} = f\frac{R_{\rm blr}\Delta V^2}{G}, \tag{2}$$

where $R_{\rm blr} = c\tau_{\rm cent}$ is the RM BLR size, G is the gravitation constant, c is the speed of light and f is an unknown scale factor that depends mainly on the BLR geometry and kinematics. This relation allowed us to estimate SMBH masses that can be related to the luminosity of the BLR: $M_{\rm bh} \propto L^{0.79\pm0.09}$ (Peterson et al. 2004; Vestergaard & Peterson 2006; Bentz et al. 2009b). However, the statistical scatter of masses in this relation is larger than a factor 3 for all the estimated masses by Kaspi et al. (2000, Collin et al. 2006).

Many efforts have been made to improve this mass–luminosity relationship that is vital to study the evolution of mass and accretion rate of SMBHs as a function of their age (via the redshift), and the co-evolution between AGNs and host galaxies. Some authors improved the measurement of the time lag $\tau_{\rm cent}$ interpolating the light curves with a damped random walk model (Kelly, Bechtold & Siemiginowska 2009; Zu, Kochanek & Peterson 2011), if possible simultaneously through several lines with different scale factors. Others have tried to improve the estimation of the projection factor f from model fits of the line profile and the time cross-correlation function (Krolik 2001; Onken et al. 2004; Collin et al. 2006; Goad, Korista & Ruff 2012). They show that in relatively flat models, such as discs (Krolik 2001) or bowl geometry (Goad et al. 2012) the main parameter affecting f is the global inclination i of the BLR. The estimation of ΔV from the 'mean' and 'rms' spectrum depends on the relative contributions to the line width of the global velocity field, such as global rotation, inflow or outflow, and more local contributions, such as microturbulence inside the clouds as well as the macroturbulent motion of the clouds themselves.

Another important achievement of RM is the size–luminosity, i.e. lag–luminosity relationship. In spite of all efforts to improve the time lag estimation (Kelly et al. 2009; Zu et al. 2011) as well as to isolate the BLR luminosity from the host galaxy (Bentz et al. 2006), the dispersion of lags around the best fit of the lag–luminosity relation is between 0.13 and 0.21 dex (Bentz et al. 2013) while an accuracy better than 0.05 dex would be necessary to allow the abundant QSOs to be as good standard candles as the scarce Type Ia supernova.

Recent RM high-quality data sets allowed some successful reconstructions of $\Psi(\tau, v)$ and the detection of inflow and outflow signatures (Bentz et al. 2010; Grier et al. 2013). Direct modelling of RM data using a Bayesian inverse problem approach improves the number and accuracy of fitted parameters (Brewer et al. 2011; Pancoast, Brewer & Treu 2011, 2014a; Pancoast et al. 2014b). Additional observational constraints are however necessary, to independently remove degeneracies of model parameters and improve the accuracy of their fit. We will show that a good candidate is optical interferometry that can provide useful angular and dynamic constraints on unresolved sources when it is used in its spectro-interferometry or differential interferometry mode.

2.2 Optical interferometry

Multitelescopes optical interferometry (OI) is intended to provide very high angular resolution information, and ideally images, with spatial (or angular) resolution $\sim\lambda/B$, where λ is the observation

wavelength and B is the interferometer baseline, i.e. the maximum distance between apertures. Resolved observations of AGNs have been a goal for OI since its redefinition by Labeyrie in the 1970s (Labeyrie 1978; Labeyrie et al. 1986) but these targets are generally too faint for most existing facilities, except for low spectral resolution observations in the near- and mid-infrared, with 8–10 metre aperture telescopes, only available at the VLTI and the Keck interferometer (KI). Since Jaffe et al. (2004), more than 45 AGNs have been successfully observed in the N and K bands. This allowed us to constrain the size of the innermost dust torus structure and revealed its complexity. Burtscher et al. (2013) reject the existence of a simple size–luminosity relation in AGNs, because the $L^{0.5}$ scaling of bright sources fails to properly represent fainter sources. There are clearly several components, with at least a cooler more equatorial structure and a hotter more polar one. However, Kishimoto et al. (2014) still tries to find an unification scheme based on the idea that in low-luminosity AGNs the inner torus is more shallow than in high-luminosity ones, because a latitudinal dependent radiation pressure blows away all material far from the equatorial plane in high-luminosity AGNs. Thus low-luminosity AGNs would have much more dust clouds in the polar direction. Both the KI and the VLTI measurements, summarized in Kishimoto et al. (2012), show that in the K band, the dust torus inner rim size is fairly close to an $R_{\rm rim} \propto L^{0.5}$ size as first indicated by the infrared RM observations of Suganuma et al. (2006), with a size excess with regard to $\propto L^{0.5}$ that increases as L decreases but remains small in the K band. In Section 5, we will use this Suganuma size as a lower limit of the inner rim size to estimate the feasibility of AGN OI observations.

The OI observation of AGN BLRs faces two major difficulties. First, a spectral resolution greater than 500 is required, which impacts the sensitivity of the instrument and places AGNs out of reach of the first generation VLTI instruments. A solution would be to assist the instrument with a fringe tracker (FT) that would enable the use of exposure time greater than the atmospheric coherence time for differential piston. As the limiting magnitude of current FT remains lower than $K = 9.5$, we developed a new observing and data processing technique, based on the visible OI data processing by Berio et al. (1999), that allows us to observe fainter sources in medium and high spectral resolution without FT. This allowed the first successful observation of the BLR of 3C 273 (Petrov et al. 2012). Secondly, the sizes deduced from RM observations suggest typical angular diameters for BLRs to be much smaller than the formal angular resolution of current facilities observing in the K band, and we have to use the super-resolution power of differential spectro-interferometric measurements.

2.2.1 Spectro-interferometric measurements

Petrov et al. (2007) provide a thorough description of the spectro-interferometric instrument AMBER and its uses. This section offers a concise summary of the concepts of interferometry that are of direct relevance to the application presented in this paper. An interferometer with baseline B yields the complex visibility of the source, i.e. the normalized Fourier transform $\tilde{O}(\boldsymbol{u}, \lambda)$ of the source brightness distribution $O(\boldsymbol{r}, \lambda)$ at the spatial frequency $\boldsymbol{u} = \boldsymbol{B}/\lambda$

$$\tilde{O}(\boldsymbol{u}, \lambda) = \frac{\int\int O(\boldsymbol{r}, \lambda) \mathrm{e}^{-2\pi \mathrm{i} \boldsymbol{u}.\boldsymbol{r}} \, \mathrm{d}^2\boldsymbol{r}}{\int\int O(\boldsymbol{r}, \lambda) \, \mathrm{d}^2\boldsymbol{r}} = V_*(\lambda) \mathrm{e}^{\mathrm{i}\phi_*(\lambda)}. \quad (3)$$

The modulus $V_*(\lambda)$ of $\tilde{O}(\boldsymbol{u}, \lambda)$ is given by the contrast of the fringes and called source absolute visibility. It needs to be calibrated on a known reference source, which limits its accuracy. The position of the fringes yields the phase $\phi_*(\lambda)$ of the source complex visibility. It can be measured only with regard to some internal phase reference or iteratively constrained by closure phase relationships of triplets of baselines when at least three baselines are available. In addition to the absolute visibility and closure phase, a spectro-interferometric instrument like AMBER produces differential quantities such as the differential visibility $V_{\rm diff}(\lambda) = V_*(\lambda)/V_*(\lambda_{\rm r})$ and the differential phase $\phi_{\rm diff}(\lambda) = \phi_*(\lambda) - \phi_*(\lambda_{\rm r})$, where $\lambda_{\rm r}$ is the wavelength of a reference channel, for example in the continuum near the emission line. As the differential measurements use an internal reference, they are much more accurate than the absolute measurements and allow us to measure the small effects produced by quite unresolved sources.

2.2.2 Differential interferometry of non-resolved sources

A non-resolved source has a global angular size Λ that is smaller than the interferometer resolution limit λ/B. In equation (3), this implies that $O(\boldsymbol{r}, \lambda)$ is different from 0 only for values of $\boldsymbol{r} < \lambda/\boldsymbol{B} = 1/\boldsymbol{u}$, i.e. the integral in equation (3) can be limited to values $\boldsymbol{u} \cdot \boldsymbol{r} < 1$. Petrov (1989) shows that the interferometric phase for such a source is given by

$$\phi_*(\lambda, \lambda_{\rm r}) = -2\pi \boldsymbol{u} \cdot [\boldsymbol{\epsilon}(\lambda) - \boldsymbol{\epsilon}(\lambda_{\rm r})] \, , \quad (4)$$

where the quantity

$$\boldsymbol{\epsilon}(\lambda) = \frac{\int\int \boldsymbol{r} O(\boldsymbol{r}, \lambda) \, \mathrm{d}^2\boldsymbol{r}}{\int\int O(\boldsymbol{r}, \lambda) \, \mathrm{d}^2\boldsymbol{r}} \quad (5)$$

is the photocentre of the source. This result has been obtained from a first-order-limited development of the complex visibility $\tilde{O}(\boldsymbol{u}, \lambda)$. Extending this development to higher terms shows (Rakshit & Petrov 2014) that the source visibility V_* is given by

$$V_* = 1 - \alpha^2, \quad \text{where } \alpha = \frac{\pi\Lambda}{\sqrt{2}\left(\frac{\lambda}{B}\right)}, \quad (6)$$

and the closure phase decreases as α^3. The differential phase that decreases only proportionally to the source size has the highest super-resolution power, while the closure phase is accessible only on resolved sources. In Section 5, we discuss the accuracy limits on the differential visibility and phase for a list of AGNs, but let us first show how these measurements can be used. As a guideline for the reader, we remind that for non-resolved sources, the differential phase gives the difference in position between the photocentre of the object in the reference channel and this in the λ channel while the differential visibility gives their difference in size.

3 GEOMETRIC AND KINEMATIC MODEL OF THE BLR

We developed a geometric and kinematic model of the BLR surrounding an SMBH, to predict all interferometric and RM observables. This model is quite similar to the ones used when interpreting RM observations, for example by Pancoast et al. (2012). Line profile modelling strongly suggests that the BLR is made of a very large number of clouds with individual sizes negligible with regard to the BLR size (Arav et al. 1997, 1998). The covering factor of the BLR clouds is of the order of 10 per cent (Collin et al. 2006; Goad et al. 2012) and most BLR clouds are seen directly by the observer if they are not masked by the dust torus. These basic hypothesis underlie RM and are well supported by its success.

We start with a 3D distribution of clouds, considered as point sources. Each cloud is defined by its spherical coordinates r, θ, ϕ in a reference system local to the BLR, with z as a symmetry axis. The coordinates are generated randomly with constraints of the desired BLR geometry.

The radius r must respect the radial distribution of clouds $R_{\rm d}(r)$ that is defined here as a normal distribution of standard deviation $\sigma_{\rm blr}$ limited by an inner radius $R_{\rm in}$ below which we assume the gas to be fully ionized and unable to contribute to a low-ionization line.

$$P(l < r < l + {\rm d}l) = \frac{1}{\sigma_{\rm blr}\sqrt{(2\pi)}} \exp\left(-\frac{l^2}{2\sigma_{\rm blr}^2}\right) \quad \text{for } r \geq R_{\rm in}. \quad (7)$$

The declination angle θ is randomly selected to have $-\omega \leq \theta \leq \omega$, where $0 \leq \omega \leq 90^\circ$ is the 'opening angle' of the BLR. For $\omega \simeq 0$, we have a flat disc. Many authors (Collin et al. 2006; Decarli et al. 2008; Fine et al. 2008) have shown that a proper modelling of line profile implies a thick BLR that we choose to represent here using this opening angle as in Pancoast et al. (2012). The azimuthal angle is randomly selected to have $0 \leq \phi \leq 2\pi$. These spherical coordinates r, θ, ϕ are used to define the tangential and radial velocity of the cloud, as discussed below. To maintain the axis symmetry of the cloud distribution an additional random rotation around z is added to each cloud position and velocity vector.

From r, θ, ϕ spherical referential we can define the cloud velocity vector considering several possible components:

(a) An orbital component, tangential to the circle:

$$V_{\rm orb} = V_{\rm a}\left(\frac{R_{\rm in}}{r}\right)^{\beta}, \quad (8)$$

where β defines different rotation velocity laws (Stee 1996). For a Keplerian motion, $\beta = 0.5$ and $V_{\rm a} = \sqrt{\frac{GM_{\rm bh}}{R_{\rm in}}}$.

(b) A radial component (inflow or outflow):

$$V_{\rm rad} = V_{\rm c}\left(\frac{R_{\rm in}}{r}\right)^{\gamma}, \quad (9)$$

where γ is the power-law index of this radial velocity. Free-fall corresponds to $\gamma = 0.5$ and $V_{\rm c} = \sqrt{\frac{2GM_{\rm bh}}{R_{\rm in}}}$. $\gamma = -1$ is an outflow case with outflow velocity amplitude $V_{\rm c}$ set at the inner radius $R_{\rm in}$ of the BLR (Welsh & Horne 1991).

The composition of these orbital and radial velocity laws constitutes the global velocity field of the BLR. We have also considered a local macroturbulent velocity component $V_{\rm turb}$ with random orientation. Several authors (Collin et al. 2006; Goad et al. 2012) relate the amplitude $V_{\rm turb}$ to the thickness $H(r)$ of the BLR at the radius r

$$|V_{\rm turb}| = V_{\rm orb}\, P_{\rm turb}\, H(r). \quad (10)$$

In our model $H(r) = r\sin\omega$. The multiplicative parameter $P_{\rm turb}$ tunes the amplitude of the turbulence velocity. The macroturbulence is zero both for flat discs ($\omega = 0$) and for $P_{\rm turb} = 0$.

To obtain the geometrical distribution with respect to the observer, in its X,Y,Z coordinate system, we introduce a global rotation about the y-axis of angle i ($i = 0$ is for 'face on' object, and for Sy1 the typically value of i is less than 40°) and then a global rotation around the z-axis to introduce the position angle Θ. In the following we consider that Θ is known, as it can be deduced either from the jet position angle, from polarization measurements or from broad-band OI observation. It is also possible to introduce this parameter in the model fit as soon as we have several baseline orientations.

The cloud apparent brightness can be affected by a geometrical effect related to its optical thickness and to its position, named 'anisotropy' by several authors (O'Brien, Goad & Gondhalekar 1994; Goad et al. 2012; Pancoast et al. 2014a,b). If the cloud is optically thick, then the observer sees only the fraction of its surface facing him. If the cloud is optically thin, then all points of the cloud contribute to its intensity in all directions. This effect, similar to a 'moon phase', is described as

$$I(\phi) = (1 - F_{\rm anis}\cos\phi\sin i), \quad (11)$$

where the anisotropy factor $F_{\rm anis}$ goes from 0 for optically thin clouds to 1 for optically thick clouds. In the present stage of development, our model includes only this simple description of anisotropic cloud emission as well as the simple anisotropy of a skewed torus inner rim described in Section 5.4. A more detailed analysis of the anisotropy of the BLR emission as well as of its dust surroundings has to be undertaken in a future paper through a radiative transfer modelling using for example the photo-ionizing code CLOUDY (Ferland et al. 1998, 2013) that constrains the cloud opacity and provides the radial distribution of its emission.

Each cloud is emitting a line with profile $L_{\rm XYZ}(\lambda)$ depending from the local physical conditions and hence from the cloud position. This profile is convolved by the instrument spectral PSF $P_I(\lambda)$. If we observe at relatively low spectral resolution, from 200 to 1500, we can consider that $P_I(\lambda)$ is much broader than $L_{\rm XYZ}(\lambda)$ and, as a first approximation, we can consider that the line shape details are lost in the convolution. Thus, in the current version of our model all clouds are emitting the same line profile $L(\lambda)$, but for its intensity that depend on r and can be included in the radial intensity distribution $R_{\rm d}(r)$. This gives $L_{\rm XYZ}(\lambda)\, P_I(\lambda) \simeq R_{\rm d}(r)\, L(\lambda)$. We choose to represent the local line profile $L(\lambda)$ by a Gaussian function centred at the emission line wavelength λ_0 and with standard deviation σ_0 that is one of the parameters of the model: $L(\lambda) = \mathcal{N}(\lambda - \lambda_0, \sigma_0)$.

For each cloud, the line is Doppler shifted by the projected velocity component $V_z(X, Y, Z)$ and the contribution of each cloud to the BLR intensity is

$$I_{\rm blr}(X, Y, Z, \lambda) = R_{\rm d}(X, Y, Z)\,\mathcal{N} \times \left[\lambda - \lambda_0\left(1 + \frac{V_z(X, Y, Z)}{c}\right), \sigma_0\right]. \quad (12)$$

Since we are focusing on low-ionization hydrogen lines such as Paschen and Brackett series that are produced far from the central source, the relativistic effects such as relativistic Doppler shift and gravitational redshift are negligible and hence we do not take them into account.

The BLR intensity seen by the observer $I_{\rm blr}(X, Y, \lambda)$ is obtained by adding the contribution $I_{\rm blr}(X, Y, Z, \lambda)$ of all clouds located in a box $(X, X + {\rm d}X, Y, Y + {\rm d}Y)$ and by normalizing it with its maximum amplitude. Fig. 1 represents two distributions of cloud. The upper panel shows a flat Keplerian disc ($\omega = 0$, $\beta = 0.5$, $V_{\rm rad} = 0$, $i = 30^\circ$, $R_{\rm in} = 1000R_g$, where $R_g \equiv GM_{\rm bh}/c^2$). The lower panel shows a spherical distribution of Keplerian orbits ($\omega = 90^\circ$). The colours represent the velocity in the direction of the observer. Note that the velocity range in the spherical case is twice larger than the flat Keplerian case with the same central mass and BLR size.

Continuum model: In the K band, the continuum emission is strongly dominated by the hot dust near the sublimation radius $R_{\rm rim}$ (Kishimoto et al. 2007, 2009). As this structure remains unresolved both for the VLTI and the KI, we have access only to its equivalent radius. We choose to represent it by a narrow ring whose radius ($R_{\rm rim}$) will give the right visibility observed in the continuum, when such a measurement is available, or $\propto L^{0.5}$ with a proportionality constant deduced from Suganuma et al. (2006). For most of this paper, we

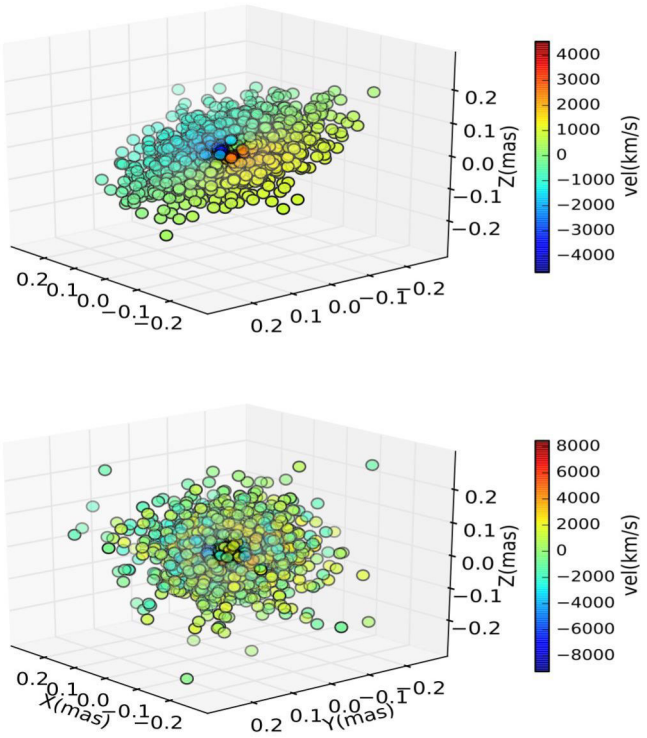

Figure 1. Cloud distribution with the velocity ($\mathrm{km\,s^{-1}}$) in colour code. $M_{\rm bh} = 1e8\,\mathrm{M}_\odot$, $i = 30°$, $R_{\rm in} = 1000R_g$, $\sigma_{\rm blr} = 0.1$ mas with flat Keplerian disc geometry $\omega = 0°$ (upper plot) and spherical geometry $\omega = 90°$ (lower plot).

consider that the ring is uniform, and we do not introduce any skewing related to the inclination, although such a function is easy to introduce in a parametric form. A skewing of the continuum image, with a 'face on' side brighter than the 'back on' side will introduce a measurable phase effect that is briefly discussed in Section 5.4. The continuum brightness distribution $I_{\rm con}(X, Y)$ is normalized to have $\int\int I_{\rm con}(X, Y)\,\mathrm{d}X\mathrm{d}Y = 1$.

Model parameters and its observables: The global intensity is obtained by adding the BLR and continuum intensities

$$I(X, Y, \lambda) = I_{\rm con}(X, Y) + F\, I_{\rm blr}(X, Y, \lambda), \tag{13}$$

where F is the maximum emission line flux, for a measured spectrum $S_M(\lambda_c) = 1$ in the continuum.

This F factor is a characteristic of the emission line chosen for the interferometric observations. The equations show that all differential interferometry signals are proportional to $F/(1 + F)$ but their shape is unaffected. This means that the value F matters only when we are discussing the signal-to-noise ratio (SNR) and the feasibility of interferometric observations. In Section 4, where we discuss the parameters signatures, we use $F = 0.6$ (Table 1), which is the value we observed on 3C 273 for Pa α. It is also close to the $F = 0.69$ mean Pa α value that can be found in Landt et al. (2008). In the feasibility Section 5 we use the best emission line in the K-band set by the redshift of each target. This line is chosen among Pa α, Pa β, Pa γ or Br α and the line strength elements given in Landt et al. (2008) are taken into account in Section 5.

A Fourier transform of the intensity distribution $I(X, Y, \lambda)$ yields the complex visibility, its modulus and phase, with the subsequent absolute and differential visibility and differential phase as mentioned in Section 2.2.

Table 1. Model parameters and the observables.

Parameter	Symbol	Ref. value[a]
BH mass	$M_{\rm bh}$	$1e8\,\mathrm{M}_\odot$
BLR inner radius	$R_{\rm in}$	$200R_g$
BLR width	$\sigma_{\rm blr}$	0.4 mas
Inclination	i	30°
Opening angle	ω	0°
Rest line width	σ_0	$85\,\mathrm{km\,s^{-1}}$
Macroturbulence	$P_{\rm turb}$	0
Anisotropy	$F_{\rm anis}$	0
Continuum size	$R_{\rm rim}$	0.25 mas
Disc position angle	Θ	90°
Object redshift	z	0.02
Emission line flux	F	0.6
Measure	**Symbol**	**Observing technique**
Absolute visibility	$V_{\rm abs}(\lambda)$	OI
Differential visibility	$V_{\rm diff}(\lambda)$	OI
Differential phase	$\phi_{\rm diff}(\lambda)$	OI
Spectrum	$s(\lambda)$	RM or OI
2D Response function	$\psi(v, \tau)$	RM
1D Response function	$\psi(\tau)$	RM

Note. [a]if not stated.

The time delay, between the continuum and the emission line echo, is a function of the corresponding cloud position and defined by

$$\tau(r, Z) = \frac{r - Z}{c}. \tag{14}$$

We compute normalized histogram of time delays τ and velocities V_z in the observer direction to obtain the 2D echo diagram $\Psi(v, \tau)$. The integration of $\Psi(v, \tau)$ over time gives the 1D response function $\Psi(\tau)$, whose centroid is the equivalent time lag $\tau_{\rm cent}$, and the integration over velocity gives the 1D line profile $\Psi(v)$ whose width yields the equivalent range ΔV of the global velocity field.

For a flat Keplerian disc model, narrow-band line images are plotted in the upper panel of Fig. 2 for different spectral channels. As we enter the line at maximum redshift, a line image appears in addition to the continuum, the photocentre shifting perpendicularly to the rotation axis. The photocentre shifts (lower-left panel) goes through an extrema around channels B and C, then cancels in channel D at the centre of line, where the image is symmetric. The blue wing images (E to G) mirror the red wing and the photocentre is shifted in the opposite direction. The emission line profile (lower-right panel) shows a double peaked profile as expected for a thin Keplerian rotation. The line intensity shows maxima (B and F channels) related to the inclination and the equivalent outer edge of the BLR. We see that the images in channels B and F show maximum intensity and extension in the direction $\perp$ to the axis. This corresponds to local minima in the visibility in $\perp$ baseline. The maximum intensity and extension in the $\parallel$ direction is in channel D yields the local visibility minima in $\parallel$ baseline.

4 OBSERVABLE SIGNATURES OF THE MODEL PARAMETERS

In this section, we illustrate the effect of the main model parameters on the OI and RM observables. We have tried to analyse the parameters in an order that allows us to partially separate their observable effects and isolate typical spectro-interferometric signatures. We

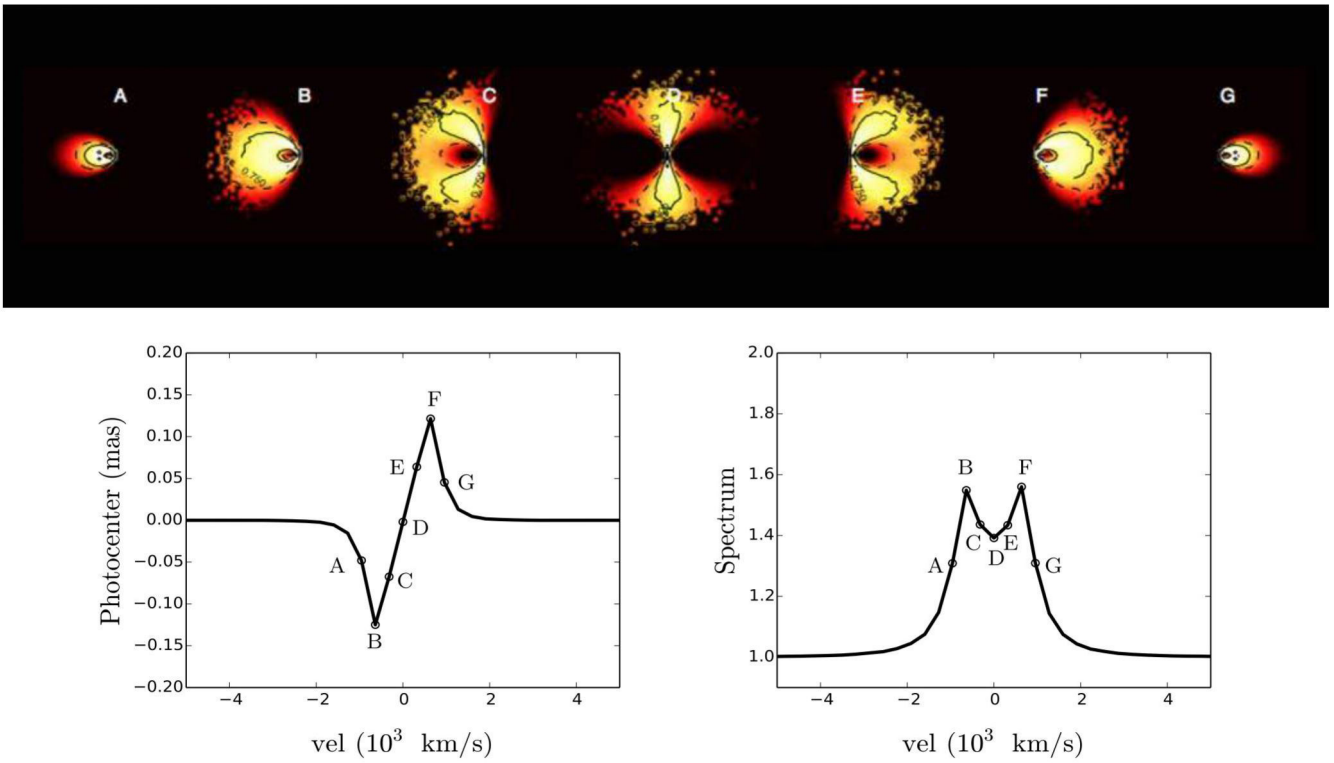

Figure 2. Line intensity map (upper panel) across the emission line for a flat Keplerian disc geometry for seven different spectral channels (marked with the letter). Photocentre displacement perpendicular to the rotation axis (lower-left panel) and emission line profile (lower-right panel) for different spectral channels with resolution $R = 1500$ is plotted. This model is computed considering $\sigma_{\rm blr} = 0.4$ and $i = 30°$.

will discuss first the measurement of the equivalent angular sizes of the BLR that is mostly related to the global amplitude of visibility measurements. Then we will examine how differential visibility and phase can solve the major BLR model ambiguities: the degeneracy between inclination (i), thickness (ω) and the balance between local and global velocity field, that we chose to represent, in a first step, by the width σ_0 of the line profile including all local velocity effects. Finally, we will show how the components of the global velocity field can be separated by differential phase measurements and examine the signatures of other physical phenomena such as the clouds optical thickness and the macroturbulent component of the local velocity field.

4.1 Interferometric BLR size

An estimation of the angular size of the BLR is critical to constrain the $r_{\rm blr}$–L and the $M_{\rm bh}$–L relations. Combined with the RM linear size measurement, it can yield a direct distance measurement (Elvis & Karovska 2002). This angular size can be constrained by a broad-band measurement of the absolute visibility in the continuum combined with a relatively low spectral resolution differential visibility measurement with only one measurement in the emission line.

The left-hand panel of Fig. 3 displays the absolute visibility as a function of $R_{\rm rim}$. With a typical visibility accuracy of current VLTI instruments $\sigma_{\rm avis} \simeq 0.03$, we see that the smallest $R_{\rm rim}$ that can be estimated in the K band with the VLTI baselines is $R_{\rm rim} \simeq 0.15$ mas. An FT, such as the one built-in in GRAVITY (Eisenhauer et al. 2008), should allow us to reduce the absolute visibility error down to $\sigma_{\rm avis} \simeq 0.005$, making it possible to measure down to $R_{\rm rim} \lesssim 0.06$ mas.

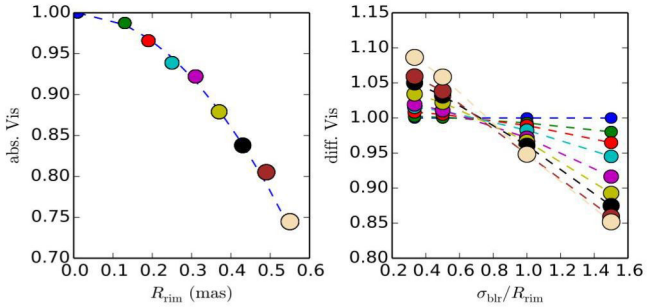

Figure 3. Absolute visibility in the continuum as a function of $R_{\rm rim}$ (left-hand panel) and differential visibility in the line as a function of $\sigma_{\rm blr}/R_{\rm rim}$ (right-hand panel) for 130 m baseline and parallel to the rotation axis.

The right-hand panel in Fig. 3 displays the differential visibility as a function of the ratio of $\sigma_{\rm blr}/R_{\rm rim}$. This measurement exhibits a very good accuracy ($\sigma_{\rm dvis} \lesssim 0.001$) limited only by fundamental noises. It cannot yield the relative sizes $\sigma_{\rm blr}/R_{\rm rim}$ when $|V_{\rm diff} - 1| < 0.001$, if $R_{\rm rim} \lesssim 0.1$ mas at the VLTI, i.e. $(\lambda/B)/R_{\rm rim} \gtrsim 35$. This sets a limit for the super-resolution factor that can be expected from visibility measurements. The uncertainty on the angular size of the BLR will be dominated by the absolute visibility accuracy that is therefore a key specification for BLR size estimation. Note that Fig. 3 confirms the prediction of equation (6) and sets the equivalence between the size parameters $R_{\rm rim}$ and $\sigma_{\rm blr}$: a flat Keplerian BLR model produces the same visibility than a thin ring when $\sigma_{\rm blr}/R_{\rm rim} \simeq 0.7$. If we have differential visibilities for two different baselines (with $(\lambda/B)/R_{\rm rim} \gtrsim 35$ for the shortest baseline), we can obtain $\sigma_{\rm blr}$ and $R_{\rm rim}$ without absolute visibility measurements, but the accuracy of this method has not been evaluated yet.

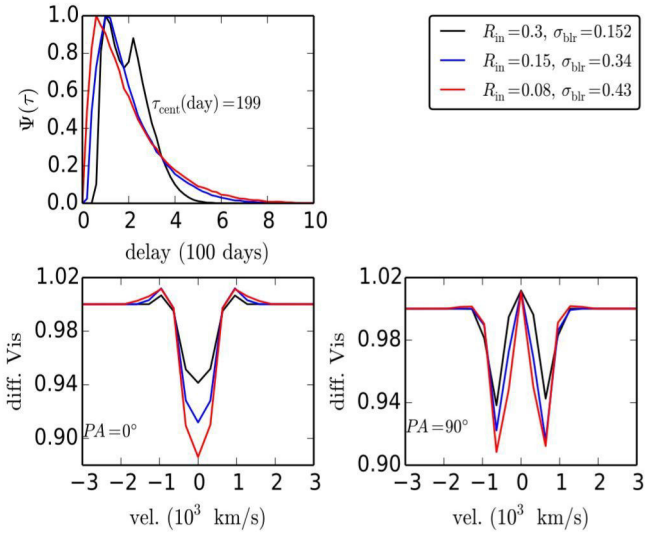

Figure 4. RM 1D response function (upper panel) and visibility in the ∥ (lower-left panel) and the ⊥ (lower-right panel) baselines for different BLR geometries that produce same τ_{cent} but different visibilities.

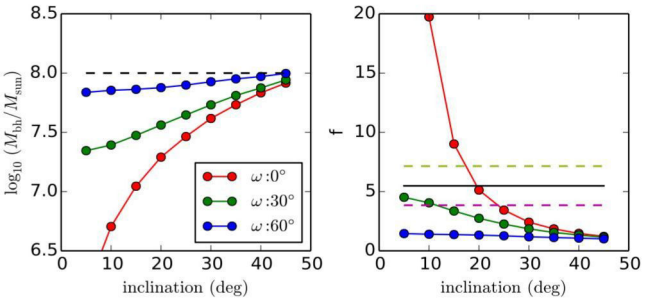

Figure 5. M_{bh} (left-hand panel) and scale factor (right-hand panel) as a function of inclination for different opening angles $\omega = 0°$ (red), 30° (green) and 60° (blue). The input mass of this simulation is 10^8 $M_\odot$. We see that an error on i or ω can result in a very large mass error.

4.2 Interferometric and RM BLR sizes

The different parts of the source contribute to the interferometric and RM sizes with different weights. To illustrate this, we consider different flat geometries with different combinations of R_{in} and σ_{blr} that produce the same equivalent time lag τ_{cent}, from a hollow thin torus (large R_{in} and small σ_{blr}, black line in Fig. 4) to an extended BLR with almost no central hole (small R_{in} and large σ_{blr}, red line in Fig. 4). Fig. 4 shows that these combinations produce very different visibilities. The peak of $\Psi(\tau)$ grows with R_{in} but the centroid τ_{cent} remains constant. The overall shape of the differential visibility $V_{diff}(\lambda)$ curves remains stable, respectively looking like a 'v' and 'w' for the ∥ and the ⊥ baselines. Their amplitude is almost proportional to σ_{blr}. Measuring QSO distances from a combination of OI and RM observations requires a calibration of this effect that will also influence the size–luminosity relation. This will be the scope of next paper on the combination of OI with RM.

4.3 Fundamental geometrical and kinematics parameters

Now that we have estimated the interferometric angular size of the BLR we will constrain the three key parameters that describe the global BLR structure: i, ω and σ_0. Collin et al. (2006), Fine et al. (2010) and Goad et al. (2012) have shown that these parameters dominate the RM scale factor f and hence the virial BH mass estimate. This is illustrated by Fig. 5 where the measured BH mass (left-hand panel) and the scale factor f (right-hand panel) are plotted as a function of i for various values of ω. These values result from the velocity range ΔV estimated by the standard dispersion σ_l of the line profile and the typical time lag τ_{cent} obtained from our model with a fixed input mass and different values of i and ω. f is the ratio of model input mass to the output mass $M_{out} = c\tau_{cent}\Delta V^2/G$. Fig. 5 shows that changes in i and ω can introduce more than a factor 10 error on the mass estimate and shows how important it is to constrain these parameters.

Fig. 6 shows the RM observables for a grid of $(i - \omega)$ with different line widths σ_0 considering a fixed BLR size $\sigma_{blr} = 0.4$ mas. The spectra are plotted on the left-hand panel and the 1D response functions are plotted on the right-hand panel. The green curves show the spectra obtained with a fixed $\sigma_0 = 85\,\mathrm{km\,s^{-1}}$. The width of the spectrum is sensitive to the inclination and the opening angle. For small ω, increasing i clearly leads to the typical double peaked line profile of a Keplerian thin disc. Increasing ω broadens the line profile and blurs the double peaks until it forms flat top line profile, independent of i as we approach a spherical structure with large ω. The red curves represent the line profiles broadened by a change in σ_0 in order to obtain an equivalent global line width $\Delta V = 3300\,\mathrm{km\,s^{-1}}$ in all cases. The corresponding σ_0 is indicated in each picture. The σ_0 broadening blurs all the line details, but for the largest opening angles. The 1D delay transfer function $\Psi(\tau)$ is independent of σ_0. Its exact shape very slightly changes as a function of i that shifts its maximum, and ω that makes the drop sharper for small delays. The RM BLR size $c\tau_{cent}$ is not constrained by these parameters. The overall conclusion of this figure is that RM alone cannot separate i, ω and σ_0 from ΔV and τ_{cent} measurements only. However, a detail line profile analysis could discriminate these parameters up to a certain accuracy.

To show the effect of i, ω and σ_0 on OI observables we plotted the differential phase (left-hand panel) and the differential visibility (right-hand panel) in Fig. 7 for the ∥ (dotted) and the ⊥ (solid) baselines. The photocentre shift between the line-emitting region and the continuum source increases with i, which increases the line of sight velocities. It globally decreases with ω that makes the isoradial velocity regions more and more symmetric. Differential phase for a large opening angle shows sharp turns whereas the high local velocity case shape is much smoother and with reduced amplitude. An increase in σ_0, which blurs the isovelocity zones, also decreases the differential phase amplitude, but for an identical amplitude, the $\phi_{diff}(\lambda)$ function shows much sharper angles for a high ω than for a high σ_0.

Differential visibility is even sharper marker of the different models, if we have sufficient spectral resolution, i.e. sufficient SNR. In low spectral resolution, differential visibility is of little help. However, fine shape of the differential visibility spectacularly differs in different cases. Large opening angles yield a 'w' shape that is independent from the direction of the baseline, while flat structures yield differential visibilities very sensitive to the baseline orientation, as it could be expected from Fig. 2, showing that the global size of the individual spectral bins is strongly different in the rotation axis and in the perpendicular direction. A large local velocity field removes this baseline direction dependence, but changes the curve shape and width.

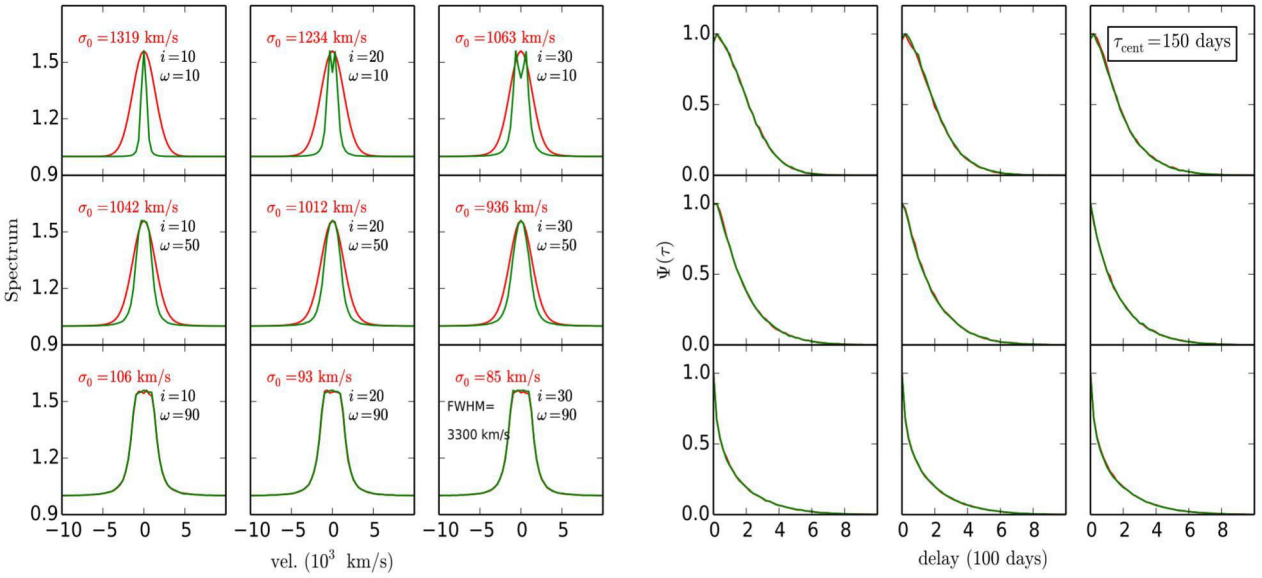

Figure 6. Spectrum (left-hand panel) and 1D response function $\Psi(\tau)$ (right-hand panel) for different inclinations and opening angles. Green curves in each plot obtained with $\sigma_0 = 85\,\mathrm{km\,s^{-1}}$ whereas the red curves are for different σ_0 values as mentioned in the left-hand panel.

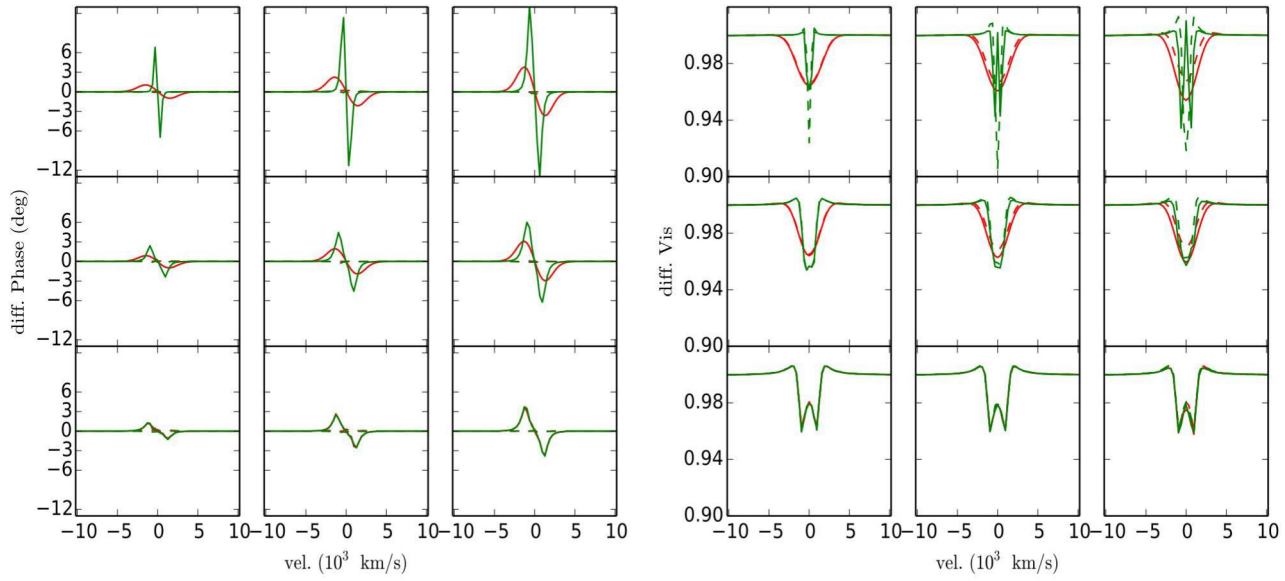

Figure 7. Differential phase in degree (left-hand panel) and differential visibility (right-hand panel) in the ∥ (dotted) and the ⊥ (solid) baselines for the same grid as in Fig. 6.

4.4 Kinematics of the global velocity field

Understanding the global kinematics of the BLR has been a long-standing problem as the sparsely sampled RM data were usually not sufficient to recover emission line as a function of velocity. However, recently various authors have found signatures of rotation, inflow or outflow in the BLR, analysing high-quality RM data and recovering $\Psi(v, \tau)$ (Pancoast et al. 2012, 2014a; Grier et al. 2013). On the other hand, OI has been successful to provide signatures of rotation and expansion velocity in circum-stellar discs (Stee 1996; Meilland et al. 2007, 2012). To find constrains that OI can provide on the kinematics of BLR, we simulated OI as well as RM observables.

Fig. 8 shows the spectrum, the interferometric differential visibility and the differential phase together with the RM 2D and 1D response function for Keplerian rotation and free-fall kinematics models in a thin disc (for details about the echo functions, see Welsh & Horne 1991). We consider four baselines with different position angles: U1 ($B = 130$ m, PA $= 0°$), U2 ($B = 130$ m, PA $= 90°$), U3 ($B = 80$ m, PA $= 0°$) and U4 ($B = 80$ m, PA $= 90°$).

For a Keplerian rotation law, as strongly suggested by Fig. 2, we see that for a baseline perpendicular to the rotation axis (baseline with PA $= 90°$) the difference between the line and the continuum photocentre grows as we enter the line, cancels in the line centre and reverses in the second half of the line. This gives a typical 'S' shaped differential phase with an amplitude proportional to the resolution factor α defined by equation (6). In the direction of the rotation axis (baseline with PA $= 0°$), the photocentre displacement

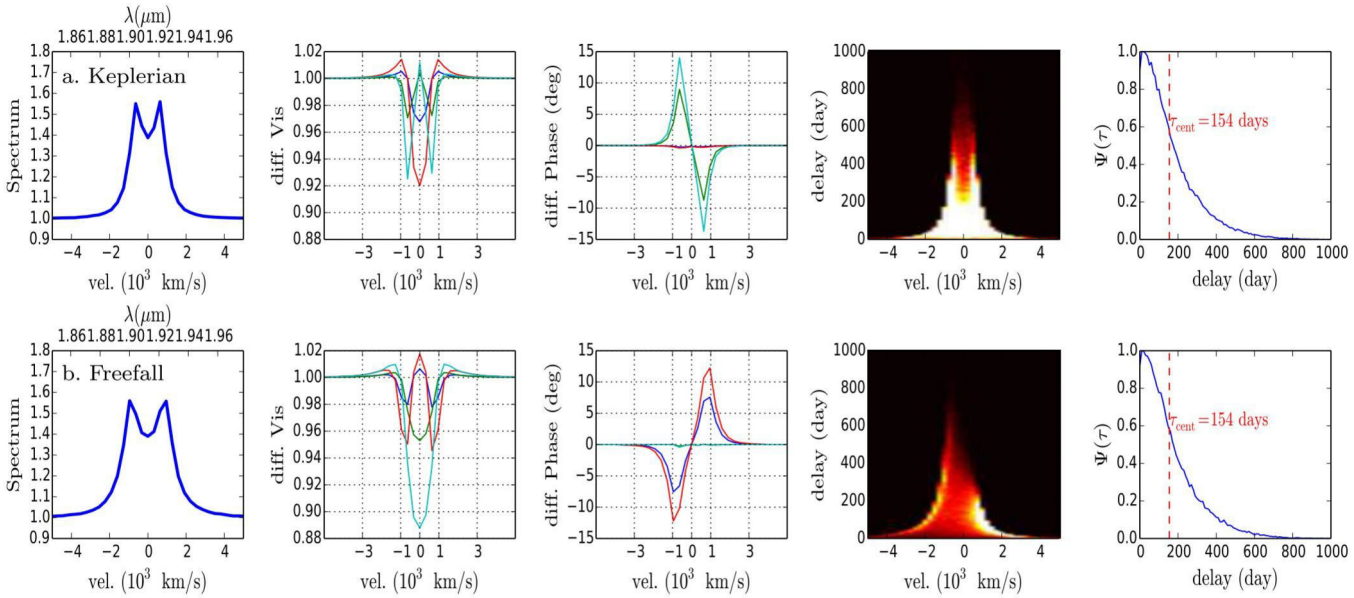

Figure 8. Spectrum (left), differential visibility (left-middle), differential phase (middle), 2D response function (middle-right), 1D response function (right) is plotted for different velocity profiles and for flat geometry cases; Keplerian (upper row) and free-fall inflow (lower row). OI observables are computed using U1 (red), U2 (cyan), U3 (blue) and U4 (green) baselines.

and the differential phase are 0. The differential visibility globally displays a 'w' shape in the $\perp$ direction and a 'v' shape in the $\parallel$ direction, with an amplitude depending on α and going from a peak over the continuum visibility (BLR smaller than the inner dust rim) to a visibility drop with a depth growing with α. For an inflow, the velocity amplitudes are larger for the same BH mass, as shown by the line profile and the 2D echo diagram, but this can be compensated by a mass change and hence introduces a mass uncertainty. The general shape of the curves is similar but the $\parallel$ and the $\perp$ directions are exchanged. The photocentre shift is now $\parallel$ to the rotation axis. The same exchange between the $\parallel$ and the $\perp$ directions can be observed on the differential visibility. The 2D echo diagram is different but this difference can be seen only on very high quality data.

The decisive capacity of differential measurements with OI to discriminate between rotation and inflow/outflow is further illustrated by Fig. 9 that shows the rotation of the global photocentre shift with λ as the ratio between rotation and expansion changes, as first illustrated by Chalabaev (1992) for circumstellar discs. Here the y direction is defined by the projected axis of symmetry, i.e. the position angle of the disc $\Theta = 90^\circ$. In this context, Stee (1996) has shown that the trajectory of the photocentre displacement vector $\epsilon(\lambda)$ yields the strongest constraint on the velocity law index β and Meilland et al. (2007, 2012) have shown that the equatorial disc of Be stars is strongly dominated by a Keplerian rotation ($\beta = 0.5$). The same approach can be applied to disc BLRs.

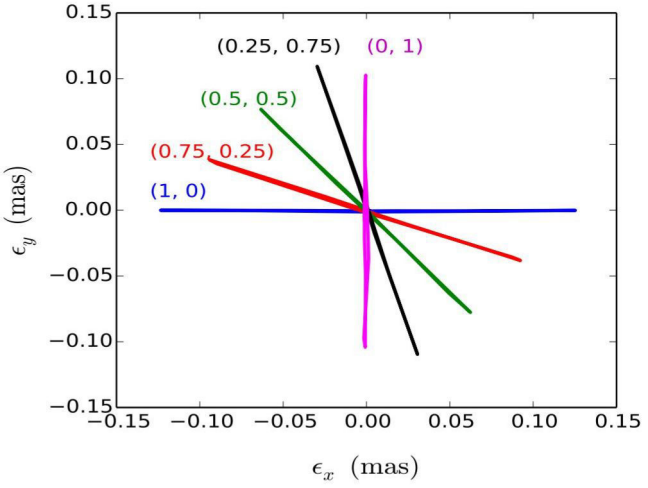

Figure 9. Photocentre displacement in the sky plane for different combinations (V_k, V_f) of Keplerian ($V_k \times V_a$) and free-fall velocity ($V_f \times V_c$) amplitude. The photocentre for pure Keplerian case is represented in blue whereas pure free-fall is presented in magenta. In figure, y is the projected direction of the symmetry axis, i.e. position angle $\Theta = 90$.

4.5 Macroturbulence

Several authors have introduced models where the dynamics of the clouds is dominated by random macroturbulence (Collin et al. 2006; Fine et al. 2008, 2010; Goad et al. 2012; Pancoast et al. 2014a). Macroturbulence in the BLR can provide the internal pressure required to support the disc vertical extent (Shakura & Sunyaev 1973). Collin et al. (2006) suggested various disc geometries and implemented a turbulent velocity that depends on the scaleheight of disc. Goad et al. (2012) showed that for an object of low inclination, macroturbulence dominates the Keplerian velocity and can produce significant broadening.

We use a similar approach and introduce a macroturbulent velocity component in our model defined by equation (10). Fig. 10 shows the effect of macroturbulence on the spectrum (upper), the differential phase (middle) and the differential visibility (lower) in the $\perp$ baseline, for different opening angles ω and turbulence parameters $P_{\rm turb}$. Macroturbulence broadens the line profile and enhances the response of the line wings. From the general shape of all the other observables, it is impossible to discriminate between the effect of an increase of the local line width σ_0 and that of an increased macroturbulence. However, even if we cannot tell if the local velocity field is dominated by σ_0 or by macroturbulence, we can separate

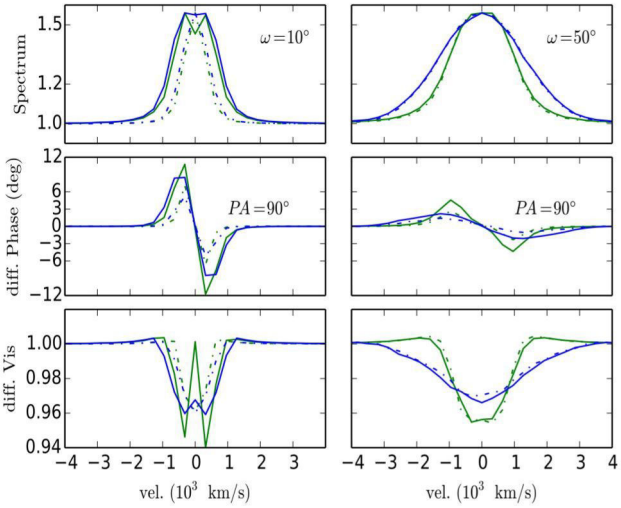

Figure 10. The effect of macroturbulence on different observables for two different inclinations 10° (dash-dot line) and 20° (solid line), and two different opening angles 10° (left-hand column) and 50° (right-hand column). The macroturbulence parameters $P_{\rm turb} = 0$ is plotted in green whereas $P_{\rm turb} = 4$ is plotted in blue.

it from the global velocity field and therefore obtain all the global geometric and kinematic parameters.

Neither RM nor DI can allow an experimental separation of the effects of the local line width and of the macroturbulence as long as we analyse them in terms of equivalent broadening of $s(\lambda)$, $V(\lambda)$, $\Phi(\lambda)$. In all cases, it should affect the balance between the line wings and the line core (the ratio between FWHM and standard dispersion σ_I of the line profile) in a similar way for all observables. A more advanced physical analysis of the local line profiles and of the macroturbulent velocity statistics could yield parameters that could be discriminated by advanced model fits of RM and DI data with very high SNR. However, for the present study, the key point is that they both can be represented by a single parameter (either σ_0 or $P_{\rm turb}$) whose choice does not have any impact on the other parameter estimates.

4.6 Anisotropy

The emission line optical depth of each cloud determines the anisotropy of the re-emitted light, from an isotropic emission for an optically thin cloud to a maximum anisotropy, with dark and bright sides for a thick cloud. O'Brien et al. (1994) computed this for different strong emission lines and suggested that lines with a large ionization parameter are emitted anisotropically at some radii. Anisotropy increases the time lag almost without changing the line profile, which can be a cause of error for the mass estimate (Goad & Wanders 1996).

To compute the effect of anisotropy, we use equation (11) and its effect on the differential phase is shown in Fig. 11. We see a strong effect in the direction of the rotation axis and no effect in the $\perp$ direction. This is because the inclusion of anisotropy reduces the emission on the near-side and increases to the far-side, enhances its brightness and shifts the photocentre towards its direction. The photocentre along the $\parallel$ direction changes rapidly while the photocentre in the $\perp$ direction remains unchanged. Differential phase is therefore a good marker of anisotropy, particularly if we have a priori information on the axis position angle.

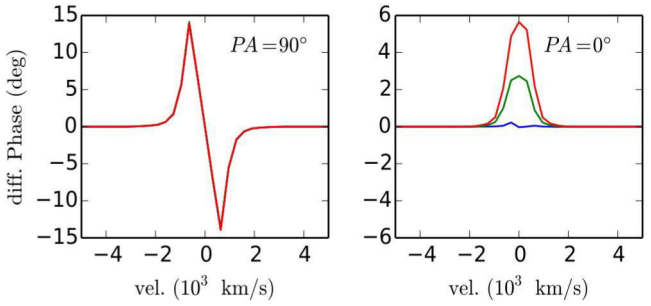

Figure 11. Differential phase in the $\perp$ (left-hand panel) and the $\parallel$ (right-hand panel) baselines for a flat Keplerian disc is plotted for various anisotropic cases: $F_{\rm anis} = 0$ (blue), 0.5 (green) and 1.0 (red).

5 FEASIBILITY OF INTERFEROMETRIC OBSERVATION OF BLR

The potential of OI depends on the number of objects that can be observed. As the VLTI is the only interferometer having near-infrared instruments with a high enough spectral resolution (i.e. $R \geq 500$) to spectrally resolve BLR emission lines because of its 8-m Unit telescopes (UTs), we evaluate this number for current, upcoming and possible VLTI instruments. Other interferometric facilities such as CHARA or NPOI are equipped with substantially smaller telescopes.

In the case of each VLTI instrument, we examine the possibility to observe a target, i.e. to detect and maintain the fringes on the target itself; and the accuracy of its absolute visibility, differential visibility and differential phase.

5.1 Current, incoming and possible VLTI instruments

Our feasibility analysis has been made for the following instruments.

AMBER (Petrov et al. 2007) is the first-generation near-IR spectro-interferometric VLTI instrument. With its standard frame-by-frame processing, it cannot observe AGN in medium resolution (MR), as the current VLTI FT, used to stabilize fringes, is limited to about $K < 9$. However, AMBER can already operate in an alternative mode, called AMBER+ (Petrov et al. 2012), where the full dispersed fringe image is processed, in a way equivalent to a coherent integration of all spectral channels, whatever the SNR per channel is. On the QSO 3C 273 in MR ($R = 1500$), the fringes were detected with an SNR = 3 in typically 1 s. To obtain differential visibility and phase with a sufficient accuracy (respectively, 0.02–0.03 and 1°–2°), it has been necessary to bin the spectral channels down to a resolution 250 as we had only ∼1 h of actual observation. The results achieved with AMBER+ on 3C 273 have been used to validate our SNR computations.

OASIS ('Optimizing AMBER for Spectro-Interferometry and Sensitivity') is a light AMBER modification proposed by Petrov et al. (2014) that could be installed in a few months if ESO opens few days slot in the VLTI planning. It uses spectral encoding to separate the fringe peaks, allowing us to code the interferogram on 4 pixels instead of the 32 pixels currently used in AMBER. Moreover, the spatial filters with fibres, which are not critical for differential observables, would be bypassed by optimized optics that yields a gain in transmission by a factor ∼ 7 with respect to the current AMBER instrument. OASIS would use the current spectrograph and detector of AMBER.

OASIS+ would be a major improvement of AMBER+ with OASIS. It would use a specific spectrograph optimized for BLR obser-

Table 2. Parameters for fringe detection limit[a] and differential observation of BLR[b] plot.

Instrument	Parameters												
	n_T	t_{DIT} (s)	n_p	σ_{RON}	n_{th}	V_{inst}	n_λ	N_{EXP}	n_0	A (cm^2)	S	T	R^c
AMBER	3	0.2	32	11	1.07	0.25	512	100[a], 36 000[b]	45	497 628	0.5	0.01	3000
AMBER+	3	0.2	32	11	1.07	0.25	512	100[a], 36 000[b]	45	497 628	0.5	0.01	3000
OASIS	3	0.2	4	11	1.07	0.25	512	100[a], 36 000[b]	45	497 628	0.5	0.01 × 7	3000
OASIS+	3	0.1	4	3	1.07	0.5	512	200[a], 72 000[b]	45	497 628	0.5	0.01 × 7	1000
GRAVITY	4	60	4[d]	11	1.07	0.75	512	120[b]	45	497 628	0.5	0.01	1000
OASIS+FT	3	60	4	3	1.07	0.75	512	120[b]	45	497 628	0.5	0.01 × 7	1000

Notes. [c]Resolution per spectral pixel. The actual spectroscopic resolution is typically $R/2$.
[d]GRAVITY has a pair wise beam combiner and must be analysed as a 2T interferometer, with 1/3 of the flux in each aperture.

vations with a fixed resolution of 1000 and this would allow using a SELEX detector with much lower read-out noise. It could be developed as a visitor instrument in the 1 million euros range. We note that OASIS+, or any other successor of the second-generation VLTI instruments, is not in the current ESO plans, but it gives an idea of what could be ultimate VLTI performance for AGNs.

GRAVITY (Eisenhauer et al. 2008) is the second-generation VLTI near-IR spectro-interferometric instrument that will be commissioned around 2016. Its main characteristic of interest for a BLR programme is that it has an internal FT that should allow cophased observations up to $K = 10.5$. This allows much longer individual frame time, a higher instrumental visibility and a more stable one. The current GRAVITY plans do not foresee using it without its FT, but an AMBER+ type of processing is possible and would allow performances intermediate between AMBER+ and OASIS for $K > 10.5$.

OASIS+FT refers to the use of OASIS+ with a second-generation FT, with a limiting sensitivity larger than $K = 10.5$. Such an FT would allow increasing the accuracy of the measurements just like the one in GRAVITY, and it would also extend the possibilities of GRAVITY. Currently proposed designs show that FT magnitudes higher than 13 in the K band should be achievable (Meisner, Jaffe & Le Poole 2012; Petrov et al. 2014). The development of such an FT should be a priority for an extended AGN programme with the VLTI.

Table 2 summarizes the observing parameters for these different instruments and modes.

5.2 Interferometric signal and noise

From a general formalism described in Petrov, Roddier & Aime (1986) and updated in Vannier et al. (2006), it is easy to show that the noise on the coherent flux computed from each all-in-one multi-axial interferogram (like in AMBER) is given by

$$\sigma_c = \sqrt{n_T n_* t_{DIT} + n_p \sigma_{RON}^2 + n_T n_{th} t_{DIT}}, \quad (15)$$

where n_* is the source flux per spectral channel, frame and second, n_T is the number of telescopes, t_{DIT} the frame exposure time, n_p is the number of pixels (for multi-axial instruments up to $n_T = 4$, we have $n_p = 4n_T(n_T - 1)/2$), σ_{RON}^2 is the variance of the detector read-out noise and n_{th} is the background flux per spectral channel, frame and second. In the K band, this value is much smaller than the detector noise and hence can be neglected for short exposures. However, for long exposures such as in cophased mode n_{th} should be taken into account. In the K band, $n_{th} = 1.07$ photons s^{-1} cm^{-2} μm^{-1}. For a pair-wise instrument like GRAVITY, the same formula applies with $n_p = 4$ and the flux of each telescope has to be divided by $(n_T - 1)$ that is the number of pairs each aperture is involved in.

The classical SNR on the coherent flux, per spectral channel and per frame (Vannier et al. 2006; Lagarde et al. 2012) is then given by

$$SNR_0 = \frac{C}{\sigma_c} \simeq \frac{n_* t_{DIT} V_{inst}}{\sigma_c}, \quad (16)$$

where V_{inst} is the instrument visibility.

The source flux per spectral channel per frame and per second is given by

$$n_* = n_0 A S T \delta\lambda 10^{-0.4 K_{mag}}, \quad (17)$$

where n_0 is the number of photons per second per cm^2 per μm from a star with $K_{mag} = 0$, outside earth atmosphere, $n_0 = 45 \times 10^6$ photons s^{-1} cm^{-2} μm^{-1}, A is the collecting area of telescope, S is the Strehl ratio with the VLTI adaptive optics system MACAO, T is the overall transmission of the atmosphere, the VLTI and the instrument and $\delta\lambda$ is the spectral bandwidth $= \lambda_0/R$, where R is the resolution.

Standard processing: As the coherent flux C is affected by a random atmospheric phase, we have to average its squared modulus $|C|^2$ over all available spectral channels and several frames. The SNR of such a quadratic average is given by

$$SNR_{std} = \frac{SNR_0^2}{\sqrt{1 + 2SNR_0^2}} \sqrt{N_{EXP} n_\lambda}, \quad (18)$$

where n_λ is the number of spectral channels and $N_{EXP} = \frac{t_{EXP}}{t_{DIT}}$ is the total number of t_{DIT} frames processed in the t_{EXP} total time.

AMBER+ processing: We have developed a new approach where the full-dispersed fringe image is processed, in a way equivalent to a coherent integration of all spectral channels, whatever the SNR_0 per channel is. This data processing is explained in Petrov et al. (2012). Then we still have to make a quadratic average of the other frames and the SNR of this processing is given by

$$SNR_+ = n_\lambda \frac{SNR_0^2}{\sqrt{1 + 2n_\lambda SNR_0^2}} \sqrt{N_{EXP}}. \quad (19)$$

This allowed a gain of typically $\sqrt{n_\lambda}$ which made possible the first observation of 3C 273 with a spectral resolution $R = 1500$. The fringes were detected with a typical $SNR_+ = 3$ in 1 s exposures.

The phase is estimated from the average coherent flux and its accuracy is given by

$$\sigma_\phi = \frac{\langle C \rangle}{\sigma_c \sqrt{2\, n_b}} = \frac{1}{SNR_0 \sqrt{2\, n_b} \sqrt{N_{EXP}}} \quad (20)$$

with $N_{EXP} = 36000$ for 2 h of observations and n_b is the number of binning.

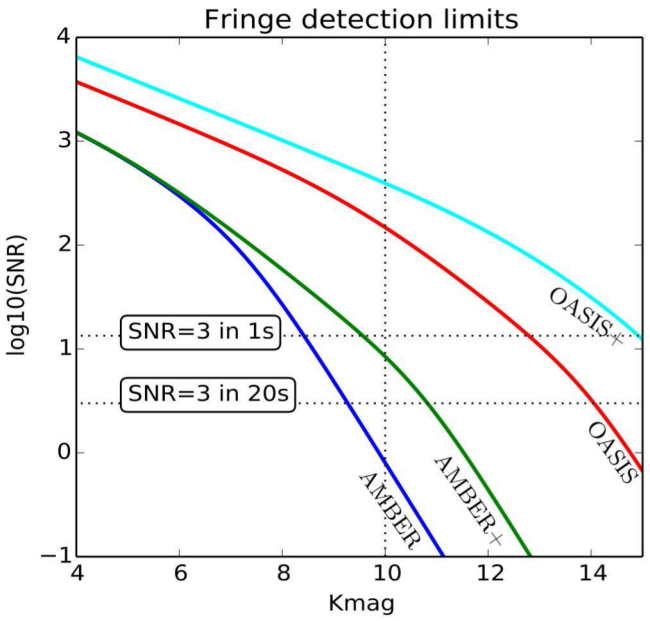

Figure 12. Fringe detection (log10(SNR)) limits for different VLTI instruments. From left to right: standard AMBER performance with 0.2 s frames (blue), current AMBER+ measured performance with incoherent TF2D processing (green), OASIS module (red) and OASIS+ module (cyan). The AMBER+ curve (given here for a maximum of 20 s) is compatible with our experimental result of fringe detection with SNR = 3 in 1 s. The horizontal dotted black line shows the threshold fringe detection limit of SNR = 3 in 1 s and 20 s. The vertical dotted black line corresponds to $K_{\rm mag} = 10$.

In AMBER+, an SNR analysis (Petrov et al. 2014) shows that

$$\sigma_{\phi+} = \sigma_\phi \sqrt{2\frac{\sigma_\phi^2}{n_\lambda} + \frac{1+n_\lambda}{n_\lambda}}. \quad (21)$$

5.3 Fringe detection limit

In Fig. 12, we plotted the fringe detection limit $\log_{10}$(SNR) as a function of $K_{\rm mag}$ using equations (18) and (19) for different instruments like standard AMBER performance with 0.2 s per frame, AMBER+ performance with incoherent TF2D processing, OASIS module and OASIS+ module. The parameters used for the calculation are presented in Table 2. We found AMBER+ could reach up to $K_{\rm mag} \sim 10.5$ and the potential limit of the new OASIS and OASIS+ >13.

We note that fringe detection limit for GRAVITY was not included in that computation as GRAVITY will use an internal FT working up to $K_{\rm mag} = 10.5$. Nevertheless, it should be possible to use GRAVITY without the internal FT in a mode similar to AMBER+ mode, allowing us to observe beyond $K_{\rm mag} = 10.5$, with performances intermediate between AMBER+ and OASIS.

5.4 Signal estimation

In the following, we estimate three interferometric quantities: the absolute visibility in the continuum ($V_{\rm c}$), the amplitude of the differential visibility ($\Delta V_{\rm diff}$) and differential phase ($\Delta\phi_{\rm diff}$) variations in the line.

To estimate the absolute visibility signal, we used equation (6). The amplitude of the differential visibility variation in the line is given by

$$\Delta V_{\rm diff} = 1 - V_*/V_{\rm c} = \frac{1}{V_{\rm c}} \frac{V_{\rm c}F_{\rm c} + V_{\rm l}F_{\rm l}}{F_{\rm c} + F_{\rm l}}, \quad (22)$$

where V_* is the source visibility, $V_{\rm l}$ the source visibility averaged over the line, $V_{\rm c}$ the visibility in the nearby continuum and $F_{\rm l}$ and $F_{\rm c} = 1$ are the line and continuum flux, respectively.

We consider two extreme cases for the differential visibility signal: $R_{\rm blr} \ll R_{\rm rim}$ and $R_{\rm blr} = 2R_{\rm rim}$. In the first case, we assume that the BLR is fully unresolved by the interferometer, i.e. $V_{\rm blr} = 1$. Thus, using equation (22) for the unresolved BLR (i.e. $V_{\rm l} = 1$), we obtain

$$\Delta V_{\rm diff} = -\frac{F_{\rm l}}{1+F_{\rm l}} \frac{\alpha_{\rm c}^2}{1-\alpha_{\rm c}^2}. \quad (23)$$

For the large BLR case, the line visibility can be written as $V_{\rm l} = 1\text{–}2\ (2\alpha_{\rm c})^2$, consequently

$$\Delta V_{\rm diff} = 3\frac{F_{\rm l}}{1+F_{\rm l}} \frac{\alpha_{\rm c}^2}{1-\alpha_{\rm c}^2}. \quad (24)$$

Finally, the typical differential phase amplitude for the BLR is given by

$$\Delta\phi_{\rm diff} = \pi \frac{F_{\rm l}}{1+F_{\rm l}} \alpha_{\rm l} \cos\omega, \quad (25)$$

where $\alpha_{\rm l} = \frac{2R_{\rm blr}}{\lambda/B}$. If the inner rim of the dust torus is inclined and skewed, differential interferometry will also be sensitive to the difference between the global line and the continuum apparent photocentre with maximum amplitude of

$$\Delta\phi_{\rm diff} \simeq \frac{\pi}{2} \frac{F_{\rm l}}{1+F_{\rm l}} \alpha_{\rm c} \sin i. \quad (26)$$

5.5 Selection of targets

We collected a list of all Sy1 and QSOs observable with the VLTI found in the SIMBAD catalogue with search criteria $K_{\rm mag} < 13$, $V_{\rm mag} < 15$ and dec $<15°$. For each source, we estimate the inner rim radius from its magnitude thanks to an extrapolation of Suganuma et al. (2006) known measurements. From this rim radius, we evaluate the possible values of the continuum visibility, differential visibility and phase. These values are compared to the SNR estimates deduced from the source estimated K magnitude. We use the CMB-corrected redshift for each target from NED and K magnitude from 2MASS point source catalog. We collected the list of objects from Bentz et al. (2013) that have classical RM BLR size. Then we fitted the radius with their K magnitude and extrapolate for the objects that do not have the RM BLR size.

For each target, we use the strongest emission line in the K band given the actual redshift of the target. To compute the interferometric observables we used the following values for the normalized line flux $F_{\rm l}$.

(i) $F_{\rm l} = 0.6$ when Pa α is in the K band ($0.08 \leq z < 0.25$)
(ii) $F_{\rm l} = 0.3$ when Pa β is in the K band ($0.4 \leq z < 0.87$)
(iii) $F_{\rm l} = 0.06$ when Br γ is in the K band ($z < 0.08$)
(iv) $F_{\rm l} = 0.12$ when Pa γ is in the K band ($z \geq 0.87$).

These mean values are deduced from the IR line intensity measurements in Landt et al. (2008). The dispersion of line strengths is very large. For example the Brγ line flux goes from 0.01 to 0.18 with a 0.07 mean. This limited data set does not allow good statistics but

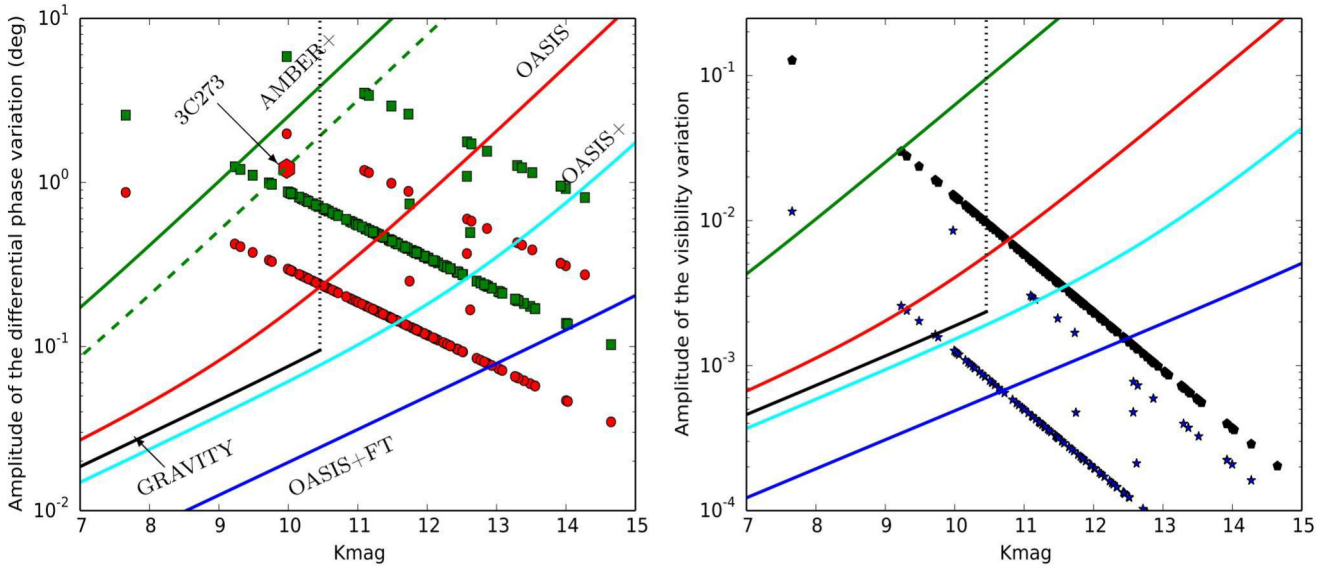

Figure 13. Feasibility of observation of BLR with maximum VLTI 135 m baseline. The left image shows the accuracy of the differential phase in degrees, for the different instruments described in the text (full lines labelled by the instrument name). The differential phase error is dominated by fundamental noise at least down to 0.05°. The points represent the expected differential phase for all Sy1 AGNs and QSOs brighter than $K = 15$ observable in Paranal ($\delta < 15°$). Each source is represented by a red circle, corresponding to the minimum differential phase signal from the RM BLR size estimates, and a green square, corresponding to the maximum differential phase for a skewed continuum image. The 3C 273 point (red octagon) represents the actual differential phase accuracy obtained with AMBER+. This value is on the dotted green line corresponding to the actual spectral channel binning and observation time on 3C 273. The right image represents the differential visibility accuracy from the fundamental noises for different instruments (full lines). The systematic error on differential visibility is below 10^{-3}. For instruments used without an FT (AMBER+, OASIS, OASIS+), the absolute visibility accuracy cannot be better than 0.03. For instruments operated with an FT (GRAVITY, OASIS+FT), we expect to go below 0.003. The points represent the absolute visibility (black polygons) and the differential visibility (blue stars) expected for each source, according to the inner rim size estimated from its luminosity. The horizontal scale gives the estimated K magnitude of the central source.

we used it to estimate that about one third of the targets where Brγ must be used, will eventually be impossible to observe ($F_\mathrm{l} < 0.02$) while our signal estimates are actually pessimistic for half of the targets where F_l is larger than the mean values used here.

5.6 Feasibility of observation

Fig. 13 summarizes the feasibility of observation of BLRs with current, upcoming, and possible VLTI instruments. We found that AMBER+ would observe at most a few sources whereas the GRAVITY will provide high-quality differential measurements on 10–15 sources for which it would also give decisive absolute visibility measurement. On the other hand, OASIS would at least double the number of differential phase measurement (with respect to GRAVITY). Moreover, OASIS+ would again double this accessible number of targets then the OASIS number. A new generation FT would boost the GRAVITY list of targets. The ultimate VLTI performance would be obtained with the new generation FT and OASIS+. Remember that an instrument accessing more targets also gives much better results on the brighter targets.

6 PARAMETER UNCERTAINTY FROM SIMULATED DATA

In Section 4, we described the observables signatures of the main BLR parameters and in Section 5 we evaluated SNR of OI measurements. Eventually, the BLR model parameters will be estimated from a global model fit of RM and OI observables. In this section, we give a first estimate of the accuracy of some parameters after a global fit of OI observables with the SNR of a few typical observations.

6.1 Simulated data sets

To estimate uncertainty of the parameters from OI data, we created mock data sets using the values mentioned in Table 3 and Table 4, considering Gaussian noise on all the spectro interferometric observables. We considered AMBER+ and GRAVITY with absolute visibility accuracy of 3 and 0.5 per cent, respectively. For AMBER+, we considered $\sigma_{\phi_\mathrm{D}} = 0.01$ radian and $\sigma_{V_D} = \sqrt{2} \times \sigma_{\phi_\mathrm{D}}$ (using Petrov et al. 1986 relation between the accuracy of differential visibility and phase set by fundamental noise for unresolved sources). For GRAVITY, we took $\sigma_{\phi_\mathrm{D}} \simeq 0.002$ radian. We considered 0.2 per cent uncertainty on the line flux measurement.

6.2 Recovering parameters from simulated data sets

In order to recover the parameters of the data sets and their associated uncertainties, we optimized the likelihood function that we considered to be Gaussian and defined by

$$p(\mathrm{data}|\mathrm{model}) = \prod_{i=1}^{N} \frac{1}{\sqrt{(2\pi\sigma_i^2)}} \exp\left[-\frac{(\mathrm{data}_i - \mathrm{model}_i)^2}{2\sigma_i^2}\right], \quad (27)$$

where σ_i is the uncertainty on data$_i$. Maximizing the likelihood is identical to minimizing the χ^2. We considered all OI observables, i.e. spectrum, differential visibility, differential phase and absolute visibility are the part of our data sets and minimized the global χ^2. According to Bayes' theorem, the posterior probability distribution

Table 3. Simulated data with fixed $\sigma_0 = 85$ km s^{-1}.

		True parameters			
Data set	Instrument	$\sigma_{\rm blr}$ (mas)	$\log(M_{\rm bh}/{\rm M}_\odot)$	$i(^\circ)$	$\omega(^\circ)$
A	AMBER+	0.4	8	30	40
B	GRAVITY	0.4	8	30	40
C	AMBER+	0.4	8	15	60
		Recovered parameters			
Data set		$\sigma_{\rm blr}$ (mas)	$\log(M_{\rm bh}/{\rm M}_\odot)$	$i(^\circ)$	$\omega(^\circ)$
A		$0.378^{+0.015}_{-0.010}$	$8.059^{+0.126}_{-0.123}$	$24.8^{+5.4}_{-3.5}$	$39.2^{+9.0}_{-7.3}$
B		$0.379^{+0.017}_{-0.015}$	$8.020^{+0.085}_{-0.056}$	$28.5^{+2.0}_{-2.8}$	$37.2^{+4.7}_{-4.7}$
C		$0.386^{+0.026}_{-0.024}$	$7.997^{+0.106}_{-0.076}$	$15.7^{+4.4}_{-3.2}$	$58.7^{+6.9}_{-9.4}$

Table 4. Simulated data with fixed $\sigma_{\rm blr} = 0.4$ mas.

		True parameters			
Data set	Instrument	$\log(M_{\rm bh}/{\rm M}_\odot)$	$i(^\circ)$	$\omega(^\circ)$	$\Delta v_0(2.35\,\sigma_0)$ km s^{-1}
D	AMBER+	8	30	40	500
E	AMBER+	8	30	40	1500
F	AMBER+	8	10	60	1500
		Recovered parameters			
Data set		$\log(M_{\rm bh}/{\rm M}_\odot)$	$i(^\circ)$	$\omega(^\circ)$	$\Delta v_0(2.35\,\sigma_0)$ km s^{-1}
D		$8.008^{+0.088}_{-0.059}$	$28.3^{+3.0}_{-2.8}$	$36.6^{+4.9}_{-4.2}$	$684.8^{+86.8}_{-137.8}$
E		$8.138^{+0.060}_{-0.065}$	$20.8^{+5.4}_{-2.4}$	$40.9^{+3.3}_{-6.6}$	$1324.2^{+172.4}_{-169.7}$
F		$8.004^{+0.134}_{-0.085}$	$18.5^{+9.3}_{-5.5}$	$58.0^{+8.8}_{-18.4}$	$1481.2^{+81.4}_{-171.5}$

p(model|data) is linked with the prior function p(model) which includes any previous knowledge about the parameters:

$$p(\text{model}|\text{data}) \propto p(\text{model}) \times p(\text{data}|\text{model}). \quad (28)$$

We assigned uniform prior to all the parameters except black hole mass for which we used log uniform prior.

To sample the parameters efficiently we used EMCEE package, developed by Foreman-Mackey et al. (2013), which is PYTHON implementation of Affine Invariant Markov Chain Monte Carlo (MCMC) ensemble sampler by Goodman & Weare (2010).

EMCEE explores the full posterior distribution using set of random walkers in each step and the result of the walkers is used for the next step in order to optimize the maximum likelihood. We run EMCEE with 200 walkers and 200 steps. After few steps the samples converge and we consider 150 steps as 'burn-in' phase. Final 50 steps are considered as post burn-in phase and used to estimate the parameters and the uncertainties.

An example of the post burn distribution of samples is shown in Fig. 14, which is obtained for data set B. The scatter plots show the 2D distribution of samples with 1σ ellipse representing the covariance matrix whereas the histograms show 1D cut of the samples. The ellipses indicate moderated degeneracy of the parameters $M_{\rm bh}$–i and $M_{\rm bh}$–ω as well as i–ω, which globally underline the critical sensitivity to the inclination i. For all data sets, the recovered parameters and their 1σ uncertainties are given in Tables 3 and 4. Most of the parameters are recovered within 1σ uncertainty. The maximum uncertainty in $\sigma_{\rm blr}$ is obtained in the case of data set C, which is $0.386^{+0.026}_{-0.024}$ mas. Inclination has maximum uncertainty $24.8^{+5.4}_{-3.5}$ degree, which is found in the case of data set A. Opening angle is constrained well in all data sets and 1σ uncertainty is less than 10°.

As discussed in Section 4.1, OI can provide a semi-independent estimate of the BLR size that can also be deduced from the RM typical time lag. Thus we can concentrate on the degeneracy between i, ω and σ_0 that impacts on the mass measurement. The results of a model fitted with a fixed $\sigma_{\rm blr}$ are given in Table 4.

From a fit of the OI data only, we obtain a good constraint on all the parameters with AMBER+ quality level, with a mass accuracy between ~0.08 and ~0.13 dex. The largest value is obtained for a quite low 10° inclination. This uncertainty is quite similar to that achieved by Pancoast et al. (2011) with simulated RM data. However, when Pancoast et al. (2012) fit the real RM data of Mrk 50, they found a much larger uncertainty that they attribute to the modelling error. Remember that the statistical uncertainty of 0.15 dex obtained in traditional RM result (Bentz et al. 2009a; Denney et al. 2010) neglects the scatter of 0.44 dex in the RM scale factor f (Greene et al. 2010; Woo et al. 2010). In that context, our 0.08–0.13 dex results dealing specifically with the major causes of f dispersion are very encouraging, even if it is a minimum value because this first global fit of OI data uses a very simplified model and a quite limited number of parameters. The more accurate measurements of GRAVITY than AMBER+ will bring very substantial progress, as already indicated by data set B. A global fit of OI and RM data will further improve accuracy of the parameters.

7 DISCUSSION, CONCLUSION AND PERSPECTIVES

This paper is the first in a series on the application of OI to observe QSO BLRs that have or can also be observed with RM. We have presented a three-dimensional model that self-consistently infers the BLR structure from differential interferometry and predicts

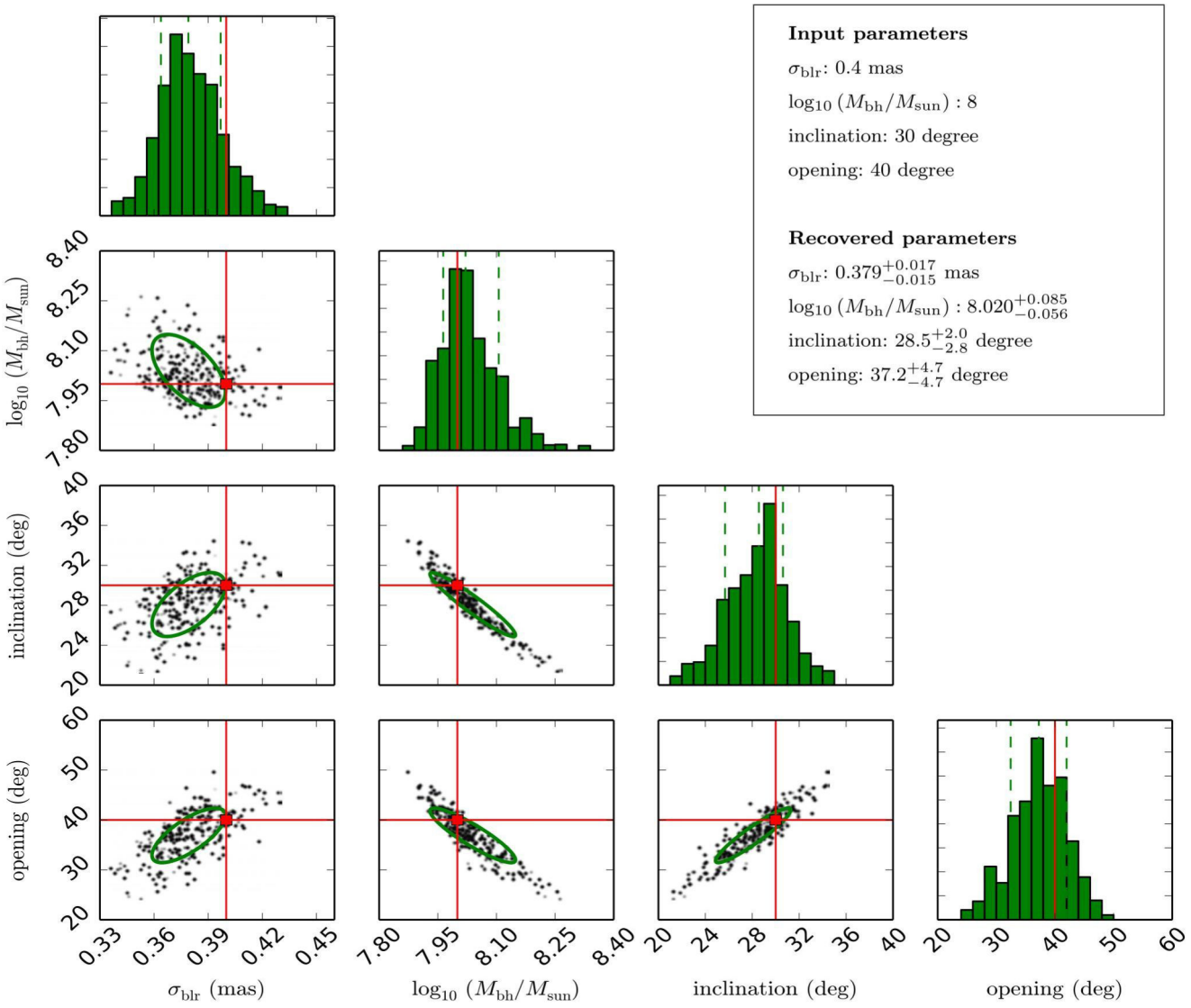

Figure 14. EMCEE post-burn distributions for data set B. The red line shows actual input parameters of this data set. The scatter plots show the projected two-dimensional distributions and green ellipses represents the 1σ regions of the projected covariance matrix. The histograms show the projected one-dimensional distributions with dotted green lines representing mean and the 1σ uncertainties. From top-to-bottom and left-to-right, the panels show BLR width $\sigma_{\rm blr}$, $\log_{10}(M_{\rm bh}/{\rm M}_{\odot})$, inclination i and opening angle ω.

the RM observables. We have restricted ourselves to a limited set of parameters, as our first goal was to understand the typical OI signatures of the BLR features and to evaluate the potential of the QSO BLR observations with the VLTI. However, our model can be very easily updated by changing the properties of the list of clouds making up the BLR, for example with a different radial distribution or by forcing the clouds to be located on a specific surface such as in bowl-shaped BLR models.

We show that OI, with a spectral resolution of the order of 1000, will remove the degeneracies between the inclination i, the opening angle ω and the local velocity field contribution σ_0 that are the main cause for the dispersion of mass estimates from RM using only the equivalent time lag and width of the emission lines. MCMC model fits with the EMCEE package applied to the simulated differential visibility and phase data sets confirmed that OI alone can measure the BH mass, i, ω and σ_0, if we have a good estimate of the BLR angular size. The resulting mass estimate accuracy will be of the order or better than 0.08 dex with AMBER+, (except at inclinations lower than 10°), and will be further improved with GRAVITY. This is much better than the standard mass dispersion of 0.30–0.44 dex that includes the effect of f dispersion (Bentz et al. 2009a; Woo et al. 2010). It is similar to the best advanced model fits of RM data by Pancoast et al. (2011, 2014a). Combining OI and RM will validate these model fits and increase the number of usable equations and therefore the number of parameters that can be fitted and well separated.

We have underlined the importance of high-accuracy absolute visibility measurements. A key condition is the possibility to use an FT that stabilizes the OI transfer function and reduces its calibration errors. However, there are many targets where absolute visibility measurements will not be accurate enough while we will still have accurate differential visibilities and phases. Then it will be necessary to obtain the size information from RM measurements, but this assumes that we can compute the scaling factor between OI and RM sizes discussed in Section 4.1 as well as the scaling factor between OI and RM observations made in different

emission lines. We will come back to this key point at the end of this discussion.

When the global angular size of the BLR has been estimated, either from direct OI observables or from properly scaled RM observables, differential visibilities and phases, or even differential phases alone, are sufficient for accurate mass estimates, if the interferometric observations feature a sufficient SNR. In addition to i, ω and σ_0, these observables constrain the other BLR characteristics such as the nature of the global velocity field (rotation and inflow–outflow velocity laws) or the cloud optical thickness.

To evaluate the potential of interferometric observations of QSO BLRs with the current and near-future VLTI instruments, we have computed the expected accuracy for absolute visibility, differential visibility and phase with current (AMBER+), near-future (GRAVITY) and possible (OASIS, OASIS+ and OASIS+FT) VLTI instruments. This SNR analysis has been checked on our real 3C 273 data from AMBER+ and the values for the other instruments are deduced from elementary cross-multiplications based on the known changes in detector noise, number of pixels, transmission and exposure time of the new instruments. We have considered the possible SNR for all QSOs and Seyfert 1 AGNs observable at Paranal brighter than $K = 15$ that is the potential limit for VLTI observations with OASIS+.

Even if all these BLRs will remain quite unresolved with the VLTI in the K band, we see that measurements are nevertheless possible on many targets. GRAVITY, limited by its internal fringe tracker at $K = 10.5$, will give absolute and differential measurements on half a dozen sources. For about 15 sources, we will have only absolute visibility (but no differential visibility) and differential phase that still allows us to fit all parameters with some loss in accuracy. OASIS would allow 50 per cent increase in the number of targets with absolute visibility and differential phase and would double the number of sources with differential phase measurements. OASIS+ would yield all observables on more than 40 targets. An FT reaching $K \simeq 13$ would be a major breakthrough by extending the number of GRAVITY targets to about 30 and of OASIS+ targets to about 60 and by improving the accuracy on all measurements. This seems well within the reach of the currently proposed designs (Meisner et al. 2012; Petrov et al. 2014). The full sample of VLTI targets would allow trying a general unification of BLR model by studying for example the cross-relations of the key parameters such as the projection factor f, the BLR thickness ω, the local velocity field parameter σ_0 or the rotation-to-inflow velocity ratio as a function of the luminosity. The VLTI, with its full potential, could allow exploring four to five decades of luminosity range. Full imaging of BLRs requires improving the angular resolution by a factor at least 10 that requires a major breakthrough on sensitivity of OI in the visible, on CHARA for example, or the construction of a new interferometer with larger baselines. These are long-term goals, while differential interferometry of QSOs with the VLTI has already started with AMBER, will substantially expand very soon with GRAVITY and can reach its full potential with a new generation FT and a specialized small instrument like OASIS+ in quite less than 5 years.

This paper concentrates on the typical signatures of the BLR parameters in optical interferometric measurements, and on the improvement of the black hole mass estimates. The next papers in our series will treat the issue of distance measurements from combined RM and optical interferometric measurements and, later the improvement and hopefully unification of BLR and dust torus models. The combination of OI and RM measurements raises the problem of the scaling factors between the BLRs seen in different hydrogen lines. Indeed, RM is currently available in the visible while OI with large apertures is developing first in the near-IR. Eventually, there will be RM measurements in the Paα and Paβ as discussed for example by Landt et al. (2013) who show that near-IR offers several advantages over the visible, but it would take some time to accumulate a relevant quantity of data.

On the other hand, OI in the visible might reach the sensitivity needed for some QSO BLR observations around 2020.

For the VLTI applications of the next years, we still have to estimate the scaling factor between different lines. It should be relatively easy to obtain a good approximation from the application of a code like CLOUDY (Ferland et al. 1998, 2013) to the known global geometry of the cloud distribution given by DI alone. Then, it will be possible to combine OI and RM, and to have a better modelling of the scale factor converging iteratively towards the right combination of RM in the visible and DI in the IR. This will be a crucial step, in particular for direct distance estimates from the combination of angular and linear measurements. This study will be the main focus of the second paper in that series concentrating on the measurement of QSO distances and on the calibration of the size–luminosity law, in order to allow QSOs to be used as standard cosmological candles. Another aspect is the combination of BLR observation with the torus observations and in some cases images of the innermost parts of the dust torus with the second generation VLTI instrument MATISSE (Lopez et al. 2012). This will require some substantial modelling to study the dust structure at various wavelengths and use this information to complement the available differential observation of BLR in lines. Thus it will be critical that MATISSE observes all sources on which we can obtain BLR data, with MATISSE itself in the L-band but also with all K-band instruments.

ACKNOWLEDGEMENTS

We thank Walter Jaffe (Leiden University) for a decisive discussion about SNR in coherent and incoherent integration modes, Stephane Lagarde (OCA, Nice) for its initial help with the modelling of interferometric observables, Florentin Millour (OCA, Nice) for its contribution to AMBER+, Frantz Martinache (OCA, Nice) for reading and improving the manuscript, Makoto Kishimoto (Kyoto University), Alessandro Marconi (University of Florence) and Gerd Weigelt (MPIfR, Bonn) for enlightening discussions about OI and AGNs and Daniel Moser Faes (Universidade de São Paulo) for useful discussion about EMCEE.

This research used the SIMBAD data base, which is operated at CDS, Strasbourg, France, the NASA/IPAC Extragalactic Database (NED), which is operated by the Jet Propulsion Laboratory, California Institute of Technology, under contract with NASA and data products from the Two Micron All Sky Survey, which is a joint project of the University of Massachusetts and the Infrared Processing and Analysis Center/California Institute of Technology, funded by the NASA and the National Science Foundation.

SR is supported by the Erasmus Mundus Joint Doctorate Program by Grant Number 2011-1640 from the EACEA of the European Commission.

SR also thanks Jaba and Sunil Rakshit and Neha Sharma (ARIES, India) for their support and encouragement during this work.

REFERENCES

Antonucci R., 1993, ARA&A, 31, 473
Arav N., Barlow T. A., Laor A., Blandford R. D., 1997, MNRAS, 288, 1015

Arav N., Barlow T. A., Laor A., Sargent W. L. W., Blandford R. D., 1998, MNRAS, 297, 990
Bennert V. N., Treu T., Woo J.-H., Malkan M. A., Le Bris A., Auger M. W., Gallagher S., Blandford R. D., 2010, ApJ, 708, 1507
Bentz M. C., Peterson B. M., Pogge R. W., Vestergaard M., Onken C. A., 2006, ApJ, 644, 133
Bentz M. C., Peterson B. M., Netzer H., Pogge R. W., Vestergaard M., 2009a, ApJ, 697, 160
Bentz M. C. et al., 2009b, ApJ, 705, 199
Bentz M. C. et al., 2010, ApJ, 720, L46
Bentz M. C. et al., 2013, ApJ, 767, 27
Berio P., Mourard D., Bonneau D., Chesneau O., Stee P., Thureau N., Vakili F., Borgnino J., 1999, J. Opt. Soc. Am. A, 16, 872
Blandford R. D., McKee C. F., 1982, ApJ, 255, 419
Brewer B. J. et al., 2011, ApJ, 733, L33
Burtscher L. et al., 2013, A&A, 558, A149
Chalabaev A., 1992, in Beckers J. M., Merkle F., eds, ESO Conf. Workshop Proc. Vol. 39, Photocenter Versus Wavelength for a Gaseous Disk Envelope. ESO, Garching bei Munchen, p. 403
Collin S., Kawaguchi T., Peterson B. M., Vestergaard M., 2006, A&A, 456, 75
Decarli R., Labita M., Treves A., Falomo R., 2008, MNRAS, 387, 1237
Denney K. D. et al., 2010, ApJ, 721, 715
Eisenhauer F. et al., 2008, in Schöller M., Danchi W. C., Delplancke F., eds, Proc. SPIE Conf. Ser. Vol. 7013, Optical and Infrared Interferometry. SPIE, Bellingham, p. 70132A
Elvis M., Karovska M., 2002, ApJ, 581, L67
Ferland G. J., Korista K. T., Verner D. A., Ferguson J. W., Kingdon J. B., Verner E. M., 1998, PASP, 110, 761
Ferland G. J. et al., 2013, Rev. Mex. Astron. Astrofis., 49, 137
Fine S. et al., 2008, MNRAS, 390, 1413
Fine S., Croom S. M., Bland-Hawthorn J., Pimbblet K. A., Ross N. P., Schneider D. P., Shanks T., 2010, MNRAS, 409, 591
Foreman-Mackey D., Hogg D. W., Lang D., Goodman J., 2013, PASP, 125, 306
Goad M., Wanders I., 1996, ApJ, 469, 113
Goad M. R., Korista K. T., Ruff A. J., 2012, MNRAS, 426, 3086
Goodman J., Weare J., 2010, Commun. Appl. Math. Comput. Sci., 5, 65
Greene J. E. et al., 2010, ApJ, 721, 26
Grier C. J. et al., 2013, ApJ, 764, 47
Jaffe W. et al., 2004, Nature, 429, 47
Kaspi S., Smith P. S., Netzer H., Maoz D., Jannuzi B. T., Giveon U., 2000, ApJ, 533, 631
Kelly B. C., Bechtold J., Siemiginowska A., 2009, ApJ, 698, 895
Kishimoto M., Hönig S. F., Beckert T., Weigelt G., 2007, A&A, 476, 713
Kishimoto M., Hönig S. F., Tristram K. R. W., Weigelt G., 2009, A&A, 493, L57
Kishimoto M., Hönig S. F., Antonucci R., Barvainis R., Kotani T., Millour F., Tristram K. R. W., Weigelt G., 2012, J. Phys. Conf. Ser., 372, 012033
Kishimoto M. et al., 2014, A&A, submitted
Krolik J. H., 2001, ApJ, 551, 72
Labeyrie A., 1978, ARA&A, 16, 77
Labeyrie A., Schumacher G., Dugue M., Thom C., Bourlon P., 1986, A&A, 162, 359
Lagarde S. et al., 2012, in Delplancke F., Rajagopal J. K., Malbet F., eds, Proc. SPIE Conf. Ser. Vol. 8445, Optical and Infrared Interferometry III. SPIE, Bellingham, p. 84452J
Landt H., Bentz M. C., Ward M. J., Elvis M., Peterson B. M., Korista K. T., Karovska M., 2008, ApJS, 174, 282
Landt H., Ward M. J., Peterson B. M., Bentz M. C., Elvis M., Korista K. T., Karovska M., 2013, MNRAS, 432, 113
Lopez B. et al., 2012, in Delplancke F., Rajagopal J. K., Malbet F., eds, Proc. SPIE Conf. Ser. Vol. 8445, Optical and Infrared Interferometry III. SPIE, Bellingham, p. 84450R
Marconi A., Maiolino R., Petrov R. G., 2003, Ap&SS, 286, 245
Meilland A. et al., 2007, A&A, 464, 59
Meilland A., Millour F., Kanaan S., Stee P., Petrov R., Hofmann K.-H., Natta A., Perraut K., 2012, A&A, 538, A110
Meisner J. A., Jaffe W. J., Le Poole R. S., 2012, in Delplancke F., Rajagopal J. K., Malbet F., eds, Proc. SPIE Conf. Ser. Vol. 8445, Optical and Infrared Interferometry III. SPIE, Bellingham, p. 84451L
O'Brien P. T., Goad M. R., Gondhalekar P. M., 1994, MNRAS, 268, 845
Onken C. A., Ferrarese L., Merritt D., Peterson B. M., Pogge R. W., Vestergaard M., Wandel A., 2004, ApJ, 615, 645
Pancoast A., Brewer B. J., Treu T., 2011, ApJ, 730, 139
Pancoast A. et al., 2012, ApJ, 754, 49
Pancoast A., Brewer B. J., Treu T., 2014a, MNRAS, 445, 3055
Pancoast A., Brewer B. J., Treu T., Park D., Barth A. J., Bentz M. C., Woo J.-H., 2014b, MNRAS, 445, 3073
Peterson B. M., 1993, PASP, 105, 247
Peterson B. M., 2001, in Aretxaga I., Kunth D., Mújica R., eds, Advanced Lectures on the Starburst-AGN Connection, Variability of Active Galactic Nuclei. World Scientific, Singapore, p. 3
Peterson B. M. et al., 2004, ApJ, 613, 682
Petrov R. G., 1989, in Alloin D. M., Mariotti J.-M., eds, NATO ASIC Proc. 274: Diffraction-Limited Imaging with Very Large Telescopes Differential Interferometry. Kluwer, Dordrecht, p. 249
Petrov R., Roddier F., Aime C., 1986, J. Opt. Soc. Am. A, 3, 634
Petrov R. G., Malbet F., Richichi A., Hofmann K.-H., Mourard D., Amber Consortium, 2001, C. R. Phys., 2, 67
Petrov R. G. et al., 2007, A&A, 464, 1
Petrov R. G., Millour F., Lagarde S., Vannier M., Rakshit S., Marconi A., weigelt G., 2012, in Delplancke F., Rajagopal J. K., Malbet F., eds, Proc. SPIE Conf. Ser. Vol. 8445, Optical and Infrared Interferometry III. SPIE, Bellingham, p. 84450W
Petrov R. G. et al., 2014, in Rajagopal J. K., Creech-Eakman M. K., Malbet F., eds, Proc. SPIE Conf. Ser. Vol. 9146, Optical and Infrared Interferometry IV. SPIE, Bellingham, p. 91462P
Rakshit S., Petrov R. G., 2014, in Rajagopal J. K., Creech-Eakman M. K., Malbet F., eds, Proc. SPIE Conf. Ser. Vol. 9146, Optical and Infrared Interferometry IV. SPIE, Bellingham, p. 91460Q
Shakura N. I., Sunyaev R. A., 1973, A&A, 24, 337
Stee P., 1996, A&A, 311, 945
Suganuma M. et al., 2006, ApJ, 639, 46
Urry C. M., Padovani P., 1995, PASP, 107, 803
Vannier M., Petrov R. G., Lopez B., Millour F., 2006, MNRAS, 367, 825
Vestergaard M., Peterson B. M., 2006, ApJ, 641, 689
Watson D., Denney K. D., Vestergaard M., Davis T. M., 2011, ApJ, 740, L49
Welsh W. F., Horne K., 1991, ApJ, 379, 586
Woo J.-H. et al., 2010, ApJ, 716, 269
Zu Y., Kochanek C. S., Peterson B. M., 2011, ApJ, 735, 80

This paper has been typeset from a TEX/LATEX file prepared by the author.

VLTI/AMBER differential interferometry of the broad-line region of the quasar 3C273

Romain G. Petrov*[a], Florentin. Millour[a], Stéphane Lagarde[a], Martin Vannier[a], Suvendu Rakshit[a], Alessandro Marconi[b] and Gerd Weigelt[c]
[a]Laboratoire Lagrange, UMR 7293, University of Nice Sophia-Antipolis, CNRS, Observatoire de la Côte d'Azur, BP 4229, 06304 Nice Cedex 4, France; [b]Department of Physics and Astronomy, University of Florence, Largo Enrico Fermi 2, 50125, Firenze, Italy; [c]Max Planck Institute für Radioastronomie, Auf dem Hügel 69, 53121, Bonn, Germany.

ABSTRACT

Unveiling the structure of the Broad-Line Region (BLR) of AGNs is critical to understand the quasar phenomenon. Resolving a few BLRs by optical interferometry will bring decisive information to confront, complement and calibrate the reverberation mapping technique, basis of the mass-luminosity relation in quasars. BLRs are much smaller than the angular resolution of the VLT and Keck interferometers and they can be resolved only by differential interferometry very accurate measurements of differential visibility and phase as a function of wavelength. The latter yields the photocenter variation with λ, and constrains the size, position and velocity law of various regions of the BLR. AGNs are below the magnitude limit for spectrally resolved interferometry set by currently available fringe trackers. A new "blind" observation method and a data processing based on the accumulation of 2D Fourier power and cross spectra permitted us to obtain the first spectrally resolved interferometric observation of a BLR, on the K=10 quasar 3C273. A careful bias analysis is still in progress, but we report strong evidence that, as the baseline increases, the differential visibility decreases in the Pa_α line. Combined with a differential phase smaller than 3°, this yields an angular equivalent radius of the BLR larger than 0.4 milliarcseconds, or 1000 light days at the distance of 3C273, much larger than the reverberation mapping radius of 300 light days. Explaining the coexistence of these two different sizes, and possibly structures and mechanisms, implies very new insights into the BLR of 3C273.

Keywords: Quasars, AGN, Broad Line Region, Optical Interferometry, Differential Interferometry, Spectro-astrometry. Data Processing.

1. INTRODUCTION

1.1 QSOs and their BLR

Quasars and Active Galactic Nuclei (AGN) are extremely bright sources almost certainly powered by accretion onto a central super massive black hole (SMBH). They dominate the night sky in many wavelength domains and radiate 1/5 of the power in the Universe. They are important to the evolution of their galaxy and, as they can be observed at very high redshifts, they are tags to the global evolution of the Cosmos. They are the seed of extreme physical processes and one of the main targets of relativistic astrophysics.

The main components of an AGN are the central SMBH surrounded by a very compact accretion disk emitting mainly in the continuum. The nucleus is surrounded by a dust torus that obscures the central region in type 2 AGNs[1]. Some of the material inflowing from the galaxy is eventually ejected, and might contribute to the high-velocity jets.

Type 1 Active Galactic Nuclei are not obscured by the dust torus and show broad emission lines (and sometimes absorption lines), with widths of several thousands of km/s. This broad line region (BLR), sometimes called the "atmosphere" of the quasar[2], is the crossroad of the inflow and outflow of material. Understanding the broad line regions "is of critical importance to understand the quasar phenomenon: (1) to understand how the accretion/outflow processes

* Contact: romain.petrov@unice.fr; phone +33 04 92 00 39 61; lagrange.oca.eu.

Optical and Infrared Interferometry III, edited by Françoise Delplancke, Jayadev K. Rajagopal, Fabien Malbet,
Proc. of SPIE Vol. 8445, 84450W · © 2012 SPIE · CCC code: 0277-786/12/$18 · doi: 10.1117/12.926595

work in AGNs and (2) to understand the geometry and kinematics of the BLR to correct the AGN black hole mass measurement"[3]. So far, the morphological information about BLRs is given by reverberation mapping (RM), which studies the delay needed for an intensity variation generated near the accretion disk in the continuum to be echoed by the different velocity bins of an emission line. This yields an echo diagram $\psi(V,t)$ that in theory can constrain very strongly the morphology of the BLR. In practice, we can generally measure only the line profile ($L(V) = \int \psi(V,t)dt$), which yields a radial velocity amplitude ΔV and the mean delay τ between the continuum flux variation and the global response of a central part of the emission line. The delay τ is related to the equivalent width of the delay transfer function $\int \psi(V,t)dt$. These two measures yield an estimate of the black hole mass, taken to be:

$$M_{BH} = fr\Delta V^2/G \quad (1)$$

where $r = \tau c$ is the reverberation mapping radius of the BLR. The projection factor f, the radius r and the line width ΔVdepend on the exact morphology and kinematics of the BLR, and the resulting uncertainty on the BH mass can exceed a factor three[3], with important consequences on the broadly used general mass-luminosity relationship for QSOs.

1.2 Interferometric observations of AGN dust tori

After pioneering works by Jaffe[4] and Swain[5] in 2004, a handful of Sy1 AGNs have been successfully observed in the last two years by optical interferometry in low spectral resolution in the K band, with the Keck Interferometer[6] and with the VLTI[7]. The broadband absolute visibility in the K band is fairly high but reveals a partial resolution of the AGN image in the near-infrared continuum. There are several contributions to the continuum spectra: the dust torus, probably dominated by its hotter part that is at the inner rim; the central very compact accretion disk, the gas in the BLR itself and the synchrotron emission. From theory, spectral energy distribution, light curves and polarizations considerations, Kishimoto[6,8] evaluates that the K band continuum image is dominated by the ring-like inner rim of the dust torus and derives its equivalent radius. Higher spectral resolution observations in an emission line can select the contribution of the gas producing the BLR and constrain its position and angular size, as discussed below.

1.3 Differential interferometry of BLRs

The largest reverberation mapping radii reach a few hundreds of light days. At the distance of the nearest Quasars, this corresponds to angular sizes of the order of typically 100 μas, well below the resolution limit of any current optical interferometer.

It is possible to obtain angular information on non-resolved sources by measuring the displacement of their photocenter with wavelength. This has been proposed first in the context of speckle interferometry[9], extended to long baseline interferometry[10] and has been one of the design parameters of the VLTI focal instrument AMBER[11], which has given several results with an accuracy better than 30 μas[12]. For sources much smaller than the resolution limit λ/B, a photocenter displacement $\varepsilon(\lambda)$ in the direction of the baseline B will produce a differential phase $\phi(\lambda)$ given by[10]:

$$\phi(\lambda) = 2\pi\frac{B}{\lambda}\varepsilon(\lambda) \quad (2)$$

If α is the equivalent angular size of the source, the closure phase $\Psi(\lambda)$ decreases as α^3, the visibility drop $1 - V(\lambda)$ decreases as α^2, and the amplitude of the differential phase $\phi(\lambda)$ decreases as α, which makes it the most useful observable to seek angular information on non resolved targets observed at high SNR[13]. In this paper we will discuss and illustrate the method on the quasar 3C273. Figure 1 displays the expected velocity field of a Keplerian disk BLR and the corresponding photocenter and differential phase variations[14], observed through the Paschen α line in spectral bins of 400 km/s. For the quasar 3C273 the expected photocenter displacement is of the order of 20 μas, i.e. about 0.5% of the interferometer resolution. Measuring it requires an accumulated SNR=200 on the coherent flux. With AMBER[11] on the VLTI with the UTs, this can be achieved in typically 10 to 20 minutes if we are fringe tracking and 2 or 3 hours if we have to observe in the "blind mode" described below. Measuring a photocenter displacement will constrain the geometry of the BLR. For example, a Keplerian disk and a virialized 3D distribution of clouds with the same reverberation mapping radius r and line width ΔV have very different photocenter displacements. The photocenter $\vec{\varepsilon}(\lambda)$ for a Keplerian disk is illustrated in figure 1. The 3D distribution will give zero photocenter displacement. Combining photocenter displacement measures with the reverberation mapping information should allow us to identify a model for the BLR structure and velocity field. Then, photocenter measures yield the velocity as a function of radius function and hence the mass of the SMBH. It will allow a more precise estimate of the RM projection factor f, a better separation between global and local velocity field effects and then a better measure of ΔV. This will constrain the mass of the observed

quasar and of all quasars with similar RM properties. In addition, the combination of the angular photocenter measure with the linear RM radius yields a direct estimate of quasar distance.

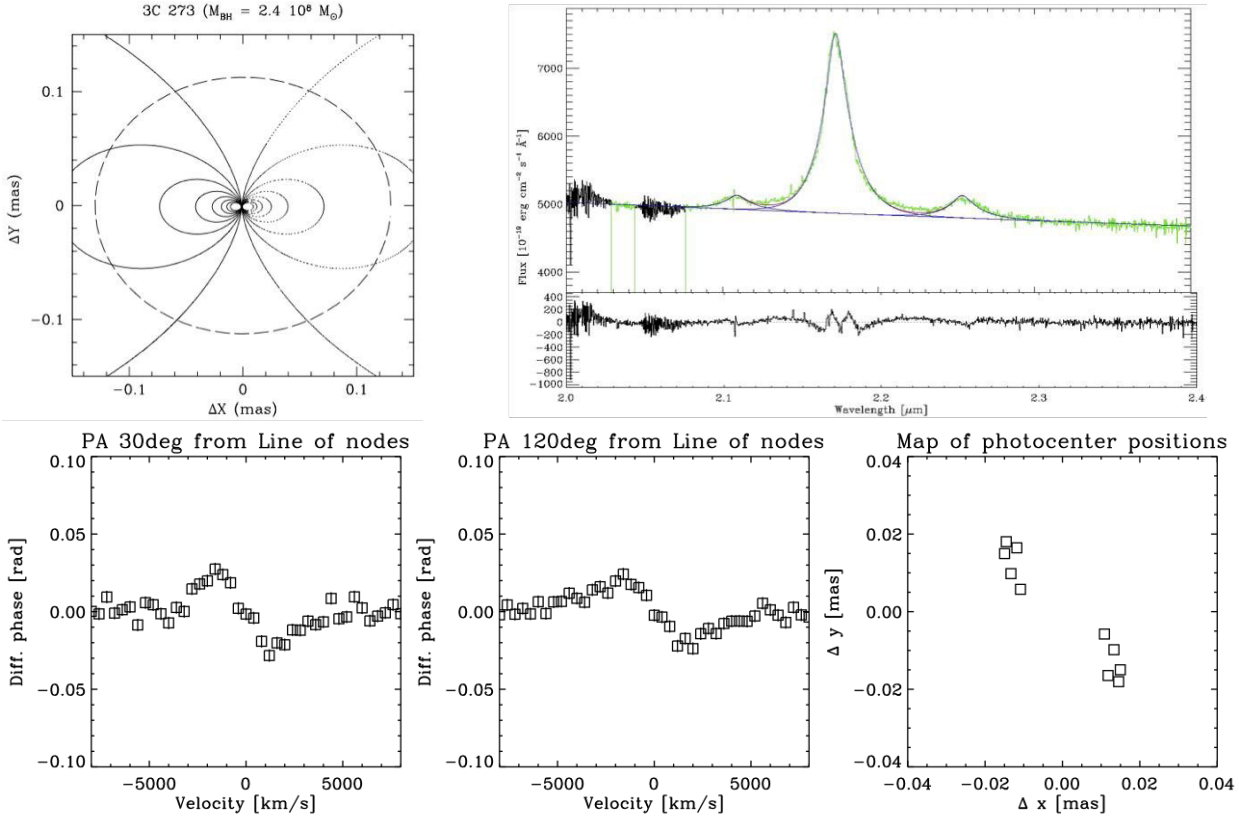

Figure 1: Evaluation of the photocenter displacement and differential phase for a Keplerian disc BLR in 3C273. Top left: equal radial velocity curves in a Keplerian disk with 30° inclination. The curves delimitate 400 km/s bins. The photocenter of the BLR in each bin is reduced by the contribution of the continuum, indicated by the measured Pa_α line profile (top-right). The resulting photocenter, in the bottom right figure, has amplitude of $\pm 20 \mu as$. With a 100m baseline this gives phase amplitude of up to 0.05 radians (2.5°) depending of the angle between the baseline and the photocenter displacement direction, as illustrated in the bottom-left and bottom-center figures. The error boxes have a size of 2°.

1.4 3C273

3C273 is the brightest nearby quasar and one of the "brightest known sources in the Universe". It is red-shifted enough for the Pa_α line to be in the K band and this makes it particularly suited for these observations because the emission is at least two times stronger in Pa_α than in Br_γ. The main characteristics of 3C273 are:

- Magnitude: K=9.7
- Red shift: z=0.16
- Paschen α line center: 2.17 μm
- Paschen α line width: $\Delta V = 3400\ km/s$
- Reverberation mapping radius, in H_γ: 307^{+69}_{-91} corresponding to 95 μas[15]
- Reverberation mapping radius, in H_α: 514^{+65}_{-64} corresponding to about 160 μas[15]
- Absolute visibility in the K band (Keck Interferometer, 84 m projected baseline) [8]: 0.978 ± 0.017
- Radius of the inner rim of torus: 0.81 ± 0.34 pc corresponding to 0.296 ± 0.124 mas[8]

2. BLIND MODE OBSERVATIONS AND 2DFT DATA PROCESSING

To study the BLR we need to resolve spectrally the emission line. A spectral resolution of 200 gives a few points in the line and global constraints on the BLR position and size. A resolution higher than 500 gives access to more than 10 velocity bins and to a fit of the global velocity law. In the near infrared, optimized observations at such resolutions imply the use of a fringe tracker to stabilize the fringes and allow exposure times longer than the piston coherence time, necessary to get out of the detector noise regime. When we first proposed differential interferometry observations of BLRs with the AMBER/VLTI instrument[11], we assumed fringe tracking and our "conservative" estimation for photocenter accuracy was of about 2 μas in 1 hour of observation for K=10. This would allow to apply the technique to two dozens of targets.

The ESO call for proposals[16] for the AMBER/VLTI instrument offers medium resolution observations only at magnitude permitting fringe tracking, which is 7.5 with the UTs in the CfP and can approach 8.5 in very good conditions. The severe limitation of FT limiting magnitude seems a general situation. The reason is that current fringe trackers need a sufficient SNR in extremely short exposures, to be able to freeze the piston at a fraction of wavelength. The consequence is that it will be very difficult to have fringe trackers allowing the observations of AGNs in medium spectral resolution.

Actually, it is not necessary to detect fringes in each individual frame. With the medium spectral resolution of AMBER, the coherence length in the K band is of about 3 mm. The atmospheric piston jitter has a RMS amplitude of typically a few tens of microns and the delay line model errors and drift are below 100 μm/mn. So, after centering the fringes on a bright calibrator, we have at least half an hour to observe a faint target with the guarantee that the fringes are present in the data, even if each individual frame looks just as detector noise. We still have to make exposures short enough to have a good contrast of the fringes. We have to integrate values which are not sensitive to the piston value but still contain information about the source visibility, differential phase and closure phase.

2.1 2DFT fringe detection

All the interferometric quantities that can be averaged in spite of an unknown and variable phase in individual interferograms can be used to reduce data recorded in blind mode. This includes the modulus of Fourier interferograms, yielding source visibility, the Fourier bi-spectrum, yielding closure phase, and cross spectra between different spectral channels yielding the chromatic differential phase and visibility. We have chosen to use the 2D Fourier transform of x-λ interferograms, similar to this used in REGAIN/GI2T and later VEGA/CHARA[17]. It has the advantage to allow a straightforward and unambiguous detection of the average group delay after some integration time and is therefore easy to use as a low frequency coherencing sensor correcting slow drifts of the OPD. It has also some similarity with the tool that we use to analyze the dark current and sky images on our detector and correct our data from detector fringes[18].

Let's $i_m(x,\lambda)$ be the AMBER x-λ image, with its 3 dispersed fringe patterns, illustrated in figure 2a. As a first step, we resample the data to obtain the interferogram $i(x,\sigma)$ where the fringes in all spectral channels have the same interfringe (corresponding to an average wavelength $\bar{\lambda} = 1/\bar{\sigma}$) and the spectral channels are equally spaced in wavenumber σ=1/λ. This is done by a bilinear interpolation and should have a limited impact on the quality of the data since our frames are substantially oversampled both in spatial and spectral directions. The Fourier transform of $i(x,\sigma)$ in each spectral channel yields the 1d Fourier interferogram $I(u,\sigma)$ which can be written as :

$$I(u,\sigma) = \mathcal{F}_x[i(x,\sigma)] = n(\sigma)F(u,\sigma)\sum_i n_i + \sum_{i,j>i}\sqrt{n_i n_j}\,\Omega(\mathrm{u},\sigma)e^{2i\pi\sigma p_a^{ij}} \quad (3)$$

where $n_i$is the total contribution of telescope i to the number of photons in the interferogram ; $n(\sigma)$ is the source spectrum as seen by the instrument ; $F(u,\sigma)$ is the Fourier transform of the resampled interferometric window, $p_a^{ij}$is the achromatic part of the piston difference on the baseline i-j and $\Omega(\mathrm{u},\sigma)$ is the Fourier transform of the source seen by the instrument, defined by :

$$\Omega(u,\sigma) = n(\sigma)V_I(u,\sigma)V_*(u,\sigma)\exp\left[\, i\phi_*(u,\sigma) + i\phi_I(u,\sigma) + 2i\sigma p_c^{ij}(\sigma)\right] * \quad F(u,\sigma) \quad (4)$$

where $V_I(u,\sigma)\ and\ V_*(u,\sigma)$ are the instrument and source visibility at the spatial frequency u and wavenumber σ; $\phi_I(u,\sigma)\ and\ \phi_*(u,\sigma)$ are the corresponding instrument and source phase and $p_c^{ij}(\sigma)$ is the chromatic part of the piston difference :

$$p^{ij}(\sigma) = p_i(\sigma) - p_j(\sigma) = p_a^{ij} + p_c^{ij}(\sigma) \quad (5)$$

where the achromatic OPD difference p_a^{ij} corresponds to what is usually called the « piston » difference between beams i and j and $p_c^{ij}(\sigma)$ contains all the wavelength dependent terms of the OPD, which are dominated by the dispersion in the VLTI tunnels and AMBER fibers. p_a^{ij} very rapidly varies with time while $p_c^{ij}(\sigma)$ is dominated by terms evolving more slowly as the source zenith distance changes. To simplify the equations in the following, we shall assume that the window function $f(x,\sigma)$ is flat and with constant size and hence $F(u,\sigma) = \delta(u)$.

A Fourier transform of the interferogram in equation (3) in the wavenumber direction yields the 2D Fourier transform :

$$\hat{I}(u,v) = \mathcal{F}_\sigma[I(u,\sigma)] = \hat{n}(v) * \hat{F}(u,v) \sum_i n_i + \sum_{i,j>i} \sqrt{n_i n_j}\, \hat{\Omega}(\mathrm{u},v) * \delta(v - p_a^{ij}) \quad (6)$$

and its average power spectrum :

$$D(u,v) = < \left|\hat{I}(u,v)\right|^2 > = \left|\hat{n}(v) * \hat{F}(u,v)\right|^2 \sum_i n_i + \sum_{i,j>i} \sqrt{n_i n_j}\, \left|\hat{\Omega}(\mathrm{u},v)\right|^2 * < \delta\left(v - p_a^{ij}\right) > \quad (7)$$

$D(u,v)$ displays a low frequency peak and one fringe peak for each baseline at the position $u = B_{ij}\bar{\sigma}$ and $v = p_a^{ij}$ as illustrated in figure 2d.

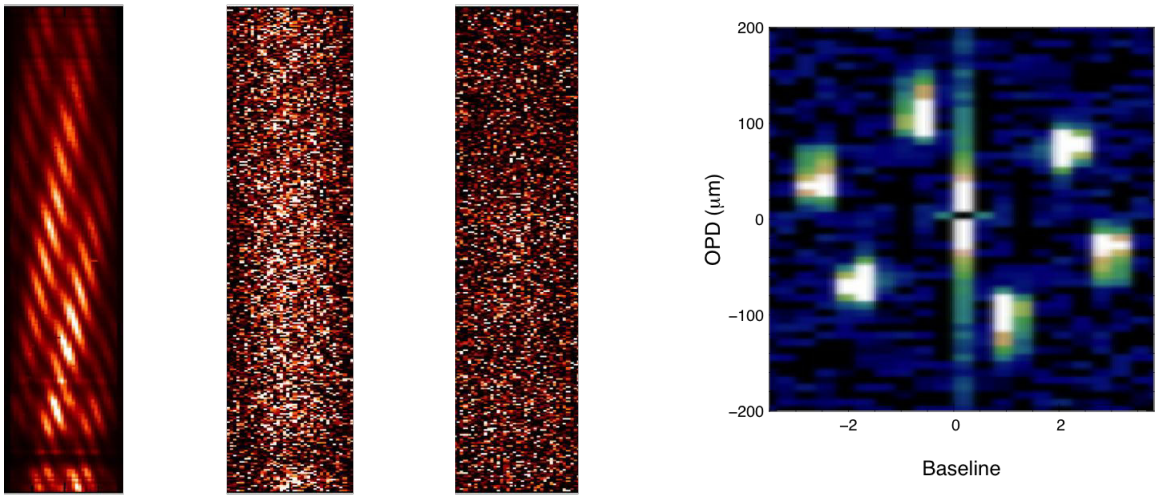

Figure 2: Principle of fringe detection in blind mode observations. The 3 left figures are x-λ interferograms with fringes dispersed in the vertical direction. The magnitudes are K=4 (left), K=8.5 (center) and K=9.7 (right). The rightmost figure represents a 10' average 2D FT of the interferograms for K=9.7.

The fringe peak will grow with the number of frames, as long as it moves by less than its size, while the noise level will grow only like the square root as the number of frames. The typical size of the fringe peak is given by the spectral coverage of the initial interferogram. For AMBER in medium resolution this is between $\lambda_1 = 2\mu m$ and $\lambda_1 = 2.3\mu m$, yielding a fringe peak width of $\lambda_1\lambda_2/(\lambda_2 - \lambda_1) = \lambda^2/\Delta\lambda = 15\mu m$. Under standard conditions, it takes at least a few seconds for the piston to drift by that value, and this sets a limit of the technique: we can observe sources producing a fringe peak of sufficient SNR in a few seconds to allow a piston measurement and correction. If the classical limit of the instrument is set by the necessity to detect SNR=3 fringes in say 100 ms and we consider that blind observing can manage the same SNR=3 criteria over say 10s, then we can afford a fringe peak SNR per frame of 0.3. In detector noise regime, this corresponds to a source 10 times fainter and hence a gain of 2.5 magnitudes. The gain is even more important with regard to a fringe tracker that must reach an SNR of the order of 3 in much shorter frame times.

In Figure 2a, we display a standard AMBER x-λ individual interferogram, for a K=4 bright source. The 3 fringe systems are clearly seen. Figure 2b shows a K=8.5 interferogram. Fringes are quite hard to see, but frame-by-frame data processing detects fringes and measures a piston in at least in some frames. This is the limit of the standard AMBER data processing. In figure 2c, with K=9.7, any frame-by-frame processing fails. The 2DFT processing yields the average power spectrum displayed in figure 2d with 3 clear fringe peaks. Piston offsets have been introduced to clearly separate the fringe peaks. The peak blur corresponds to the piston drift in 10 mn. We see here that it is smaller than 50 µm.

The position of the fringe peak in the 2DFT modulus can be used to evaluate and correct the piston value. Figure 3 displays the cuts of figure 2d in the piston direction at the frequency of each baseline, as they evolve in time. The position of the fringe peak yields the absolute piston (group delay) evolution with time.

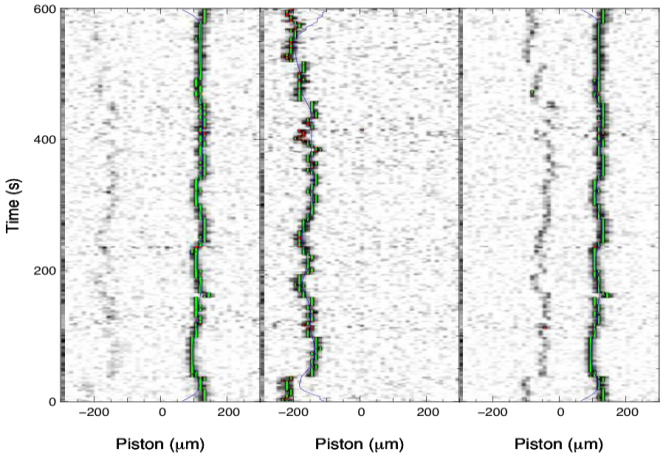

Figure 3: Measurement of piston (OPD group delay) by 2DFT processing on 3C273. Each plot shows a cut of figure 2d at the fringe peak frequency, in the piston direction (here x), repeated over time (here y). The fringe peak is green when it is more than 3 times higher than the background noise. The power spectra are averaged over 1s. We see that we are still not at the sensitivity limit. Note than on baselines 1-2 (left) and 1-3 (right) the OPD remains stable, within a 15 μm fringe peak, for very long periods of time. This plot also allows estimations of the rms error on the fringe peak position, of the order of 15 μm for baseline 1-2 to about 50 μm for baseline 2-3.

2.2 Differential observables in 2DFT data processing

When we observe in blind mode and plan to reduce the data with 2DFT algorithm, piston offsets ensure that the fringe peaks are well separated in the piston direction and cannot overlap, solving the problem of baseline cross-talk common to AMBER and other all-in-one multi-axial beam combiners. These offsets are apparent in figure 2d. They are of the order of 100 μm, which remains very small with regard to the coherence length of 3 mm. As the fringe peaks are well separated, we will say that we process them individually and in equations (3) and (4) we will use only the part specific to each baseline. The new interferogram for the baseline ij is:

$$I^{ij}(\sigma) = \sqrt{n_i n_j}\,\Omega^{ij}(\sigma)\, e^{2i\pi\sigma p_a^{ij}} \tag{8}$$

with
$$\Omega^{ij}(\sigma) = \Omega\big(u = B_{ij}\,\bar{\sigma}, \sigma\big) = n(\sigma) V_I^{ij}(\sigma) V_*^{ij}(\sigma) \exp\big[\, i\phi_I^{ij}(\sigma) + i\phi_*^{ij}(\sigma) + 2i\pi\sigma p_c^{ij}(\sigma)\big] \tag{9}$$

The estimation of the differential measurables at the frequency u_{ij}, is based on the computation, for each σ, of the differential cross spectrum (DCS) $W^{ij}(\sigma)$ between a 2D interferogram in which all channels but the channel σ have been forced to zero and a 2D interferogram in which only the channel σ has been forced to zero[†]:

$$\begin{aligned} W_\sigma^{ij}(\nu) &= \mathcal{F}[I^{ij}(\sigma').\delta(\sigma'-\sigma)].\mathcal{F}\big[I^{ij}(\sigma').\big(1-\delta(\sigma'-\sigma)\big)\big]^* \\ &= n_i n_j \Omega^{ij}(\sigma)\left[\widehat{\Omega^{ij}}\big(\nu - p_a^{ij}\big) - \Omega^{ij}(\sigma)\right] e^{-2i\pi\sigma(\nu - p_a^{ij})} \end{aligned} \tag{10}$$

If we know exactly the achromatic piston p_a^{ij} from 2DFT power spectrum, we have

$$W_\sigma^{ij}\big(\nu = p_a^{ij}\big) = n_i n_j \Omega^{ij}(\sigma)\big[\widehat{\Omega^{ij}}(0) - \Omega^{ij}(\sigma)\big] = n_i n_j \Omega^{ij}(\sigma)\big[\textstyle\int \Omega^{ij}(\sigma')\, d\sigma' - \Omega^{ij}(\sigma)\big] \tag{11}$$

[†] To make sure that the DCS does not contain power spectrum terms affected by a quadratic bias.

The term $R(\sigma) = \int \Omega^{ij}(\sigma')\, d\sigma' - \Omega^{ij}(\sigma)$ is very close to be constant. For the simplicity of the equations above, we will write $R(\sigma) \simeq R$, even if the actual $R(\sigma)$ is used in the practical data processing. If we assume that $n_i = n_j = n$ *and* $V_I^{ij}(\sigma) = V_I$, we see that $\left|W_\sigma^{ij}\left(p_a^{ij}\right)\right| \simeq n(\sigma) V_I^{ij}(\sigma) n^2 V_I^2$: the DCS is proportional to the square of the flux and the square of the instrumental visibility but its *variations* with σ are proportional to the source differential visibility.

From the measures in the photometric channel of the spectrum $n(\sigma)$ and the fluxes n_i and n_j and from the DCS on the science and the reference sources we build :

$$E^{ij}(\sigma) = \frac{W_{\sigma*}^{ij}(p_{a*}^{ij}) \Big/ n_*(\sigma)\, n_{i*} n_{j*}}{W_{\sigma cal}^{ij}(p_{acal}^{ij}) \Big/ n_{*cal}(\sigma)\, n_{ical} n_{jcal}} = \frac{\Omega_*^{ij}(\sigma) R_*}{\Omega_{cal}^{ij}(\sigma) R_{cal}} \tag{12}$$

Assuming that the instrumental visibility and phase are the same for the science and the reference, we get :

$$E^{ij}(\sigma) = V_*^{ij}(\sigma) \exp\left\{ i\phi_*^{ij}(\sigma) + 2i\pi\sigma \left[p_{c*}^{ij}(\sigma) - p_{ccal}^{ij}(\sigma)\right]\right\} \frac{R_*}{R_{cal}} \tag{13}$$

To avoid errors in the calibration of the ratio R_*/R_{cal}, for example from changes in the instrumental visibility, we divide $E^{ij}(\sigma)$ by its average over σ and we get finally the estimators of differential visibility and phase :

$$\phi_{d*}^{ij}(\sigma) = \arg\left(\frac{E^{ij}(\sigma)}{<E^{ij}(\sigma)>_\sigma}\right) = \phi_*^{ij}(\sigma) + 2\pi\sigma\Delta p_c(\sigma) \tag{14}$$

$$V_{d*}^{ij}(\sigma) = \frac{\Re\left[E^{ij}(\sigma) e^{-i\phi_{d*}^{ij}(\sigma)}\right]}{<\Re\left[E^{ij}(\sigma) e^{-i\phi_{d*}^{ij}(\sigma)}\right]>_\sigma} = \frac{V_*^{ij}(\sigma)}{<V_*^{ij}(\sigma)>_\sigma} \tag{15}$$

The term $2\pi\sigma\Delta p_c(\sigma)$ is the change in chromatic dispersion between science and calibrator. These two terms can be minimized by a correction of the computed chromatic OPD. Since we are looking for sharp differential phase variations through the emission line, we simply perform a polynomial fit of the chromatic OPD and the phase offset for all spectral channels outside the spectral line.

3. OBSERVATIONS AND DATA PROCESSING

We observed the quasar 3C273 in May 2011 with AMBER in medium resolution and the UTs 1,2 and 4. We used frame times of 300 ms, and collected about 200 photons per channel and per frame. This represents about 3 photons per pixel and is well below the detector read out noise of 11e^-. The seeing conditions were very good, from 0.5 to 0.8 arcseconds, stable between 0.6 and 0.7 most of the time. During the half observing night presented here, we collected 47 exposures on 3C273, each with 200 frames of 300 ms. That is 1h20' of open shutter time on 3C273 but only 47' of actual integration. In addition, we recorded a collection of calibrators of different magnitudes. In spite of the fairly long DIT, the VLTI/AMBER visibility was between 0.2 and 0.4, depending on the baseline and the conditions.

3.1 Calibrator differential visibilities

Figure 4 illustrates the data processing on a set of calibrators. Figure 4a shows the measured spectrum $n(\sigma)$, 4b shows the measured cross spectrum $W_\sigma^{ij}\left(p_a^{ij}\right)$ and figure 4c shows the calibrator differential visibility. We used 4 calibrators with magnitudes K=6.6, K=9, K=8.2 and K=9. We see that the behavior of the differential visibility is very stable and can be calibrated with an accuracy better than 1% on the K=9 target. We observe that the differential visibility is bent, mainly because the effect of chromatic OPD has not been corrected in this « first » data processing. The spectral 508 channels obtained in the AMBER medium resolution observations have been binned by groups of 16 for SNR reasons (on the science target) and we have now 0.009 μm per channel, corresponding to a resolution R=240.

3.2 3C273 differential visibilities

Figure 5 shows results on 3C273. In figure 5a we see the spectrum of 3C273. We note the same telluric and instrumental lines as for the calibrators, at 2.01 and 2.06 μm and the Paα emission line red-shifted at 2.17 μm. Figure 5b and 5c show the differential cross spectrum and the differential visibility for a 50 m baseline (5b) and 125 m (5c). The emission line appears very clearly in the DCS in figure 5b while it is quite erased in the DCS in figure 5c. This indicates a differential visibility decrease in the line when the baseline increases, which can be seen in the differential visibility plots. However, figure 5 also shows a flux dependent bias of the DCS, which strongly affects the differential visibility in the telluric lines and casts suspicion on the variation in the emission line. In addition, the general shape of the differential visibility in the continuum is far from 1 and changes with the baseline. A bias analysis is needed before confirming the differential visibility measure in the line.

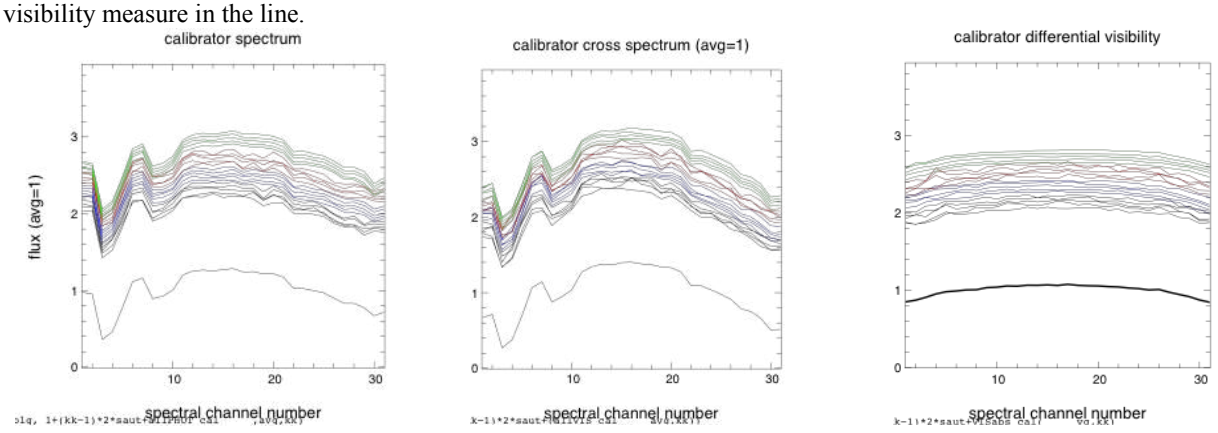

Figure 4: differential visibility measured on a calibrator. Figure 4a (left): calibrator spectrum $n(\sigma)$. Figure 4b (center): calibrator DCS $\left|W_\sigma^{ij}\left(p_a^{ij}\right)\right| \simeq n(\sigma)V_l^{ij}(\sigma)n^2V_l^2$. Figure 4c (right): calibrator differential visibility $V_{d*}^{ij}(\sigma)$. All function are divided by their avergage value over σ. They are shifted in the plot for visibility. The wavelength range goes from 1.99 to 2.31 μm. The black curve around 1 represents the time average. The color curves represent 4 different calibrators. From top to bottom the calibrator magnitudes where K=6.6 (green), K=9 (red), K=8.2 (blue) and K=9 (black). All curves are plotted for the baseline UT1-UT4=125m.

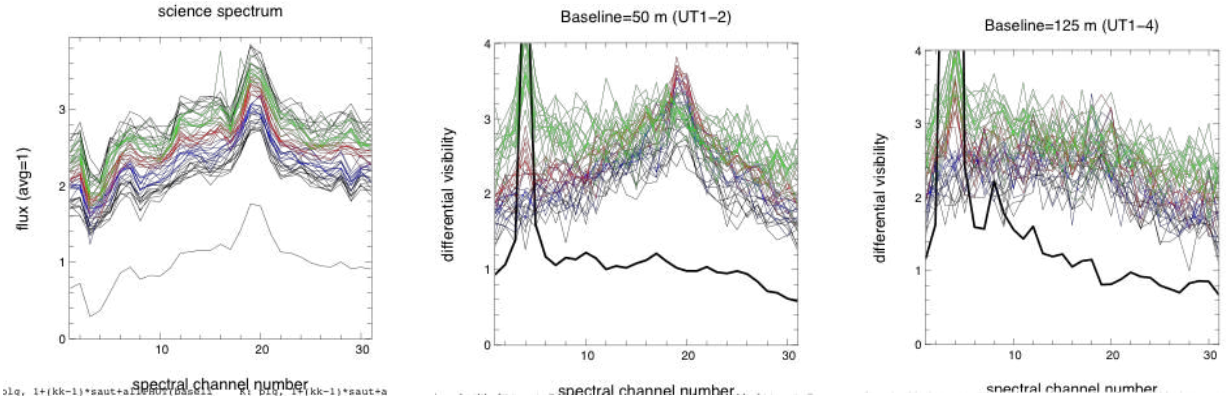

Figure 5: differential cross spectrum and differential visibility on 3C273. Figure 5a (left): 3C273 spectrum. Figure 5b and 5c: differential cross spectrum (top, thin, color curves) and differential visibility (bottom, thick, black curves). Figure 5b (center) is for the 50m UT1-2 baseline. Figure 5c (right) is for the 125m UT1-4 baseline.

3.3 Differential phases

Figure 6 shows the differential phases obtained on the calibrators and on 3C273. On the calibrators the differential phase displays the expected differential chromatic OPD. The 3C273 differential phases are always flat. The 3C273 observations were affected by the same chromatic OPDs, since 3C273 and all calibrators were less than 2° apart, and they were interlaced in time. This reveals a bias on the differential phase at the faintest magnitudes.

3.4 Bias analysis

Both the differential visibility and phase show biases on 3C273 that do not appear or appear only marginally on the faintest calibrators. The differential cross-spectral measures are not affected by the "quadratic noise bias" that appears in power spectra containing terms of squared zero mean noise.

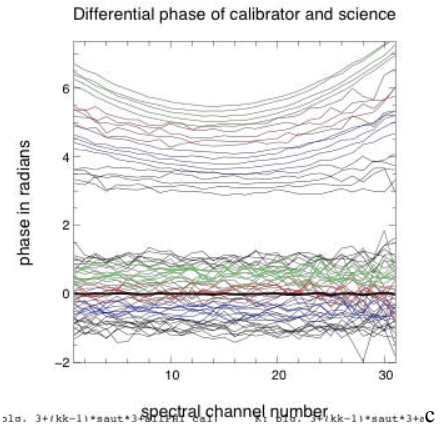

Figure 6: Differential phases in radians. All curves are at 0 average and shifted for visualization. The top curves, between « 3 and 7 rad » are for the same exposures on calibrators than in figure 4. The bottom curves represent the differential phases on the 3C273 exposures described for figure 5. The thick black line represents the average differential phase on 3C273. The color codes in 3C273 and in the calibrators are matched in time: we obtained first the black curves on 3C273, then the black curves on a calibrator, then the blue curves on the science followed by the blue curves on a calibrator and so on.

On 3C273, the DCS is overestimated in the lowest parts of the telluric lines. A careful look at the calibrator plots show that some of the exposures on the faintest calibrator are slightly biased in the bottom of the 2.01 line. The K=9 calibrator is fainter in this line than 3C273 in the continuum around the emission line and in first approximation we should say that the 3C273 measures are not biased around the emission line. We have used an estimate of this bias as a function of the correlated flux made in all available channels outside the emission line. It reduces, but does not cancel, the bias in the telluric line and does not change much the visibility variation in the emission line. This does not really correct the general shape of the differential visibility and differential phase of 3C273 in the continuum, which is mainly due to the "piston error" bias analyzed in the next section.

3.5 « Piston error » bias

Our differential visibility estimator in equation (11) assumes that we have an accurate estimate of the achromatic piston p_a^{ij}. If we make an error Δp on the estimation of the piston, the differential cross spectrum becomes

$$W_\sigma^{ij} = n_i n_j \Omega^{ij}(\sigma) < \left[\widehat{\Omega^{ij}}(\Delta p) - \Omega^{ij}(\sigma)\right] e^{-2i\pi\sigma(\Delta p)} > \tag{16}$$

and our measures are affected by a bias term

$$B(\sigma) = < \left[\widehat{\Omega^{ij}}(\Delta p) - \Omega^{ij}(\sigma)\right] e^{-2i\pi\sigma(\Delta p)} > \tag{17}$$

This term cannot be corrected using the calibrator, since the piston error depends on the source magnitude and on the observation conditions. $B(\sigma)$ depends on the source visibility, on the variations of instrument visibility with σ and on the chromatic OPD, since all these effects will change $\widehat{\Omega^{ij}}(\Delta p)$. In particular, the biases on the DCS detected in the telluric lines will behave like strong and random variations of $V_I^{ij}(\sigma)$ and hence of $\widehat{\Omega^{ij}}(\Delta p)$. Figure 7 displays a Monte Carlo simulation of the effect of $B(\sigma)$ on the differential visibility and phase. We have simulated a target with a flat visibility, but for a sharp local variation of 10% at the position of the emission line, and a zero differential phase but for a sharp local variation of 0.05 radians. The object is affected by window and gain table correction errors, which bend the overall differential visibility, and by variable local biases that mimic the behavior of the DCS the telluric lines. The differential phase is affected by a variation of the chromatic OPD similar to the one observed on the calibrators through the 3C273 observations. Figure 7a displays the evolution of the real differential visibility and phase through the observations. To evaluate the bias term, we have generated one random piston error per frame, with a standard deviation

of 5 μm in figure 7b (good calibrator case) and of 50 μm in figure 7c (worst 3C273 case). Each plot in figure 7b and 7c represents an exposure of 200 frames. We see that with a small piston error, the bias has almost no effect on the differential measures. This is coherent with the good measurements on the calibrators. With a strong piston error, both the differential visibility and phase are severely biased, and their error bars are increased. The average broadband visibility is substantially modified. However the sharp variations in the line are very well maintained for the differential visibility and somehow maintained for the differential phase. The global curvature of the differential phase is strongly affected, which looks similar to what we observe on the differential phase of 3C273. However, even when we simulate with exaggerated parameters, we do not seem able to « kill » a sharp differential phase feature of more than typically 3°. The simulation legitimates corrections of the « smooth » curvatures in the differential visibility and phase by a polynomial fit outside the emission line and outside the telluric lines.

The simulation also shows that when the source is « flat », i.e. when all chromatic OPD, window and detector biases are corrected from « models » in each frame before computing the 2DFTs, the tolerance to piston errors is much higher. This is currently being implemented in the data processing.

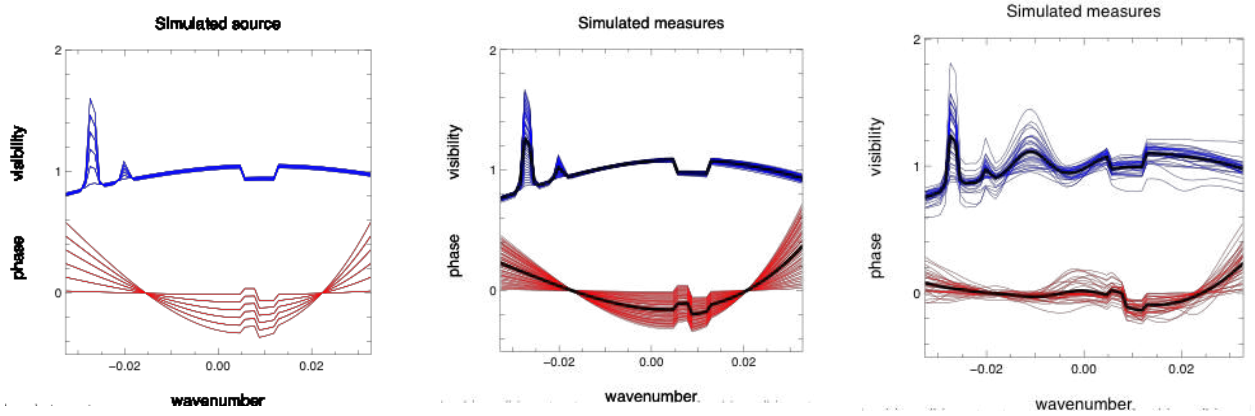

Figure 7: simulation of the « piston error bias » effect on the differential visibility and phase. Figure 7a (left): simulated source. In blue (top) the source differential visibility. In red (bottom) the source differential phase in radians. The chromatic OPD and the telluric line bias evolve like in the observations. Figure 7b (center): simulated measures with a piston rms=5 μm rms. The measures are almost unaffected. Figure 7c (right): simulated measures with a piston rms=50 μm rms. The measures are severely affected but sharp differential variations survive.

4. RESULTS AND DISCUSSION

Figure 8 shows the differential visibilities and phases obtained on 3C273 after calibration and our best current bias correction, based mainly on a polynomial fit of the measures outside the emission and absorption lines.

The differential visibility shows a drop in the emission line, which increases with the baseline. The various biases (and debiasing procedures) can create differential visibility artifacts and change the amplitude of the differential visibility drops, but cannot cancel them. From the simulation in the previous section, a very conservative error on our bias correction is of 0.02 per spectral channel. We finally have:

$$\frac{V_{line}(50m)}{V_{cont}(50m)} = 0.98 \pm 0.03, \quad \frac{V_{line}(80m)}{V_{cont}(80m)} = 0.94 \pm 0.04, \quad \frac{V_{line}(125m)}{V_{cont}(125m)} = 0.92 \pm 0.04$$

The errors per spectral bin *add linearly* the error estimated from statistical differences between the 47 exposures and the bias correction error. The spectral extension is of at least 2 spectral bins, i.e. 2500 km/s, which confirms that we are seeing BLR features.

About the differential phase, the most reasonable current statement is that there are no features larger than 3°, which corresponds to a photocenter displacement of 30 μas in the 125 m baseline direction.

This result is a surprise, which strongly stimulated our bias analysis. The BLR was supposed compact (<130 μas) and contained in the dust torus and thus the differential visibility was supposed to increase in the line (see figure 9). Let us

give a very preliminary interpretation of our measures in simple geometric terms. All features observed in the K band continuum and in the emission line are small (less than 1 mas) with regard to the VLTI best resolution of 3.5 mas. Then each feature can be defined by its contribution to the total flux, its equivalent width and its photocenter shift, both in the direction of the projected observation baseline. The smaller scale details will not affect the measures at our baselines, beyond their impact on width, photocenter and flux. So we decide to represent the continuum image by a centered

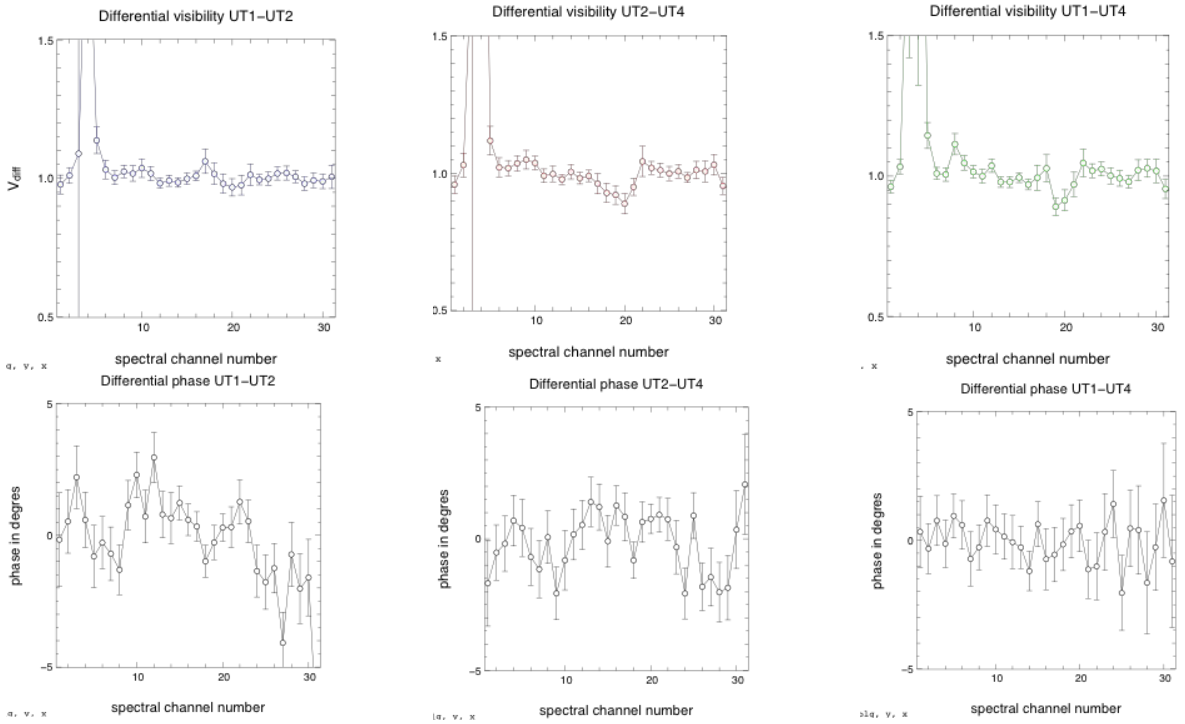

Figure 8: Provisional differential visibility (top) and phase (bottom) for a 50m (left), 80 m (center) and 125 m baselines. The differential visibility shows a drop in the emission line (see spectrum plot in figure 5a), which increases with the baseline. About the differential phase, the most reasonable statement is to say that there are no features larger than 2°. The error bars in the plots are estimated by the temporal dispersion over the 47 exposures.

Gaussian of FWHM adjusted to fit the absolute visibility measurements with the 84 m KI baseline[8]. This corresponds to a Gaussian with FWHM $= w_{cont} \approx 0.4\,mas$. The BLR is represented by a second Gaussian, with an intensity adjusted to fit the observed line profile over the continuum shown in figure 1. We change the width w_{BLR} and the center x_{BLR} of the BLR gaussian to try to fit our differential visibility measures. The results are displayed in figure 9. A centered compact BLR of angular size 0.13 mas, in agreement with the reverberation mapping + distance prediction, produces a differential visibility increase in the line of about 3%. To explain our visibility drops, we need either a very large centered BLR, with $w_{BLR} > 0.8\,mas$, or a compact ($i.e. w_{BLR} < 0.5\,mas$) BLR shifted by $x_{BLR} > 0.5\,mas$ with regard to the continuum photocenter. Qualitatively, an offset between the BLR and the continuum image makes sense. The continuum image contains contributions from various structures including the torus, with a possibly brighter face-on inner rim. There is actually no good reason for this image to be exactly centered on the accretion disk, except maybe for a face-on torus. Quantitatively, a shift $x_{BLR} > 0.5\,mas$ hardly fits in structure with an apparent radius $< 0.3\,mas$. But the critical difficulty of this interpretation is that the BLR shift would yield a photocenter displacement in the line of at least 250 μas in the direction of the baseline displaying the visibility drop, as shown in figure 9c. This corresponds to a differential phase of 25°, which does not appear in our differential phase measures with $|\phi(\lambda)| < 3°$ on all baselines. On all our baselines, the BLR FWHM is larger, or at least comparable to the diameter of the equivalent continuum ring, and the photocenter of the BLR coincides with this of the continuum image within 30 μas in the direction of the longest baseline (UT1-UT4) and 60 μas in the direction of the shortest one (UT1-UT2).

So, we must favor a centered and large BLR, of angular size larger than 0.8 mas, in the direction UT1-UT4 ($60° \; E \rightarrow N$), corresponding to a 0.4 mas radius of more than 1300 light days (if there is no major error on the distance of 3C273). This is in contradiction with the 300 ld RM radius observed in H_γ. Some investigation is needed to evaluate the possible ratio between the RM radii in Pa_α and H_γ. However, even if the RM radius can change with the line (it is $r = 514^{+65}_{-64}$ in H_α), at least two types of arguments tend to discard a BLR much larger in Pa_α than in H_γ. First the Pa_α line profile is extremely similar to the H_β in km/s. Second the higher energy transitions of Pa_α are usually more likely related to "inner" and hence "smaller" structures. Thus, we at least provisionally conclude that the 3C273 BLR has two different characteristic scales: the interferometric radius, larger than 1000 light days, and the RM radius, of the order of 300 light days. The angular visibility and the RM time delay correspond to integrals with different weightings of the different BLR parts. A detailed morphological modeling is needed to investigate their relative variation. It seems possible to imagine a BLR with two components: something compact around the accretion disk that dominates the RM, and is not resolved with our current differential phase accuracy, and a larger or shifted component, strong enough for a significant contribution to the angular intensity distribution, slow enough to explain that it has not been detected by spectroscopy and located in the right place, in the moment of our observations, to avoid introducing a photocenter shift in spite of its large size.

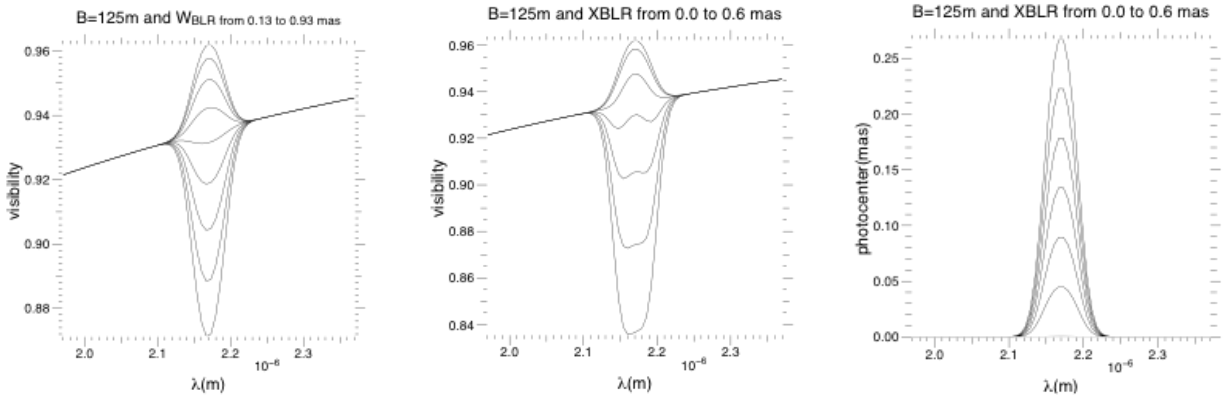

Figure 9: grid of « models » to interpret our differential visibility and phase measures. Left: visibility on a 125 m baseline for a centered BLR with widths ranging from 0.13 to 0.93 with 0.1 mas step (from top to bottom). Center, the same visibility for a compact 0.13 mas BLR shifted with regard to the continuum photocenter by a value ranging from 0 to 0.6 mas (top to bottom). Right: photocenter displacement in the baseline direction for the shifted BLR case (the photocenter displacement for the centered BLR is zero, and increases with the shift).

5. CONCLUSION

We have reported the first observations of the BLR of a quasar by optical interferometry. In medium spectral resolution, our so-called "blind mode" new observation technique allows a gain of at least two magnitudes with regard to the current fringe tracker. We believe that this must be used to revise the limiting magnitudes for spectrally resolved interferometric observations. Data processing based on the accumulation of 2D Fourier Transforms power spectra allowed an efficient fringe monitoring and slow coherencing on our K=10 target and we were probably at least one magnitude below the ultimate limit of the technique. The use of 2D FT cross spectra allowed to measure the differential visibility with an accuracy of 3% and a differential phase with an accuracy of about 3°. This allows measuring the source photocenter displacement with accuracy better than 30 micro arc seconds, and to constrain differential sizes smaller than 0.2 mas, to be compared with the standardly computed VLTI resolution of 3.5 mas.

We have analyzed the fundamental bias of this data processing technique, and taken it into account in the calibration of the data. Our current accuracy on the differential phase is limited by this bias correction. The data will be reprocessed with procedures less sensitive to the bias, and it is still possible to expect a final phase accuracy near 1°, in principle sufficient to resolve even compact 0.1 mas Keplerian structures.

The results show that the visibility of 3C273 is lower in the Pa_α emission line than in the K band continuum, and that the visibility drop increases with the baseline length, while the differential phase is smaller than 3° on all baselines. They imply that the BLR seen by interferometry is fairly large, with a radius of at least 1000 light days, comparable or slightly larger than the dust ring radius estimated from broadband low spectral resolution observations with the Keck interferometer. This result is quite surprising, mainly with regard to the 300 light days reverberation mapping radius. After a careful analysis of the data and of the possible biases, and even if this work is still in progress, we believe that a BLR with two different scales, and hence two different structures, the more than 1000 ld interferometric radius and the 300 ld reverberation mapping radius should be considered as a serious working hypothesis.

ACKNOWLEDGEMENTS

The data has been obtained during the ESO run 087.B-0754 (A), an AMBER Consortium Guaranteed Time Observation. The authors thank Dr. Makoto Kishimoto, from the MPIfR, and Dr. Philippe Stee, from the Lagrange Laboratory, for the very useful discussions and comments.

REFERENCES

[1] Urry, C.M. and Padovani, P., "Unified Schemes for Radio-Loud Active Galactic Nuclei" PASP, 107,803 (1995).
[2] Elvis, M., "A structure for Quasars",ApJ 545,1, pp 63-76 (2000).
[3] Peterson, B. M. and Horne, K., "Reverberation mapping of active galactic nuclei", AN 325, 3, pp 248-251 (2004).
[4] Jaffe, W., et al, "The central dusty torus in the active nucleus of NGC 1068", Natur.429,6987, pp 47-49 (2004).
[5] Swain, M. R., "Observing NGC 4151 with the Keck Interferometer", Proc. SPIE 5491, p1 (2004).
[6] Kishimoto, M., et al., "Exploring the inner region of type 1 AGNs with the Keck interferometer", A&A 507,pp L57-L60 (2009).
[7] Weigelt, G., et al, "VLTI/AMBER observations of the Seyfert nucleus of NGC 3783", A&A 541, L9 (2012).
[8] Kishimoto, M., et al., "The innermost dusty structure in active galactic nuclei as probed by the Keck interferometer", A&A, 527 (2011).
[9] Beckers, J. M., "Differential speckle interferometry", AcOpt, 29, pp 361-362 (1982).
[10] Petrov, R. G., "Differential interferometry", dli..conf.., NATO (ASI) Series C, 274, pp 249, (1989).
[11] Petrov, R.G., et al., "AMBER, the near-infrared spectro-interferometric three-telescope VLTI instrument", A&A 464, pp 1-12, (2007).
[12] Kraus, S., "New opportunities with spectro-interferometry and spectro-astrometry", Proc. SPIE 8445, (2012).
[13] Petrov, R. G., Roddier, F. and Aime, C., "Signal-to-noise ratio in differential speckle interferometry", JOSAA,3,pp634-644, (1986).
[14] Marconi, A, Maiolino, R and Petrov, R.G., « Extragalactic Astronomy with the VLTI: a new window on the Universe », Ap&SS.286, pp245-254, (2003).
[15]Kaspi, S., et al., "Reverberation Measurements for 17 Quasars and the Size-Mass-Luminosity Relations in Active Galactic Nuclei", ApJ,533,pp631-649, (2000);
[16] ESO Call for Proposals P90, website: www.eso.org/sci/observing/proposals/CfP90.pdf.
[17] Berio, P., et al., "Spectrally resolved Michelson stellar interferometry. I. Exact formalism in the multispeckle mode", JOSAA, 16, pp 872-881, (1999).
[18] Li Causi, G.; Antoniucci, S.; Tatulli, E., "De-biasing interferometric visibilities in VLTI-AMBER data of low SNR observations", A&A, 479, pp589-595, (2008).

AGN BLR structure, luminosity and mass from combined Reverberation Mapping and Optical Interferometry observations.

Suvendu Rakshit[a] and Romain G. Petrov[a]

[a] Laboratoire Lagrange, UMR 7293, University of Nice Sophia-Antipolis, CNRS, Observatoire de la Cote D'Azur, BP 4229, 06304, Nice Cedex 4, France;

ABSTRACT

Unveiling the structure of the Broad-Line Region (BLR) of AGN is critical to understand the quasar phenomenon. Detail study of the geometry and kinematic of these objects can answer the basic questions about the central BH mass, accretion mechanism and rate, growth and evolution history. Observing the response of the BLR clouds to continuum variations, Reverberation Mapping (RM) provides size-luminosity and mass-luminosity relations for QSOs and Sy1 AGNs with the goal to use these objects as standard candles and mass tags. However, the RM size can receive different interpretations depending on the assumed geometry and the corresponding mass depends on an unknown geometrical factor as well on the possible confusion between local and global velocity dispersion. From RM alone, the scatter around the mean mass is as large as a factor 3. Though BLRs are expected to be much smaller than the current spatial resolution of large optical interferometers (OI), we show that differential interferometry with AMBER, GRAVITY and successors can measure the size and constrain the geometry and kinematics on a large sample of QSOs and Sy1 AGNs. AMBER and GRAVITY (K$\sim$ 10.5) could be easily extended up to K= 13 by an external coherencer or by advanced "incoherent" data processing. Future VLTI instrument could reach K$\sim$ 15. This opens a large AGN BLR program intended to obtain a very accurate calibration of mass, luminosity and distance measurements from RM data which will allow using many QSOs as standard candles and mass tags to study the general evolution of mass accretion in the Universe. This program is analyzed with our BLR model allowing predicting and interpreting RM and OI measures together and illustrated with the results of our observations of 3C273 with the VLTI.

Keywords: QSO: BLR; Interferometry: VLTI; Reverberation Mapping: AGN: Black Hole: Mass: Luminosity

1. INTRODUCTION

The extreme power of AGN comes from the accretion of matter onto central supermassive black hole (SMBH) which is surrounded by accretion disc (AD). Broad line region (BLR), a collection of gas clouds that feeds the central source and observed in case of Sy1 AGNs, is situated somewhere between AD and clumpy dusty "Torus" which is the source of mid infrared continuum emission. The torus obscures the central part of Sy 2 objects. Detail spectroscopic monitoring, over a long time domain, of the so called "Reverberation mapping (RM)" technique allows to measure the continuum flux $C(t)$, originates from the central accretion disc region, and the line flux $L(t)$, which is the result of absorption of continuum flux and re-emission by the BLR clouds, and makes possible to estimate the size of the line emitting region by simple cross-correlation and the mass of central SMBH by a simple viral relation[1]

$$M_{bh} = f\frac{R_{blr}\Delta V^2}{G}, \tag{1}$$

where $R_{blr} = c\tau_{cent}$ is the BLR size, τ_{cent} is the centroid of the 1D response function $\Psi(\tau)$, ΔV is the width of the line, G is the gravitation constant, c is the speed of light and f is an unknown scale factor that depends mainly on the geometry and kinematic of the object. In flat BLR geometry, the inclination of the object is the principle parameter that effect f.[1–3]

A remarkable achievement for RM is to provide a relationship, between the size of the emission line region and the luminosity of the object, $R_{blr} \sim L^{\alpha}$.[4,5] Because of the simplicity of $R_{blr} - L$ relation, it is quite easy to obtain

Contact: Suvendu.Rakshit@oca.eu or suvenduat@gmail.com; lagrange.oca.eu

Optical and Infrared Interferometry IV, edited by Jayadev K. Rajagopal, Michelle J. Creech-Eakman, Fabien Malbet, Proc. of SPIE Vol. 9146, 91460Q • © 2014 SPIE • CCC code: 0277-786X/14/$18
doi: 10.1117/12.2056436 Proc. of SPIE Vol. 9146

mass-luminosity relation $M_{bh} - L^{0.79\pm0.09}$ via eq.1[1,6,7] however the scatter around this relation is quite large. The origin of this scatter is due to: A. The scatter in the size-luminosity relation which is due to inaccurate time lag and distance measurement of the individual sources.[4,8] B. Measurement of the line width ΔV also produces uncertainty in the mass estimation as the ratio of two line width measures (full width at half maximum FWHM and line dispersion σ_{line}) depend on the object and its own spectral properties. C. The interpretation and estimation of the unknown scale factor f which depends on object intrinsic properties is doubtable as using single values for time lag and line width neglect the morphology of AGN and gives large uncertainty in AGN BH mass estimation.[5,9]

For a better calibration of these relations much efforts are going on, such as: A. Improve traditional cross correlation technique by direct modeling the driving continuum and line light curve as damped random work considering the correlated noise, de-trending and interpolation.[10–12] B. Obtain recent RM data with much higher sampling rate and free from any temporal gaps in the light curves to provide strong constraint, recover detail velocity delay map of the emission line and accurate lag measurement.[13] C. Correct the luminosity from the contribution of host galaxy starlight for accurate distance measurement.[4,8]

After many years of effort the physics of BLR is still unknown. Detail modeling will help to improve our understanding about BLR; geometry and kinematics. Ref. 14 modeled directly the RM data to recover the parameters and their uncertainties however resolving these objects spatially with high angular observing technique like interferometry in near IR or optical can constrain the geometry and morphology and calibrate the RM technique[15] and differential interferometry[16] could be very useful for this task.[17] Ref. 18 suggested that interferometric measurements of BLR size of quasars allows directly determination of geometrical distances on cosmic scales and long baseline ground based optical and near IR interferometer, like VLTI/AMBER,[19] has the potential of measuring the size of BELR with very high spatial resolution.[18]

The outline of this work is as follows. In §2 we described the optical interferometry and its measures with an emphasis on the observables of differential interferometry and a description of the signal and noise in OI. In §3 we described our kinematics model to explain OI and RM measures. Feasibility of present and future optical interferometric observation of the BLR of AGNs with current and future VLTI instrument and the signal to noise ratio needed for detail statistic is explained in §4. Our discussion is in §5 and conclusion is in §6.

2. OPTICAL INTERFEROMETRY

Optical interferometry is intended to provide high angular resolution information that makes possible to study inner part of the object with very details. Modern interferometers like CHARA and VLTI with longer baselines can provide resolution down to 0.1 mas. The resolution necessary to access the dusty region of AGN is within the capability of current interferometers in IR with 8-10 m class telescopes. Since 2004[20] more than 45 AGNs have been successfully observed in the K and N bands in LR. This has constrained the size of the innermost dust torus structure and revealed its complexity. Ref. 21 rejects the existence of a simple size-luminosity relation in AGNs, because the $L^{0.5}$ scaling of bright sources fails to represent properly fainter sources. Kishimoto (2014) still tries to find an unification scheme based on the idea that in low luminosity AGNs the inner torus is more shallow than in high luminosity ones, because a latitudinal radiation pressure blows away all material far from the equatorial plane in high luminosity AGNs. Thus low luminosity AGNs have much more dust clouds in the polar direction. Both the KI and the VLTI measurements, summarized in Ref. 22, show that in the K band, the dust torus inner rim size is fairly close to a $R_{rim} \propto L^{0.5}$ size that can be deduced from the infrared RM measures of Ref. 23, with a size excess with regard to $\propto L^{0.5}$ that increases as L decreases but remains small in the K band. In §4 we will use the Suganuma size as a lower limit of the inner rim size to estimate the feasibility of AGN OI observations.

The observation of BLR of AGN is more difficult because it needs a resolution higher than typically 500. The common sense in OI is that such MR observations need the use of a fringe tracker freezing the fringes from the phase jitter introduced by the atmosphere and allowing longer frame times in order to overcome the detector noise limits. Since the limiting magnitude of current fringe trackers has been lower than K= 9, the observation of BLRs has been postponed until a FT can be operated at magnitudes K> 10, which is supposed to be the case with the 2nd generation VLTI instrument GRAVITY expected to reach K= 10.5 in 2016. In 2011, we have

developed a new observation technique, called "blind mode observation" and a new data processing method for AMBER called "FT2D integration",[24] inspired from the data processing used in the visible on GI2T and later on the VEGA/CHARA instrument.[25] This gave a gain in the limiting magnitude for AMBER medium resolution observations (R=1500) from K$\sim$ 7.5 to K$\sim$ 10.5 and allowed the first successful observations of the BLR of the QSO 3C273. These observations are described in Ref. 24.

A second difficulty of BLR observations is that the BLR sizes expected from RM are much smaller than the telescope diffraction limit. For example, in the case of 3C273, the maximum RM radius of 570 ld given in Ref. 5 correspond to 0.36 mas angular diameter, to be compared to the 3.4 mas resolution of the VLTI in the K band. As anticipated in Ref. 26 and explained in the next sections, differential interferometry allows very accurate measurement of the differential visibility and phase that can constrain strongly unresolved objects. The main results on 3C273 are:

a) The BLR of 3C273 is much larger (radius 1500 ± 500 ld, or angular diameter 0.9 ± 0.3 mas) than expected from RM (from 250 to 570 ld) in Ref. 5 and actually larger than the inner rim of the dust torus (950 ± 400 ld in Ref. 27).

b) The BLR structure is very far from a flat disc dominated by global velocities. The orbits of the BLR clouds are either distributed in a very large opening angle range or affected by very strong local turbulent velocities.

The success of these observations triggered the development of the modeling tools described in Rakshit et al. (2014) and summarized in this paper. The description of the 3C273 observation and their interpretation are described in another paper (Petrov, 2014) but we will use the measurement accuracies actually achieved in section §5 where we discuss the possibility to observe AGN BLRs with existing or close in the future OI instruments.

2.1 Spectro-interferometric measurements

An interferometer with baseline B yields the complex visibility of the source, i.e. the normalized Fourier Transform $\tilde{O}(\mathbf{u}, \lambda)$ of the source brightness distribution $O(\mathbf{u}, \lambda)$ at the spatial frequency $\mathbf{u} = \mathbf{B}/\lambda$.

$$\tilde{O}(\mathbf{u}, \lambda) = \frac{\int\int O(\mathbf{r}, \lambda) e^{-2\pi i \mathbf{u}.\mathbf{r}} \, \mathrm{d}^2\mathbf{r}}{\int\int O(\mathbf{r}, \lambda) \, \mathrm{d}^2\mathbf{r}} = V_*(\lambda) e^{i\phi_*(\lambda)}, \tag{2}$$

where the modulus $V_*(\lambda)$ of $\tilde{O}(\mathbf{u}, \lambda)$ is given by the contrast of the fringes and called source absolute visibility whereas source phase $\phi_*(\lambda)$ is given by the position of the fringes at the frequency $\frac{\mathbf{B}}{\lambda}$. If we have enough number of baselines (u-v points) to sample the frequency plane (u-v plane) with a step f within a diameter B_{max} it is possible to reconstruct the source brightness distribution $O(\mathbf{r}, \lambda)$ with a resolution $R = \lambda/B_{max}$ within a field $F = \lambda/f$ by inverse Fourier transform of $\tilde{V}(\mathbf{u}, \lambda)$.

To summarize, a spectro-interferometric instrument produces the following measurable in each spectral channel: (1) the source spectrum $s(\lambda)$ which is deduced from the photometric measures, (2) the source absolute visibility $V(\lambda)$ with an uncertainty of at least 0.03 because of the need to calibrate it on a reference source, (3) the source differential visibility $V_{diff}(\lambda)$, (4) the source differential phase $\phi_{diff}(\lambda)$ and (d) the source closure phase $\Psi(\lambda)$.

The accuracy of the "self-calibrated" quantities, $V_{diff}(\lambda)$, $\phi_{diff}(\lambda)$ and $\Psi(\lambda)$ are strongly dominated by the fundamental noise limits set by the photon noise, the detector noise and the thermal background photon noise, at least for MR observations over a small wavelength range.

2.1.1 Differential interferometry of non-resolved sources

A non-resolved source has a global angular size Λ smaller than the interferometer resolution limit λ/B. In eq.2, this implies that $O(\mathbf{r}, \lambda)$ is different from 0 only for values of $r < \lambda/B = 1/u$, i.e. the integral in eq.2 can be limited to values $\mathbf{u}.\mathbf{r} < 1$. Since Ref. 16 we know that the interferometric phase for such a source is given by

$$\phi_{*ij}(\lambda) = 2\pi \mathbf{u}_{ij} \boldsymbol{\epsilon}_{ij}(\lambda), \tag{3}$$

where the quantity

$$\boldsymbol{\epsilon}_{ij}(\lambda) = \frac{\int\int \mathbf{r} O(\mathbf{r},\lambda)\,\mathrm{d}^2\mathbf{r}}{\int\int O(\mathbf{r},\lambda)\,\mathrm{d}^2\mathbf{r}} \tag{4}$$

is the photocenter of the source for single mode interferometry $u_{ij} = \frac{B_{ij}}{\lambda}$. From Appendix A we can say that:

- The closure phase decreases as α^3 where $\alpha = \frac{\Lambda B}{\lambda}$ and stops to be usable very rapidly when the source gets unresolved. As the closure phase is necessary for a full image reconstruction, we see that images of BLRs are excluded if we don't have baselines allowing to approach $\alpha = 1$, i.e. at least 1 km for near IR observations.
- The differential phase decreases only as α, which makes it possible to measure it for very unresolved sources, given a sufficient SNR.
- The visibility and the differential visibility decreases as α^2. As we will see in §4.4, this allows measurements to some targets with the existing VLTI baselines.

3. DYNAMICAL MODEL OF BLR[‡]

In order to produce simultaneously OI and RM measures we developed a model considering that the BLR consists of large number of line emitting clouds each defined by own position, intensity and velocity components. This model is described in detail in Rakshit et al. (2014) and here we just make a short summary.

The radial position r of the clouds are taken from a gaussian distribution with two parameters R_{in} and width σ_{blr}

$$l = \mathcal{N}(R_{in}, \sigma_{blr}) \quad \text{and} \quad r = l \quad \text{for } l \geq R_{in} \tag{5}$$

For velocity, we considered orbital, radial inflow, outflow and random turbulence components:

a) An orbital component:

$$V_{rot} = V_r(\frac{R_{in}}{r})^{\beta}, \tag{6}$$

The parameter β defines different orbital velocity components. For Keplerian motion $\beta = 0.5$ and amplitude $V_r = \sqrt{\frac{GM_{bh}}{R_{in}}}$

b) A radial component (inflow or outflow):

$$V_{rad} = V_c(\frac{R_{in}}{r})^{\gamma}, \tag{7}$$

where γ is power law index of radial component of velocity. $\gamma = 0.5$ is the freefall of clouds with amplitude $V_c = -\sqrt{\frac{2GM_{bh}}{R_{in}}}$ and $\gamma = -1$ is the outflow case with the outflow velocity amplitude V_c set at the inner radius R_{in} of the BLR.

c) A random macroturbulence velocity component V_{turb} that increases the local velocity. Its amplitude depends on the local thickness of the BLR.[2]

First, we created a 2D distribution of the clouds and then we applied: (a) A random rotation to the cloud position with angle ω ($-\omega \leq \theta$(polar angle)$\leq +\omega$) along y axis to pull up a 3D configuration from the 2D configuration. The angle ω is defined as opening angle or illumination angle of the cloud distribution. For $\omega = 90°$, the geometry become spherical whereas $\omega = 0$ converge to the flat geometry. (b) A random rotation to restore the axisymmetry of the cloud distribution by removing the concentration of clouds at the intersection of the orbits i.e., $+Ymax$ and $-Ymax$.

To define the observer reference system, we rotate the clouds: (a) About y-axis with inclination angle i to model the system's inclination with respect to the observer line of sight. We defined $i = 0°$ for face-on

[‡]For detail description of the model and the result, see Rakshit et al. (2014)

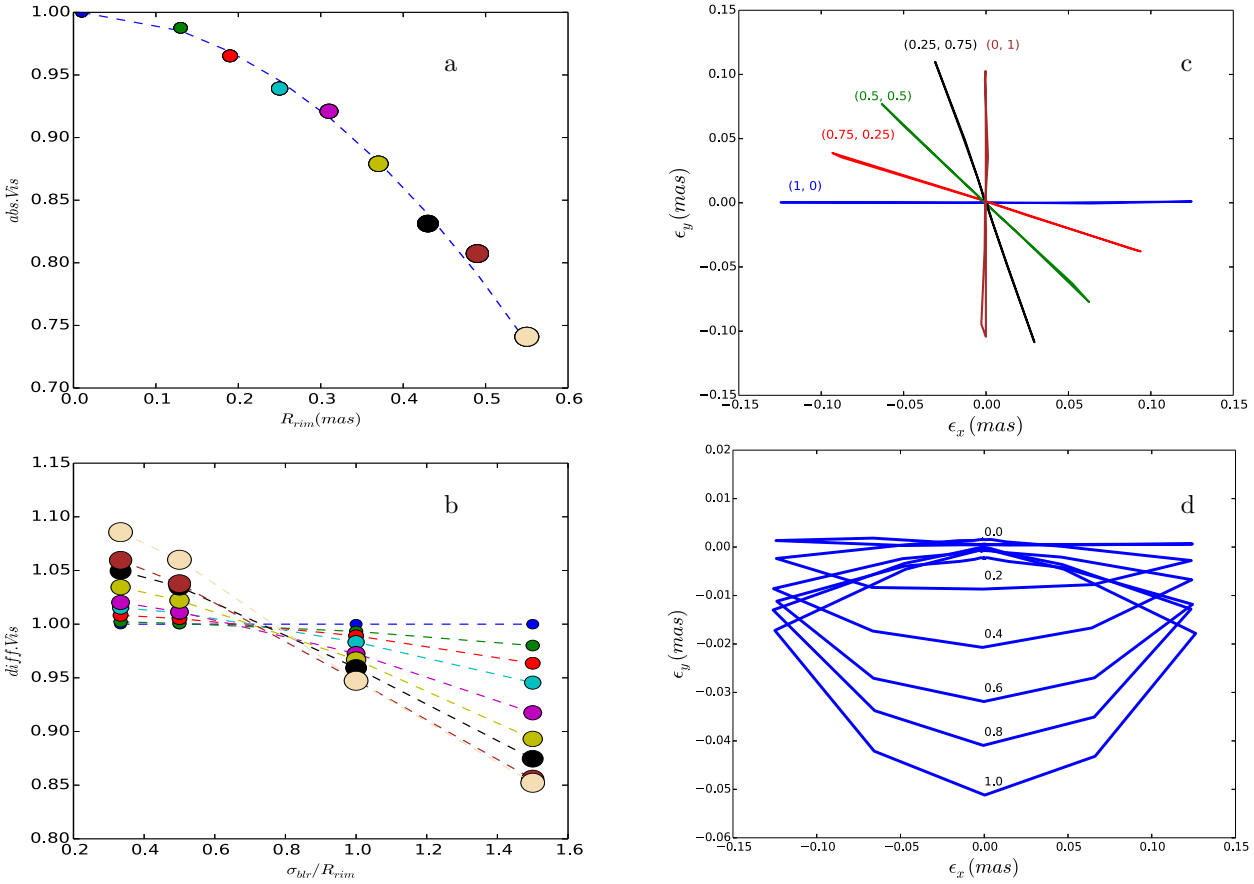

Figure 1. a. Absolute visibility in the continuum as a function of R_{rim} (upper panel). b. Differential visibility as a function of σ_{blr}/R_{rim} (lower panel) for $PA = 0°$. c. Photocenter displacement in the sky plane for different combinations (V_k, V_f) of Keplerian ($V_k \times V_r$) and freefall velocity ($V_f \times V_c$) amplitude. The photocenter for pure Keplerian case is represented in blue whereas pure freefall is presented in brown. d. Photocenter displacement on the sky plane with anisotropy.

configuration and $i = 90°$ for edge-on configuration. (b) About z axis with an angle PA_{disk} defined as the position angle of the system (from **N** to **E**). The position angle 0° means the orientation of semi major axis is along North (+y axis)-South (-y axis) and usually constrained by the orientation of radio jet for QSOs.

We considered that each clouds contributes to the BLR intensity distribution by adding a spectrum which is Gaussian in shape with width $\sigma 0_{line}$ shifted by its projected line of sight velocities. Object intensity distribution is summed of the continuum and the BLR intensity distribution. We modeled continuum emission as thin ring of radius R_{rim}. The main parameters that define our model are: 1. Mass of central BH: M_{BH}. 2. Inclination angle: i. 3. Opening angle: ω. 4. Local line width: $\sigma 0_{line}$. 5. Size of the BLR: σ_{blr}. 6. The size continuum rim: R_{rim}.

3.1 BLR size estimation

The plot in Fig.1a allows to discuss the accuracy on the R_{rim} resulting from error in absolute visibility $\sigma_{avis} = 0.03$ on the VLTI. It appears that the lower limit for possible measures is $R_{rim} = 0.15$ mas. Accessing smaller R_{rim} requires either longer baselines (i.e. a future interferometer) or more accurate visibilities.

Fig.1b illustrates the measurement of the ratio σ_{blr}/R_{rim} from the differential visibility. We see that, even for a very small σ_{dvis}, the estimation of the size ratio is strongly dominated by the uncertainty on the continuum size, i.e. the absolute visibility accuracy. Thus differential visibility allows to say if the BLR is larger or smaller than the inner dust rim, but any accurate BLR size measurement requires an accurate absolute visibility measurement

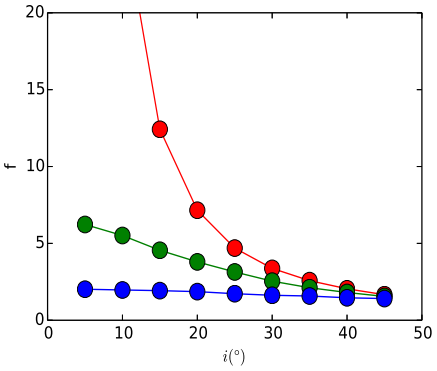

Figure 2. The scale factor f is plotted as a function of inclination for different opening angles $\omega = 0°$ (red), $30°$ (green) and $60°$ (blue). f strongly depends on i and ω. To constrain f, it is necessary to understand to geometry of the object.

in the continuum. If σ_{avis} is improved, then very accurate differential visibility gives access to BLR sizes much smaller than R_{rim}, of the order of 0.2 R_{rim} for a typical value of $R_{rim} = 0.2$ mas.

The second generation VLTI instrument GRAVITY is expected to allow a big improvement in the error of differential visibility, σ_{dvis}, at least in the magnitude range (up to K $\sim$ 10.5) allowing to use its internal fringe tracker that will stabilize the instrument visibility.

3.2 Kinematics

Fig.1c shows the displacement of the photocenter in the sky plane for different ratios of Keplerian and freefall velocity amplitude. Global direction of photocenter displacement with respect to the rotation axis yields the rotation/expansion velocities ratio which also pointed out by Ref. 28 in a similar model for circumstellar disks. In a similar way Ref. 29 has shown that the shape of the differential phase is the best constraint on the velocity law index β and γ.

3.3 Anisotropy

The cloud line optical depth is a key factor to determine the probability of line photon escaping the cloud. The response of the emission line cloud hence depends on the anisotropic emission of the BLR. Calculation of anisotropic response for different strong broad emission line in AGN spectra[30] suggested that line with large ionization parameter emitted anisotropically at some radii. Anisotropic emission could be constrained by detail modeling of BLR clouds. To test the effect of anisotropy on the interferometric measurement we define a simple "moon phase" like anisotropy in the form of

$$I(\phi) = (1 - F_{anis} \cos\phi \sin i) \tag{8}$$

where F_{anis} is anisotropy parameter ranging between 0 (complete isotropy and optically thin cloud) to 1 (complete anisotropy and optically thick cloud).

Fig.1d shows the displacement of photocenter (using eq.4) in the sky plane for flat Keplerian disk geometry. As anisotropy increases the photocenter moves towards the direction of increased emission and hence photocenter in the parallel direction changes rapidly while the photocenter in perpendicular direction remain unchanged.

3.4 The effect of inclination and opening on RM scale factor

It is straightforward to calculate RM scale factor using the centroid of response function τ_{cent} and line dispersion σ_l (putting $\Delta V = \sigma_l$ in eq.1). Fig.2 shows the virial scale factor as a function of inclination for different BLR geometries. In all cases $f > 1$, which means the estimated mass is less than the mass we input in the model. As inclination increases the scale factor decreases and hence the estimated mass become closer to the input mass. For low inclination, the output mass is lower for thin geometry (small ω) than the thick (larger ω) and hence the scale factor is large for thin geometry than thick geometry. For higher inclination the output mass or the scale factor appear to converge with each other for different geometries. For any inclination lower than typically $30°$ to $40°$, i and ω introduce a large f uncertainty, that can be drastically reduced if we can constrain one of these

parameters from other observations. The uncertainty of such estimation, from models of the jet and of the line profile is very large and though the inclination is the major factor in mass determination but currently we do not have accurate measurement of inclination of type 1 objects. Without having accurate inclination measurement it would be very difficult to constrain the scale factor.

4. INTERFEROMETRIC OBSERVATION OF BLR

In this section we will discuss the possibility to observe QSOs and Sy1 AGNs with various VLTI instruments that already exist, are under construction or could exist in a near feature. In each case we will examine:

1) The possibility to observe the target, i.e. to detect and maintain the fringes on the target itself.

2) The accuracy of the absolute visibility, differential visibility and differential phase that can be obtained on this target.

4.1 Interferometric signal and noise

From a general formalism described in Ref. 31 and updated in Ref. 32, it is easy to show that the noise on the coherent flux computed from each multi-axial all in one interferogram is given by:

$$\sigma_C = \sqrt{n_T n_* t_{DIT} + n_p \sigma_{RON}^2 + n_T n_{th} t_{DIT}}, \tag{9}$$

where n_* is the source flux per spectral channel, frame and second, n_T is the number of telescopes, t_{DIT} is the frame exposure time, n_p is the number of pixels (or of measures), σ_{RON}^2 is the variance of the detector read-out noise and n_{th} is the background flux per spectral channel, frame and second. In K band this value is much smaller than the detector noise and hence can be negligible for short exposures. However for long exposures such as in cophased mode n_{th} should be taken into account. In K band $n_{th} = 1.07$ photons $see^{-1}cm^{-2}\mu m^{-1}$.

The classical SNR on the coherent flux, per spectral channel and per frame[32,33] is then given by (see also; MATISSE performance Analysis report, Doc No: VLT-TRE-MAT-15860-9007)

$$SNR_1 = \frac{C}{\sigma_C} \simeq \frac{n_* t_{DIT} V}{\sigma_c}, \tag{10}$$

where V is the visibility module. The source flux per spectral channel per frame and per second is given by

$$n_\star = n_0 \mathrm{AST} \delta\lambda 10^{-0.4\mathrm{K}}, \tag{11}$$

where n_0 is the number of photons per cm^2, μm and sec from a star with K = 0, outside earth atmosphere, $n_0 = 45 \times 10^6$ photons $sec^{-1}cm^{-2}\mu m^{-1}$, A is the collecting area of telescope, S is the Strehl ratio with the VLTI Adaptive optics system MACAO, T is the overall transmission of the atmosphere, the VLTI and the instrument, and $\delta\lambda$ is the spectral band width $= \lambda_0/\mathrm{R}$, where R is the resolution.

Standard processing: as the coherent flux C is affected by a random atmospheric phase, we have to average its squared modulus $|C|^2$ over all available spectral channels and several frames. The SNR of such a quadratic average is given by:

$$SNR(|C|^2) = \frac{SNR_1^2}{\sqrt{1 + 2SNR_1^2}} \sqrt{N_{EXP} n_\lambda}, \tag{12}$$

where n_λ is the number of spectral channels, $N_{EXP} = \frac{t_{EXP}}{t_{DIT}}$ is the total number of t_{DIT} frames processed in the t_{EXP} total time.

AMBER+ processing: we have developed a new approach where the full dispersed fringe image is processed, in a way equivalent to a coherent integration of all spectral channels, whatever the SNR1 per channel is. This data processing is explained in Ref. 24. Then we still have to make a quadratic average of the other frames and the SNR of this processing is given by

$$SNR_+(|C|^2) = n_\lambda \frac{SNR_1^2}{\sqrt{1 + 2n_\lambda SNR_1^2}} \sqrt{N_{EXP}}, \tag{13}$$

This allowed a gain of typically $\sqrt{n_\lambda}$ which made possible the first observation of 3C273 with a spectral resolution R=1500. The fringes where detected with a typical $SNR+(|C|^2) = 3$ in 1 s exposures.

The phase is estimated from the average coherent flux and its accuracy is given by

$$\sigma_\phi = \frac{< C >}{\sigma_C \sqrt{2}} = \frac{1}{SNR_1 \sqrt{2} \sqrt{N_{EXP}}} \tag{14}$$

with $N_{EXP} = 36000$ for 2 hours of observations.

In AMBER+, a SNR analysis (Petrov et al, 2014 SPIE) shows that

$$\sigma_{\phi+} = \sigma_\phi \sqrt{2 \frac{\sigma_\phi^2}{n_\lambda} + \frac{1 + n_\lambda}{n_\lambda}} \tag{15}$$

The above equations are used in §4 to calculate the SNR on coherent and the number of target accessible with the current and upcoming VLTI instruments.

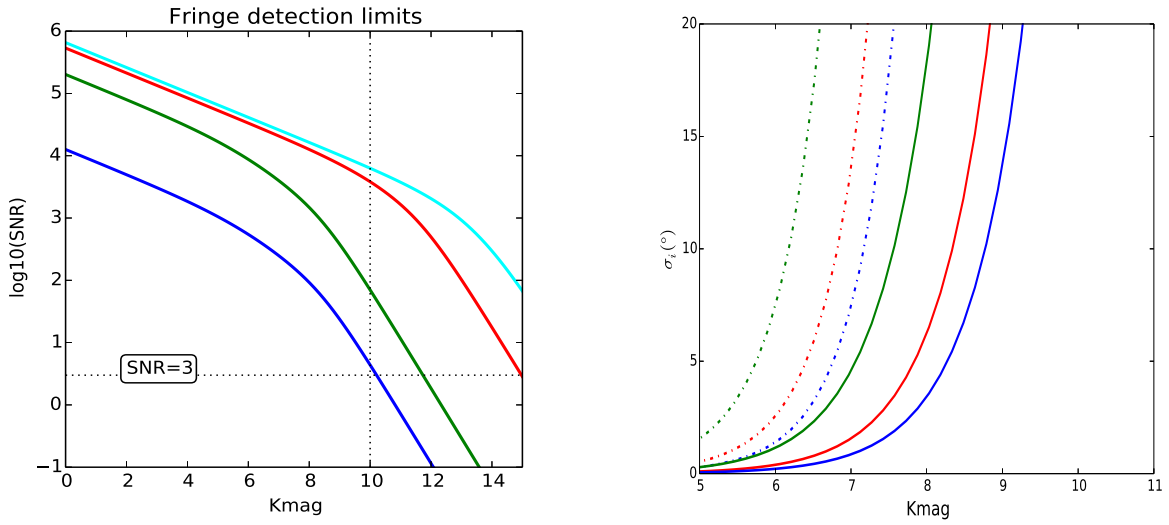

Figure 3. Left: Fringe detection (log10(SNR)) limits for different VLTI instruments: from left to right: standard AMBER performance with 0.2 s frames (solid blue), current AMBER+ measured performance with incoherent TF2D processing (solid green), OASIS module (solid red) and OASIS+ module (solid cyan). The AMBER+ curve (given here for a maximum of 20s) is compatible with our experimental result of fringe detection with SNR=3 in 1 s on 3C273. The horizontal dotted black line shows the threshold fringe detection limit of SNR=3 and vertical dotted black line corresponds to K = 10. Right: Accuracy on inclination with K magnitude for AMBER+(dashed-dot) and GRAVITY(solid) for different inclination $i = 5°$(green), $15°$(red) and $30°$(blue).

4.2 VLTI INSTRUMENTS

We focus on the VLTI because we believe that the 8m UTs are a key feature for an AGN MR program. Table 1 summarizes the observing parameters for the different instruments.

AMBER: AMBER[19] is the existing first generation near infrared spectro-interferometric VLTI instrument. With its standard frame-by-frame processing, it cannot observe AGNs in medium resolution (MR) without a fringe tracker that stabilize the fringes. The current VLTI fringe trackers are limited to about K< 9. AMBER can be used in low resolution for absolute visibility measurements in the continuum.

AMBER+: AMBER+[24] refers to a new observing mode and data processing of AMBER data, as discussed in §4.1. It allowed observing successfully the QSO 3C273 in MR (R=1500). The fringes were detected with a SNR=3 in typically 1s. To obtain differential visibility and phase with a sufficient accuracy (respectively 0.02

to 0.03 and 1° to 2°) it has been necessary to bin the spectral channels down to a resolution 250. The results achieved with AMBER+ on 3C273 have been used to validate our SNR computations.

OASIS: OASIS ("Optimizing AMBER for Spectro-Interferometry and Sensitivity") is a low-cost module that could easily be installed on AMBER and use the AMBER+ software (Petrov, 2014). It has been designed to optimize the AMBER+ mode for medium spectral resolution observations. Its two main characteristics are: 1. It uses a spectral encoding to separate the fringe peaks, instead of the standard AMBER or MATISSE spatial encoding. Thus each interferogram can be coded on 4 pixels per spectral line instead of 32 like in AMBER (24 in GRAVITY). 2. The spatial filters with fibers are bypassed by optimized optics, allowing to use both polarizations together, which yields a gain in transmission of about 7 with regard to the current AMBER instrument.

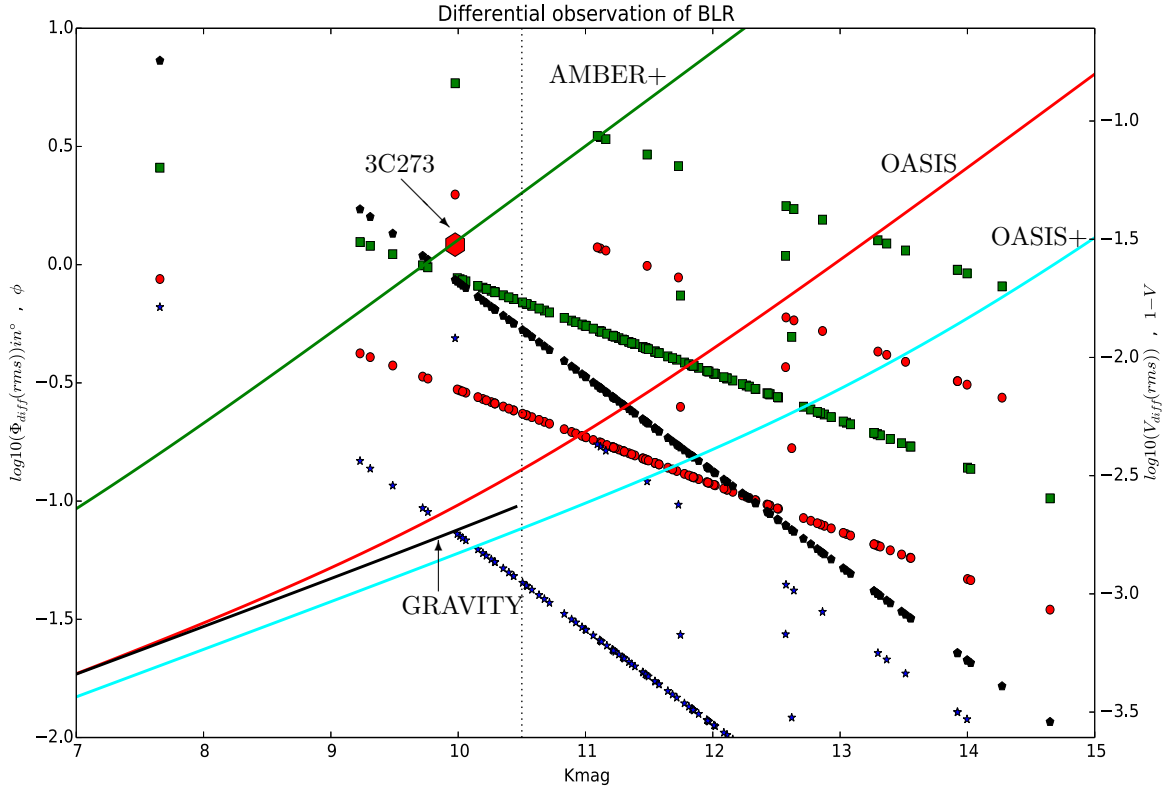

Figure 4. Feasibility of observation of BLR with 135 m baseline: the lines represent the log of differential phase error in deg (left side) and differential visibility error (right side). for the current AMBER+ processing (solid green), with the OASIS module (solid red), with the OASIS+ module (solid cyan) and with upcoming VLTI instrument GRAVITY (solid black). Each symbol represents one Sy 1 AGN observable at Paranal, from SIMBAD database; differential phase from skewed and inclined inner dust rings (filled green square), differential phase expected from R_{blr} estimates from visible RM (filled red circle), differential visibility measurements (1-Vd) (filled blue star) and absolute visibility(1-V_{abs}) in black filled polygon. The vertical black dotted line shows the magnitude limit of GRAVITY.

GRAVITY: GRAVITY[34] is a 2nd generation VLTI spectro-interferometric instrument in K band. It should be commissioned in 2015-16. Its main characteristic of interest for a BLR program is that it has an internal fringe tracker that should allow cophased observations up to K=10.5. This allows much longer individual frame times, a higher instrumental visibility and a more stable one. The current GRAVITY plans do no foresee operation without its fringe tracker, but it should be possible to implement on it a GRAVITY+ TF2D mode allowing to observe beyond K=10.5, with performances intermediate between AMBER+ and OASIS.

OASIS+: OASIS uses the spectrograph and the detector of AMBER. OASIS+ would use OASIS with a new SELEX detector and a spectrograph optimized for BLRs, with a spectral resolution R=500. OASIS+, or

any other successor of the 2nd generation VLTI instruments, is not in the current ESO plans, but it gives an idea of what could be ultimate VLTI performance for AGNs.

Table 1. Parameters for fringe detection limit[a] and differential observation of BLR[b] plot.

Instrument	**Parameters**												
	n_T	$t_{DIT}(s)$	n_p	σ_{RON}	n_{th}	V_{inst}	n_λ	N_{EXP}	n_0	A(cm^2)	S	T	R
AMBER	3	0.2	64	11	1.07	0.25	256	100[a], 36000 [b]	45	497628	0.5	0.02	1500
AMBER+	3	0.2	64	11	1.07	0.25	256	100[a], 36000[b]	45	497628	0.5	0.02	1500
OASIS	3	0.2	8	11	1.07	0.25	256	100[a], 36000[b]	45	497628	0.5	0.02 × 7	1500
OASIS+	3	0.1	8	3	1.07	0.5	256	100[a], 36000[b]	45	497628	0.5	0.02 × 7	500
GRAVITY	4	60	48[c]	11	1.07	0.75	256	120[b]	45	497628	0.5	0.01 × 2	500

[c]Pair wise, 8 per pair

4.3 Fringe detection limit

In left panel of Fig.3 we plotted the fringe detection limit log(SNR) with K mag. using the parameters listed in Table 1 for different instrument like standard AMBER performance with 0.2 sec frames (blue), AMBER+ performance with incoherent TF2D processing (green), OASIS module (red) and OASIS+ module (cyan). We found that the AMBER+ could reach up to K $\sim$ 10.5 and the potential limit of the new OASIS and OASIS+ $>$ 13. The accuracy on the inclination with K mag. is plotted in right panel of Fig.3 for different instrument AMBER+ (dotted) and GRAVITY (solid) for various inclination 5°(green), 15°(red) and 30°(blue).

4.4 Targets and amplitude of signals

We collected a list of all Sy1 and QSOs observable with the VLTI found in the SIMBAD catalog with specific search criteria K $<$ 13, V $<$ 15 and dec $<$ 15°. For each source we estimate the inner rim radius from its magnitude thanks to an extrapolation of Ref. 23 known measurements. From this rim radius we evaluate the possible values of the continuum visibility and the differential visibility and phase. These values are compared to the SNR estimates.

We use the CMB corrected redshift for each target from NED. The K mag. of each object is corrected taking the K mag. from 2MASS point source catalog when available (i.e. for almost all source). We subtracted the contribution of host galaxy, which is taken 0.2 in K.[35]

We collected the list of objects from Ref. 4 that has classical RM BLR size. Then we fitted the radius with their K mag. and extrapolate for the objects that do not have the RM BLR size. In a similar way we obtained dust sublimation radius from IR RM observation of Ref. 23 and extrapolate for the objects that has no IR measurement.

To estimate absolute visibility signal we used the following equation deduced from the appendix A.

$$V_c = 1 - 2\alpha_c^2, \tag{16}$$

where $\alpha_c = \frac{2R_{rim}}{\lambda/B}$.

Differential visibility yields the relative values of inner rim radius R_{rim}[23] and R_{blr}.[4] If $R_{rim} << R_{blr}$, the differential visibility yields R_{rim}. If they are different and both smaller than λ/B, R_{rim} and R_{blr} can be deduced independently from measurements at different baselines. The differential visibility signal is typically

$$V_{diff} \simeq -\frac{S_l}{S_l + S_c}\frac{\alpha_c^2}{1-\alpha_c^2} \quad \text{when } R_{blr} << R_{rim} \tag{17}$$

$$\simeq +3\frac{S_l}{S_l + S_c}\frac{\alpha_c^2}{1-\alpha_c^2} \quad \text{when } R_{blr} = 2R_{rim}, \tag{18}$$

where S_l is the line strength and S_c is the continuum strength for R_{blr} ranging from 0 to $2R_{rim}$ and $S_c = 1$. The typical differential phase amplitude for the BLR only is given by

$$\phi_{diff} = \pi \frac{S_l}{S_l + S_c} \alpha_l cos(\omega), \tag{19}$$

where $\alpha_l = \frac{2R_{blr}}{\lambda/B}$ and ω is the opening angle of the disc.

If the inner rim of the dust torus is inclined and skewed, differential interferometry will also be sensitive to the difference between the continuum apparent photocenter with maximum amplitude of

$$\phi_{diff} \simeq \frac{\pi}{2} \frac{S_l}{S_l + S_c} \alpha_c sini \tag{20}$$

For line strength, we considered:

- $S_l = 0.6$ when Pa α is in the K band ($0.08 \leq z < 0.25$)
- $S_l = 0.3$ when Pa β is in the K band ($0.4 \leq z < 0.87$)
- $S_l = 0.3$ when Pa β is in the H band ($0.25 \leq z < 0.4$)
- $S_l = 0.06$ when Br γ is in the K band ($z < 0.08$)
- $S_l = 0.12$ when Pa γ is in the K band ($z \geq 0.87$)

The above eq. 18-20 are certainly model dependent but they are sufficient for an estimation of the possibility to observe a target. We will use the above equation in §4 to estimate the SNR from different interferometric instruments and the number of possible BLR of AGNs accessible by present and upcoming interferometers in VLTI.

4.5 Potential Performance

Fig.4 shows the feasibility of observation of BLRs with current and upcoming VLTI instruments like current AMBER+ processing (solid green), with the possible low cost OASIS module (solid red), the OASIS+ module (solid cyan) and next generation upcoming VLTI instrument GRAVITY (solid black). Each symbol represents one Sy 1 AGN observable at Paranal, from SIMBAD database; differential phase from skewed and inclined inner dust rings (filled green square) from eq.20, differential phase expected from R_{blr} estimates from visible RM (filled red circle) from eq.19 and differential visibility measurements (1-Vd) from eq.18 (filled blue star). Any signal with accuracy better than these amplitudes will yield useful constraints.

We found that with the improved modules like OASIS and OASIS+ on AMBER we shall be able to access few objects where we can get all the differential interferometric measures, two times more objects shall provide differential phase signal even if the interferometric radius is as small as the BLR radius and asymmetry in the inclined skewed disk (or a BLR phase effect for an extended BLR) could be detectable with differential interferometry for three times more object. The upcoming instrument GRAVITY with its new fringe tracking capability up to K = 9.5 for Sy 1 AGNs and K = 10.5 for QSOs is likely to provide all interferometric measures on many of the targets.

For a good estimation of continuum and BLR sizes we need accurate absolute visibility measurement. Differential visibility and phases with medium spectral resolution (R> 1000) is necessary to constrain the geometry of the BLR. Differential phase alone, possibly assisted by lower spectral resolution differential visibility (in the 250-500 range) can provide size and global velocity estimates, i.e. masses if we have an a priori knowledge of the model.

5. DISCUSSION

From our dynamical model, we showed that the differential visibility, due to its higher accuracy, allows accurate measurement of BLR size for a known model. If we also have the absolute visibility measurement, we can have an almost model independent size measurement. Our model and the SNR estimates show that the absolute visibility, differential visibility and differential phase at medium spectral resolution can strongly constrain the parameters of a fairly complex model. This could be implemented in a global model fitting way. The study of the corresponding parameter degeneracy and final accuracy would be an extension of the current work.

We found that the BH mass measurement is very sensitive to global velocity of the BLR clouds as well as the scale factor f which depends on the geometry (ω and i) and local line width (here, $\sigma 0_{line}$) that can represent the combination of microturbulence inside the clouds with macroturbulent motion of the clouds. The RM 1D response function produced in different combinations of these parameters are similar and hence RM can not discriminant these three parameters. However both the differential visibility and differential phase measures with a sufficient spectral resolution (typically > 1000) allow to discriminate them. The effect is more obvious in the differential visibility but the differential phase can be measured accurately on smaller targets.

An independent estimate of the inclination would very substantially improve the accuracy on ω and $\sigma 0_{line}$. This estimates could be obtained from detail line profile fitting and radio emission from jets for individual objects though the uncertainty is too large and the necessary jet observations from the visible to the X-ray domain are not easily available on all targets. Based on the emission line fitting Ref. 36 has found that the inclination of BLR is $24^\circ - 30^\circ$ and Ref. 37 suggested the inclination of the BLR can be $19^\circ - 42^\circ$. X-ray studies of Sy 1 suggested that the BLR inclination should be low.[38,39] Thus we should rely on the OI interferometric measures of the ratio of visibilities between the major and minor axis of the dust rim. This needs low spectral resolution observations of the K band continuum with accurate absolute visibility measurements. GRAVITY would give $\sim 13^\circ$ accuracy on 30° inclined object for K=9, if we achieve an absolute visibility accuracy of 0.003 like the FLUOR instrument on CHARA. We expect that GRAVITY will achieve this kind of accuracy but this still has to be proven. Our work sets a specification for this measure for a full use of the AGN BLR program.

To allow more precise estimates of the mass-luminosity relation, which would be a major contribution to the study of SMBH and host galaxy evolution, we hope that it will be possible to calibrate a law linking the RM projection factor to the luminosity: $f_{RM} = f(L)$. This needs a calibration of the $\omega = f(L)$ and $\sigma 0_{line} = f(L)$ laws. The study of $\omega = f(L)$ needs differential visibilities and phases with a spectral resolution higher than 1000. If we access all targets permitted by VLTI instrument, as shown in Fig.4, we cover a wide luminosity range 10^{43}-10^{48} ergs/s.

Combined measurement of BLR size of the same object with RM and OI will allow to measure the distance of QSO by "Quasar Parallax" according to Ref. 40, however we need OI to constrain a model to be able to connect angular size from OI to the linear size estimated by RM. With the help of differential phase measurement we could constrain the interferometric size of the BLR upto redshift $z \simeq 1.7$.

The RM lag-luminosity relationship can also be very substantially improved by a better geometrical model. The potential gain will be studied in a next paper.

VLTI is the only interferometer that allows to observe AGN at medium spectral resolution thanks to its large apertures however its baseline is limited to 135m. The upcoming VLTI instrument GRAVITY will be commissioned in 2015-2016. Its impact on the AGN program critically depends on the performances of its internal fringe tracker, but the announced limiting magnitude of K=10.5 seems very reasonable and maybe even slightly conservative. OASIS module could be installed on AMBER in a few months, as soon as ESO accepts to include the corresponding extremely moderate workload in the VLTI planning. OASIS+ which is the AMBER improvement, dedicated to AGN observations, could be a visitor instrument in the 1M euros range and can be developed in less than two years, but, for management reasons, its installation on the VLTI must wait at least the full completion of the 2nd generation general user instruments GRAVITY and MATISSE, i.e. at least 2018. The possibilities of all these instruments, and in particular of GRAVITY and OASIS, can be boosted by the implementation of a new generation Fringe Tracker with a limiting magnitude larger than this of GRAVITY. Concepts allowing to reach the K=12 to K=13 range have been proposed[41] and phase-A studies are at different completion degrees. If fast decisions are made, such a device could be available around 2018.

The ultimate goal would be full images with R=1000 though the emission lines. The angular resolution of BLR requires accurate closure phases and therefore kilometric baselines in the near infrared, i.e. the development of a new facility. It can also be achieved in the visible with the current CHARA baselines, but would require a medium resolution limiting magnitude in the V=13-14 with 1 m telescopes. In both cases, it is not yet possible to give a date for these achievements.

6. CONCLUSION

A large number of BLR, up to K> 13, will be accessible with the upcoming VLTI instruments GRAVITY and possible future instrument OASIS, which will unveil the morphology of the BLR and hence it will make possible to answer the central SMBH growth and evolution history and would allow the test of a further unification step, based on the dependence of key parameters from the luminosity. New generation FT and OASIS+ (or another VLTI module optimized for AGNs), will allow using the full VLTI potential, as it is limited by its baselines. The future developments of this work include: A. The presentation and interpretation of the observation of 3C273 with AMBER+/VLTI. B. The analysis of a full model fitting approach, based on more detailed measurement accuracies achieved on recent 3C273 data. C. The physical modeling of clouds, using the cloudy model, and allowing to compute the clouds spectral response and their contribution to luminosity in interaction with the global geometrical and kinematic parameters. D. An analysis of the contribution of OI interferometry in the thermal infrared with the MATISSE VLTI instrument.

APPENDIX A. ANGULAR SIZE AND OI MEASURES

We can derive simple expressions of the visibility and the closure phase if we assume, without the loss of generality that the object has two components:

a) A symmetric component, with total flux $1-a$ and equivalent radius R.

b) An asymmetric component, with total flux a ($a<1$) located at a position $P=pR$ (with $p<1$)

For a simple evaluation, we shall derive the interferometric measures for the following example of such an object:

$$O(r,\lambda)=\frac{(1-a)\delta(r-R)}{2}+\frac{(1-a)\delta(r+R)}{2}+a\delta(r-P) \tag{21}$$

Eq.4 can be expanded as

$$\begin{aligned}\tilde{O}(\mathbf{u},\lambda)&=1-i2\pi\frac{\int\int \mathbf{u}.\mathbf{r}O(\mathbf{r},\lambda)\,\mathrm{d}^2\mathbf{r}}{\int\int O(\mathbf{r},\lambda)\,\mathrm{d}^2\mathbf{r}}-\frac{(2\pi)^2}{2}\frac{\int\int (\mathbf{u}.\mathbf{r})^{\mathbf{2}}O(\mathbf{r},\lambda)\,\mathrm{d}^2\mathbf{r}}{\int\int O(\mathbf{r},\lambda)\,\mathrm{d}^2\mathbf{r}}+i\frac{(2\pi)^3}{6}\frac{\int\int (\mathbf{u}.\mathbf{r})^{\mathbf{3}}O(\mathbf{r},\lambda)\,\mathrm{d}^2\mathbf{r}}{\int\int O(\mathbf{r},\lambda)\,\mathrm{d}^2\mathbf{r}}+...\\&=1-iUM_1+\frac{UM_2}{2}+i\frac{UM_3}{6}+...,\end{aligned} \tag{22}$$

where $U=2\pi\mathbf{u}$ and $M_n=\int\int(\mathbf{r}^nO(\mathbf{r},\lambda)d^2r)$ is the nth order moment of the brightness distribution $O(\mathbf{r},\lambda)$. The moments of the example brightness distribution are:

$$M_n=(1-a)R^n+a(PR)^n=a(PR)^n=1 \tag{23}$$

Using the above values in eq.22 and doing some further calculation after neglecting the higher order terms of UR we obtain:

$$\phi_{*ij}(\lambda)=-U\epsilon(\lambda)+\frac{U^3}{6}R^2\epsilon^2(\lambda)\left[3(1-a)+3ap^2(\lambda)-p^2(\lambda)\right] \tag{24}$$

$$\Psi_{123}=-\frac{\epsilon(\lambda)R^2}{6}\left[3(1-a)+3ap^2(\lambda)-p^2(\lambda)\right]\times\left(U_1^3+U_2^3+U_3^3\right) \tag{25}$$

$$V_{*ij}=1-\frac{U^2R^2}{2}\left[(1-a)+ap^2(\lambda)\right]+\frac{\epsilon^2(\lambda)U^2}{2}, \tag{26}$$

where $\epsilon(\lambda)=aPR$.

For non-resolved sources, we note $\alpha=\frac{\Lambda}{\lambda/B}=\frac{2R}{\lambda/B}>UR$.

ACKNOWLEDGMENTS

This research has made use of the SIMBAD database which is operated at CDS, Strasbourg, France and the NASA/IPAC Extragalactic Database (NED) which is operated by the Jet Propulsion Laboratory, California Institute of Technology, under contract with NASA. This publication also makes use of data products from the Two Micron All Sky Survey, which is a joint project of the University of Massachusetts and the Infrared Processing and Analysis Center/California Institute of Technology, funded by the National Aeronautics and Space Administration and the National Science Foundation. SR thanks Neha Sharma for providing criticisms to improve this manuscript.

SR is supported by the Erasmus Mundus Joint Doctorate Program by Grant Number 2011-1640 from the EACEA of he European Commission.

REFERENCES

[1] B. M. Peterson *et al.*, "Central Masses and Broad-Line Region Sizes of Active Galactic Nuclei. II. A Homogeneous Analysis of a Large Reverberation-Mapping Database.," *apj* **613**, 682–699 (2004).

[2] S. Collin *et al.*, "Systematic effects in measurement of black hole masses by emission-line reverberation of active galactic nuclei: Eddington ratio and inclination.," *aa* **456**, 75–90 (2006).

[3] M. R. Goad *et al.*, "The broad emission-line region: the confluence of the outer accretion disc with the inner edge of the dusty torus," *mnras* **426**, 3086–3111 (2012).

[4] M. C. Bentz *et al.*, "The Low-luminosity End of the Radius-Luminosity Relationship for Active Galactic Nuclei," *apj* **767**, 27 (2013).

[5] S. Kaspi *et al.*, "Reverberation Measurements for 17 Quasars and the Size-Mass-Luminosity Relations in Active Galactic Nuclei.," *apj* **533**, 631–649 (2000).

[6] M. E. Kaiser *et al.*, "The Resolved Narrow-Line Region in NGC 4151," *apj* **528**, 260–275 (2000).

[7] M. Vestergaard and B. M. Peterson, "Determining Central Black Hole Masses in Distant Active Galaxies and Quasars. II. Improved Optical and UV Scaling Relationships," *apj* **641**, 689–709 (2006).

[8] M. C. Bentz *et al.*, "The Radius-Luminosity Relationship for Active Galactic Nuclei: The Effect of Host-Galaxy Starlight on Luminosity Measurements," *apj* **644**, 133–142 (2006).

[9] M. C. Bentz *et al.*, "The Radius-Luminosity Relationship for Active Galactic Nuclei: The Effect of Host-Galaxy Starlight on Luminosity Measurements. II. The Full Sample of Reverberation-Mapped AGNs," *apj* **697**, 160–181 (2009).

[10] Y. Zu *et al.*, "An Alternative Approach to Measuring Reverberation Lags in Active Galactic Nuclei," *apj* **735**, 80 (2011).

[11] K. D. Denney *et al.*, "Diverse Kinematic Signatures from Reverberation Mapping of the Broad-Line Region in AGNs," *apjl* **704**, L80–L84 (2009).

[12] C. L. MacLeod *et al.*, "Modeling the Time Variability of SDSS Stripe 82 Quasars as a Damped Random Walk," *apj* **721**, 1014–1033 (2010).

[13] C. J. Grier *et al.*, "Reverberation Mapping Results for Five Seyfert 1 Galaxies," *apj* **755**, 60 (2012).

[14] A. Pancoast *et al.*, "The Lick AGN Monitoring Project 2011: Dynamical Modeling of the Broad-line Region in Mrk 50," *apj* **754**, 49 (2012).

[15] R. G. Petrov *et al.*, "AMBER: the near-infrared focal instrument for the Very Large Telescope Interferometer," in *Interferometry in Optical Astronomy*, P. Léna and A. Quirrenbach, Eds., *Society of Photo-Optical Instrumentation Engineers (SPIE) Conference Series* **4006**, 68–79 (2000).

[16] R. G. Petrov, "Differential Interferometry," in *NATO ASIC Proc. 274: Diffraction-Limited Imaging with Very Large Telescopes*, D. M. Alloin and J.-M. Mariotti, Eds., 249 (1989).

[17] A. Marconi *et al.*, "Extragalactic Astronomy with the VLTI: a new window on the Universe," *apss* **286**, 245–254 (2003).

[18] M. Karovska *et al.*, "Distances on Cosmological Scales with VLTI," *apss* **286**, 261–266 (2003).

[19] R. G. Petrov *et al.*, "AMBER, the near-infrared spectro-interferometric three-telescope VLTI instrument," *aap* **464**, 1–12 (2007).

[20] W. Jaffe *et al.*, "The central dusty torus in the active nucleus of NGC 1068," *nat* **429**, 47–49 (2004).

[21] L. Burtscher *et al.*, "A diversity of dusty AGN tori. Data release for the VLTI/MIDI AGN Large Program and first results for 23 galaxies," *aap* **558**, A149 (2013).
[22] M. Kishimoto *et al.*, "Probing the innermost dusty structure in AGN with mid-IR and near-IR interferometers," *Journal of Physics Conference Series* **372**, 012033 (2012).
[23] M. Suganuma *et al.*, "Reverberation Measurements of the Inner Radius of the Dust Torus in Nearby Seyfert 1 Galaxies," *apj* **639**, 46–63 (2006).
[24] R. G. Petrov *et al.*, "VLTI/AMBER differential interferometry of the broad-line region of the quasar 3C273," in *Society of Photo-Optical Instrumentation Engineers (SPIE) Conference Series*, *Society of Photo-Optical Instrumentation Engineers (SPIE) Conference Series* **8445** (2012).
[25] D. Mourard *et al.*, "VEGA: Visible spEctroGraph and polArimeter for the CHARA array: principle and performance," *aap* **508**, 1073–1083 (2009).
[26] R. G. Petrov, "Spectro-Interferometry and Differential Interferometry with Amber and The VLTI," *Publications de l'Observatoire Astronomique de Beograd* **91**, 21–34 (2012).
[27] M. Kishimoto *et al.*, "The innermost dusty structure in active galactic nuclei as probed by the Keck interferometer," *aap* **527**, A121 (2011).
[28] A. Chalabaev, "Photocenter Versus Wavelength for a Gaseous Disk Envelope," in *European Southern Observatory Conference and Workshop Proceedings*, J. M. Beckers and F. Merkle, Eds., *European Southern Observatory Conference and Workshop Proceedings* **39**, 403 (1992).
[29] P. Stee, "On the kinematics of the envelope of γ Cassiopeiae.," *aap* **311**, 945–950 (1996).
[30] P. T. O'Brien *et al.*, "Response Functions as Diagnostics of the Broadline Region in Active Galactic Nuclei - Part Two - Anisotropic Line Emission," *mnras* **268**, 845 (1994).
[31] R. Petrov *et al.*, "Signal-to-noise ratio in differential speckle interferometry," *Journal of the Optical Society of America A* **3**, 634–644 (1986).
[32] M. Vannier *et al.*, "Colour-differential interferometry for the observation of extrasolar planets," *mnras* **367**, 825–837 (2006).
[33] S. Lagarde *et al.*, "MATISSE: concept, specifications, and performances," in *Society of Photo-Optical Instrumentation Engineers (SPIE) Conference Series*, *Society of Photo-Optical Instrumentation Engineers (SPIE) Conference Series* **8445** (2012).
[34] F. Eisenhauer *et al.*, "GRAVITY: getting to the event horizon of Sgr A*," in *Society of Photo-Optical Instrumentation Engineers (SPIE) Conference Series*, *Society of Photo-Optical Instrumentation Engineers (SPIE) Conference Series* **7013** (2008).
[35] T. Minezaki *et al.*, "Inner Size of a Dust Torus in the Seyfert 1 Galaxy NGC 4151," *apjl* **600**, L35–L38 (2004).
[36] M. Eracleous and J. P. Halpern, "Doubled-peaked emission lines in active galactic nuclei," *apjs* **90**, 1–30 (1994).
[37] M. Eracleous and j. . a. k. . G. y. . . m. . m. v. . . p. . . d. . . a. . h. a. . P. others, title = "The Resolved Fe K alpha Line of the Broad-Line Radio Galaxy 3C 390.3 and Its Implications"
[38] K. Nandra *et al.*, "ASCA Observations of Seyfert 1 Galaxies. II. Relativistic Iron K alpha Emission," *apj* **477**, 602 (1997).
[39] K. Nandra *et al.*, "The Properties of the Relativistic Iron K-Line in NGC 3516," *apjl* **523**, L17–L20 (1999).
[40] M. Elvis and M. Karovska, "Quasar Parallax: A Method for Determining Direct Geometrical Distances to Quasars," *apjl* **581**, L67–L70 (2002).
[41] R. G. Petrov *et al.*, "Hierarchical Fringe Tracking," in *Society of Photo-Optical Instrumentation Engineers (SPIE) Conference Series*, *Society of Photo-Optical Instrumentation Engineers (SPIE) Conference Series* **9146** (2014).

Bibliography

E. A. Fath. The northern limit of the zodiacal light. *Lick Observatory Bulletin*, 5:45–49, 1908. doi: 10.5479/ADS/bib/1908LicOB.5.45F.

C. K. Seyfert. Nuclear Emission in Spiral Nebulae. *ApJ*, 97:28, January 1943. doi: 10.1086/144488.

C. Hazard, M. B. Mackey, and A. J. Shimmins. Investigation of the Radio Source 3C 273 By The Method of Lunar Occultations. *Nature*, 197:1037–1039, March 1963. doi: 10.1038/1971037a0.

M. Schmidt. 3C 273 : A Star-Like Object with Large Red-Shift. *Nature*, 197:1040, March 1963. doi: 10.1038/1971040a0.

B. J. Boyle, T. Shanks, S. M. Croom, R. J. Smith, L. Miller, N. Loaring, and C. Heymans. The 2dF QSO Redshift Survey - I. The optical luminosity function of quasi-stellar objects. *MNRAS*, 317:1014–1022, October 2000. doi: 10.1046/j.1365-8711.2000.03730.x.

C. M. Urry and P. Padovani. Unified Schemes for Radio-Loud Active Galactic Nuclei. *PASP*, 107:803, September 1995. doi: 10.1086/133630.

R. Antonucci. Unified models for active galactic nuclei and quasars. *ARA&A*, 31:473–521, January 1993. doi: 10.1146/annurev.aa.31.090193.002353.

R. R. J. Antonucci and J. S. Miller. Spectropolarimetry and the nature of NGC 1068. *ApJ*, 297:621–632, October 1985. doi: 10.1086/163559.

D. Lynden-Bell. Galactic Nuclei as Collapsed Old Quasars. *Nature*, 223:690–694, August 1969. doi: 10.1038/223690a0.

X.-B. Wu, F. Wang, X. Fan, W. Yi, W. Zuo, F. Bian, L. Jiang, I. D. McGreer, R. Wang, J. Yang, Q. Yang, D. Thompson, and Y. Beletsky. An ultraluminous quasar with a twelve-billion-solar-mass black hole at redshift 6.30. *Nature*, 518:512–515, February 2015. doi: 10.1038/nature14241.

R. Wang, C. L. Carilli, R. Neri, D. A. Riechers, J. Wagg, F. Walter, F. Bertoldi, K. M. Menten, A. Omont, P. Cox, and X. Fan. Molecular Gas in z ˜ 6 Quasar Host Galaxies. *ApJ*, 714:699–712, May 2010. doi: 10.1088/0004-637X/714/1/699.

L. Ferrarese and D. Merritt. A Fundamental Relation between Supermassive Black Holes and Their Host Galaxies. *ApJ*, 539:L9–L12, August 2000. doi: 10.1086/312838.

K. Gebhardt, R. Bender, G. Bower, A. Dressler, S. M. Faber, A. V. Filippenko, R. Green, C. Grillmair, L. C. Ho, J. Kormendy, T. R. Lauer, J. Magorrian, J. Pinkney, D. Richstone, and S. Tremaine. A Relationship between Nuclear Black Hole Mass and Galaxy Velocity Dispersion. *ApJ*, 539:L13–L16, August 2000a. doi: 10.1086/312840.

M. C. Bentz, B. M. Peterson, R. W. Pogge, and M. Vestergaard. The Black Hole Mass-Bulge Luminosity Relationship for Active Galactic Nuclei From Reverberation Mapping and Hubble Space Telescope Imaging. *ApJ*, 694:L166–L170, April 2009a. doi: 10.1088/0004-637X/694/2/L166.

R. D. Blandford and C. F. McKee. Reverberation mapping of the emission line regions of Seyfert galaxies and quasars. *ApJ*, 255:419–439, April 1982. doi: 10.1086/159843.

N. I. Shakura and R. A. Sunyaev. Black holes in binary systems. Observational appearance. *A&A*, 24:337–355, 1973.

R. Narayan and I. Yi. Advection-dominated accretion: A self-similar solution. *ApJ*, 428:L13–L16, June 1994. doi: 10.1086/187381.

M. A. Abramowicz, B. Czerny, J. P. Lasota, and E. Szuszkiewicz. Slim accretion disks. *ApJ*, 332:646–658, September 1988. doi: 10.1086/166683.

T. Okuda, G. V. Lipunova, and D. Molteni. The jets and disc of SS 433 at super-Eddington luminosities. *MNRAS*, 398:1668–1677, October 2009. doi: 10.1111/j.1365-2966.2009.15169.x.

H. Netzer. *The Physics and Evolution of Active Galactic Nuclei*. November 2013.

J. A. Baldwin, G. J. Ferland, K. T. Korista, F. Hamann, and M. Dietrich. The Mass of Quasar Broad Emission Line Regions. *ApJ*, 582:590–595, January 2003. doi: 10.1086/344788.

N. Arav, T. A. Barlow, A. Laor, and R. D. Blandford. Keck high-resolution spectroscopy of MRK 335: constraints on the number of emitting clouds in the broad-line region. *MNRAS*, 288:1015–1021, July 1997.

N. Arav, T. A. Barlow, A. Laor, W. L. W. Sargent, and R. D. Blandford. Are AGN broad emission lines formed by discrete clouds? Analysis of Keck high-resolution spectroscopy of NGC 4151. *MNRAS*, 297:990–998, July 1998. doi: 10.1046/j.1365-8711.1998.297004990.x.

B. M. Peterson. *An Introduction to Active Galactic Nuclei*. February 1997.

J. A. Baldwin and H. Netzer. The emission-line regions of high-redshift QSOs. *ApJ*, 226:1–20, November 1978. doi: 10.1086/156578.

G. J. Ferland, R. L. Porter, P. A. M. van Hoof, R. J. R. Williams, N. P. Abel, M. L. Lykins, G. Shaw, W. J. Henney, and P. C. Stancil. The 2013 Release of Cloudy. *Revista Mexicana de Astronoma y Astrofsica*, 49:137–163, April 2013.

J. Baldwin, G. Ferland, K. Korista, and D. Verner. Locally Optimally Emitting Clouds and the Origin of Quasar Emission Lines. *ApJ*, 455:L119, December 1995. doi: 10.1086/309827.

J. A. Baldwin. Luminosity Indicators in the Spectra of Quasi-Stellar Objects. *ApJ*, 214:679–684, June 1977. doi: 10.1086/155294.

C. M. Gaskell. What broad emission lines tell us about how active galactic nuclei work. *New Astr.*, 53:140–148, July 2009. doi: 10.1016/j.newar.2009.09.006.

W. Jaffe, K. Meisenheimer, H. J. A. Röttgering, C. Leinert, A. Richichi, O. Chesneau, D. Fraix-Burnet, A. Glazenborg-Kluttig, G.-L. Granato, U. Graser, B. Heijligers, R. Köhler, F. Malbet, G. K. Miley, F. Paresce, J.-W. Pel, G. Perrin, F. Przygodda, M. Schoeller, H. Sol, L. B. F. M. Waters, G. Weigelt, J. Woillez, and P. T. de Zeeuw. The central dusty torus in the active nucleus of NGC 1068. *Nature*, 429:47–49, May 2004. doi: 10.1038/nature02531.

L. Burtscher, K. Meisenheimer, K. R. W. Tristram, W. Jaffe, S. F. Hönig, R. I. Davies, M. Kishimoto, J.-U. Pott, H. Röttgering, et al. A diversity of dusty AGN tori. Data release for the VLTI/MIDI AGN Large Program and first results for 23 galaxies. *A&A*, 558:A149, October 2013. doi: 10.1051/0004-6361/201321890.

M. Kishimoto, S. F. Hönig, R. Antonucci, R. Barvainis, T. Kotani, F. Millour, K. R. W. Tristram, and G. Weigelt. Probing the innermost dusty structure in AGN with mid-IR and near-IR interferometers. *Journal of Physics Conference Series*, 372(1):012033, July 2012. doi: 10.1088/1742-6596/372/1/012033.

M. Suganuma, Y. Yoshii, Y. Kobayashi, T. Minezaki, K. Enya, H. Tomita, T. Aoki, S. Koshida, and B. A. Peterson. Reverberation Measurements of the Inner Radius of the Dust Torus in Nearby Seyfert 1 Galaxies. *ApJ*, 639:46–63, March 2006. doi: 10.1086/499326.

S. Koshida, T. Minezaki, Y. Yoshii, Y. Kobayashi, Y. Sakata, S. Sugawara, K. Enya, M. Suganuma, H. Tomita, T. Aoki, and B. A. Peterson. Reverberation Measurements of the Inner Radius of the Dust Torus in 17 Seyfert Galaxies. *ApJ*, 788:159, June 2014. doi: 10.1088/0004-637X/788/2/159.

T. Storchi Bergmann. The Narrow Line Region in 3D: mapping AGN feeding and feedback. In B. L. Ziegler, F. Combes, H. Dannerbauer, and M. Verdugo, editors, *IAU Symposium*, volume 309 of *IAU Symposium*, pages 190–195, February 2015. doi: 10.1017/S1743921314009648.

M. L. Lister, M. H. Cohen, D. C. Homan, M. Kadler, K. I. Kellermann, Y. Y. Kovalev, E. Ros, T. Savolainen, and J. A. Zensus. MOJAVE: Monitoring of Jets in Active Galactic Nuclei with VLBA Experiments. VI. Kinematics Analysis of a Complete Sample of Blazar Jets. *Astrophys. J.*, 138:1874–1892, December 2009. doi: 10.1088/0004-6256/138/6/1874.

A. P. Marscher, S. G. Jorstad, J.-L. Gómez, M. F. Aller, H. Teräsranta, M. L. Lister, and A. M. Stirling. Observational evidence for the accretion-disk origin for a radio jet in an active galaxy. *Nature*, 417:625–627, June 2002.

M. Elvis, B. J. Wilkes, J. C. McDowell, R. F. Green, J. Bechtold, S. P. Willner, M. S. Oey, E. Polomski, and R. Cutri. Atlas of quasar energy distributions. *ApJ*, 95:1–68, November 1994. doi: 10.1086/192093.

K. R. W. Tristram. *Mid-infrared interferometry of nearby Active Galactic Nuclei*. PhD thesis, Max-Planck-Institut für Astronomie, Königstuhl 17, 69117 Heidelberg, Germany, 2007.

K. A. Arnaud, G. Branduardi-Raymont, J. L. Culhane, A. C. Fabian, C. Hazard, T. A. McGlynn, R. A. Shafer, A. F. Tennant, and M. J. Ward. EXOSAT observations of a strong soft X-ray excess in MKN 841. *MNRAS*, 217:105–113, November 1985.

I. M. George and A. C. Fabian. X-ray reflection from cold matter in active galactic nuclei and X-ray binaries. *MNRAS*, 249:352–367, March 1991.

E. P. T. Liang. On the hard X-ray emission mechanism of active galactic nuclei sources. *ApJ*, 231:L111–L114, August 1979. doi: 10.1086/183015.

R. Barvainis. Hot dust and the near-infrared bump in the continuum spectra of quasars and active galactic nuclei. *ApJ*, 320:537–544, September 1987. doi: 10.1086/165571.

M. Haas, R. Chini, K. Meisenheimer, M. Stickel, D. Lemke, U. Klaas, and E. Kreysa. On the Far-Infrared Emission of Quasars. *ApJ*, 503:L109–L113, August 1998. doi: 10.1086/311543.

A. Marconi and L. K. Hunt. The Relation between Black Hole Mass, Bulge Mass, and Near-Infrared Luminosity. *ApJ*, 589:L21–L24, May 2003. doi: 10.1086/375804.

P. Salucci, E. Szuszkiewicz, P. Monaco, and L. Danese. Mass function of dormant black holes and the evolution of active galactic nuclei. *MNRAS*, 307:637–644, August 1999. doi: 10.1046/j.1365-8711.1999.02659.x.

A. Marconi, G. Risaliti, R. Gilli, L. K. Hunt, R. Maiolino, and M. Salvati. Local supermassive black holes, relics of active galactic nuclei and the X-ray background. *MNRAS*, 351:169–185, June 2004. doi: 10.1111/j.1365-2966.2004.07765.x.

B. M. Peterson. Variability of Active Galactic Nuclei. In I. Aretxaga, D. Kunth, and R. Mújica, editors, *Advanced Lectures on the Starburst-AGN*, page 3, 2001.

M.-H. Ulrich, A. Boksenberg, M. V. Penston, G. E. Bromage, J. Clavel, A. Elvius, G. C. Perola, and M. A. J. Snijders. The ultraviolet spectrum of NGC 4151 from 1978 to 1990 - General characteristics and evolution. *ApJ*, 382:483–500, December 1991. doi: 10.1086/170735.

R. R. J. Antonucci and R. D. Cohen. Time development of the emission lines and continuum of NGC 4151. *ApJ*, 271:564–574, August 1983. doi: 10.1086/161223.

M. C. Bentz, J. L. Walsh, A. J. Barth, Y. Yoshii, J.-H. Woo, X. Wang, T. Treu, C. E. Thornton, R. A. Street, et al. The Lick AGN Monitoring Project: Reverberation Mapping of Optical Hydrogen and Helium Recombination Lines. *ApJ*, 716:993–1011, June 2010a. doi: 10.1088/0004-637X/716/2/993.

Y. Zu, C. S. Kochanek, and B. M. Peterson. An Alternative Approach to Measuring Reverberation Lags in Active Galactic Nuclei. *ApJ*, 735:80, July 2011. doi: 10.1088/0004-637X/735/2/80.

S. Collin, T. Kawaguchi, B. M. Peterson, and M. Vestergaard. Systematic effects in measurement of black hole masses by emission-line reverberation of active galactic nuclei: Eddington ratio and inclination. *å*, 456:75–90, 2006. doi: 10.1051/0004-6361:20064878.

B. M. Peterson, T. J. Balonek, E. S. Barker, J. Bechtold, R. Bertram, N. G. Bochkarev, M. J. Bolte, D. Bond, et al. Steps toward determination of the size and structure of the broad-line region in active galactic nuclei. II - an intensive study of NGC 5548 at optical wavelengths. *ApJ*, 368:119–137, February 1991. doi: 10.1086/169675.

Shai Kaspi, Paul S. Smith, Hagai Netzer, Dan Maoz, Buell T. Jannuzi, and Uriel Giveon. Reverberation Measurements for 17 Quasars and the Size-Mass-Luminosity Relations in Active Galactic Nuclei. *ApJ*, 533:631–649, 2000. doi: 10.1086/308704.

B. M. Peterson, L. Ferrarese, K. M. Gilbert, S. Kaspi, M. A. Malkan, D. Maoz, D. Merritt, H. Netzer, C. A. Onken, R. W. Pogge, M. Vestergaard, and A. Wandel. Central Masses and Broad-Line Region Sizes of Active Galactic Nuclei. II. A Homogeneous Analysis of a Large Reverberation-Mapping Database. *ApJ*, 613:682–699, 2004. doi: 10.1086/423269.

M. C. Bentz, J. L. Walsh, A. J. Barth, N. Baliber, V. N. Bennert, G. Canalizo, A. V. Filippenko, M. Ganeshalingam, et al. The Lick AGN Monitoring Project: Broad-line Region Radii and Black Hole Masses from Reverberation Mapping of Hβ. *ApJ*, 705:199–217, November 2009b. doi: 10.1088/0004-637X/705/1/199.

M. C. Bentz, K. D. Denney, E. M. Cackett, M. Dietrich, J. K. J. Fogel, H. Ghosh, K. Horne, C. Kuehn, T. Minezaki, et al. A Reverberation-based Mass for the Central Black Hole in NGC 4151. *ApJ*, 651:775–781, November 2006. doi: 10.1086/507417.

C. J. Grier, B. M. Peterson, R. W. Pogge, K. D. Denney, M. C. Bentz, P. Martini, S. G. Sergeev, S. Kaspi, T. Minezaki, et al. Reverberation Mapping Results for Five Seyfert 1 Galaxies. *ApJ*, 755:60, August 2012. doi: 10.1088/0004-637X/755/1/60.

B. J. Brewer, T. Treu, A. Pancoast, A. J. Barth, V. N. Bennert, M. C. Bentz, A. V. Filippenko, J. E. Greene, M. A. Malkan, and J.-H. Woo. The Mass of the Black Hole in Arp 151 from Bayesian Modeling of Reverberation Mapping Data. *ApJ*, 733:L33, June 2011. doi: 10.1088/2041-8205/733/2/L33.

A. Pancoast, B. J. Brewer, T. Treu, A. J. Barth, V. N. Bennert, G. Canalizo, A. V. Filippenko, E. L. Gates, J. E. Greene, W. Li, M. A. Malkan, D. J. Sand, D. Stern, et al. The Lick AGN Monitoring Project 2011: Dynamical Modeling of the Broad-line Region in Mrk 50. *ApJ*, 754:49, July 2012. doi: 10.1088/0004-637X/754/1/49.

A. Pancoast, B. J. Brewer, T. Treu, D. Park, A. J. Barth, M. C. Bentz, and J.-H. Woo. Modelling reverberation mapping data - II. Dynamical modelling of the Lick AGN Monitoring Project 2008 data set. *MNRAS*, 445:3073–3091, December 2014a. doi: 10.1093/mnras/stu1419.

Shai Kaspi, W. N. Brandt, Dan Maoz, Hagai Netzer, Donald P. Schneider, and Ohad Shemmer. Reverberation Mapping of High-Luminosity Quasars: First Results. *ApJ*, 659:997–1007, 2007. doi: 10.1086/512094.

Misty C. Bentz, Kelly D. Denney, Catherine J. Grier, Aaron J. Barth, Bradley M. Peterson, Marianne Vestergaard, and et al. The Low-luminosity End of the Radius-Luminosity Relationship for Active Galactic Nuclei. *ApJ*, 767:27, 2013. doi: 10.1088/0004-637X/767/2/149.

Misty C. Bentz, Bradley M. Peterson, Hagai Netzer, Richard W. Pogge, and Marianne Vestergaard. The Radius-Luminosity Relationship for Active Galactic Nuclei: The Effect of Host-Galaxy Starlight on Luminosity Measurements. II. The Full Sample of Reverberation-Mapped AGNs. *ApJ*, 697:160–181, 2009c. doi: 10.1088/0004-637X/697/1/160.

G. J. Ferland and R. F. Mushotzky. Broad line region clouds and the absorbing material in NGC 4151. *ApJ*, 262:564–577, November 1982. doi: 10.1086/160448.

A. P. Koratkar and C. M. Gaskell. Radius-luminosity and mass-luminosity relationships for active galactic nuclei. *ApJ*, 370:L61–L64, April 1991. doi: 10.1086/185977.

K. Horne, B. M. Peterson, S. J. Collier, and H. Netzer. Observational Requirements for High-Fidelity Reverberation Mapping. *PASP*, 116:465–476, May 2004. doi: 10.1086/420755.

M. Kishimoto, S. F. Hönig, R. Antonucci, T. Kotani, R. Barvainis, K. R. W. Tristram, and G. Weigelt. Exploring the inner region of type 1 AGNs with the Keck interferometer. *A&A*, 507:L57–L60, December 2009a. doi: 10.1051/0004-6361/200913512.

M. Kishimoto, S. F. Hönig, R. Antonucci, R. Barvainis, T. Kotani, K. R. W. Tristram, G. Weigelt, and K. Levin. The innermost dusty structure in active galactic nuclei as probed by the Keck interferometer. *A&A*, 527:A121, March 2011a. doi: 10.1051/0004-6361/201016054.

M. Kishimoto, S. F. Hönig, R. Antonucci, F. Millour, K. R. W. Tristram, and G. Weigelt. Mapping the radial structure of AGN tori. *A&A*, 536:A78, December 2011b. doi: 10.1051/0004-6361/201117367.

J.-H. Woo, T. Treu, A. J. Barth, S. A. Wright, J. L. Walsh, M. C. Bentz, P. Martini, V. N. Bennert, et al. The Lick AGN Monitoring Project: The M_{BH}-σ_* Relation for Reverberation-mapped Active Galaxies. *ApJ*, 716:269–280, June 2010. doi: 10.1088/0004-637X/716/1/269.

B. M. Peterson and A. Wandel. Keplerian Motion of Broad-Line Region Gas as Evidence for Supermassive Black Holes in Active Galactic Nuclei. *ApJ*, 521: L95–L98, August 1999. doi: 10.1086/312190.

K. Gebhardt, J. Kormendy, L. C. Ho, R. Bender, G. Bower, A. Dressler, S. M. Faber, A. V. Filippenko, R. Green, C. Grillmair, T. R. Lauer, J. Magorrian, J. Pinkney, D. Richstone, and S. Tremaine. Black Hole Mass Estimates from Reverberation Mapping and from Spatially Resolved Kinematics. *ApJ*, 543: L5–L8, November 2000b. doi: 10.1086/318174.

Christopher A. Onken, Laura Ferrarese, David Merritt, Bradley M. Peterson, Richard W. Pogge, Marianne Vestergaard, and Amri Wandel. Supermassive Black Holes in Active Galactic Nuclei. II. Calibration of the Black Hole Mass-Velocity Dispersion Relationship for Active Galactic Nuclei. *ApJ*, 615:645–651, 2004. doi: 10.1086/424655.

M. Elvis and M. Karovska. Quasar Parallax: A Method for Determining Direct Geometrical Distances to Quasars. *ApJ*, 581:L67–L70, December 2002. doi: 10.1086/346015.

A. Labeyrie. Attainment of Diffraction Limited Resolution in Large Telescopes by Fourier Analysing Speckle Patterns in Star Images. *A&A*, 6:85, May 1970.

H. W. Babcock. The Possibility of Compensating Astronomical Seeing. *PASP*, 65:229, October 1953. doi: 10.1086/126606.

J. M. Beckers. Adaptive optics for astronomy - Principles, performance, and applications. *ARA&A*, 31:13–62, 1993. doi: 10.1146/annurev.aa.31.090193.000305.

J. E. Baldwin, C. A. Haniff, C. D. Mackay, and P. J. Warner. Closure phase in high-resolution optical imaging. *Nature*, 320:595–597, April 1986. doi: 10.1038/320595a0.

A. Glindemann, R. Abuter, F. Carbognani, F. Delplancke, F. Derie, A. Gennai, P. B. Gitton, P. Kervella, B. Koehler, S. A. Leveque, S. Menardi, A. Michel, F. Paresce, T. P. Duc, A. Richichi, M. Schoeller, M. Tarenghi, A. Wallander, and R. Wilhelm. The VLT Interferometer: a unique instrument for high-resolution astronomy. In P. Léna and A. Quirrenbach, editors, *Interferometry in Optical Astronomy*, volume 4006 of *Society of Photo-Optical Instrumentation Engineers (SPIE) Conference Series*, pages 2–12, July 2000.

S. Jankov. Astronomical Optical Interferometry. II. Astrophysical Results. *Serbian Astronomical Journal*, 183:1–35, December 2011. doi: 10.2298/SAJ1183001J.

R. G. Petrov. Differential Interferometry. In D. M. Alloin and J.-M. Mariotti, editors, *NATO ASIC Proc. 274: Diffraction-Limited Imaging with Very Large Telescopes*, page 249, 1989.

R. G. Petrov, F. Malbet, G. Weigelt, P. Antonelli, U. Beckmann, Y. Bresson, A. Chelli, M. Dugué, G. Duvert, et al. AMBER, the near-infrared spectro-interferometric three-telescope VLTI instrument. *A&A*, 464:1–12, March 2007. doi: 10.1051/0004-6361:20066496.

C. Haniff. An introduction to the theory of interferometry. *New Astr.*, 51:565–575, October 2007. doi: 10.1016/j.newar.2007.06.002.

R. G. Petrov, T. Elhalkouj, A. Boskri, J.-P. Folcher, S. Lagarde, Y. Bresson, Z. Benkhaldoun, M. Lazrek, and S. Rakshit. Hierarchical fringe tracking. In *Society of Photo-Optical Instrumentation Engineers (SPIE) Conference Series*, volume 9146 of *Society of Photo-Optical Instrumentation Engineers (SPIE) Conference Series*, page 2, July 2014. doi: 10.1117/12.2056677.

R. G. Petrov. Spectro-Interferometry and Differential Interferometry with Amber and The VLTI. *Publications de l'Observatoire Astronomique de Beograd*, 91: 21–34, December 2012.

A. Meilland, P. Stee, M. Vannier, F. Millour, A. Domiciano de Souza, F. Malbet, C. Martayan, F. Paresce, R. G. Petrov, A. Richichi, and A. Spang. First direct detection of a Keplerian rotating disk around the Be star α Arae using AMBER/VLTI. *A&A*, 464:59–71, March 2007. doi: 10.1051/0004-6361:20064848.

R. G. Petrov, F. Millour, S. Lagarde, M. Vannier, S. Rakshit, A. Marconi, and G. weigelt. VLTI/AMBER differential interferometry of the broad-line region of the quasar 3C273. In *Society of Photo-Optical Instrumentation Engineers (SPIE) Conference Series*, volume 8445 of *Society of Photo-Optical Instrumentation Engineers (SPIE) Conference Series*, July 2012. doi: 10.1117/12.926595.

P. R. Lawson, W. D. Cotton, C. A. Hummel, F. Baron, J. S. Young, S. Kraus, K.-H. Hofmann, G. P. Weigelt, M. Ireland, et al. 2006 interferometry imaging beauty contest. In *Society of Photo-Optical Instrumentation Engineers (SPIE) Conference Series*, volume 6268 of *Society of Photo-Optical Instrumentation Engineers (SPIE) Conference Series*, page 1, June 2006. doi: 10.1117/12.670409.

S. Rakshit and R. G. Petrov. AGN BLR structure, luminosity and mass from combined reverberation mapping and optical interferometry observations. In *Society of Photo-Optical Instrumentation Engineers (SPIE) Conference Series*, volume 9146 of *Society of Photo-Optical Instrumentation Engineers (SPIE) Conference Series*, page 0, July 2014. doi: 10.1117/12.2056436.

J. M. Beckers. Differential speckle interferometry. *Optica Acta*, 29:361–362, April 1982. doi: 10.1080/713820871.

R. Arsenault, J. Alonso, H. Bonnet, J. Brynnel, B. Delabre, R. Donaldson, C. Dupuy, E. Fedrigo, J. Farinato, N. N. Hubin, L. Ivanescu, M. E. Kasper, J. Paufique, S. Rossi, S. Tordo, S. Stroebele, J.-L. Lizon, P. Gigan, F. Delplancke, A. Silber, M. Quattri, and R. Reiss. MACAO-VLTI: An Adaptive Optics system for the ESO VLT interferometer. In P. L. Wizinowich and D. Bonaccini, editors, *Adaptive Optical System Technologies II*, volume 4839 of *Society of Photo-Optical Instrumentation Engineers (SPIE) Conference Series*, pages 174–185, February 2003. doi: 10.1117/12.458836.

F. Puech, S. Lévêque, M. Sarazin, and R. J. Mathar. Temperature and humidity environmental conditions in the VLTI. In *Society of Photo-Optical Instrumentation Engineers (SPIE) Conference Series*, volume 6268 of *Society of Photo-Optical Instrumentation Engineers (SPIE) Conference Series*, page 40, June 2006. doi: 10.1117/12.671453.

C. Leinert, U. Graser, F. Przygodda, L. B. F. M. Waters, G. Perrin, W. Jaffe, B. Lopez, E. J. Bakker, A. Böhm, O. Chesneau, W. D. Cotton, et al. MIDI - the 10 \mum instrument on the VLTI. *Ap&SS*, 286:73–83, 2003. doi: 10.1023/A:1026158127732.

J.-B. Le Bouquin, J.-P. Berger, B. Lazareff, G. Zins, P. Haguenauer, L. Jocou, P. Kern, R. Millan-Gabet, W. Traub, et al. PIONIER: a 4-telescope visitor instrument at VLTI. *A&A*, 535:A67, November 2011. doi: 10.1051/0004-6361/201117586.

B. Lopez, S. Wolf, S. Lagarde, P. Abraham, P. Antonelli, J. C. Augereau, U. Beckman, J. Behrend, N. Berruyer, et al. MATISSE: perspective of imaging in the mid-infrared at the VLTI. In *Society of Photo-Optical Instrumentation Engineers (SPIE) Conference Series*, volume 6268 of *Society of Photo-Optical Instrumentation Engineers (SPIE) Conference Series*, page 0, June 2006. doi: 10.1117/12.671636.

F. Eisenhauer, G. Perrin, W. Brandner, C. Straubmeier, A. Richichi, S. Gillessen, J. P. Berger, S. Hippler, A. Eckart, et al. GRAVITY: getting to the event horizon of Sgr A*. In *Society of Photo-Optical Instrumentation Engineers (SPIE) Conference Series*, volume 7013 of *Society of Photo-Optical Instrumentation Engineers (SPIE) Conference Series*, July 2008. doi: 10.1117/12.788407.

E. Tatulli, F. Millour, A. Chelli, G. Duvert, B. Acke, O. Hernandez Utrera, K.-H. Hofmann, S. Kraus, F. Malbet, et al. Interferometric data reduction with AMBER/VLTI. Principle, estimators, and illustration. *A&A*, 464:29–42, March 2007. doi: 10.1051/0004-6361:20064799.

A. Chelli, O. H. Utrera, and G. Duvert. Optimised data reduction for the AMBER/VLTI instrument. *A&A*, 502:705–709, August 2009. doi: 10.1051/0004-6361/200811039.

A. Marconi, R. Maiolino, and R. G. Petrov. Extragalactic Astronomy with the VLTI: a new window on the Universe. *Ap&SS*, 286:245–254, 2003. doi: 10.1023/A:1026100831792.

P. Berio, D. Mourard, D. Bonneau, O. Chesneau, P. Stee, N. Thureau, F. Vakili, and J. Borgnino. Spectrally resolved Michelson stellar interferometry. I. Exact formalism in the multispeckle mode. *Journal of the Optical Society of America A*, 16:872–881, April 1999. doi: 10.1364/JOSAA.16.000872.

G. Li Causi, S. Antoniucci, and E. Tatulli. De-biasing interferometric visibilities in VLTI-AMBER data of low SNR observations. *A&A*, 479:589–595, February 2008. doi: 10.1051/0004-6361:20077629.

E. Rokaki, A. Lawrence, F. Economou, and A. Mastichiadis. Is there a disc in the superluminal quasars? *MNRAS*, 340:1298–1308, April 2003. doi: 10.1046/j.1365-8711.2003.06414.x.

M. Eracleous and J. P. Halpern. Doubled-peaked emission lines in active galactic nuclei. *ApJ*, 90:1–30, January 1994. doi: 10.1086/191856.

J. E. Smith, A. Robinson, S. Young, D. J. Axon, and E. A. Corbett. Equatorial scattering and the structure of the broad-line region in Seyfert nuclei: evidence for a rotating disc. *MNRAS*, 359:846–864, May 2005. doi: 10.1111/j.1365-2966.2005.08895.x.

S. Fine, S. M. Croom, P. F. Hopkins, L. Hernquist, J. Bland-Hawthorn, M. Colless, P. B. Hall, L. Miller, A. D. Myers, R. Nichol, K. A. Pimbblet, N. P. Ross, D. P. Schneider, T. Shanks, and R. G. Sharp. Constraining the quasar population with the broad-line width distribution. *MNRAS*, 390:1413–1429, November 2008. doi: 10.1111/j.1365-2966.2008.13691.x.

S. Fine, S. M. Croom, J. Bland-Hawthorn, K. A. Pimbblet, N. P. Ross, D. P. Schneider, and T. Shanks. The CIV linewidth distribution for quasars and its implications for broad-line region dynamics and virial mass estimation. *MNRAS*, 409:591–610, December 2010. doi: 10.1111/j.1365-2966.2010.17107.x.

M. R. Goad, K. T. Korista, and A. J. Ruff. The broad emission-line region: the confluence of the outer accretion disc with the inner edge of the dusty torus. *MNRAS*, 426:3086–3111, 2012. doi: 10.1111/j.1365-2966.2012.21808.x.

C. J. Grier, B. M. Peterson, K. Horne, M. C. Bentz, R. W. Pogge, K. D. Denney, G. De Rosa, P. Martini, C. S. Kochanek, Y. Zu, B. Shappee, et al. The Structure of the Broad-line Region in Active Galactic Nuclei. I. Reconstructed Velocity-delay Maps. *ApJ*, 764:47, February 2013. doi: 10.1088/0004-637X/764/1/47.

A. Pancoast, B. J. Brewer, and T. Treu. Geometric and Dynamical Models of Reverberation Mapping Data. *ApJ*, 730:139, April 2011. doi: 10.1088/0004-637X/730/2/139.

A. Pancoast, B. J. Brewer, and T. Treu. Modelling reverberation mapping data - I. Improved geometric and dynamical models and comparison with cross-correlation results. *MNRAS*, 445:3055–3072, December 2014b. doi: 10.1093/mnras/stu1809.

P. T. O'Brien, M. R. Goad, and P. M. Gondhalekar. Response Functions as Diagnostics of the Broadline Region in Active Galactic Nuclei - Part Two - Anisotropic Line Emission. *MNRAS*, 268:845, June 1994.

P. Stee. On the kinematics of the envelope of γ Cassiopeiae. *A&A*, 311:945–950, July 1996.

W. F. Welsh and K. Horne. Echo images of broad-line regions in active Galactic nuclei. *ApJ*, 379:586–591, October 1991. doi: 10.1086/170530.

M. Kishimoto, S. F. Hönig, T. Beckert, and G. Weigelt. The innermost region of AGN tori: implications from the HST/NICMOS type 1 point sources and near-IR reverberation. *A&A*, 476:713–721, December 2007. doi: 10.1051/0004-6361:20077911.

M. Kishimoto, S. F. Hönig, K. R. W. Tristram, and G. Weigelt. Possible evidence for a common radial structure in nearby AGN tori. *A&A*, 493:L57–L60, January 2009b. doi: 10.1051/0004-6361:200811062.

M. C. Bentz, K. Horne, A. J. Barth, V. N. Bennert, G. Canalizo, A. V. Filippenko, E. L. Gates, M. A. Malkan, T. Minezaki, T. Treu, J.-H. Woo, and J. L. Walsh. The Lick AGN Monitoring Project: Velocity-delay Maps from the Maximum-entropy Method for Arp 151. *ApJ*, 720:L46–L51, September 2010b. doi: 10.1088/2041-8205/720/1/L46.

A. Meilland, F. Millour, S. Kanaan, P. Stee, R. Petrov, K.-H. Hofmann, A. Natta, and K. Perraut. First spectro-interferometric survey of Be stars. I. Observations and constraints on the disk geometry and kinematics. *A&A*, 538:A110, February 2012. doi: 10.1051/0004-6361/201117955.

A. Chalabaev. Photocenter Versus Wavelength for a Gaseous Disk Envelope. In J. M. Beckers and F. Merkle, editors, *European Southern Observatory Conference and Workshop Proceedings*, volume 39 of *European Southern Observatory Conference and Workshop Proceedings*, page 403, March 1992.

M. Goad and I. Wanders. The Effect of a Variable Anisotropic Continuum Source upon the Broad Emission Line Profiles and Responses. *ApJ*, 469:113, September 1996. doi: 10.1086/177764.

D. Foreman-Mackey, D. W. Hogg, D. Lang, and J. Goodman. emcee: The MCMC Hammer. *PASP*, 125:306–312, March 2013. doi: 10.1086/670067.

J. Goodman and J. Weare. Ensemble samplers with affine invariance. *Commun. Appl. Math. Comput. Sci.*, 5:65, 2010. doi: 10.2140/camcos.2010.5.65.

K. D. Denney, B. M. Peterson, R. W. Pogge, A. Adair, D. W. Atlee, K. Au-Yong, M. C. Bentz, J. C. Bird, D. J. Brokofsky, et al. Reverberation Mapping Measurements of Black Hole Masses in Six Local Seyfert Galaxies. *ApJ*, 721: 715–737, September 2010. doi: 10.1088/0004-637X/721/1/715.

J. E. Greene, C. Y. Peng, M. Kim, C.-Y. Kuo, J. A. Braatz, C. M. V. Impellizzeri, J. J. Condon, K. Y. Lo, C. Henkel, and M. J. Reid. Precise Black Hole Masses from Megamaser Disks: Black Hole-Bulge Relations at Low Mass. *ApJ*, 721: 26–45, September 2010. doi: 10.1088/0004-637X/721/1/26.

R. G. Conway, S. T. Garrington, R. A. Perley, and J. A. Biretta. Synchrotron radiation from the jet of 3C 273. II - The radio structure and polarization. *A&A*, 267:347–362, January 1993.

S. C. Unwin, M. H. Cohen, J. A. Biretta, T. J. Pearson, G. A. Seielstad, R. C. Walker, R. S. Simon, and R. P. Linfield. VLBI monitoring of the superluminal quasar 3C 273, 1977-1982. *ApJ*, 289:109–119, February 1985. doi: 10.1086/162868.

W. Kundt and Gopal-Krishna. The jet of the quasar 3C 273. *Journal of Astrophysics and Astronomy*, 7:225–236, September 1986. doi: 10.1007/BF02714211.

R. G. Conway and R. J. Davis. Synchrotron radiation from the jet of 3C 273. 3: The speed and direction of the jet. *A&A*, 284:724–730, April 1994.

M. S. Mikhailova, E. Y. Bannikova, and V. M. Kontorovich. Determining the Inclination of the Kiloparsec-Scale Jet of the Quasar 3C 273 Based on Competition

of Mechanisms for the Knot X-ray Emission. *Astronomy Reports*, 54:481–488, June 2010. doi: 10.1134/S1063772910060016.

Ł. Stawarz. On the Jet Activity in 3C 273. *ApJ*, 613:119–128, September 2004. doi: 10.1086/423022.

S. Paltani, T. J.-L. Courvoisier, and R. Walter. The blue-bump of 3C 273. *A&A*, 340:47–61, December 1998.

T. J.-L. Courvoisier, E. I. Robson, D. H. Hughes, A. Blecha, P. Bouchet, K. Krisciunas, and H. E. Schwarz. Rapid infrared and optical variability in the bright quasar 3C273. *Nature*, 335:330–333, September 1988. doi: 10.1038/335330a0.

J. N. Bahcall, S. Kirhakos, D. P. Schneider, R. J. Davis, T. W. B. Muxlow, S. T. Garrington, R. G. Conway, and S. C. Unwin. Hubble Space Telescope and MERLIN Observations of the Jet in 3C 273. *ApJ*, 452:L91, October 1995. doi: 10.1086/309717.

S. Rakshit, R. G. Petrov, A. Meilland, and S. F. Hönig. Differential interferometry of QSO broad-line regions - I. Improving the reverberation mapping model fits and black hole mass estimates. *MNRAS*, 447:2420–2436, March 2015. doi: 10.1093/mnras/stu2613.

H. Landt, M. J. Ward, M. Elvis, and M. Karovska. Constraints on the outer radius of the broad emission line region of active galactic nuclei. *MNRAS*, 439: 1051–1062, March 2014. doi: 10.1093/mnras/stu031.

M. R. Goad. PhD thesis, , Univ. College London, (1995), 1995.

S. Paltani and M. Türler. The mass of the black hole in 3C 273. *A&A*, 435: 811–820, June 2005. doi: 10.1051/0004-6361:20041206.

A. W. Graham, C. A. Onken, E. Athanassoula, and F. Combes. An expanded M_{bh}-σ diagram, and a new calibration of active galactic nuclei masses. *MNRAS*, 412:2211–2228, April 2011. doi: 10.1111/j.1365-2966.2010.18045.x.

J. A. Meisner, W. J. Jaffe, and R. S. Le Poole. The Nova Fringe Tracker: a second-generation cophasing facility for up to six telescopes at the VLTI. In *SPIE conference series*, volume 8445 of *Proc SPIE*, July 2012. doi: 10.1117/12.927136.

R. Petrov, F. Roddier, and C. Aime. Signal-to-noise ratio in differential speckle interferometry. *Journal of the Optical Society of America A*, 3:634–644, May 1986. doi: 10.1364/JOSAA.3.000634.

M. Vannier, R. G. Petrov, B. Lopez, and F. Millour. Colour-differential interferometry for the observation of extrasolar planets. *MNRAS*, 367:825–837, April 2006. doi: 10.1111/j.1365-2966.2006.10015.x.

S. Lagarde, S. Robbe-Dubois, R. G. Petrov, B. Lopez, W. J. Jaffe, L. Venema, P. Berio, P. Antonelli, et al. MATISSE: concept, specifications, and performances. In *Society of Photo-Optical Instrumentation Engineers (SPIE) Conference Series*, volume 8445 of *Society of Photo-Optical Instrumentation Engineers (SPIE) Conference Series*, July 2012. doi: 10.1117/12.926285.

H. Landt, M. C. Bentz, M. J. Ward, M. Elvis, B. M. Peterson, K. T. Korista, and M. Karovska. The Near-Infrared Broad Emission Line Region of Active Galactic Nuclei. I. The Observations. *ApJ*, 174:282–312, February 2008. doi: 10.1086/522373.

S. F. Hönig, D. Watson, M. Kishimoto, and J. Hjorth. A dust-parallax distance of 19 megaparsecs to the supermassive black hole in NGC 4151. *Nature*, 515: 528–530, November 2014. doi: 10.1038/nature13914.

B. Lopez, S. Lagarde, P. Antonelli, W. Jaffe, et al. Perspective of imaging in the mid-infrared at the Very Large Telescope Interferometer. In *SPIE conference series*, volume 8445 of *Proc SPIE*, July 2012. doi: 10.1117/12.926238.

J. D. Monnier, S. Kraus, D. Buscher, J.-P. Berger, C. Haniff, M. Ireland, L. Labadie, S. Lacour, H. Le Coroller, R. G. Petrov, J.-U. Pott, S. Ridgway, J. Surdej, T. ten Brummelaar, P. Tuthill, and G. van Belle. Planet formation imager (PFI): introduction and technical considerations. In *Society of Photo-Optical Instrumentation Engineers (SPIE) Conference Series*, volume 9146 of *Society of Photo-Optical Instrumentation Engineers (SPIE) Conference Series*, page 10, July 2014. doi: 10.1117/12.2057262.

S. M. Carroll, W. H. Press, and E. L. Turner. The cosmological constant. *ARA&A*, 30:499–542, 1992. doi: 10.1146/annurev.aa.30.090192.002435.

A. G. Riess, A. V. Filippenko, P. Challis, A. Clocchiatti, A. Diercks, P. M. Garnavich, R. L. Gilliland, C. J. Hogan, et al. Observational Evidence from Supernovae for an Accelerating Universe and a Cosmological Constant. *Astrophys. J.*, 116:1009–1038, September 1998. doi: 10.1086/300499.

S. Perlmutter, G. Aldering, G. Goldhaber, R. A. Knop, P. Nugent, P. G. Castro, S. Deustua, S. Fabbro, A. Goobar, et al. Measurements of Ω and Λ from 42 High-Redshift Supernovae. *ApJ*, 517:565–586, June 1999. doi: 10.1086/307221.

A. G. Riess, P. E. Nugent, R. L. Gilliland, B. P. Schmidt, J. Tonry, M. Dickinson, and R. I. Thompson. The Farthest Known Supernova: Support for an Accelerating Universe and a Glimpse of the Epoch of Deceleration. *ApJ*, 560:49–71, October 2001. doi: 10.1086/322348.

M. Haas, R. Chini, M. Ramolla, F. Pozo Nuñez, C. Westhues, R. Watermann, V. Hoffmeister, and M. Murphy. Photometric AGN reverberation mapping - an efficient tool for BLR sizes, black hole masses, and host-subtracted AGN luminosities. *A&A*, 535:A73, November 2011. doi: 10.1051/0004-6361/201117325.

D. Watson, K. D. Denney, M. Vestergaard, and T. M. Davis. A New Cosmological Distance Measure Using Active Galactic Nuclei. *ApJ*, 740:L49, October 2011. doi: 10.1088/2041-8205/740/2/L49.

B. Czerny, K. Hryniewicz, I. Maity, A. Schwarzenberg-Czerny, P. T. Życki, and M. Bilicki. Towards equation of state of dark energy from quasar monitoring: Reverberation strategy. *A&A*, 556:A97, August 2013. doi: 10.1051/0004-6361/201220832.

Y. Kobayashi, Y. Yoshii, B. A. Peterson, T. Minezaki, K. Enya, M. Suganuma, and T. Yamamuro. Multicolor imaging photometer for the MAGNUM project. In A. M. Fowler, editor, *Infrared Astronomical Instrumentation*, volume 3354 of *Society of Photo-Optical Instrumentation Engineers (SPIE) Conference Series*, pages 769–776, August 1998.

V. L. Oknyanskij. On the Possibility for Measuring the Hubble Constant from Optical-to-NIR Variability Time Delay in AGNs. *Odessa Astronomical Publications*, 12:99, 1999.

Y. Yoshii, Y. Kobayashi, and T. Minezaki. The dust distribution in the central region of AGNs: New results from the MAGNUM telescope. *Astronomische Nachrichten*.

S. F. Hönig. Dust Reverberation Mapping in the Era of Big Optical Surveys and its Cosmological Application. *ApJ*, 784:L4, March 2014. doi: 10.1088/2041-8205/784/1/L4.

B. C. Kelly, J. Bechtold, and A. Siemiginowska. Are the Variations in Quasar Optical Flux Driven by Thermal Fluctuations? *ApJ*, 698:895, June 2009. doi: 10.1088/0004-637X/698/1/895.

C. L. MacLeod, Ž. Ivezić, C. S. Kochanek, S. Kozłowski, B. Kelly, E. Bullock, A. Kimball, B. Sesar, D. Westman, K. Brooks, R. Gibson, A. C. Becker, and W. H. de Vries. Modeling the Time Variability of SDSS Stripe 82 Quasars as a Damped Random Walk. *ApJ*, 721:1014–1033, October 2010. doi: 10.1088/0004-637X/721/2/1014.

Y.-R. Li, J.-M. Wang, L. C. Ho, P. Du, and J.-M. Bai. A Bayesian Approach to Estimate the Size and Structure of the Broad-line Region in Active Galactic Nuclei Using Reverberation Mapping Data. *ApJ*, 779:110, December 2013. doi: 10.1088/0004-637X/779/2/110.

K. Nobuta, M. Akiyama, Y. Ueda, M. G. Watson, J. Silverman, K. Hiroi, K. Ohta, F. Iwamuro, K. Yabe, N. Tamura, et al. Black Hole Mass and Eddington Ratio Distribution Functions of X-Ray-selected Broad-line AGNs at z ˜ 1.4 in the Subaru XMM-Newton Deep Field. *ApJ*, 761:143, December 2012. doi: 10.1088/0004-637X/761/2/143.

D. J. Earl and M. W. Deem. Parallel tempering: Theory, applications, and new perspectives. *Physical Chemistry Chemical Physics (Incorporating Faraday Transactions)*, 7:3910, 2005. doi: 10.1039/b509983h.

A. J. Barth, V. N. Bennert, G. Canalizo, A. V. Filippenko, E. L. Gates, J. E. Greene, W. Li, M. A. Malkan, A. Pancoast, D. J. Sand, D. Stern, et al. The Lick AGN Monitoring Project 2011: Spectroscopic Campaign and Emission-Line Light Curves. *ArXiv e-prints*, March 2015.

H. Landt, M. J. Ward, B. M. Peterson, M. C. Bentz, M. Elvis, K. T. Korista, and M. Karovska. A near-infrared relationship for estimating black hole masses in active galactic nuclei. *MNRAS*, 432:113–126, June 2013. doi: 10.1093/mnras/stt421.

D. Trevese, M. Perna, F. Vagnetti, F. G. Saturni, and M. Dadina. C IV and C III] Reverberation Mapping of the Luminous Quasar PG 1247+267. *ApJ*, 795: 164, November 2014. doi: 10.1088/0004-637X/795/2/164.

J. Stern, J. F. Hennawi, and J.-U. Pott. Spatially Resolving the Kinematics of the 100 {\mu}as Quasar Broad Line Region using Spectroastrometry. *ArXiv e-prints*, February 2015.

M. Elvis. Astronomy: Cosmic triangles and black-hole masses. *Nature*, 515:498–499, November 2014. doi: 10.1038/515498a.

G. De Rosa, B. M. Peterson, J. Ely, G. A. Kriss, D. M. Crenshaw, et al. Space Telescope and Optical Reverberation Mapping Project. I. Ultraviolet Observations of the Seyfert 1 Galaxy NGC 5548 with the Cosmic Origins Spectrograph on Hubble Space Telescope. *ArXiv e-prints*, January 2015.

F. Pozo Nuñez, M. Ramolla, C. Westhues, C. Bruckmann, M. Haas, R. Chini, K. Steenbrugge, and M. Murphy. Photometric reverberation mapping of 3C 120. *A&A*, 545:A84, September 2012. doi: 10.1051/0004-6361/201219107.

F. Pozo Nuñez, M. Haas, M. Ramolla, C. Bruckmann, C. Westhues, R. Chini, K. Steenbrugge, R. Lemke, M. Murphy, and W. Kollatschny. Modelling photometric reverberation data: a disk-like broad-line region and a potentially larger black hole mass for 3C 120. *A&A*, 568:A36, August 2014. doi: 10.1051/0004-6361/201322736.

S. Proft and J. Wambsganss. Exploration of quasars with the Gaia mission. *A&A*, 574:A46, January 2015. doi: 10.1051/0004-6361/201323280.